



Development of transition metal-free photochemical CO₂ reduction enabled by photosensitized regeneration of organohydride

謝, 衛斌

(Degree)

博士 (理学)

(Date of Degree)

2022-09-25

(Date of Publication)

2024-09-25

(Resource Type)

doctoral thesis

(Report Number)

甲第8428号

(URL)

<https://hdl.handle.net/20.500.14094/0100477854>

※ 当コンテンツは神戸大学の学術成果です。無断複製・不正使用等を禁じます。著作権法で認められている範囲内で、適切にご利用ください。



Doctoral Dissertation

**Development of transition metal-free photochemical CO₂
reduction enabled by photosensitized regeneration of
organohydride**

(有機ヒドリドの光再生を利用する非遷移金属触媒系 CO₂光還元反応の開発)

July 2022

**Graduate School of Science
Kobe University**

**Weibin Xie
謝衛斌**

Table of contents

1. Introduction.....	1
1.1. Background.....	1
1.1.1. An overview on global energy.....	1
1.1.2. Current status: carbon dioxide emission.....	2
1.1.3. Utilization of formic acid.....	3
1.1.4. General principle of photoredox catalysis.....	3
1.2. Carbon dioxide fixation.....	7
1.2.1. Carbon capture and storage.....	7
1.2.2. Carbon capture and utilization.....	7
1.2.2.1. Thermochemical conversion of carbon dioxide.....	7
1.2.2.2. Electrochemical conversion of carbon dioxide.....	8
1.2.2.3. Photocatalytic conversion of carbon dioxide.....	13
1.2.2.4. Organocatalytic conversion of carbon dioxide.....	19
2. Objectives.....	22
2.1. Previous work in our group and related report.....	22
2.2. proposal hypothesis of this work.....	24
3. Study on photocatalytic CO ₂ reduction enabled by dual catalysts.....	25
3.1. Feasibility of proposal.....	25
3.2. Demonstration of solution.....	27
3.3. Optimization of conditions and control reactions.....	27
3.4. Determination of the carbon source of formate product by labeling experiment.....	29
3.5. Investigation of gas evolution (H ₂ or CO) from photoinduced CO ₂ RR by GC.....	30
3.6. Demonstration of formation of oxalate in photoinduced CO ₂ RR.....	32
3.7. Investigation of potential photosensitizers.....	33
4. Study on photocatalytic CO ₂ reduction enabled by integrated-form catalysts.....	36
4.1. Design and synthesis of integrated-form catalysts.....	36
4.2. Exploitation of electron donor-acceptor complex.....	40
4.3. Activities of integrated-form catalysts.....	41
5. Study on stability and activity of photocatalysts and co-catalyst.....	42
6. The effects of reaction temperature on photoinduced CO ₂ RR.....	44
7. Investigation of mechanism.....	45
7.1. The reason of more than theoretical yield.....	45
7.2. The Stern-Volmer experiment.....	46
7.3. Exciplex between PC 1 and BI ⁺ (I ⁻).....	49
7.4. Optoelectronic data of PC 5 and BI ⁺ (I ⁻).....	49
7.5. Generation of 5 ^{•+} absorption bands based on magic blue experiment.....	52
7.6. Certification of 5 ^{•+} using transient absorption spectroscopy.....	54
7.7. Judgment of the reversibility of photocatalytic CO ₂ RR.....	59
7.8. Investigation of benzimidazole-based hydride for CO ₂ reduction to formate.....	59
7.9. Proposed mechanism for photoinduced reduction of CO ₂	61
8. Absorption and fluorescence spectra of photocatalysts, BI ⁺ (I ⁻) and BI ⁺ (BF ₄ ⁻).....	63
9. Photoluminescence quantum yields of photocatalysts.....	64
10. Fluorescence lifetime.....	65

11. Determination of light intensity	67
12. Determination of the quantum yield for photocatalytic CO ₂ RR	69
13. Conclusions.....	70
14. Synthesis experiments.....	72
15. Computational study on carbazole radical cation and BI radical.....	84
16. Reference	102
17. NMR spectra	108
18. List of publications.....	132

Abbreviations

CO ₂	Carbon dioxide
BIH	1,2,3-Trimethyl-2,3-dihydro-1 <i>H</i> -benzo[<i>d</i>]imidazole
BI ⁺ (I ⁻)	1,2,3-Trimethyl-1 <i>H</i> -benzo[<i>d</i>]imidazol-3-ium iodide
TON	Turnover number
TOF	Turnover frequency
GC	Gas chromatography
NADPH	Nicotinamide adenine dinucleotide phosphate
ATP	Adenosine triphosphate
ppm	Parts per million
HCO ₂ H	Formic acid
UV	Ultraviolet
BDE	Bond dissociation energy
HOMO	Highest occupied orbital
LUMO	Lowest unoccupied orbital
MLCT	Metal to ligand charge transfer
ISC	Intersystem crossing
PET	Photoinduced electron transfer
PC	Photocatalyst
CCS	Carbon capture and storage
MOFS	Metallic-organic frameworks
TEOA	Triethanolamine
TEA	Triethylamine
SET	Single electron transfer
L	Ligand
TiO ₂	Titanium dioxide
g-C ₃ N ₄	Graphitic carbon nitride
RGO	Graphene oxide
G	Graphene pristine
GO	Graphene oxide
ATA	2-Aminoterephthalate

DTA	2,5-Diaminoterephthalate
COPs	Conjugated organic polymers
TMP	2,2,6,6-Tetramethylpiperidine
NHCs	<i>N</i> -heterocyclic carbenes
CAR	<i>N</i> -ethyl-3,6-bis(dimethylamino)carbazole
CV	Cyclic voltammetry
NMR	Nuclear magnetic resonance
CO ₂ RR	CO ₂ reduction reaction
CHD	1,4-Cyclohexadiene
DMSO	Dimethyl sulfoxide
DMA	<i>N, N</i> -Dimethylacetamide
H ₂ A	Ascorbic acid
A	Dehydroascorbic acid
TMB	1,3,5-Trimethoxybenzene
4CzIPN	2,4,5,6-Tetra(9 <i>H</i> -carbazol-9-yl)isophthalonitrile
EDA	Electron donor-acceptor
BI ⁺ (BF ₄ ⁻)	1,2,3-Trimethyl-2,3-dihydro-1 <i>H</i> -benzo[<i>d</i>]imidazole tetrafluoroborate
IS	Internal standard
TD-DFT	Time-dependent density functional theory
SCE	Saturated calomel electrode
HAT	Hydrogen atom transfer
DFT	Density functional theory
THF	Tetrahydrofuran
DMF	Dimethylformamide

ABSTRACT

The ever-increasing demand for fossil fuels has exacerbated dramatic energy shortages and massive greenhouse gas emissions, particularly carbon dioxide. Using energy sources from sustainable sunlight to convert carbon dioxide into value-added chemicals is a flawless strategy to address the current predicament. As a thermodynamically stable gas (CO_2), its reduction requires a high energy intake. Besides, the selectivity of the formed products deserves consideration. Accordingly, developing an efficient photocatalytic system is an indispensable key to achieving a photocatalysis-based carbon dioxide to be reduced and practical solar energy storage.

Formic acid as a two-electron reduced product of carbon dioxide is widely adopted in the chemical industry as reductant, acid, preservatives, and C1 carbon source, in addition to serve as organic hydrogen carriers. To date, photochemical reduction of CO_2 into formic acid via transitional metal complexes or semiconductor materials as photocatalysts has been regarded as a readily effective approach. In contrast, metal-free organomolecules generally possess neither strong absorption to visible light nor enough reduction capability for CO_2 . Therefore, metal-free organomolecule as photocatalyst for photochemical conversion of CO_2 to HCOOH is exceptional.

We recently found that (dimethylamino)carbazole moieties with strong reduction ability of its excited state can function as visible light-driven photocatalysts well. We utilized the advantage to achieve photocatalytic cycle to provide electrons for regeneration of **BIH** from **BI⁺(I)**. Additionally, it was experimentally suggested that **BIH** can be captured by CO_2 radical anion along with **BI⁺(I)** and HCOO^- generated by hydrogen atom transfer. Herein, photochemical catalytic CO_2 reduction to formate has been demonstrated comprising carbazole moiety as a practical light-driven photocatalysts, benzimidazoline-based organohydride as co-catalyst, and ascorbic acid as a reductant under visible-light 400 nm of irradiation. In this case, photocatalyst and co-catalyst manifested strong durability and fast rate: based on photocatalyst ($\text{TON}_{\text{HCOO}^-} = 8820$ and $\text{TOF}_{\text{HCOO}^-} = 2205 \text{ h}^{-1}$) and based on co-catalyst ($\text{TON}_{\text{HCOO}^-} = 6070$ and $\text{TOF}_{\text{HCOO}^-} = 1520 \text{ h}^{-1}$). Current reaction system for photocatalytic CO_2 reduction reaction showed exclusive selectivity to yield formate as a sole product, while formaldehyde, oxalate, CO , and H_2 as potential evolved products were not detected by ^{13}C -labeling experiment and GC-based quantitative analysis of evolved gases experiment.

Keywords: photochemical reduction of CO_2 ; carbazole; metal-free catalyst; regeneration of **BIH**; HCOO^- .

Acknowledgements

My utmost gratitude goes to my supervisor- Associate Professor Ryosuke Matsubara who has accepted me as a member of his research team. His expertise and unwavering support have been invaluable throughout my research journey in Japan. I am indebted to Associate Professor Ryosuke Matsubara for going beyond the supervisions and tutelages of a supervisor and rendering me friendship.

Second, I would like to acknowledge Professor Masahiko Hayashi for his insightful feedback and precious advice, which has driven me to my thinking and reasoning throughout my research work.

Heartfelt thanks to my colleague- Suguru Murakami for his firm assistance in my research study, as well as life. Similarly, I would like to express my thankfulness to my laboratory comrades for their selfless assistance.

I would like to specially thank Professor Kobori, Assistant Professor Fuki, and Mr. Katsuhira for their assistance on carrying out fluorescence lifetime analysis and time-resolved absorption spectroscopy analysis. Besides, I would like to acknowledge Professor Tachikawa and Dr. Zhang for helping on the phosphorescence and GC analysis.

Special thanks to Mr. Ubaidah for his diligence in initial investigation of this work; Mr. Xu for his kind co-operation in carrying out the experiments of this study, as well as Assistant Professor Yabuta for the stimulating discussions.

Besides, I am incredibly grateful to my parents, who work hard to provide a comfortable and warm environment for me. They not only financially support me but also give encouragement and motivation on the path of my doctoral study. Without their assistance and support, I would not have been able to travel to Japan to further my studies and complete my personal goals.

This journey would not have been the same without the support from these personnel. Each of them has provided me with the essential tools that directed me to complete this research successfully.

1. Introduction

1.1. Background

1.1.1. An overview on global energy

In ancient times, wood and solar light served as mankind’s basic energy sources to engage in various activities in daily life. The progress in human civilization oversaw the development of science and technology. Thus, humans began their quest to explore more potential value-added fuels to compensate for energy depletion. In the mid-19th century, the Industrial Revolution created a shift from agricultural societies to more industrialized and urbanized ones. Under this new industrial era, coal replaced wood as the primary source of energy. Subsequently, oil and organic combustible gas were introduced to become primary sources of energy supply. These non-sustainable fossil fuels played a dominant role in the global energy supply chain. In 2019,¹ more than 84% of global energy depletion originated from unsustainable fossil fuels: mainly including 27% of coal, 33.1% of oil and 24.3% of gas. However, renewable energy or low-carbon source was only capable of supplying between 11% to 16% or so. With rapid industrial and population growth in the 21st century, the global demand for fossil fuel energy was increasing (Figure 1.1), thus, gravely threatening environmental sustainability.

Without a doubt, energy is intricately linked to human development and societal progress.² The pressing issues of energy shortages and increasing concentrations of greenhouse gas emissions (i.e., carbon dioxide) prompts humans to seek a solution. The issue of fossil fuel depletion may be resolved by shifting energy sources to low-carbon energy or sustainable energy sources, like as: hydropower, wind, solar, and nuclear. Alternatively, a promising approach lies in the reduction of carbon dioxide as feedstock to value-added fuels by using the renewable sunlight energy as an energy input. The mentioned approach as an environmentally friendly method of converting carbon dioxide to various useful low-carbon fuels is more appealing; and could potentially close the cycle on carbon sequestration programs.³⁻⁴

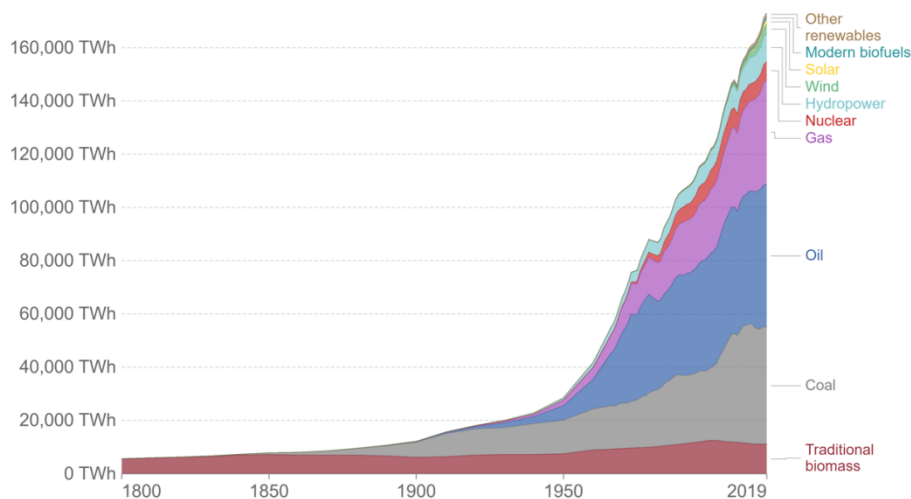


Figure 1.1. Source of global primary energy depletion. Figure is reproduced from Ritchie, H. et al.¹

1.1.2. Current status: carbon dioxide emission

In nature, green plants and other organisms absorb solar light as an energy source that splits water into oxygen and hydrogen which are then converted into NADPH/H⁺ during light reaction. Accordingly, NADPH is transduced via ATP synthase to produce ATP with the assistance of proton-motive force. In dark reactions, the ATP drives the reduction of CO₂ to more useful organic compounds.⁵⁻⁶ Hence, sunlight and CO₂ are stored in plants via photosynthesis. After millions of years, complex anaerobic fermentation of dead plants and animal carcasses forms fossil fuel resources which release CO₂ by combustion.⁷ Besides, CO₂ is generated and released into the atmosphere during respiratory processes in animals (Figure 1.2). Carbon dioxide plays an important part in the ecosystem.

With the dramatic increase in the global demand for energy consumption as exemplarily observed in the power and transportation industry, excessive carbon dioxide emission has become pressing concerns.⁸ Moreover, CO₂, the most major greenhouse gas at the surface of the Earth's atmosphere has a serious impact on climate change which causes global warming and rise in sea-levels.⁹ The atmospheric concentration of CO₂ oversees an obvious accumulation, going from around 277 ppm (parts per million) of 1750 year to 409.85 ppm of 2019 year. (Figure 1.3).¹⁰ Apart from the natural carbon element cycle that disseminates carbon dioxide between the atmospheric, oceanic, and terrestrial biosphere reservoir, anthropogenic emission of carbon dioxide similarly increases carbon dioxide concentrations on the Earth. The atmospheric concentration of carbon dioxide should be contained below 350 ppm as a recommended safe level to reduce pressure on the environment.¹¹ There is an urgent call to employ clean, renewable energy and alternate conversion of CO₂ to available value-added chemicals and useful fuels to mitigate the current crisis of global energy and further address issues with rising concentration of carbon dioxide.

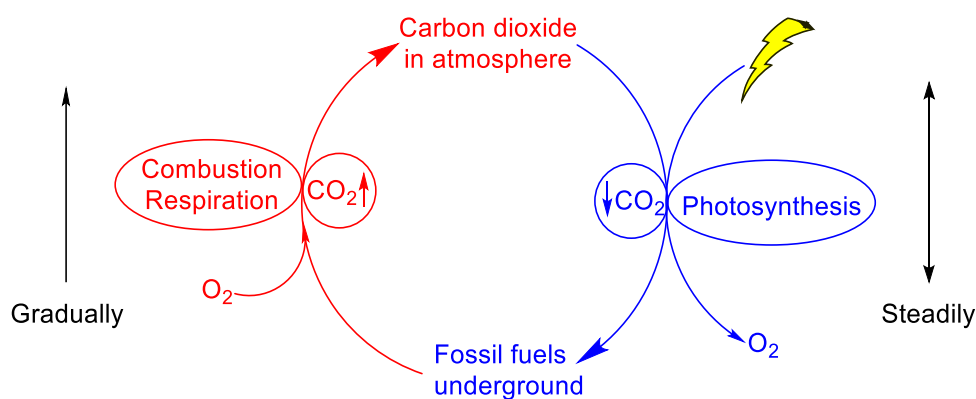


Figure 1.2. Carbon dioxide cycle in nature.

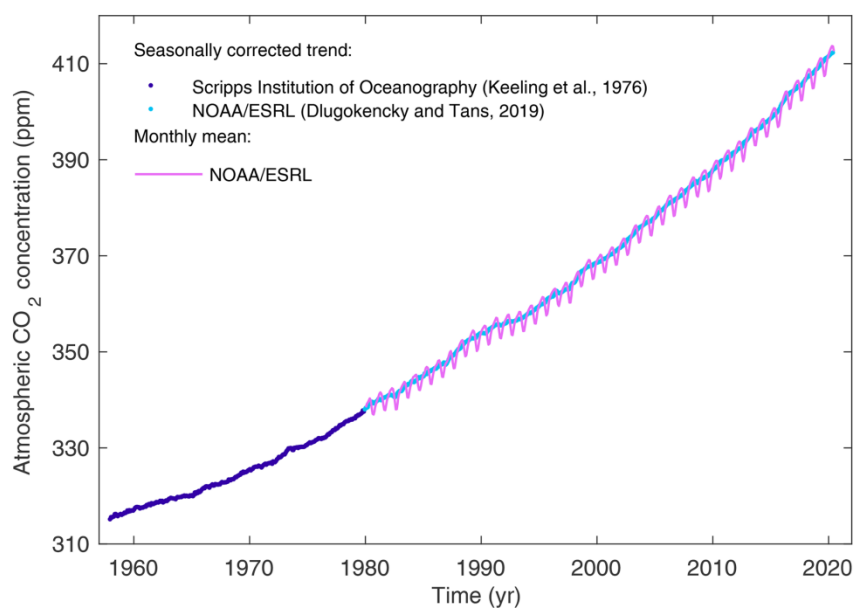


Figure 1.3. The average atmospheric CO₂ concentration on the surface (ppm). Figure is copied from Friedlingstein, P. et al.¹⁰

1.1.3. Utilization of formic acid

Formic acid (HCOOH) also known as methanoic acid, is the simplest of the carboxylic acids and formate is the form of its ester.¹² Due to its reducing properties, acidity, and aldehydic nature, formic acid is widely adopted in the chemical industry as a reducing agent, organic acid, and C1-based carbon source. Especially, it is vastly used as a preservative, organic solvent, leather, and synthetic intermediate for various pharmaceuticals.¹²⁻¹⁴ The storage capability of hydrogen is worth paying attention to. Having the lowest density among gaseous chemical elements under standard conditions, the storage of hydrogen is largely confined to high-pressure compression to enable safe transportation. Liquid formic acid which are energy-rich can be conveniently split into hydrogen with the presence of catalysts under mild conditions. Therefore, formic acid may potentially function as organic hydrogen carriers in the future, such as formic acid fuel cells.¹⁵⁻¹⁷

1.1.4. General principle of photoredox catalysis

Solar light emits an enormous amount of natural energy resource catering for use in photosynthetic plants. Yet only 2.4% of natural photosynthetic energy is stored for human consumption. Accordingly, there remains huge capacity of renewable solar energy that is available for exploitation.¹⁸ Following progress in science and technology, chemists have made a breakthrough in radical chemistry field and sparking interest in photochemistry. During initial research, researchers have focused mainly on ultraviolet light-related photocatalytic synthesis as most organic molecules favorably absorb only ultraviolet (UV) light. UV light possesses high energy levels (corresponding energy of UV range of 200 to 400 nm: 143 to 71.5 kcal/mol).¹⁹ For most organic compounds, the average bond dissociation energy (BDE) value of weak O–O is 45 kcal/mol for peroxides; whereas strong C–C bond is 84 kcal/mol.²⁰ Thus, it is no surprise that

substrates cause decomposition to occur under UV light condition. Only a few compounds can only absorb energy-low visible light of specific wavelengths. This implies that highly selective synthesis of target product renders feasibility under mild visible light conditions. The origin of visible light-catalyzed reactions is traced back to 1984, where Cano-Yelo, H. and Deronzier, A. achieved Pschorr reaction using $\text{Ru}(\text{bpy})_3(\text{BF}_4)_2$ as photocatalyst under a visible light-driven irradiation conditions.²¹

The advantages of transition metal-based photocatalyst in photophysical properties including: its excited state strongly absorbs visible light, has a sufficiently-long lifetime, and its high quantum yield. A number of successful reactions are implemented using metal complexes as photocatalysts, such as polypyridyl ligand installed Ru (II) and Ir (III) complexes. Even though transition metal photocatalysts have weak reactivity in their grounded state, their excited states can potentially function as single-electron oxidants and reductants. Upon absorption of a photon by ground state photocatalysts in the visible light region, an electron promotes from the highest occupied orbital (HOMO) of metal to the lowest unoccupied orbital (LUMO) of ligand (termed metal to ligand charge transfer (MLCT)) to afford reactive species which are regarded as the singlet excited states. Within transient time, the spin of electron is reversed by intersystem crossing (ISC) to give a relatively long lifetime triplet excited state, which has both an electron at the higher energy orbit of ligand and a vacant position in a low energy orbital of metal as compared to ground state photocatalyst. Thus, its triplet excited state exhibits strong electron-acceptor and electron-donor with substrate via electron transfer (Figure 1.4).²²⁻²⁴

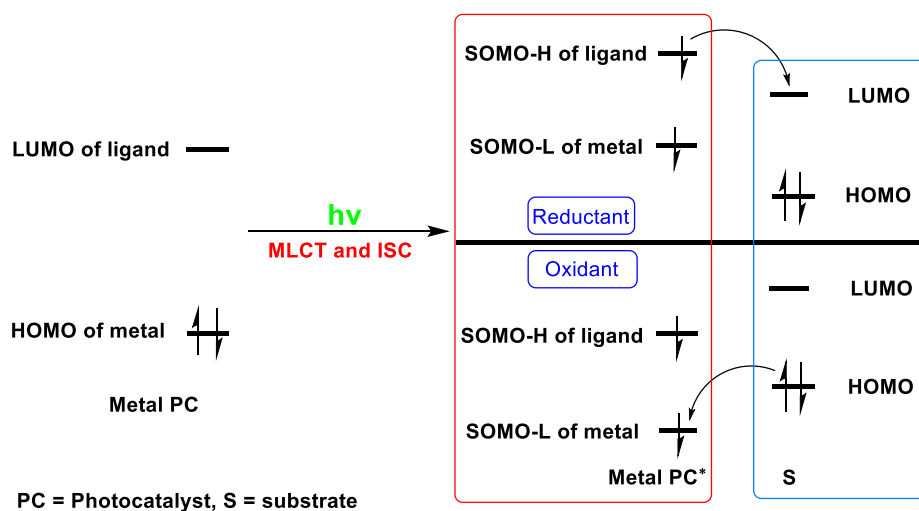


Figure 1.4. The photochemical electron transfer process of transition metal photocatalysts.

In recent years, photoredox catalysis as a powerful strategy for organic transformations has received incremental attention in organic chemistry. Since the HOMO and LUMO of metal photocatalyst originate from metal and ligand respectively, it is relatively convenient to fix their properties by changing the substituents from the ligands. During their development, researchers are gradually concerned of its associated

high costs, potential toxicity, and separation problems. These traits posed serious issues, especially, in pharmaceutical synthetic cases.²⁵⁻²⁹ Chemists have shifted their attention to alternative organic photocatalysts due to cheaper costs, simpler preparation process and being widely available. However, most organic photocatalysts with polyaromatic ring system often result in irreversible reaction with active intermediate generated under irradiated condition, which are inferior to metal photocatalysts in terms of stability.³⁰⁻³² The photochemical electron transfer process of organic photocatalyst via triplet excited state as potential oxidant or reductant is like that of metal photocatalyst. Apart from the mentioned pathway, it can also act as a singlet state-form electron-donor and electron-acceptor to participate in photoinduced electron transfer (PET) (Figure 1.5).²⁴

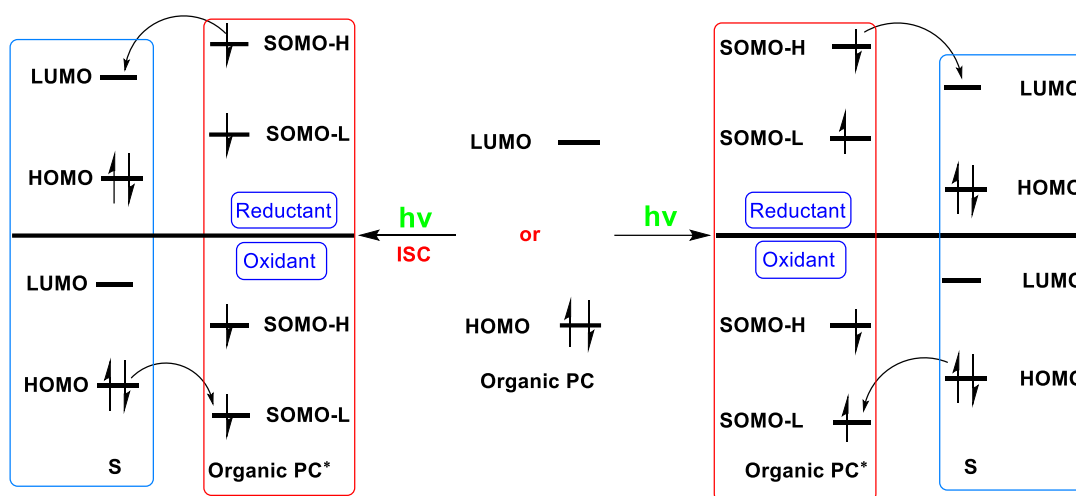


Figure 1.5. The photochemical electron transfer process of organic photocatalysts.

The interaction of excited state photocatalyst with substrate generates some active intermediates, such as: radical anion, radical cation, anion group, and cation group. Afterward, they react with each other to complete the total photocatalytic cycle. At present, the process was carried out using four various modes of common photocatalytic mechanisms, which included: electron transfer, energy transfer, atom transfer, and metal center-based photocatalysis transfer.^{23,33-34}

During electron transfer, excited-state PC as a very active species performs dual roles. First, it can donate an electron to a substrate, whereby the reductive potential of substrate matches with the oxidative potential of excited state PC. The PC radical cation then comes back to ground state PC via oxidative quenching cycle. Alternatively, it can also obtain an electron from the substrate to generate PC radical anion. Subsequently, PC radical anion is quenched by solvent or other radical species to regenerate ground state PC via reductive quenching cycle (Figure 1.6)²⁴

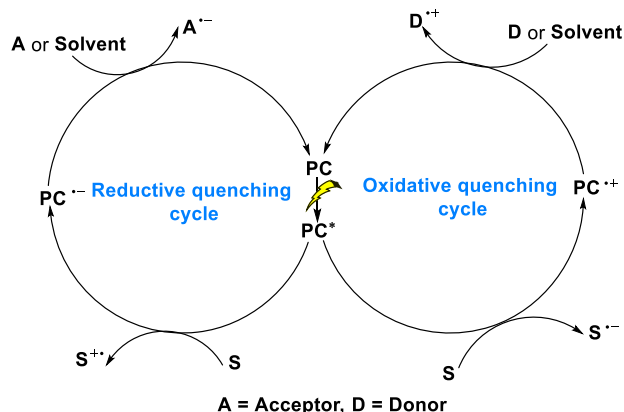


Figure 1.6. The photochemical mechanism of the electron transfer process.

During the energy transfer process, ground state PC absorbs energy under visible light-driven irradiation condition to afford excited state PC within excess energy, which is subsequently transferred to substrate by the nonradiative form to promote a series of reactions. There are two commonly received mechanisms of energy transfer, namely: energy transfer of Förster resonance and energy transfer of Dexter, respectively (Figure 1.7).^{23,33} It is noteworthy that Förster energy transfer³⁵ occurs through space form to achieve a photochemical cycle. Due to the connection of the transition moment dipole of the excited state PC with the transition moment dipole of substrate via non-radiatively energy transfer, no orbital overlap involved between the excited state PC and substrate is indicated. As a result, the distance of the excited state PC and substrate is not strictly demanded, approximately ranging from 1 to 10 nm.³⁶ However, the partial overlap of fluorescence spectrum of excited state PC and UV spectra of the substrate is necessary to perform the energy transfer (Figure 1.7a). Dexter energy transfer is often accompanied by electron exchange of an orbital overlap of substrate and excited state PC. Therefore, the distance of excited state PC and substrate requires less than 10 Å^{23,37-38} (Figure 1.7b). Most of the energy transfer proceeds via the Dexter procedure. For instance, oxygen can drive the excited state transition-metal complex to come back to ground state via Dexter energy transfer.³⁹⁻⁴⁰

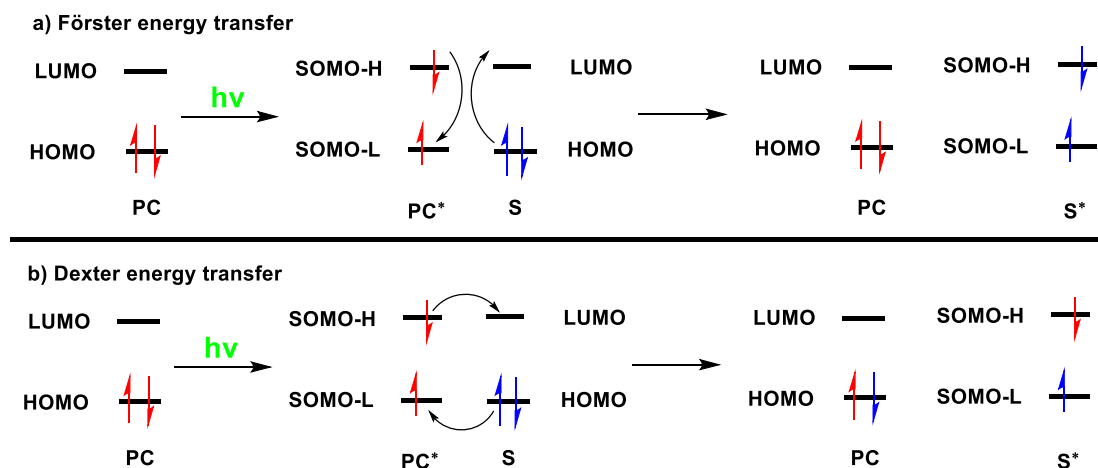


Figure 1.7. The photochemical mechanism of the energy transfer process. Figure is reproduced from Stephenson, C. R. et al.²³

1.2. Carbon dioxide fixation

1.2.1. Carbon capture and storage

Release of non-value gas from factories and anaerobic combustion of fuels forms primary sources of carbon dioxide- a greenhouse gas. Excessive emission of carbon dioxide gravely challenges stable natural ecosystems and rising sea-level. In face of such critical situation, carbon capture and storage (CCS) seems to be an effective physical tactic to cope with carbon dioxide emission.⁴¹ CCS is regarded as a complex procedure encompassing separation of carbon dioxide, transportation of CO₂, and storage of carbon dioxide. Separating carbon dioxide is compatible with large-scale sources of carbon dioxide emission. There are currently four technologies for capturing carbon dioxide, namely: procedure streams used in industry, collect after combustion, capture of oxygen fuel-based combustion and capture before combustion.⁴²⁻⁴⁴ Transportation of carbon dioxide bridges the procedure of separating carbon dioxide with storing carbon dioxide, which risk of leakage and costs remain unresolved issues.⁴²⁻⁴⁴ While geological storage and ocean storage are typical ways of storing carbon dioxide, there are still a series of barriers to overcome including technological, uncertainty, equipment, cost, feasibility, and durability.⁴²⁻⁴⁴

1.2.2. Carbon capture and utilization

1.2.2.1. Thermochemical conversion of carbon dioxide

While CO₂ is considered stable, it can be activated due to presence of its polarized C=O double bonds. The C atom possesses weak electrophilic nature as all four electrons from the carbon atom bond towards the oxygen atoms. Thus, based on the aforementioned theory, An approach that shows promise is the non-reductive transformation of CO₂ into other valuable compounds.⁴¹ For example, the incorporation of diol-type compounds, amino alcohol-type compounds and diamine-type compounds with CO₂ to yield cyclic carbonate moieties, carbamate compound, and urea in the presence of catalysts, especially heterogeneous CeO₂.⁴⁵⁻⁴⁸ The transformation of CO₂ into an intermediate of active pharmacophore produces valuable pharmaceuticals such as aspirin and salicylic acid.⁴⁷ Therefore, giving rise to a common tendency whereby CO₂ which functions as C1 synthon is incorporated into various organic molecules and intermediates in industrial applications (Figure 1.8).⁴⁸

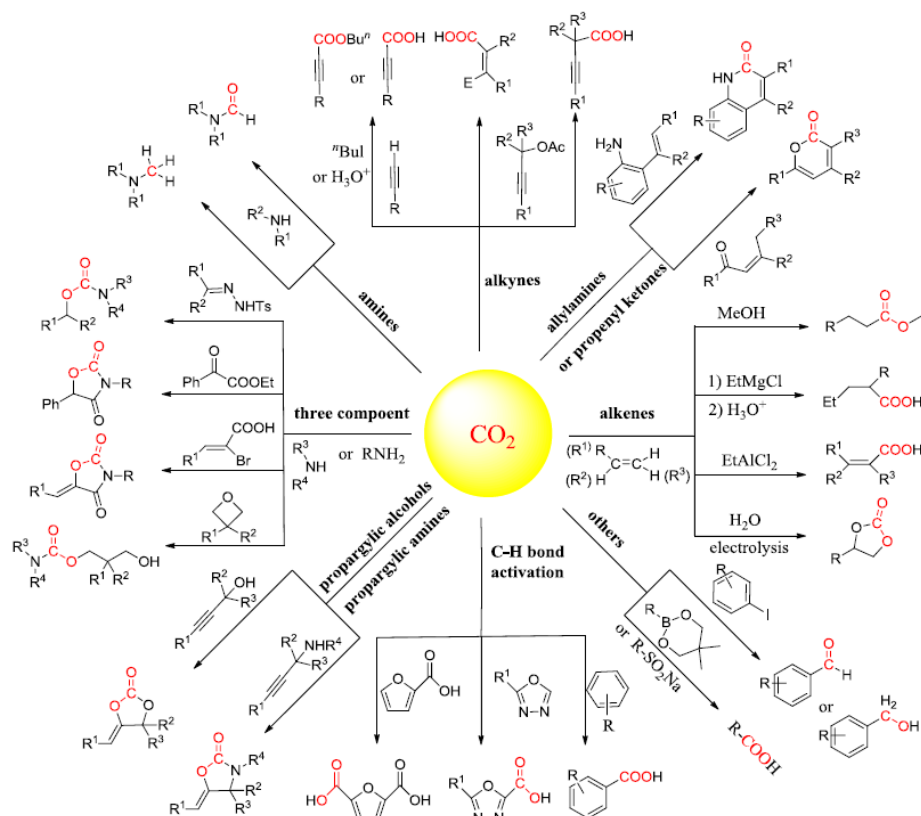
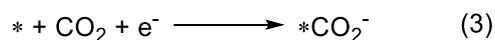
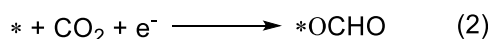


Figure 1.8. Conversion of CO₂ as C1 carbon source into diverse useful chemicals. Figure is reproduced from Jiang, H. et al.⁴⁸

1.2.2.2. Electrochemical conversion of carbon dioxide

The electrocatalytic reduction of carbon dioxide is a viable alternative solution to address energy crisis and global warming. CO₂ is a noble non-polar molecule, which is difficult to activate directly due to its formation of CO₂ radical anion intermediate with deeply negative redox potential (−1.9 V versus normal hydrogen electrode).¹¹ If electrocatalyst is employed to stabilize the active intermediate and bind to O or C atom of CO₂ by coordination bond or weak chemical bonds, an intermediate with less negative redox potential is easily formed.⁴⁹ Recently, Calle-Vallejo, F. and Koper, M. T. et al.⁵⁰ reviewed the activation of CO₂ by forming a few active intermediates. In equations (1) and (2), electrocatalyst is incorporated into CO₂ by concerted proton-electron transfer. The fate of *COOH is favorable to produce CO and *OCHO is more likely converted to formic acid. In equation (3), *CO₂ anion intermediate is generated via electron transfer. However, it often competes with hydrogen evolution reaction by dependence on pH solution.⁵¹⁻⁵² Therefore, electrocatalyst-assisted activation of CO₂ can be implemented by electron-proton transfer in concert, proton-electron transfer in sequence, and hydride transfer (Figure 1.9)⁵⁰.



* represents the electrocatalyst

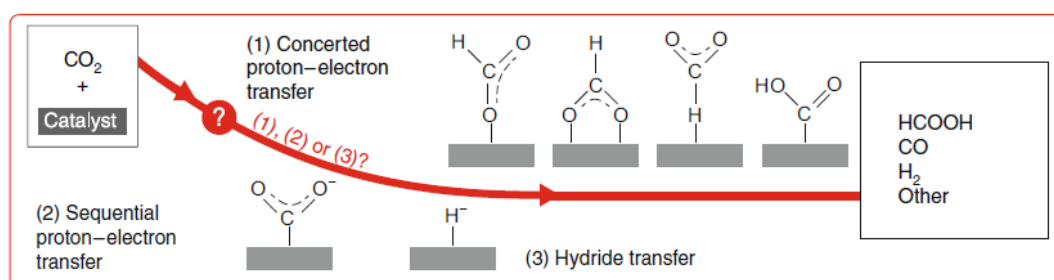


Figure 1.9 Possible electrocatalytic mechanism for initial activation of CO₂. Figure is reproduced from Calle-Vallejo, F. and Koper, M. T. et al.⁵⁰

Albeit the production of various value-added fuels is facilitated by electrocatalytic reduction of CO₂, from the economic value perspective, it may be incapable of effectively addressing actual energy crisis and carbon dioxide emissions due to its limitation of low selectivity, large overpotentials, non-renewable energy as energy source input, the chemically inert nature of CO₂ and low turnover numbers.⁵³ However, these drawbacks are determined by properties of electrocatalysts and electrolyte composition. Further exploitation of practical electrocatalysts with specific active site, durability, and strong activity are requirements for exclusive shift of CO₂ to sole chemical. Currently, the electrocatalytic reduction of CO₂ process majorly focuses on transition metal complexes, metal atom, carbon-based material, and metallic-organic frameworks (MOFS) as electrocatalysts.

Transition metal complexes: Polypyridine-based transition metal complexes such as Fe, Mn, Re, Ru, Ir, Ni, and Co⁵⁴⁻⁵⁶ have long been applied for reducing carbon dioxide electrocatalytically. Compared to metal-free organic catalyst, taking natural advantage of multiple redox states, coordination site available for CO₂, and the readily regulation ligand model could improve selectivity and activity. Presently, a wide range of polypyridine-based transition metal complex have been used for two-electron-based reduction of CO₂ that results in CO and formic acid products. Besides, efficient formation of the four-, six-, and eight-electron reduction products such as formaldehyde, methanol, and methane have also been exploited.^{49,57} Almost all these catalysts were put in an aprotic electrolyte with a high level of activity and selectivity, whereas the carbon dioxide reduction is obviously competitive with hydrogen evolution reaction in protic electrolyte. Besides, limitations in terms of their recyclability and weak stability were taken seriously due to homogeneous solvent and their short lifetimes.⁵⁷ A new approach has been exploited by fixing transition metal complexes to materials or the

surface of electrodes. their performances are evidently superior to that of sole transition metal complexes. For instance, Lau, T. C. and Robert, M. et al.⁵⁸ reported Co (II) quaterpyridine complex $[\text{Co}(\text{qpy})]^{2+}$ was installed to the surface of multi-walled carbon nanotubes (MWCNTs) for CO_2 reduction in water and its performance displayed 100% catalytic selectivity and 100% faradaic efficiency under lower overpotential and catalyst-loading (Figure 1.10).

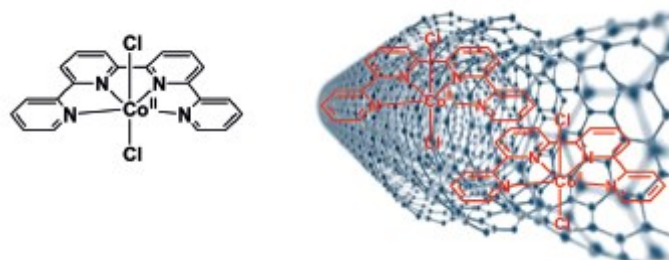
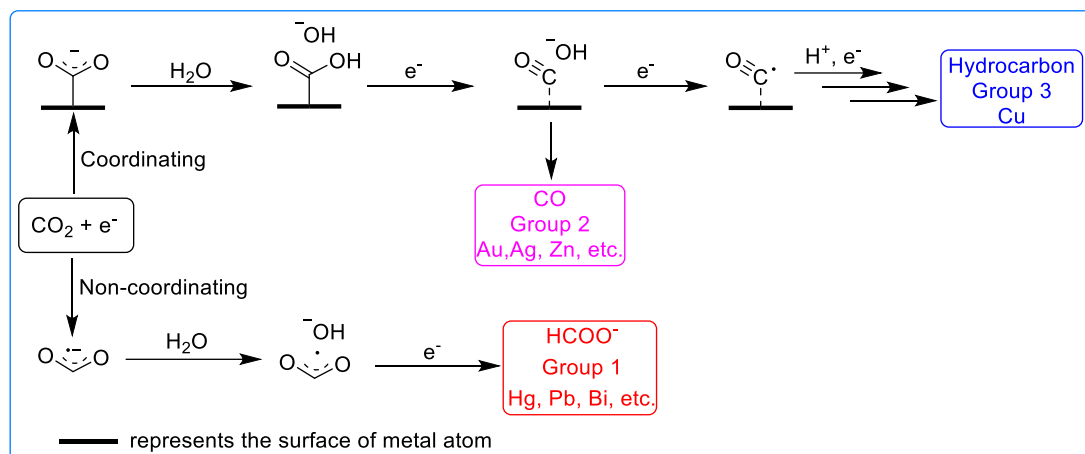


Figure 1.10. Structure of $[\text{Co}(\text{qpy})](\text{Cl})_2$ complex (left) and schematic view of the incorporated material comprising ($[\text{Co}(\text{qpy})](\text{Cl})_2$ and MWCNTs, right). Figure is reproduced from Lau, T. C. and Robert, M. et al.⁵⁸

Metal atom: Metal atom catalysts can be divided into three categories based on different selectivity available for the major product of CO, formic acid, and hydrocarbon. Group 1 metals including Hg, Pb, and Bi, et al. are favorable to afford formate product.⁵⁹ On the other hand, group 2 metals comprising of Au, Ag, and Zn, et al. demonstrate strong selectivity for CO product.⁵⁹ Group 3 metal (only Cu) performs multiple electron reduction to produce hydrocarbon, such as, CH_4 , C_2H_4 and $\text{C}_2\text{H}_5\text{OH}$.⁵⁹ During the reduction process of these metals-based catalyst, initial activation of CO_2 generates active CO_2 radical anion intermediary which is considered as the rate-limiting step. The fate of the intermediate determines the type of two-electron reduction product yielded. When the intermediate is coordinated to the surface of a metal atom-based electrode, the tendency of getting sequential hydrogen and electron to afford binding of CO with the surface of a metal atom by weak coordination bond; and separation of CO from the surface of a metal atom easily occurs. Alternatively, if non-coordination of the intermediate to the surface of a metal atom-based electrode occurs, CO_2 radical anion is readily reduced by sequential hydrogen and electron transfer to afford formate. In the Cu case, due to the strong coordination of the Cu electrode with CO_2 radical anion, CO cation and CO radical intermediates, CO radical intermediate undergoes several obtainments of electrons and protons to ultimately yield multiple electron reduction product, such as hydrocarbon (Scheme 1.1).^{49,59-60} In some cases, despite metal atom electrocatalytic reduction of carbon dioxide performances dramatic activity and selectivity; or even provides multiple electron reduction products, its toxicity and pollution indeed deserve attention for large-scale application in the future.



Scheme 1.1. Proposal mechanism for CO₂ reduction via electrochemistry on metal surfaces in water. Scheme is reproduced from Prakash, G. S. et al.⁵⁹

Carbon-based materials: At present, carbon-based catalyst has been extensively adopted for the feasibility of electrocatalyst CO₂ reductions like diamond, graphene dots, carbon fibers, nanoporous carbon, and CNTs materials doped with heteroatoms (N, F, S, and B) (Figure 1.11).⁶¹ Some advantages in terms of their performances are highlighted, such as: low cost of metal-free materials, broadly active sites for CO₂, durable stability, highly sensitive conductivity, full recyclability and environmental friendliness. Carbon-based catalysts are not only suitable for two-electron reduction cases, but also capable of multi-electron reduction, and various products are obtained, such as formic acid, CO, CH₄, and C₂H₄.⁶¹ In some cases, carbon materials without doping heteroatom show silent performance for CO₂ reduction. As a result, their activities are ascribed to heteroatoms resulting from the tendency of electronegative heteroatoms and electropositive carbon atoms in metal-free carbon material to activate CO₂. For their selectivity, it lies on the degree of incorporation of the catalytic sites with the intermediate species formed.⁵⁷ In addition, metal-doped carbon materials have also intrigued the interest of some chemists.⁶²⁻⁶⁵ Recently, Rossmeisl, J. and Strasser, P. et al.⁶⁶ has reported carbon catalysts with nitrogen and metal doping for electrochemical CO₂ reduction to CO product. First, the authors synthesized a series of active nitrogen and metal doped carbon electrocatalysts and examined the reactivity of their inherent catalytic processes, CO faradaic efficiencies, and CO turnover frequencies. It is demonstrated that M-N_x single site plays the dominant role for available CO₂ reduction into CO with very high electrocatalytic reactivity and selectivity in comparison with effects of other nitrogen moieties without metal doped. Additionally, carbon-materials embedded with bimetal atoms are also achieved for electrocatalytic reduction CO₂. Recently, Li, C. et al.⁶⁷ found that bimetallic (NiMn or NiCu) carbon nitride catalysts showed much more efficient capability than that of their mono-metal available for electrocatalytic conversion of CO₂ to CO, as a result, realizing high faradic efficiency for 90% of CO evolution over a wide potential range via a low overpotential of 0.39 V (Figure 1.12).

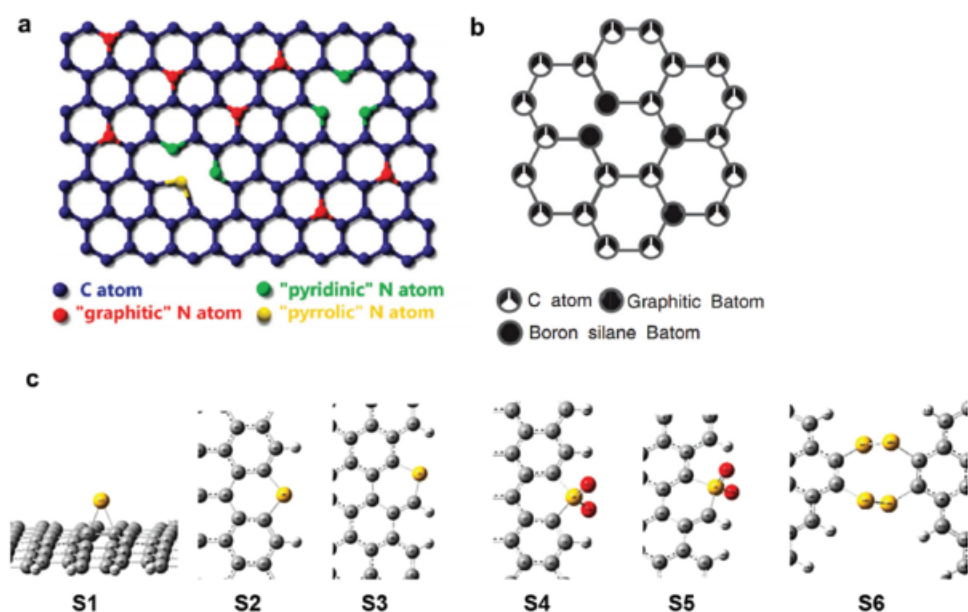


Figure 1.11 Structures of carbon materials doping various heteroatom. a. Graphene doping N. b. Graphene doping B. c. Graphene doping S. Figure is reproduced from Ma, J. and Guo, S. et al.⁶¹

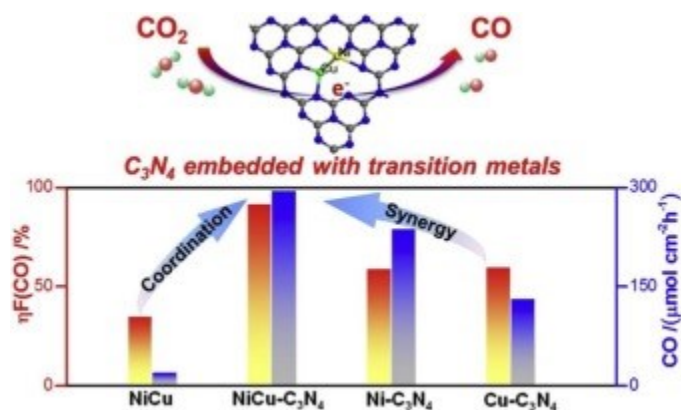


Figure 1.12 Carbon nitride doped with bimetallic atoms were much more efficient than that of mono-metal atom for electrocatalytic reduction of CO_2 . Figure is reproduced from Li, C. et al.⁶⁷

Metallic-organic frameworks (MOFs): The crystalline materials known as MOFs are organic-inorganic hybrids which consist of a regular arrangement of positively charged metal ions or clusters coupled to organic molecules to generate certain dimensional structures.⁶⁸⁻⁶⁹ MOFs present some special merits, namely: an extraordinarily large internal surface area due to its hollow structure, recyclability of MOFs materials, and the regulation of their property by readily modifying organic ligands.⁶⁸⁻⁶⁹ MOFs as an effective heterogeneous catalyst become a promising alternative for electrocatalytic reduction CO_2 .⁷⁰ Even though the advance of MOFs materials as catalysts for photocatalytic CO_2 reduction has been widely reported, the use of MOFs materials for electrocatalytic CO_2 reduction is scarcely reported.⁷¹ In 2012, Kulandainathan, M. A. et al.⁷² first employed MOFs materials ($\text{Cu}_3(\text{BTC})_2$) as catalysts

to generate oxalic acid product for electrocatalytic CO₂ reduction. Yet, only 90% of oxalic acid and 51% of the faradaic efficiency were realized under even high overpotential conditions. The author further revealed its possible mechanisms: the catalytic activity of the Cu₃(BTC)₂ material might be ascribed to Cu(I)-CO₂ adduct intermediate from which activation of Cu(II)-MOF was transferred to Cu(I) species that combined with CO₂ to form five-coordinate Co(I)-CO₂ adducts. Ligand (BTC) acted as Lewis acid to stabilize the Co(I)-CO₂ adduct intermediate. Subsequently, two Co(I)-CO₂ adducts got together to induce reduction and protonation to provide oxalic acid product (Figure 1.13).

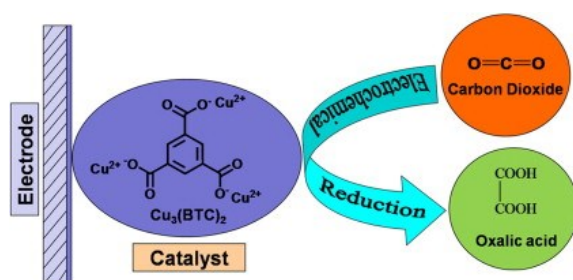


Figure 1.13 Electrochemical reduction of CO₂ using MOFs-based Cu₃(BTC)₂ as an electrocatalyst. Figure is reproduced from Kulandainathan, M. A. et al.⁷²

1.2.2.3. Photocatalytic conversion of carbon dioxide

Since CO₂ is a very stable line molecule with a profoundly higher C=O double bond energy (804.4 kJ/mol, at 298 K) as compared to other bond energy, it is the thermodynamically unfavorable factor for the reduction CO₂.⁷³ Therefore, the transformation of reduction CO₂ usually requires high-energy intakes to activate the C=O double bond. As an electron, for instance, is shifted to CO₂ to provide a very unstable CO₂ radical anion in which a powerfully negative redox potential with -1.85 V vs NHE at pH 7.0 (Table 1.1, Entry 1)⁷⁴ is formed, to date, almost none of the metal or semiconductor-based catalysts have sufficient capabilities to promote single-electron transfer in the reduction of CO₂. Alternatively, proton aided multi-electron only needs the relatively lower redox potential available for reduction of CO₂. As expected, the redox potential of -0.61 V (Table 1.1, Entry 2)⁷⁴ is a requirement for CO₂ reduction with proton assistance-based two electrons to formic acid product. Consideration must be given to the favorable provision of electrons for reduction of CO₂ other than reduction of H⁺ evolving H₂ via oxidation of H₂O. Due to this dual behavior, the selectivity of photocatalysts is key to CO₂ reduction.⁷⁵

Photoinduced reduction of CO₂ is the most enticing strategy for directly converting CO₂ into value-added fuels with renewable sunlight as ideal energy source, achieving sustainable and carbon-neutral recycling of CO₂. In general, photocatalytic reduction of CO₂ system consists of a photosensitizer, catalyst, and sacrificial electron donor. Sometimes, a molecule, such as integrated-form molecule and semiconductor material can function as dual performance (both photosensitizer and catalyst). The source of photosensitizer comes mainly from strong absorption semiconductor materials, transitional metal complexes, and rare high conjugated organic molecules.

Triethanolamine (TEOA), triethylamine (TEA), and ascorbic acid are often capable of being sacrificial electron donors. As to catalysts almost from metal complexes. At present, transition metal complex, MOF materials, metal oxide-based semiconductor materials, metal sulfides, and polymeric materials have been attractive photosensitizers for photocatalytic reduction of CO₂.⁴⁹

Entry	Equation	Product	E ⁰ (V) ^a
1	$\text{CO}_2 + \text{e}^- \longrightarrow \text{CO}_2^{\cdot-}$	Carbonate anion radical	-1.85
2	$\text{CO}_2 + 2\text{e}^- + 2\text{H}^+ \longrightarrow \text{HCOOH}$	Formic acid	-0.61
3	$\text{CO}_2 + 2\text{e}^- + 2\text{H}^+ \longrightarrow \text{CO} + \text{H}_2\text{O}$	Carbon monoxide	-0.53
4	$\text{CO}_2 + 6\text{e}^- + 6\text{H}^+ \longrightarrow \text{CH}_3\text{OH} + \text{H}_2\text{O}$	Methanol	-0.38
5	$2\text{H}^+ + 2\text{e}^- \longrightarrow \text{H}_2$	Hydrogen	-0.42

Table 1.1 Electrochemical reactions involving in aqueous CO₂ and H₂ reduction with the appropriate reduction potentials E⁰ (V vs NHE at pH 7.0). Data is reproduced from Peppel, T. and Sun, Z. et al.⁷⁴

Transition metal complexes: In the early development of CO₂ reduction, Lehn, J. M. et al.⁷⁶ discovered the photochemical shift of CO₂ to CO via Re(bipy)(CO)₃X (X = Cl, Br) or combination of dual metals (Ru(bipy)₃²⁺-Co²⁺) as catalysts. This further demonstrated the dual functionality of Re(bipy)(CO)₃X complex functioned as a photosensitizer and catalyst which behaved with stronger activity and higher selectivity than Ru(bipy)₃²⁺-Co²⁺ system. Since then, transition metal-based photosensitizer-catalyst systems were widely developed and explored, especially, Ru(II), Re(II), Ir(III) complexes as photosensitizers.^{15,77} Owing to the inherent nature of strong absorption of transition metal complexes and the long lifetime of their phosphorescence emission, they effectively function as photosensitizers to provide electrons for reduction of CO₂ under light-driven irradiation condition. Additionally, transition metal complex that possesses multiple redox states and a coordination site available for CO₂ is also the best choice as a catalyst. Consequently, one transition metal complex as a photosensitizer and another transition metal complex as a catalyst for reducing CO₂ is efficiently performed (Figure 1.14).^{13,15-16,77-78} Although high turnover number (TON) and turnover frequency (TOF) are obtained in most of the reaction systems, transition metal complexes are expensive, thus, making them a challenge for large-scale application. Besides, its selectivity poses a serious problem, since hydrogen is often formed as an evolution gas. For instance, recently, Arikawa, Y. et al.⁷⁹ have achieved photocatalytic conversion of CO₂ to HCOOH using [Ru(dmbpy)₃]²⁺ complex as a photosensitizer, (BI(OH)H) as a sacrificial reductant, and ruthenium complex with different ligands as a catalyst. Authors demonstrated that carbonyl catalyst bearing small substituents (Me)

(3b) was superior performance among four ruthenium complexes with $\text{TON}_{\text{HCOOH}} = 5634$ by tuning ligands and substitutions of catalysts. Even though high TON was obtained, its selectivity was only up to 72% due to the fact hydrogen was simultaneously evolved with 24% of selectivity (Figure 1.15).

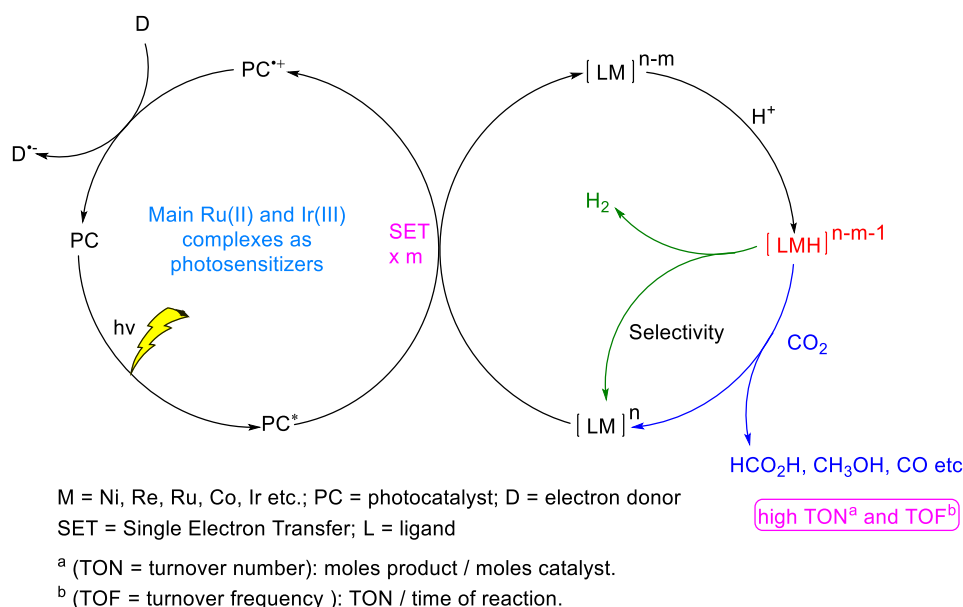


Figure 1.14. Recapitulative mechanism of photocatalytic CO_2 reduction employing transition metal complexes as photosensitizers.

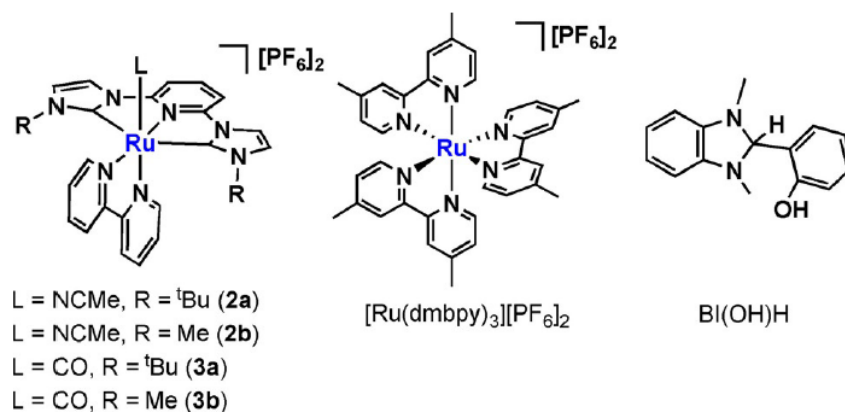


Figure 1.15. Structures of catalysts (2a, 2b, 3a, 3b), photosensitizer ($[\text{Ru}(\text{dmbpy})_3][\text{PF}_6]_2$), and sacrificial reagent (BI(OH)H). Figure is reproduced from Arikawa, Y. et al.⁷⁹

Metal oxide-based semiconductor materials: Presently, a vast array of metal oxide and mixed metal oxide-based semiconductor materials have been widely applied to the photoinduced reduction of CO_2 with high kinetic activity and strong selectivity. Additionally, they have demonstrated durable stability, non-corrosion, and readily recyclability.⁴⁹ Conduction band levels of most materials show a more negative

potential as compared to reductive potential of CO₂ to formic acid, CO, methanol, and methane. Their bandgap energy roughly matches with the range of visible-light energy to fully absorb solar energy; besides, their charge separation is easily triggered.⁸⁰ Among them, titanium dioxide (TiO₂) has been given attention due to its outstanding photochemical performance in CO₂ reduction. Since its bandgap energy is higher than the scope of visible-light energy, stand-alone TiO₂ as photocatalyst only performs a reduction of CO₂ under ultraviolet irradiation conditions. Therefore, a huge amount of visible-light energy as a renewable energy source could not be practically utilized. Additionally, fast recombination of photogenerated electron-hole pair significantly hampers redox reaction of CO₂.⁸¹ In 2015, Zhao, Y. and Zhang, J. et al.⁸² successfully synthesized TiO₂ embedded with Pt²⁺ ion and Pt atom. Doping TiO₂ has a positive effect on the yields of CH₄. This further revealed that Pt²⁺-Pt⁰/TiO₂ nanoparticle realized the lower bandgap energy induced by Pt²⁺ doping and the low recombination rate of photochemical electron-hole resulting from Pt⁰ deposition. Based on the development of TiO₂ materials, other wide bandgap metals oxide-based materials are fully exploited for reduction of CO₂. These include metal cations with d⁰ electronic configurations, such as ZrO₂, Nb₂O₅, Ta₂O₅ and mixed metal oxides (KTaO₃, SrTiO₃, and NaNbO₃)⁸³⁻⁸⁵ and metal cations with d¹⁰ electronic configurations which also involve metal-based oxide of dual metals-based oxide (Ga₂O₃ and Zn₂GeO₄).⁸⁶⁻⁸⁷ As these metal-based oxides of dual metals-based oxides possess wide bandgap energy, they only absorb UV light to facilitate electron transfer available for CO₂ reduction. Fortunately, it is an alternative approach whereby its material-compositions are regulated by a doping trace amount of metal atoms or metal cations to make their low bandgap energy for reduction of CO₂ employing renewable visible light as an energy source. Noteworthily, Cu₂O naturally possesses narrow bandgap energy, which can directly absorb visible light for photochemically reducing CO₂.⁸⁸

Metal sulfides: CO₂ is reduced to a value-added fuel using visible light. The most ideal source of solar energy is renewable visible light. The bandgap energy of most metal sulfide-based semiconductors is generally lower than light energy at 400 nm. Hence, metal sulfide materials directly obtain visible-light energy to generate electron-hole to enable participation in photocatalytic reduction of CO₂. Nevertheless, consideration must be given that the S anion of metal sulfide is susceptible to oxidation by electron-hole to break structure of metal sulfide materials.⁸⁰ CdS, one of the preferred metal sulfide materials being investigated, has a narrow bandgap of 2.4 eV which appropriately matches with the corresponding visible solar light. Its conduction band value of -0.9 eV (vs the NHE at pH 7) is fully capable of reducing CO₂ to be some related products.⁸⁹⁻⁹⁰ ZnS is the second attention member in the metal sulfide's family, which is related to its deeply negative conduction band of -1.85 eV (vs the NHE at pH 7) favorable for reduction of CO₂ to all kinds of products, such as HCOOH, CO and CH₃OH. whereas ZnS absorbs only UV light due to the disadvantage of its wide bandgap of 3.66 eV.⁹¹⁻⁹³ Recently, Ye, J. et al.⁹³ asserted that Cd²⁺ modified ZnS mediated photocatalytic conversion of CO₂ to HCOOH in 95% selectivity and 76% of quantum efficiency. The author further disclosed its reaction mechanism whereby ZnS

provided the first electron to Cd^{2+} to afford deeply negative redox potential of Cd^+ intermediate, which responded to reduction of CO_2 to form CO_2 radical anion. Afterwards, second reduction is undergone to obtain formic acid product via sequential proton-electron transfer (Figure 1.16).

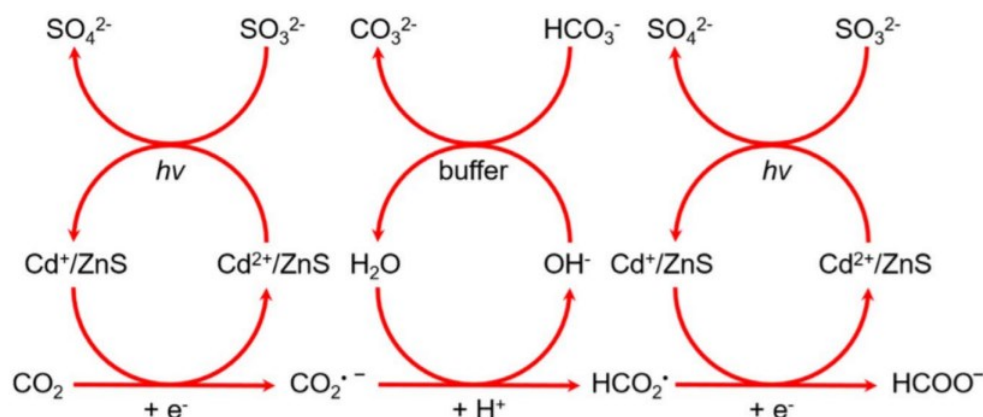
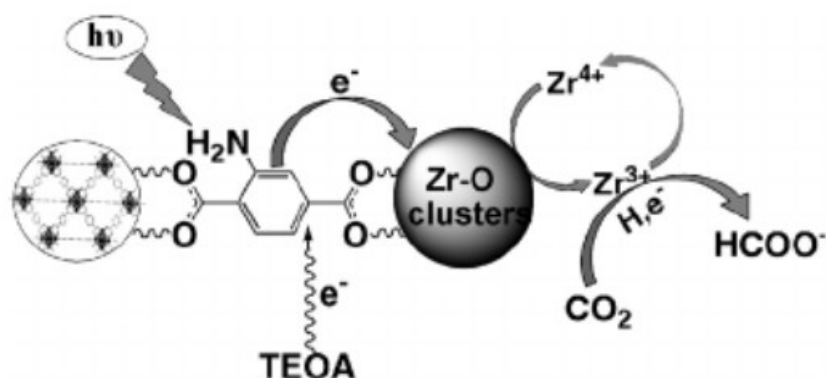


Figure 1.16. The possible mechanism of $\text{Cd}^{2+}/\text{ZnS}$ -based photocatalytic conversion of CO_2 to HCOO^- product. Figure is reproduced from Ye, J. et al.⁹³

Polymeric materials: The favorable chemical properties of polymeric materials, namely: fast charge separation and narrow bandgaps have earned recognition as effective alternate solution in utilization of CO_2 . Their physical merits include good flexibility, large surface area, and thermal stability.⁹⁴⁻⁹⁶ More importantly, their structures are readily modifiable by exfoliation, surface adjustment, and doping. After modifications, physical properties and photocatalytic activities are entirely different in comparison with the origin of polymeric materials.⁸⁰ Graphitic carbon nitride ($g\text{-C}_3\text{N}_4$) and graphene-based materials are two of the most common members in the family of polymeric materials based on these modifications and derivations.^{80,97} Graphitic carbon nitride presents a proper band edge position capable of converting CO_2 to various fuel products and its narrow bandgap (2.7–2.9 eV) located at wavelength of 460–430 nm effectively provides visible-light range for CO_2 reduction.⁹⁴⁻⁹⁵ Besides, graphitic carbon nitride is slightly embellished using doping or exfoliation to enhance its activity, selectivity, and CO_2 absorption capability. For instance, Tian, L. and Chen, X. et al.⁹⁸ have readily prepared $g\text{-C}_3\text{N}_4$ doped with multi-phosphorus and multi-amino in its surface. It possessed relatively down conduction band and valence band locations, and narrower band gap as compared with untouched graphitic carbon nitride. Data further revealed that absorption capability of CO_2 is amplified to 3.14 times, its activity is enhanced to 3.10 and 13.92 times for CO and CH_4 in order. Indeed, graphene materials also hold prominent properties like large extended surface area, strong adsorption of CO_2 and good flexibility, mainly containing reduced graphene oxide (RGO), graphene pristine (G) and graphene oxide (GO)^{96,99} which deserves our attention. For instance, GO with various oxygen-incorporated functional groups exhibits different properties and its bandgap is consistent with the concentration of oxygen based functional group. Therefore, it readily obtains specific bandgap by tuning the composition rate of oxygen-

based functional group.¹⁰⁰⁻¹⁰¹

MOF materials: MOFs are applied in absorption and disposal of exhaust gas as well as development of heterogeneous catalysts. Over the past few decades, MOF performances were implemented by immobilizing different types of photocatalytic sites into MOF materials to achieve shift of CO₂ to various fuel products via a simple mechanism. Under irradiation condition, electrons are generated in organic ligand. Subsequently, it is delivered to metal cluster or metal ion as a CO₂ reduction a chemically active site.¹⁰²⁻¹⁰⁶ For instance, Li, Z. et al.¹⁰⁷ have performed photoinduced reduction of CO₂ employing metal–organic framework (NH₂-Uio-66(Zr)) as photocatalyst and first revealed that electron flowed from its excited state organic ligand to its Zr-O cluster by ESR analysis. Besides, if mixed ligands (2-aminoterephthalate (ATA) and 2,5-diaminoterephthalate (DTA)) were installed to NH₂-Uio-66(Zr), its activity was dramatically increased due to adsorption of its light and capture of CO₂ to be stronger. (Scheme 1.2). Additionally, metal organic framework is often modified by adjusting a part of organic linker and incorporated with other photocatalytic materials. Recently, Li, J. R. et al.¹⁰⁸ have achieved the incorporation of ZIF-L (metal organic framework) with TiO₂/C (carbon/semiconductor) to form composite photocatalysts for high-performing CO₂ reduction. Through incorporation, some synergistic effects of components were prominently shown, such as well-matched band between TiO₂/C and ZIF-L and the sufficient separation of electron-hole. Besides, its active metal sites were advantageous for promoting conversion of CO₂ to 28.6 μmol h⁻¹ g⁻¹ of CO with selectivity of 99 % (Figure 1.17).



Scheme 1.2. Proposal mechanism for photoinduced conversion of CO₂ to HCOO⁻ employing NH₂-Uio-66(Zr) as photocatalyst. Scheme is reproduced from Li, Z. et al.¹⁰⁷

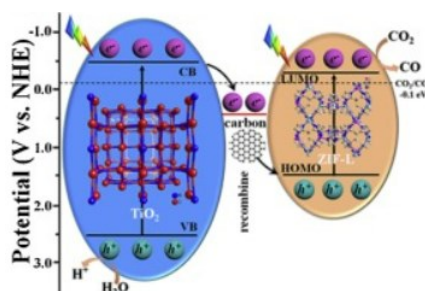


Figure 1.17. The generation and separation of electron-hole process on combination of TiO₂/C and ZnCo-ZIF-L. Figure is reproduced from Li, J. R. et al.¹⁰⁸

1.2.2.4. Organocatalytic conversion of carbon dioxide

Transition-metal-based catalytically reducing carbon dioxide is played a leading role due to its diverse oxidation states and coordination sites for available for carbon dioxide, but as an effective alternative proposal: Organocatalytic shift of CO₂ into value-added chemical fuels is also an attractive scheme. Some successful studies mainly emphasize on Frustrated Lewis pairs, *N*-heterocyclic carbenes and conjugated organic polymers (COPs) as catalysts.

Boron-based Frustrated Lewis pairs as catalysts: Frustrated Lewis pairs with dual reactivity of electrophilic site and nucleophilic site not only accepts an electron but also donates an electron simultaneously.¹⁰⁹ So, its performance is attracted much attention in facile activation of inert chemical bonds, such as H₂, CO₂ and N₂. Regarding boron-based Frustrated Lewis pairs catalytic reduction of CO₂, Reversible conversion of CO₂ using phosphine and borane-based Frustrated Lewis pair is pioneered by Grimme, S.; Stephan, D. W. and Erker, G. et al.¹¹⁰ Since this unprecedented discovery, an increasing number of amphiphilic organocatalytic activity of CO₂ schemes are exploited and activated CO₂ is readily captured by chemicals releasing hydride (Figure 1.18). Recently, Piers, W. E. et al.¹¹¹ reported that catalytic conversion of CO₂ into CH₄ enabled by Frustrated Lewis pairs comprising 2,2,6,6-tetramethylpiperidine (TMP) and tris(pentafluorophenyl) borane (B(C₆F₅)₃) employing triethylsilane as sacrificial electron donor. In this case, the rate-limiting step involving transformation of hydride to activated CO₂ was indicated that enough amount sacrificial reductant was consumed to promote the reaction towards product. Additionally, in 2013, 1-Bcat-2-PPh₂-C₆H₄ (cat = catechol) function as an amphiphilic catalyst for the reduction of CO₂ using hydroboranes as source of hydride was developed by Maron, L. and Fontaine, F. G. et al.¹¹² As the best result, methanol was generated with 2950 of TON and 973/h of TOF enabled by extra loadings of hydroboranes consumed (1000 equivalent). Vast amount of high-energy metalloid hydride species is consumed to attain the reaction equilibrium towards products in Frustrated Lewis pairs cases. Thus, the issue ought to be resolved to enable large scale application in the future.

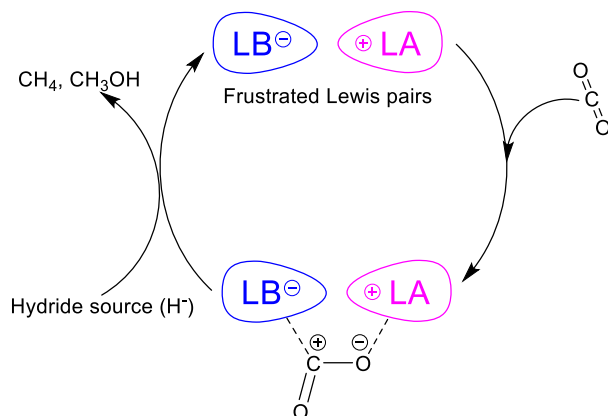


Figure 1.18. The general mechanism process of amphiphilic catalytic CO₂ reduction.

***N*-heterocyclic carbenes as catalysts:** Since *N*-heterocyclic carbenes (NHCs) with lone pair of carbene electrons are capable of nucleophilic tendency, they are widely established as ligands for metal-based catalytic reaction.¹¹³ In recently years, nucleophilic NHCs acted as metal-free catalyst were applied to activate CO₂ well. In these cases, NHCs-based catalytic CO₂ reduction was promoted in the existence of hydride source to ultimately provide methoxide, *N*-formylated or *N*-methylated products with high selectivity.¹¹⁴ As an excellent example, Zhang, Y. and Ying, J. Y. et al.¹¹⁵ successfully designed solution that NHCs catalytic conversion of CO₂ to imidazolium carboxylate as activated carbon dioxide source reacted with hydride from hydrosilane to produced methanol. In comparison with transition-metal catalyst, its performance showed exceeding effective and selective in more than 90% yield. However, the utilization of hydrosilane as a hydride donor remains an issue to be solved in the future due to cost implications (expensive).

Conjugated organic polymers (COPs) as catalysts: COPs as a metal-free photocatalytic materials have widely served for reduction of CO₂ due to its high performance in fixation of CO₂ and readily modification. Especially, some potential CO₂-philic functional groups are immobilized in conjugated organic polymers and show much more excellent performance in CO₂ capture and further conversion, such as amine, imidazole, triazine and amide group.¹¹⁶⁻¹¹⁸ Besides, as a prominent advantage, using conjugated organic polymers as photocatalyst, reduction of CO₂ efficiently couples with the oxidation of H₂O in one photocatalytic reaction system. A successful example was depicted by Liu, Z. et al.¹¹⁹ Amide-bridged COPs-based photoinduced shift of CO₂ to CO with a generation rate of 20.6 μM g⁻¹ h⁻¹ using H₂O as sacrificial reduction. Based on DFT calculations and related experiments, further indicating cyano and amide groups of amide-bridged COPs functioned as active sites for available reduction CO₂ and second amine group was responded to oxidation of H₂O. Additionally, some metal-free heteroatoms were embedded into COPs, which readily promoted photo-catalytically CO₂ reduction under visible light-driven irradiation condition. Recently, Liu, Z. et al.¹²⁰ revealed nitrogen, oxygen and phosphorus doping covalent organic polymer (NOP-COP) could effectively capture CO₂ and further

photochemically catalyzed CO_2 to CH_4 , furthermore, its performance showed strong efficiency (rate of $22.5\mu\text{M g}^{-1} \text{h}^{-1}$) and exclusive selectivity (CH_4 as a sole carbon-containing product) (Figure 1.19).

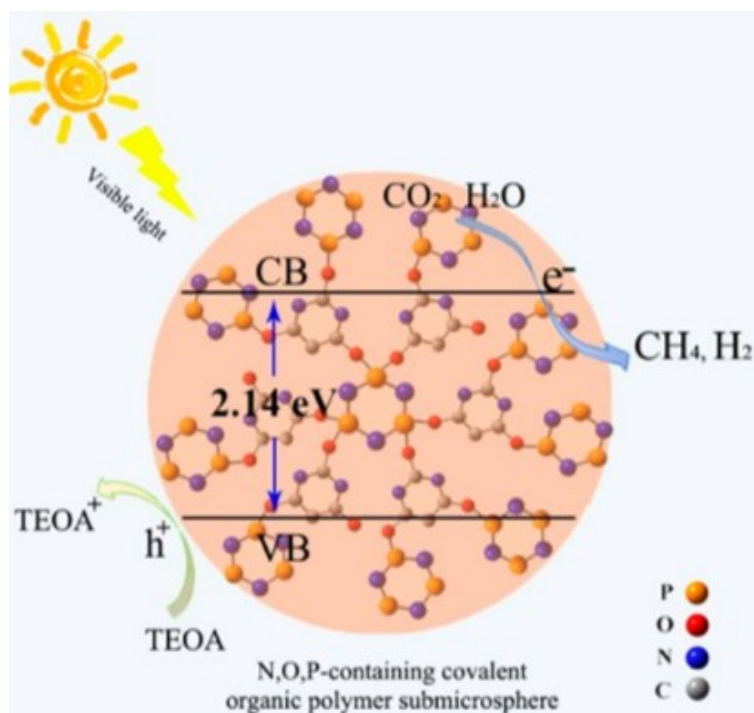
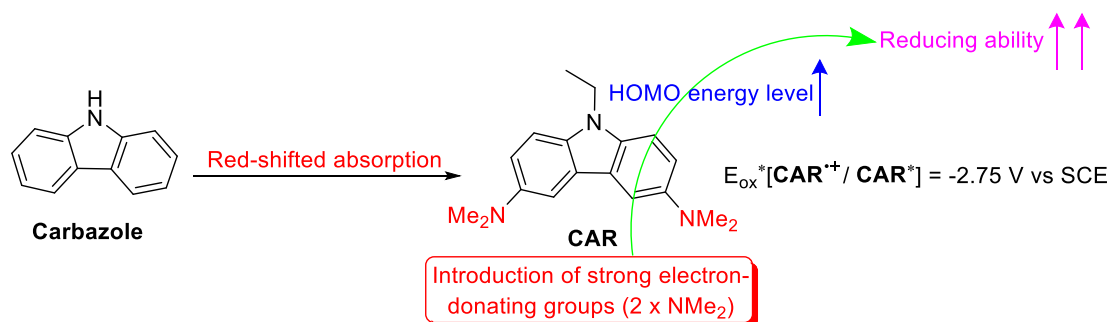


Figure 1.19. Conversion of CO_2 to CH_4 employing COP containing metal-free elements like N, O and P as photocatalyst. Figure is reproduced from Liu, Z. et al.¹²⁰

2. Objectives

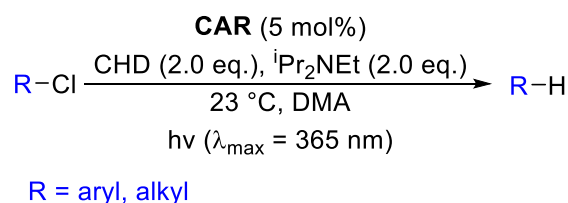
2.1. Previous work in our group and related report

In previous works, our group noticed that carbazole was converted to *N*-ethyl-3,6-bis(dimethylamino)carbazole (**CAR**), which happened red-shifted absorption in UV spectrum. Besides, when the ground state redox potential of the carbazole derivative was measured by cyclic voltammetry (CV) and its excited state oxidation potential was obtained via a classical Rehm-Weller equation with a significantly strong reducing capability in comparison with the parent carbazole (Scheme 2.1). In general, it's well known that a molecule with higher energy level in its ground state-form highest occupied molecular orbital (HOMO) possesses a lower ground state oxidative potential and a higher excited state energy leading to stronger reduction capability in its excited state according to the Rehm-Weller equation: $E_{ox}^* = E_{ox} - E_{ex} + \omega$ (E_{ox}^* refers to its excited state oxidative potential; E_{ox} refers to its ground state oxidative potential; E_{ex} refers to its excited state energy; ω refers to the work function which is usually zero).¹²¹ Based on this fact, the possible reason for introducing dual strong electron-rich dimethylamino groups in carbazole derivative would make its HOMO energy rise, resulting in the excited state 3,6-diaminocarbazole derivative with deeply minus redox potential.



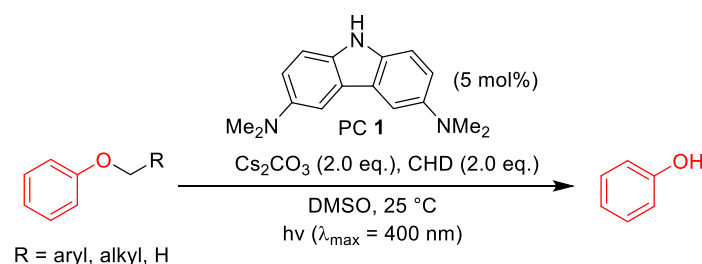
Scheme 2.1. The conversion of carbazole to **CAR** is accompanied by the change of photoelectric properties.

Next work, our group tried to utilize the advantage to reduce some molecules with the low reduction potential. For instance, the C–X (X = Cl, Br) bond split of organohalides via photochemical reduction is still a formidable issue, especially, alkyl-X bond. In 2018, Yabuta¹²² achieved different forms of organohalides that could suffer photoinduced reduction to form carbon radicals which were captured by hydrogen source using metal-free **CAR** as photocatalyst in our group (Scheme 2.2).



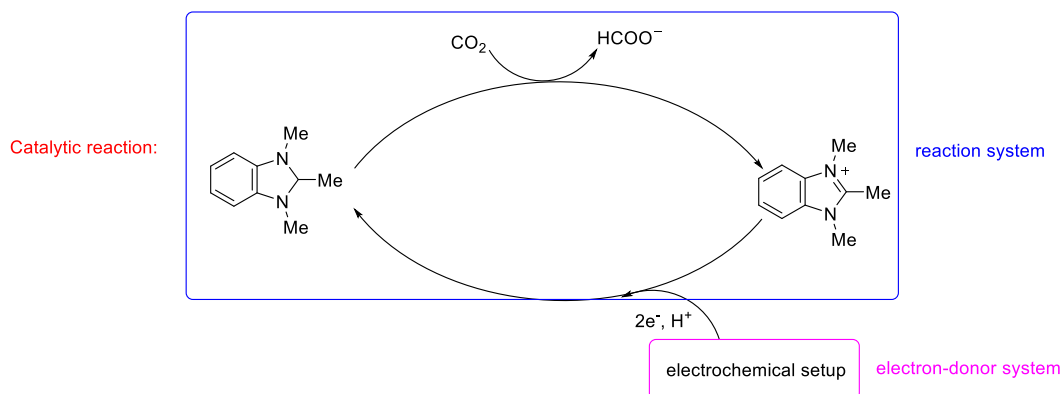
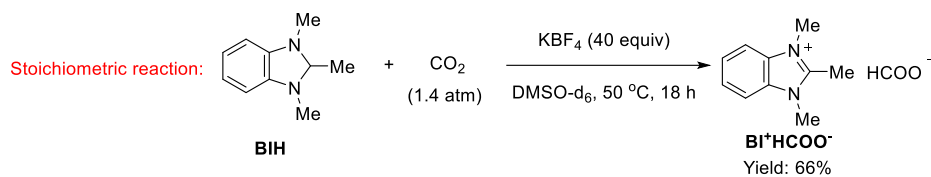
Scheme 2.2. photoinduced reductions of organohalides using **CAR** as photocatalyst

It's a prevailing point of view that activation of ether C–O bond faces a huge difficulty due to its highly thermodynamic stability. However, it's a viable chance that photocatalytic one-electron based reduction of ethers is a potential approach to cleave the C–O bond using deeply negative oxidation potential photocatalyst in excite-state. Herein, in 2021, our group informed light-driven reduction of aryl alkyl ether C–O bond to afford the corresponding phenol product using 3,6-bis(dimethylamino)-carbazole as organic photocatalyst (Scheme 2.3).¹²³



Scheme 2.3. The photochemical cleavage of C–O bond using PC 1 as photocatalyst.

Additionally, we recently noticed that Lim, C. H. and Musgrave, C. B. et al.¹²⁴ have reported that benzimidazole-based organohydrides (**BIH**) reacted with CO₂ to afford formate. This proposal was the exclusive selectivity of formate formation without hydrogen evolution compared with transition metal catalytic CO₂ reduction in a moderate yield. Even though the solution was a representative model of two-electron CO₂ reduction reaction (CO₂RR) enabled exclusively by non-metal organohydrides, **BIH** was stoichiometrically needed to reduce CO₂, besides, multi-equivalents of metal salt (KBF₄) was employed to drive the reaction toward HCOO⁻ product side, which left a significant concern that needed to be resolved later. Albeit authors were able to successfully regenerate **BIH** from (**BI**⁺) via electrochemical reduction, the regeneration process was conducted in the separated vessel from the CO₂ reduction system. That's a tricky problem to cope with large-scale application in the future (Scheme 2.4).



Scheme 2.4. The thermochemical treatment of CO₂ with **BIH** to form formate.

2.2. proposal hypothesis of this work

The fact that **BIH** is smoothly converted to **BI⁺(I⁻)** with generation of hydride that is captured by CO₂ due to its weak electrophilicity. Additionally, we recently found that (dimethylamino)carbazole moiety could function as a visible light-driven photosensitizer, especially, its excited state with strong reducing ability. So, we envisage to use these advantages to achieve photocatalytic cycle to provide electron for regeneration of **BIH** from its oxidized form **BI⁺(I⁻)** employing ascorbic acid as sacrificial reductant under 400 nm irradiation condition (Figure 2.1).

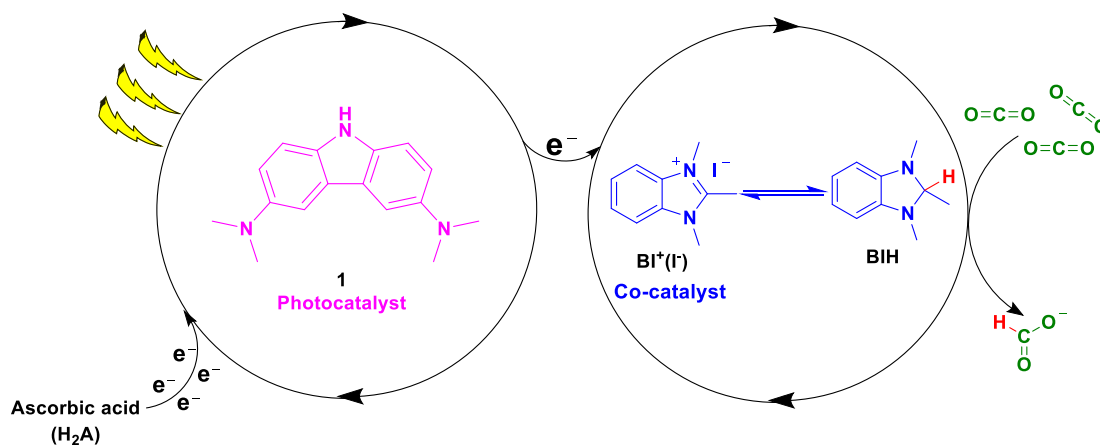
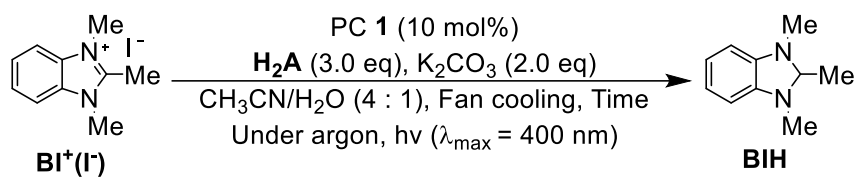


Figure 2.1. A hypothetical mechanism for metal-free photocatalytic reduction of CO₂.

3. Study on photocatalytic CO₂ reduction enabled by dual catalysts

3.1. Feasibility of proposal

Our team of researchers has recently been developing the photocatalytic reduction of organic species with lower reduction potential via photoinduced electron transfer technique using strong reducing capability of excited-state 3,6-bis(dimethylamino)-carbazole moieties as photoredox catalysts. Given their prominent optoelectronic properties that probably render them promising candidates for photocatalytically reducing carbon dioxide, we attempt to leverage on this advantage to achieve a photocatalytic cycle that smoothly provides electrons for the regeneration of **BIH** from **BI⁺(I)**. Consequently, **BIH** reduces CO₂ to generate formate enabled by assisted-hydride. Corresponding to our question on whether **BIH** possesses photochemically recyclable capability, the following was carried out. First, the photocatalytic reduction of **BI⁺(I)** to its reduced-state **BIH** using PC **1** as a photocatalyst was performed in the existence of ascorbic acid as a reductant under 400 nm irradiation condition. As a result, product **BIH** was efficiently formed in different irradiation times. What surprised us was that the reaction rate was so fast, only 15 min up to maximum yield of **BIH** (Table 3.1, entry 4). If reaction time was extended, yield of **BIH** was slightly decreased, but the yield of formate was significantly increased, which it was reasonable that a small part amount of **BIH** performed conversion of CO₂ to formate due to K₂CO₃ function as CO₂ source in our current reaction system. In order to further determine authentic structure of **BIH**, **BIH** was isolated with a 27% of yield using running column chromatography (Table 3.1, entry 9). Besides, Reduction of **BI⁺(I)** to **BIH** for 20 h with 44% of **BIH** product and 54% remaining substrate **BI⁺(I)** (Table 3.1, entry 9). This further suggests that **BI⁺(I)** and **BIH** were both chemically stable enough to be effective catalysts and the regeneration of hydride using carbazole moiety as a photocatalyst was viable. ¹H NMR spectras of experiment solutions corresponded to reaction times 0 min, 4 min, 8 min and 15 min in order (Figure 3.1) which was clearly shown that peaks of **BIH** gradually increased with that of **BI⁺(I)** decreasing.



Entry	Time	Temp./°C	BI ⁺ (I) ⁻ : BIH ^a	Yield ^b of HCOO ⁻
1	0	24	100 : 0	0%
2	4 min	33	70 : 30	1%
3	8 min	37	54 : 46	3%
4	15 min	38	34 : 66	6%
5	30 min	38	47 : 53	14%
6	1 h	37	57 : 43	35%
7	2 h	36	59 : 41	45%
8	4 h	37	60 : 40	60%
9	20 h	32	55 : 45	68%
10 ^c	15 min	25	100 : 0	0%

^a Determined by ¹H NMR analysis with 1,3,5-trimethoxybenzene as internal standard.

^b Based on the amount of K₂CO₃ as theoretical amount of formate product to calculate the yield. ^c Without light condition

Table 3.1. Reduction of benzimidazolium salt BI⁺(I⁻) to benzimidazoline BIH via visible light-driven photosensitization.

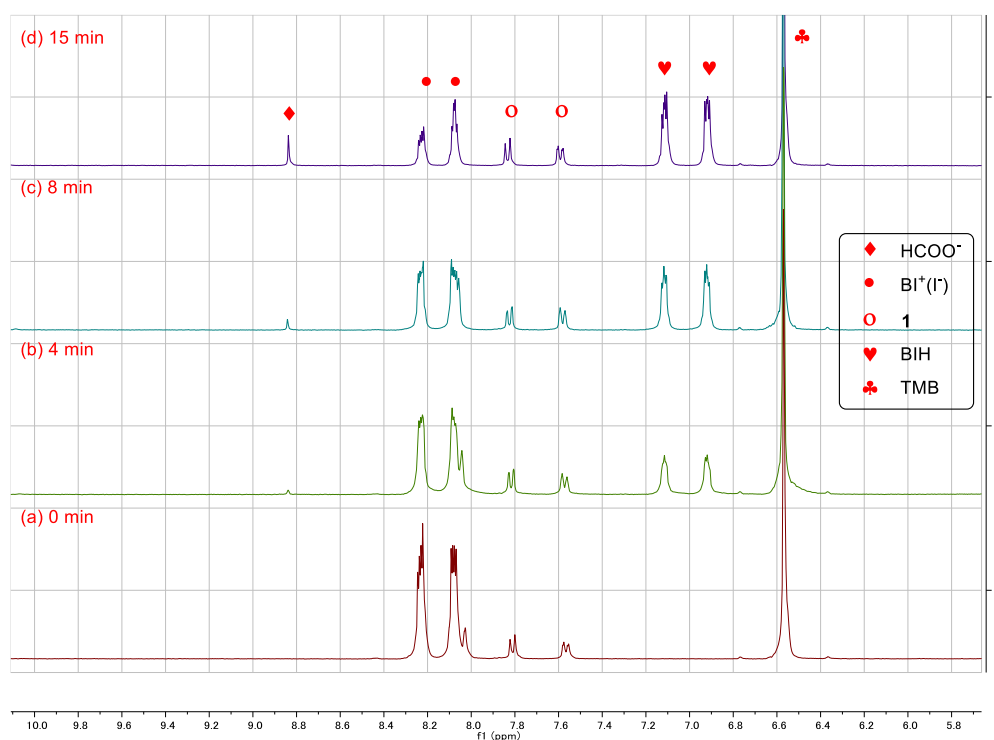
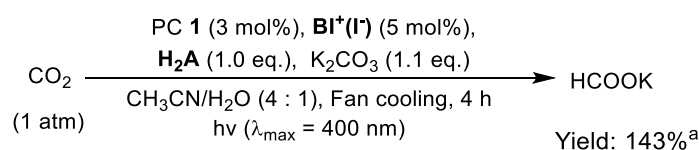


Figure 3.1. ^1H NMR spectra of experiment solutions corresponding to reaction time 0 min, 4 min, 8 min and 15 min in order.

3.2. Demonstration of solution

With reliable data above in hand, we next investigated photoinduced reduction of CO_2 using a catalytic amount of carbazole moiety as photocatalyst, $\text{BI}^+(\text{I}^-)$ as co-catalyst and ascorbic acid acted as sacrificial electron donor. A specific procedure of reaction was performed as following: A 50 mL of flame-dried screw tube was replenished with $\text{BI}^+(\text{I}^-)$ (7.2 mg, 0.025 mmol, 0.05 eq.), PC **1** (3.8 mg, 0.015 mmol, 0.03 eq.), K_2CO_3 (76.0 mg, 0.550 mmol, 1.1 eq.) and ascorbic acid (88.1 mg, 0.500 mmol, 1.0 eq.). Next, distilled H_2O (2 mL) and acetonitrile (8 mL) were transferred to reaction mixture. The solution was removed air by freeze–pump–thaw, three times. Afterward, a backfilled- CO_2 balloon was connected to the screw tube. The reaction was stirred using fan to cool reaction temperature under 400 nm of irradiation condition for 4 h (Scheme 3.1). Following the reaction, TMB (40.6 mg) as internal standard and H_2O (4 mL) were transferred into resultant reaction solution and then take 0.6 mL of the above solution for the measurement of ^1H NMR using solvent suppression technique. Based on the amount of ascorbic acid as theoretical amount of formate product, formate was produced with a 143% of yield. So, photocatalytic reduction of CO_2 was initially demonstrated using a PC **1** as photosensitizer and $\text{BI}^+(\text{I}^-)$ as co-catalyst.



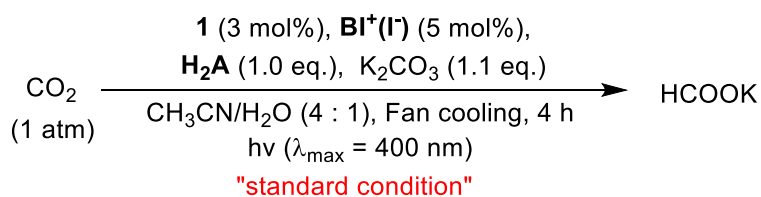
^a Based on the amount of ascorbic acid as theoretical amount of formate product to calculate the yield and determined by ^1H NMR analysis with 1,3,5-trimethoxybenzene as internal standard.

Scheme 3.1. Photocatalytic reduction of CO_2 reaction enabled by photosensitized regeneration of **BIH**.

3.3. Optimization of conditions and control reactions

At present, we have initially demonstrated that photocatalytic reduction of CO_2 was viable under designed reaction system conditions. Next, in order to obtain the best optimal condition available for conversion of CO_2 to value-added formate, it's essential to screen some basic condition. In view of previous reaction time, 20 h was enough long time for photocatalytic reduction CO_2 system and it not only decreased the TOF value but also maybe generated some byproducts to participate in the photocatalytic reaction cycle, which brought us some trouble to investigate authentic situation. So, as we first examined reaction time by controlling other parameters, 4 h was optimal reaction time with an excellent yield (Table 3.2, entries 1 to 3). Furthermore, a few of control experiments revealed that photocatalyst, light, sacrificial electron donor and base were all necessary for photoinduced CO_2 reduction (Table 3.2, entries 4 to 8). The yield was decreased up to 8% without $\text{BI}^+(\text{I}^-)$, prompting its meaningful performance as a co-catalyst (Table 3.2, entry 9). Some related papers often reported that iodide

function as a redox mediator activated reaction system by conversion of iodide to an active iodine radical. In current reaction system, catalytic amount of iodide as a counter anion of co-catalyst maybe implemented an effective influence on photocatalytic reduction of CO₂. To this end, we prepared the authentic benzimidazole (**BIH**) and its oxidized benzimidazolium salt (**BI⁺(I⁻)**) and then using them as co-catalyst, respectively to perform photoinduced reduction of CO₂ reaction under current condition. In the two cases (Table 3.2, entries 1 and 10), consistent with the working hypothesis, yield of product using **BIH** as co-catalyst was the same result as that of **BI⁺(I⁻)**, indicating iodide anion was silent in current catalytic cycle. Additionally, considering treatment of ascorbic acid with base produced its corresponding ascorbate as intermediate that authentically functioned as sacrificial electron donor. So, it was critical to further screen various bases, using other inorganic bases instead of potassium carbonate (Table 3.2, entries 11–16), prompting different forms of cations and anions of bases slightly affected the reaction to some extent. For sacrificial electron donor, employing sodium sulfite or sodium hydrogen sulfite instead of ascorbic acid, the yield was dramatically decreased, resulting in 64% and 61% in order (Table 3.2, entries 17 and 18). which didn't mean an undesired result since they only provided two-electron per molecule (100% of theoretical yield) to participate in reduction of CO₂ compared with two times oxidation of ascorbic acid to provide 4-electron per molecule. To our surprise, there's still a good yield using argon instead of CO₂ as shown from entry 19; however, minimal formate was produced in the absence of CO₂ gas using NaOH instead of K₂CO₃ (Table 3.2, entry 20), prompting that carbonate ion could function as a source of CO₂ in the photocatalytic CO₂ reduction reaction system. Additionally, Using the same condition with either increase ratio of acetonitrile or that of decrease led to the inferior to yield of standard condition (Table 3.2, entries 21 and 22); notably, the activity was suppressed when acetonitrile was replaced with other solvents such as *N, N*-dimethylacetamide (DMA) (Table 3.2, entry 23).



Entry	Variation from above "standard condition"	Yield/% ^a
1	None	143
2	3 h	121
3	5 h	136
4	Without K ₂ CO ₃	0
5	KCl (2.0 eq) instead of K ₂ CO ₃	<1
6 ^b	No light	0
7 ^b	Without H ₂ A	<1
8	Without 1	0

9	Without BI⁺(I⁻)	8
10	BIH instead of BI⁺(I⁻)	142
11	Li ₂ CO ₃ (1.1 eq) instead of K ₂ CO ₃	68
12	Na ₂ CO ₃ (1.1 eq) instead of K ₂ CO ₃	114
13	Cs ₂ CO ₃ (1.1 eq) instead of K ₂ CO ₃	122
14	KOH (2.2 eq) instead of K ₂ CO ₃	78
15	NaOH (2.2 eq) instead of K ₂ CO ₃	103 (117) ^b
16	K ₃ PO ₄ (2.2 eq) instead of K ₂ CO ₃	143
17	Na ₂ SO ₃ instead of H₂A	64 (52) ^c
18	NaHSO ₃ instead of H₂A	61 (3) ^c
19	Argon instead of CO ₂	104
20	Argon instead of CO ₂ , NaOH (2.2 eq) instead of K ₂ CO ₃	5
21	CH ₃ CN/H ₂ O (3/2 v/v) instead of CH ₃ CN/H ₂ O (4/1 v/v)	68
22	CH ₃ CN/H ₂ O (9/1 v/v) instead of CH ₃ CN/H ₂ O (4/1 v/v)	68
23	DMA/H ₂ O instead of CH ₃ CN/H ₂ O	45

^a Based on the amount of ascorbic acid as theoretical amount of formate product to calculate the yield and determined by ¹H NMR analysis with 1,3,5-trimethoxybenzene as internal standard.; ^b Reaction time: 20 h; ^c Without K₂CO₃

Table 3.2. Optimization of conditions and control experiments for photocatalytic CO₂ reduction reaction.

3.4. Determination of the carbon source of formate product by labeling experiment

It is a common phenomenon that a part of the amount of the corresponding carbon-containing products is not produced through the photocatalytic reduction of CO₂ but from the decomposition of some related reagents or solvents in reaction system. This contamination could result in the misestimation of authentic yield. Therefore, it is indispensable to prove whether the carbon element of HCOO⁻ is provided from CO₂ outside to ensure the accuracy of the results. ¹³CO₂ was used for the isotope-labeling experiment to determine the carbon source of formate (Figure 3.2A). Besides, we also employed normal experiment using ¹²CO₂ compared with that of results (Figure 3.2A'). In the ¹H NMR spectrum (Figure 3.2B), double peaks (¹J_{CH} = 192.8 Hz) at 9.06 and 8.58 ppm were due to the proton of H¹³COONa (90% yield) which occurred to couple with its ¹³C atom. it's worth noting that a relatively low singlet at 8.82 ppm corresponded to the H¹²COONa (3% yield) resulting from contamination of ¹²CO₂ released from **H₂A** (Figure 7.1) during the reaction, which the single peak was the same with the position of peak from ¹H NMR spectrum of normal experiment (Figure 3.2B'). In the ¹³C NMR spectrum of the same reaction (Figure 3.2C), a strong signal peak at 169.4 ppm was observed from corresponding H¹³COONa. Besides, a relatively weak signal peak at 124.0 ppm was ascribed to ¹³CO₂. We also noticed that a dramatic crosspeak was shown in HMQC spectrum (Figure 3.2D), revealing ¹H and ¹³C nuclei in formate occurred the direct correlation. These above results fully demonstrated that

the carbon element of HCOO^- is provided from CO_2 outside through the photocatalytic reduction of CO_2 .

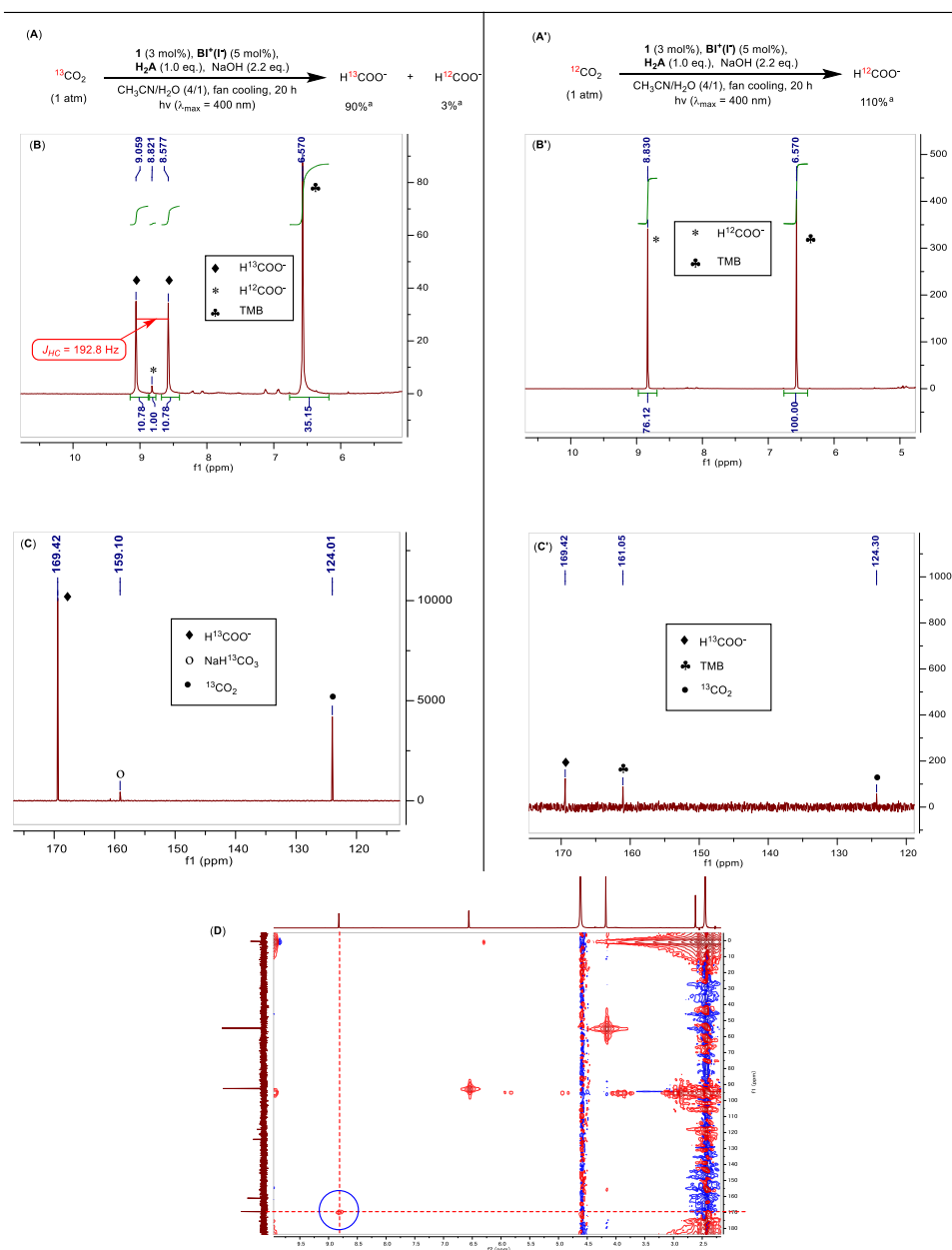


Figure 3.2. (A): Reaction conditions of labeling experiment using $^{13}\text{CO}_2$; (A'): Reaction conditions of normal experiment using $^{12}\text{CO}_2$; (B): ^1H NMR spectrum of (A) solution; (B'): ^1H NMR spectrum of (A') solution; (C): ^{13}C NMR spectrum of (A) solution; (C'): ^{13}C NMR spectrum of (A') solution; (D): HMQC spectrum of (A') solution. (^a Based on the amount of ascorbic acid as theoretical amount of formate product to calculate the yield and determined by ^1H NMR analysis with 1,3,5-trimethoxybenzene (TMB) as internal standard.)

3.5. Investigation of gas evolution (H_2 or CO) from photoinduced CO_2RR by GC

Knowingly, metal-catalyzed CO_2 reduction in which CO and H_2 generated becomes side reaction. It's indispensable that we need to determine whether CO and H_2

gaseous compounds are yielded in current reaction system. Considering that gas chromatography is a valuable instrument to investigate the components of gas samples, in addition, it is a very flexible approach to quantify amount of a sample. So, we carry out quantitative analysis of evolved gas in the headspace of photochemical reactor by GC.

First, sample of photocatalysis experiment of CO₂ reduction under standard condition was obtained as following procedure: To a 50 mL of flame-dried screw tube equipped with a septum was placed with ascorbic acid (1.0 eq., 88.1 mg, 0.500 mmol), K₂CO₃ (1.1 eq., 76.0 mg, 0.550 mmol), **BI⁺(I⁻)** (0.05 eq., 7.2 mg, 0.025 mmol), and **PC 1** (0.03 eq., 3.8 mg, 0.015 mmol) in order and then distilled water (2 mL) and CH₃CN (8 mL) were introduced into the screw tube of 36.7 mL headspace. The reaction vessel was evacuated to remove air by CO₂ bubbling for 15 min and then the cap of the screw tube was tightly sealed. Finally, the reaction was stirred under irradiation condition for 20 h.

And then making CO and H₂ standard curves using pure CO and H₂ by gas chromatography with argon as mobile phase (Ms-5A column, TCD). First, inject 2 μL, 6 μL, 8 μL and 10 μL of pure H₂ into GC, respectively (Figure 3.3) and inject 10 μL, 20 μL and 30 μL of pure CO into GC in order (Figure 3.4). Based on the between the peak areas and their amount, Standard cures H₂ and CO were made.

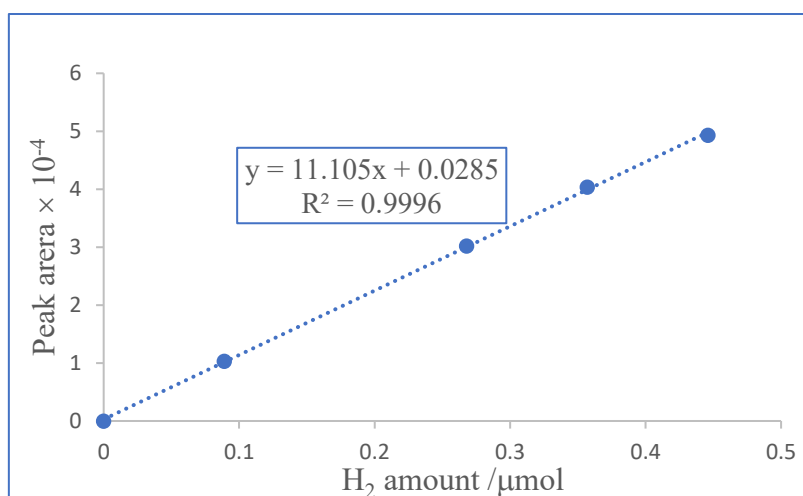


Figure 3.3. Standard curve of H₂.

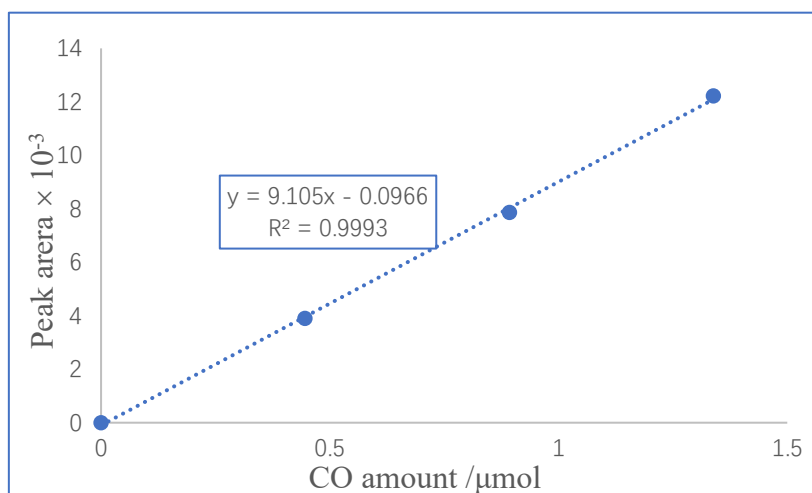


Figure 3.4. Standard curve of CO.

Eventually, inject 50 μL of sample through the septum with a microliter syringe from the screw tube of 36.7 mL headspace. The recorder of GC just gave a line without any peak. If we hypothesized photocatalytic conversion of CO_2 to H_2 or CO with 100% yield, respectively, the quantity of H_2 or CO was 0.681 μmol in 50 μL of headspace gas from the sample. Besides, setting the detection limit of standard curve for H_2 to 100 peak area and the detection limit of standard curve for CO to 50 peak area. By the calculation, H_2 and CO evolution were below the detection limit ($< 0.1\%$ yield for H_2 and $< 0.8\%$ yield for CO) (Figure 3.5), indicating photocatalytic conversion of CO_2 to formate with strong selectivity in our reaction system.

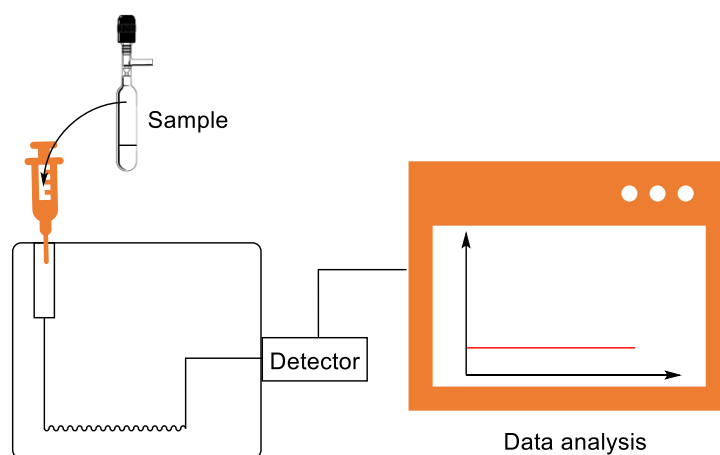


Figure 3.5. Quantitative analysis of evolved gas from sample by GC

3.6. Demonstration of formation of oxalate in photoinduced CO_2RR

^{13}C NMR spectrum of the reaction mixture from ^{13}C -labeling experiment in Figure 3.2A was compared with authentic ^{13}C NMR spectrum of sodium oxalate, in which there was not authentic peak of sodium oxalate generated in ^{13}C NMR spectrum of ^{13}C -labeling experiment (Figure 3.6). Considering that peak position of sodium oxalate was closely adjacent to that of $\text{H}^{13}\text{COONa}$, it was critical to further demonstrate to see if

two peaks were the same position. To the reaction solution of ^{13}C -labeling experiment was added sodium oxalate, via ^{13}C NMR spectrum analysis of above mixture solution, two peaks from $\text{H}^{13}\text{COONa}$ and sodium oxalate were obviously showed in the ^{13}C NMR spectrum, clearly indicating oxalate was not generated in photoinduced CO_2RR system.

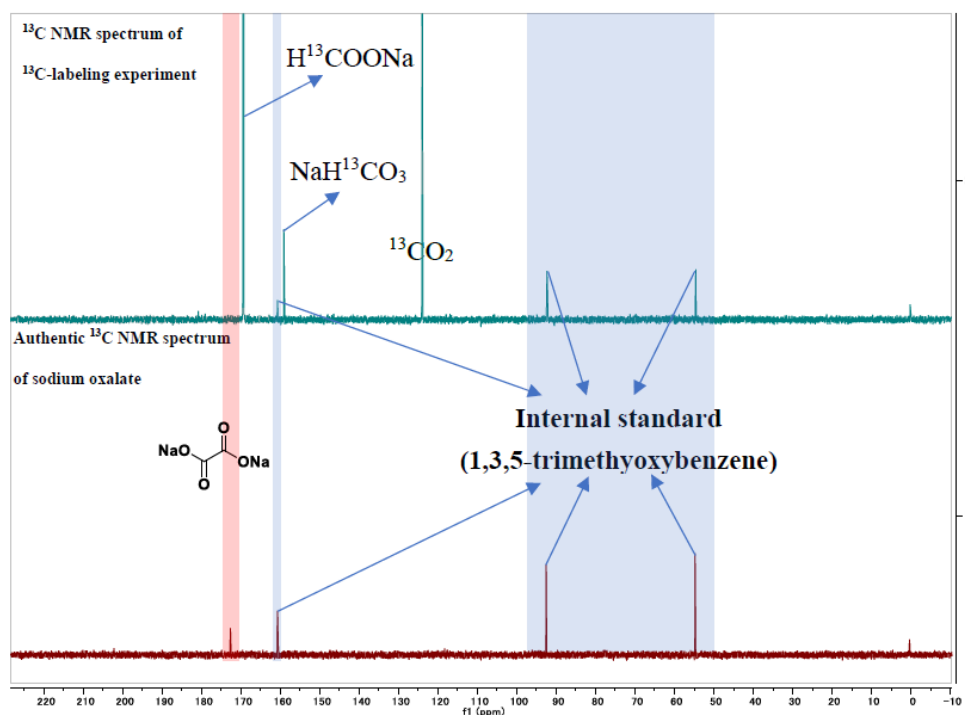
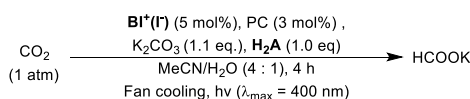


Figure 3.6. ^{13}C NMR spectra of ^{13}C -labeling experiment solution in $\text{CH}_3\text{CN}/\text{H}_2\text{O}$ (1/1 v/v) (darkcyan spectrum above) and ^{13}C NMR spectra of sodium oxalate solution in $\text{CH}_3\text{CN}/\text{H}_2\text{O}$ (1/1 v/v) (brown spectrum below). ^{13}C NMR analysis was conducted using solvent suppression technique with 1,3,5-trimethoxybenzene (TMB) as the internal standard.

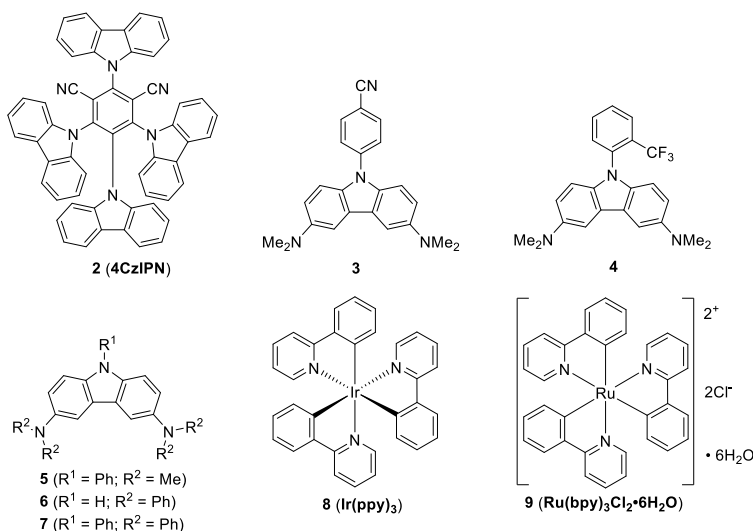
3.7. Investigation of potential photosensitizers

Next, we shifted our attention to other potential photosensitizers. As **4CzIPN** had excellent photophysical and electrochemical properties, it was widely applied in photocatalytic redox reaction. We were interested to compare the activity of bis(dimethylamino)carbazole moiety with **4CzIPN** with high oxidative potential in excited state. We found formate was not obtained using **4CzIPN** as photocatalyst (Table 3.3, entry 2). This might be due to the mismatch between its excited state's oxidation potential and the reduction potential of $\text{BI}^+(\text{I})$, thus, resulting in no activity during photoinduced electron transfer (PET). Additionally, to further investigate whether different N-substitutions affected activities of bis(dimethylamino)carbazole moieties, PC **3** to **7** were prepared in hand. These N-substituted carbazoles were screened under standard conditions. We found that PCs based on carbazole moieties with electron-withdrawing groups had no performance for photochemical conversion of CO_2 to formate (Table 3.3, entries 3 and 4) since their reducing capabilities were not enough

to shift electrons toward **BI⁺(I). Comparable yields of HCOO⁻ product was provided employing **5** to **7** as photocatalysts due to their excited state redox potentials similar to PC **1**. (Table 3.3, entries 5 to 7). Due to the merits of precious metal photosensitizers, namely: intense absorption, triplet form-based excited states with long-term lifetime, as well as high triplet-state quantum efficiency, they commonly possess strong reducing and oxidizing capability in excited state, such as Ru (II) and Ir (III) coordination complexes. Accordingly, we attempted to employ Ir(ppy)₃ and Ru(bpy)₃Cl₂·H₂O as photocatalysts to apply in the photochemical reduction of CO₂ under standard conditions. We noticed that Ir(ppy)₃ complex showed a productive efficiency in a 132% of yield which was basically equivalent to performance of bis(dimethylamino)-carbazole moiety, Additionally, formate was not yielded from Ir(ppy)₃ without **BI⁺(I). Thereby, it suggested that the occurrence of Ir(ppy)₃-photocatalyzed CO₂RR was through **BI⁺(I) that involved a process analogous to the reaction employing **1** as photocatalyst. Thus, the combination of catalysts Ir(ppy)₃ complex and **BI⁺(I) in one reaction system was a novel discovery in current study. (Table 3.3, entry 8). whereas Ru(bpy)₃Cl₂·H₂O complex was incapable of providing the formate product in current reaction system. (Table 3.3, entry 9).********



Entry	PC	Yield/% ^a
1	1	143
2	2	0
3	3	0
4	4	0 ^b
5	5	127
6	6	110
7	7	111
8	8	132 (0) ^c
9	9	0



^a Based on the amount of ascorbic acid as theoretical amount of formate product to calculate the yield and determined by ¹H NMR analysis with 1,3,5-trimethoxybenzene

as internal standard.; ^b If the reaction was performed under strong luminous intensity light condition, good yield was produced resulting from the fact that PC 4 was decomposed to active product function as productive photosensitizer; ^c Without **BI⁺(I)**

Table 3.3. Activities of different photosensitizers on photoinduced reduction of CO₂.

4. Study on photocatalytic CO₂ reduction enabled by integrated-form catalysts

4.1. Design and synthesis of integrated-form catalysts

With an established system of photocatalytic CO₂ reduction reaction, a more efficient catalyst is pursued by designing an integrated-form catalyst using a combination of both carbazole and benzimidazole into one molecule. This is to effectively execute CO₂ reduction reaction in which the carbazole provides an electron to be transmitted quickly to benzimidazole by the linker. A simple synthetic route was drafted (Figure 4.1) for execution plan.

First, we attempted to synthesize compound **1** using palladium-catalyzed C-N cross coupling (Buchwald–Hartwig reaction). Pd₂(dba)₃ and Ruphos were charged into flame-dried screw tube in THF and then stirred for 5 min at ambient temperature. Subsequently, 3,6-dibromocarbazole **10**, LiHMDS and dimethylamine hydrochloride were added into the screw tube respectively. Finally, reaction solution was heated at 90 °C for 17 h. Substrates were consumed completely to afford product **1** in a good yield.

Given the attainment of bis(dimethylamino)carbazole, we attempted to employ dihalogen-substituted alkane function as a bridge to connect carbazole and benzimidazole to produce a final integrated-form compound via two-steps synthesis. Dibromobutane acted as an alkyl-chain linker to react with compound **1** in the presence of sodium hydride by S_N2 reaction to successfully generate compound **11** product.

Using a similar synthetic method, Compound **12** was prepared via S_N2 reaction of 2-methyl-1*H*-benzimidazole with the corresponding bromoalkyl carbazole **11** with the assistance of sodium hydride.

For the synthesis of compound **13**, compound **12** was treated with iodomethane in CH₂Cl₂. However, there were hardly new compounds generated. Due to excess substrate remaining, we attempted to optimize the reaction conditions through the screening of solvent, temperature, and effect of equivalent. We realized that the amount of iodomethane and solvent had significant impacts on the result. Finally, integrated-form catalyst was synthesized in a moderate yield when using 3.0 equivalent of iodomethane and solvent (MeOH) as conditions. However, NMR analysis revealed that the product was not corresponding compound **13** but compound **14**. This could possibly be due to higher susceptibility of two tertiary amino groups of carbazole moiety **12** towards iodomethane as compared to an imino group of benzimidazole moiety **12**.

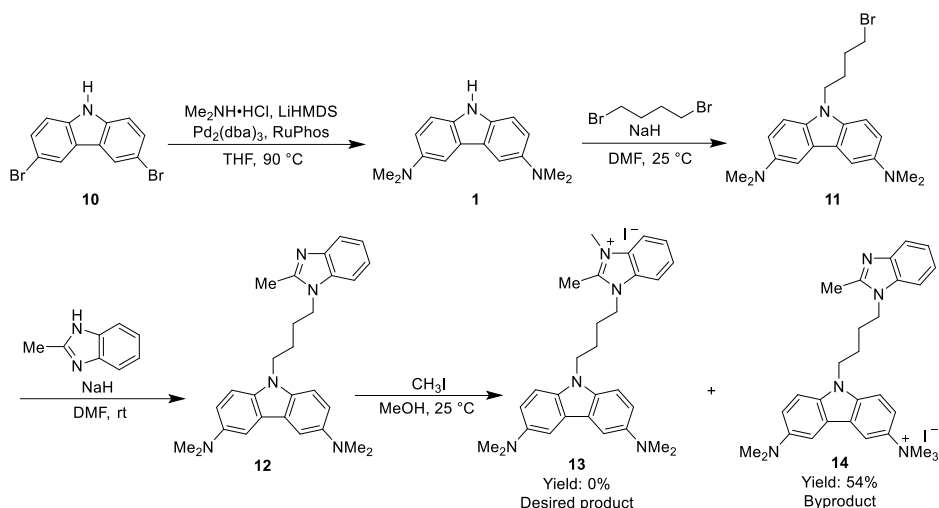


Figure 4.1. Synthetic route of integrated-form catalyst **13**.

To avoid the conversion of tertiary amino of carbazole moiety into salt, a new proposal was plotted as shown in Figure 4.2. we first prepared iodide-based benzimidazolium salt and combined carbazole moiety and benzimidazolium salt using an alkyl-chain linker.

We initially meant to synthesize compound **15** by the condensation of 4-bromobutyric acid with *o*-phenylenediamine in the presence of phosphoric acid under high temperature. Nevertheless, ignore the fact that 4-bromobutyric acid was easily converted to lactone under high temperature condition as active intermediate reacting with *o*-phenylenediamine to provide alcohol compound (Figure 4.3).

At present, product **16** was obtained. Given that alcohol compound was conveniently converted to bromide compound via Appel reaction. The alcohol compound was used as a substrate using the route proceeded in order. Methylation of compound **16** was implemented with the assistance of sodium hydroxide to provide target compound **17**. Subsequently, the imino group of compound **17** underwent methylation to form salt compound **18** in the presence of iodomethane. To obtain bromide compound, we attempted to use mild Appel reaction to convert the alcohol into an alkyl bromide using triphenylphosphine and carbon tetrabromide. The reaction was smoothly executed and most amount of substrate was converted bromide compound **19**. Benzimidazole alkyl bromide was obtained in hand. Next, with the help of sodium hydride, integrated-form catalyst **20** was synthesized by S_N2 reaction of carbazole with the corresponding bromoalkyl benzimidazole. By NMR analysis, we found a new compound generated, namely: byproduct **21** in a 90% yield resulting from decomposition of compound **19** that was extremely fragile under strong base conditions.

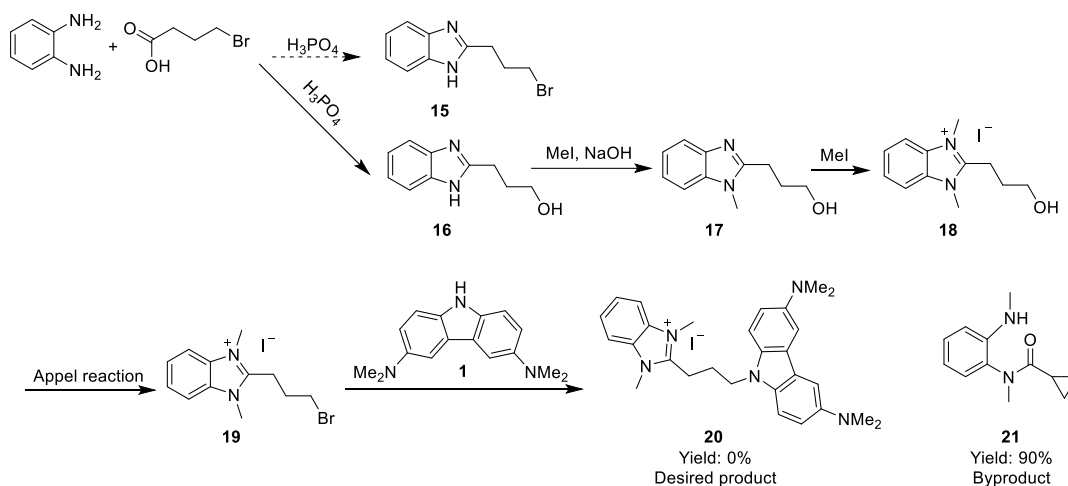


Figure 4.2. Synthetic route of integrated-form catalyst **20**.

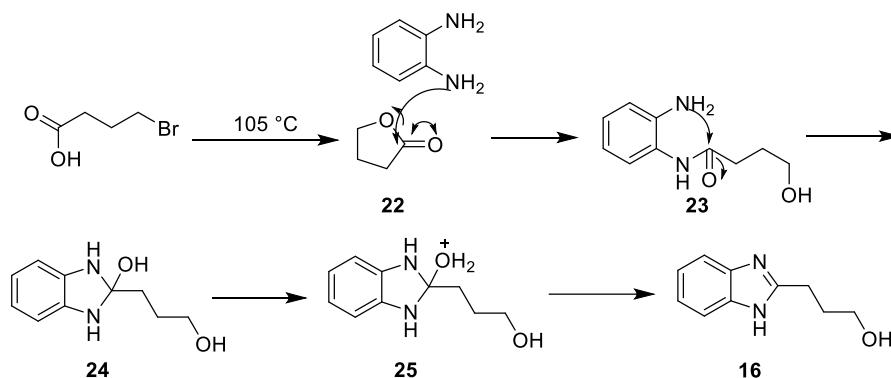


Figure 4.3. Proposal mechanism of formation of compound **16**.

Based on the different activity between iodine and chlorine, we continued attempting to design benzimidazole selectively reacted with 1-Chloro-3-iodopropane, leaving the chlorine group untouched. Subsequently, carbazole moiety attacked the resulting intermediate to produce desired product in the presence of sodium hydride.

1,2-dimethyl-1*H*-benzimidazole and 1-chloro-3-iodopropane were charged in flame-dried screw tube in benzene at 85 °C for 23 h to selectively afford choloalkyl cardazole salt **26** in a good yield. Notably, during reaction, chloride-based benzimidazolium salt was not detected. Next, we tried to prepare the final product **27** by S_N2 reaction of compound **1** with the corresponding choloalkyl cardazole salt **26** with the help of sodium hydride using THF as solvent. Nevertheless, substrate was unconsumed. We noticed choloalkyl cardazole salt **26** was not soluble in THF. We further screened solvents to make it proceed. We realized that the integrated-form reaction was compatible with DMF as solvent in a moderate yield (Figure 4.4).

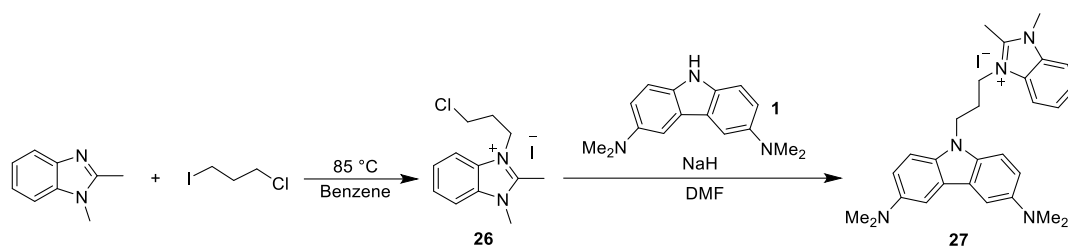


Figure 4.4. Synthetic route of integrated-form catalyst **27**.

To date, we have prepared an integrated-form catalyst bearing the iodide as a counter anion of its salt. We wonder whether counter anion of integrated-form catalyst affects its activity. Therefore, we plan to investigate the synthesis of incorporated photocatalyst with bromide as a counter anion of its salt. Based on a feasible synthetic approach of integrated-form catalyst **27**, a proposal is envisaged to utilize 1,4-dibromobutane as a bridge between carbazole and benzimidazole.

1,2-dimethyl-1*H*-benzimidazole reacted with 1,4-dibromobutane at 90 °C to afford bromoalkyl benzimidazolium salt **28** in a moderate yield. As bromoalkyl group had high reactivity as compared to chloroalkyl, compound **28** was efficiently incorporated to bis(dimethylamino)carbazole **1** to afford desired product **29** (Figure 4.5).

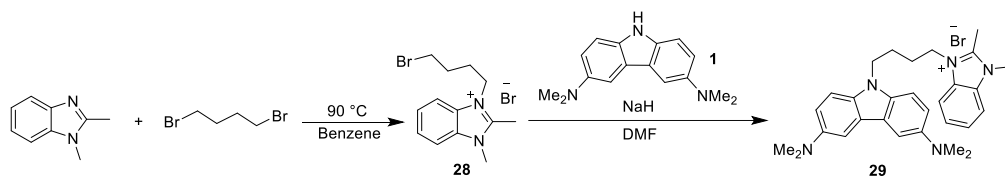


Figure 4.5. Synthetic route of integrated-form catalyst **29**.

With oxidized-state incorporated catalyst in hand, we wish to scrutinize whether reduced-state incorporated catalyst shows a better result for photo-induced reduction of CO₂. Thus, we decided to prepare related reduced-state incorporated catalyst using the following synthetic route (Figure 4.6). The previous method used readily obtained compound **26** which was reduced by sodium borohydride in the mixture solvent (CH₂Cl₂/H₂O) to afford reduced-state compound **30**. Final product **31** was prepared by combination of compound **30** with bis(dimethylamino)carbazole **1** by S_N2 reaction with the assistance of sodium hydride.

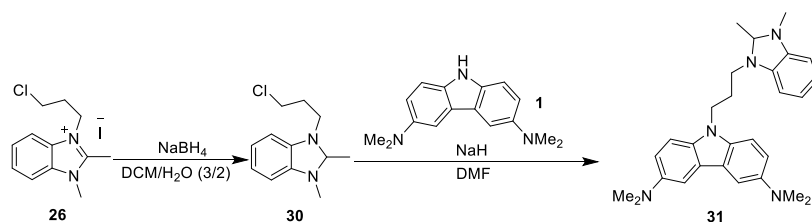


Figure 4.6. Synthetic route of integrated-form catalyst **31**.

4.2. Exploitation of electron donor-acceptor complex

It is commonly observed in the photochemical field that high reactivity of photoredox catalysis is not intrinsically dependent on an authentic photoredox catalyst; but rather the intermediate generated from the interaction between photoredox catalyst and some chemical in a reaction system. The photochemical strategy engages the combination of an electron acceptor molecule and a donor molecule which forms a new molecular aggregation in the ground state, known as an electron donor-acceptor (EDA) ¹²⁵⁻¹²⁷ complex which plays the role in an authentic photocatalyst. Such practice has been widely exploited and applied. The EDA complex as a photocatalyst is excited by light. Subsequently, an intramolecular single-electron transfer (SET) event is triggered to form radical intermediates under milder conditions as accompany with red-shift absorption of EDA complex in the ground state (Figure 4.7).¹²⁵

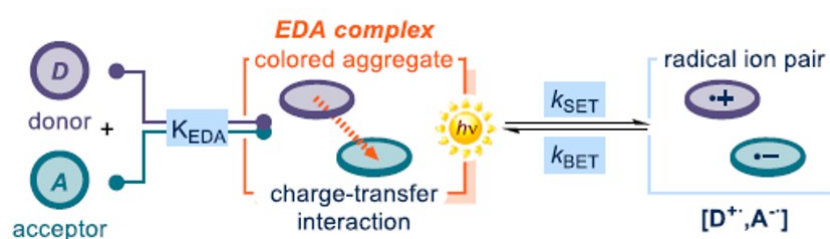


Figure 4.7. The formation process of the EDA complex. Figure is reproduced from Melchiorre, P. et al.¹²⁵

Due to current reaction system under 400 nm irradiation condition, some weak chemical bonds from photosensitizer and co-catalyst may be at risk of being broken to decrease their stability and activity. We anticipate photocatalyst and co-catalyst are converted to EDA complex in the ground state which happens red-shift absorption to extend lifetime of photosensitizer and co-catalyst and shorten reaction time by fast intramolecular electron transfer for CO₂ reduction under a wilder condition. Fortunately, photosensitizer and co-catalyst are suitable for feature of formation EDA complex: **BI⁺(I⁻)** as electron acceptor and PC **1** as electron donor. For now, a few integrated-form catalysts as potential EDA complexes have prepared in hand (Figure 4.8). Owing to red-shift absorption as an important characteristic for the formation of EDA complexes, incorporated molecules **27**, **29** and **31** were measured by UV-vis absorption spectrum and their adsorption regions didn't occur the feature of red-shift compared with that of PC **1**, indicating no discernible electronic transformation occurred between the PC and co-catalyst components of ground state incorporated molecules (Figure 8.1).

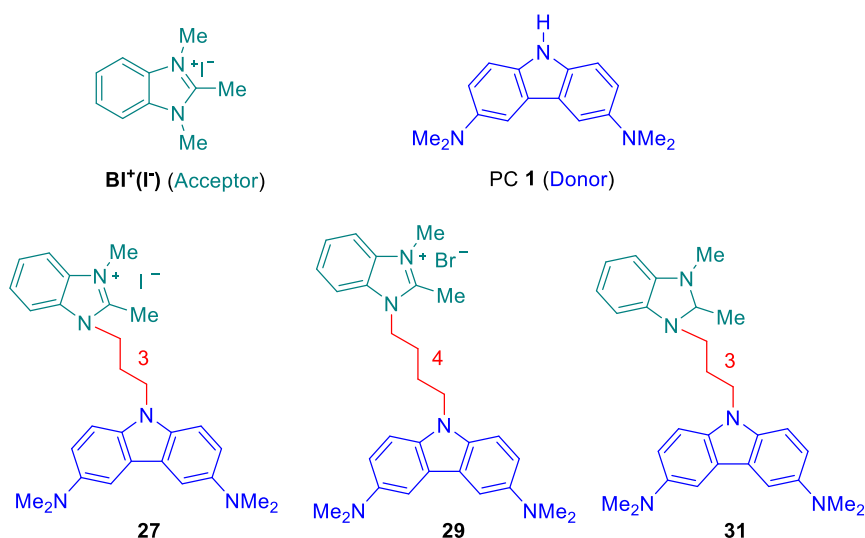
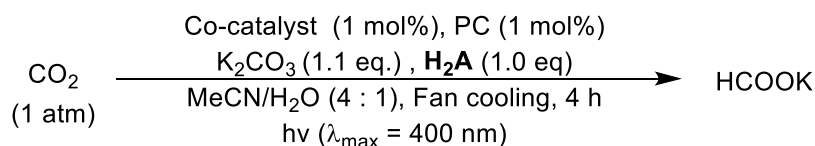


Figure 4.8. The potential EDA complexes composed of **BI⁺(I⁻)** and compound **1**.

4.3. Activities of integrated-form catalysts

Dihalogen substituted alkane function as a bridge to connect carbazole and benzimidazole as a feasible approach has successfully produced a few integrated-form photocatalysts (all-in-one catalysts) via two-steps synthesis. Photocatalytic CO₂RR employing 0.01 equivalent of stand-alone catalysts **27**, **29**, or **31** yielded HCOO⁻ product with 68, 72 or 56% yields, respectively (Table 4.1 entries 2 to 4). These results demonstrated that photoinduced CO₂RR utilizing a single molecular catalyst was theoretically feasible. However, we also noticed that their photo-activity was slightly inferior to that of separated catalysts available for photochemical reduction of CO₂ (Table 4.1 entry 1), ascribing to speedily intramolecular back electron transfer.



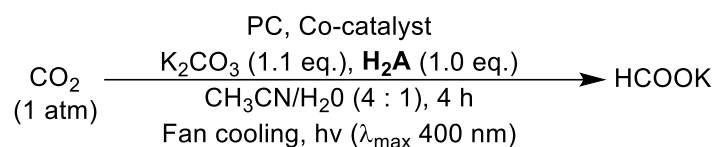
Entry	PC	Co-catalyst	Yield/% ^a
1	1	BI⁺(I⁻)	100
2	27	No	68
3	29	No	72
4	31	No	56

^a Based on the amount of ascorbic acid as theoretical amount of formate product to calculate the yield and determined by ¹H NMR analysis with 1,3,5-trimethoxybenzene as internal standard.

Table 4.1. Activities of incorporated photocatalysts on photocatalytic CO₂RR.

5. Study on stability and activity of photocatalysts and co-catalyst

Turnover number (TON) and turnover frequency (TOF) as significant parameters evaluate the performance of the catalyst, especially, in the photocatalytic reduction of CO₂ case, TON and TOF function as rulers to estimate the durability and kinetic activity of the catalyst. Building on this advantage, we could seek for the best target photocatalysts which efficiently and speedily converted substrates to products under a wild reaction condition. At present, we have screened five potential PCs (**1**, **5**, **6**, **7** and **8**) that were effectively capable of photochemical reduction of CO₂ under standard condition. First, we used catalytic amounts of PC (3 mol%) and co-catalyst (5mol%) to promote CO₂RR proceeding. Their values of TON and TOF were roughly the same as each other (Table 5.1, entries 1, 3, 5, 7 and 9). Next, we demonstrated that catalytic amount of PCs were reduced by a dramatic order of magnitude up to 0.01 mol% (Table 5.1, entries 2, 4, 6, 8 and 10). As a best result, PC **7**-based photocatalytic CO₂ reduction enabled TON and TOF to meet 8820 and 2205 h⁻¹ in order (Table 5.1, entry 8). Besides, we also investigated TON and TOF which were calculated based on co-catalyst. As catalytic amount of PC **5** was set 3 mol%, the amount of co-catalyst **BI⁺(I)** was decreased up to 0.01 mol%. Its TON and TOF exhibited dramatical increment up to 6070 and 1520/h (Table 5.1, entry 12). These dramatic values suggested that the employed photocatalysts and co-catalyst show outstanding chemical activity and physical stability for photocatalytic CO₂RR. If the catalytic amount of PC **5** and co-catalyst were concurrently lowered to 0.1 mol%, only 71% yield was generated. (Table 5.1, entry 14), while further reduction of both catalyst loadings resulted in a much lower yield. (Table 5.1, entries 15 and 16).



Entry	PC	Co-catalyst	Yield/% ^a	TON ^b	TOF/h ^b
1	1 (3 mol %)	BI⁺ (5 mol%)	143	48	12
2	1 (0.01 mol %)	BI⁺ (5 mol%)	27	2750	687
3	5 (3 mol %)	BI⁺ (5 mol%)	127	42	11
4	5 (0.01 mol %)	BI⁺ (5 mol%)	65	6510	1630
5	6 (3 mol %)	BI⁺ (5 mol%)	110	37	9
6	6 (0.01 mol %)	BI⁺ (5 mol%)	45	4480	1120
7	7 (3 mol %)	BI⁺ (5 mol%)	111	37	9
8	7 (0.01 mol %)	BI⁺ (5 mol%)	88	8820	2205
9	8 (3 mol %)	BI⁺ (5 mol%)	132	44	11
10	8 (0.01 mol %)	BI⁺ (5 mol%)	74	7375	1844
11	No	BI⁺ (5 mol%)	0	0	0

12	5 (1 mol %)	BI⁺ (0.01 mol%)	61	6070	1520
13	5 (1 mol %)	No	9	-	-

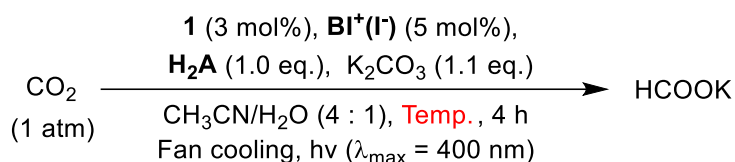
14	5 (0.1 mol %)	BI⁺ (0.1 mol%)	71	710	178
15	5 (0.01 mol %)	BI⁺ (0.1 mol%)	9	860	215
16	5 (0.01 mol %)	BI⁺ (0.01 mol%)	0	-	-

^a Based on the amount of ascorbic acid as theoretical amount of formate product to calculate the yield and determined by ¹H NMR analysis with 1,3,5-trimethoxybenzene as internal standard; ^b TON and TOF of entry 12 are calculated based on co-catalyst and TON and TOF of other entries are calculated based on PC.

Table 5.1. Study on stability and activity of photocatalysts and cocatalysts.

6. The effects of reaction temperature on photoinduced CO₂RR

Considering that photosensitizer releases tremendous heat to raise reaction solution temperature under irradiation conditions. So, it's necessary to demonstrate whether reaction temperature from outside factor affects the result of photoinduced CO₂RR. A few reactions were performed under standard condition using control temperatures (Table 6.1, entries 1 to 3). As a result, temperature of reaction solution indeed had a slight impact on yield of HCOO⁻ generated, which higher temperatures were associated with higher yields, since dehydroascorbic acid was thermodynamically converted to an enediol structural motif to perform second photocatalytic reduction of CO₂. Besides, we doubted whether HCOO⁻ product was yielded from decomposition of ascorbic acid or conversion of reagents or solvents under more than room temperature condition. The reaction of standard condition was carried out at 60 °C without light and there was no HCOO⁻ generated (Table 6.1, entry 4).



Entry	Temp./°C	Luminous intensity/mW	Yield/%
1	17	385	80
2	30	385	100
3	40	385	123
4 ^a	60	385	0

^a Without light

Table 6.1. Investigation of reaction temperature on standard reaction condition.

7. Investigation of mechanism

7.1. The reason of more than theoretical yield

During photochemical CO₂ reduction, employing **H₂A** as electron donor, the actual yield exceeded theoretical yield using the amount of ascorbic acid as theoretical amount of formate product to calculate, presuming that **H₂A** per molecule as an electron donor could provide two electrons. We opined an indirect effect occurred somewhere in the reaction. Therefore, we suspected that ascorbic acid (**H₂A**) might further undergo a second redox to supply extra electrons to allow the extra formation of formate. This result was congruent with our hypothesis if the base played a role in further activating the second reduction process. For instance, ascorbic acid converted dehydroascorbic acid (**A**), which was then hydrolyzed to form delactonized form of dehydroascorbic acid **A**. Afterwards, compound **32** solution might be further subjected primarily to decarboxylation to generate intermediate aldehyde **33** with the release of CO₂. The intermediate aldehyde underwent proton exchange to form **34**, which was a potential sacrificial reductant since it had a structural pattern of enediol comparable to **HA⁻**.¹²⁸ allowing an easier process of oxidation to produce 2 electrons needed in conversion of CO₂ into formate (Figure 7.1.). Therefore, we suggested a two-times oxidation of ascorbic acid for photoinduced reduction of CO₂ via intermediate **A** was involved.

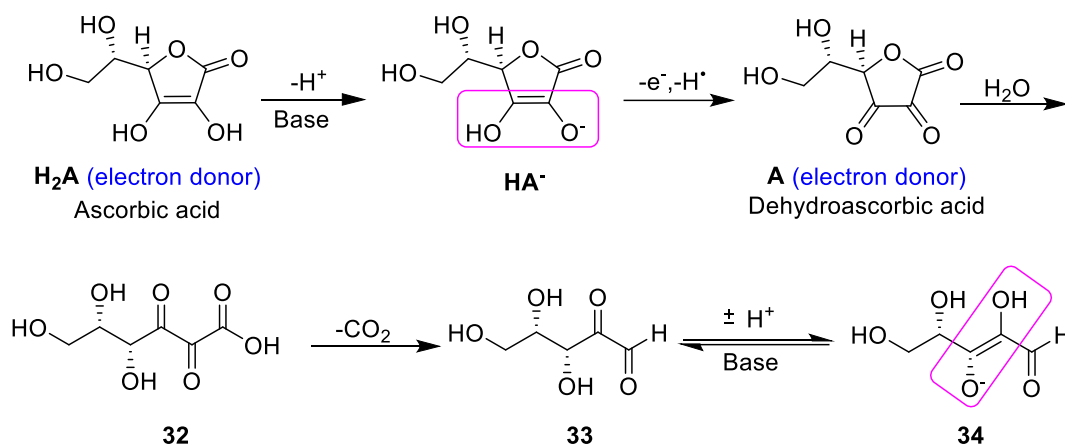
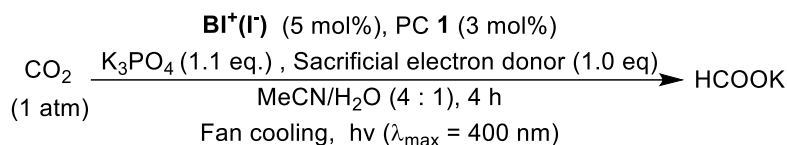


Figure 7.1. Two times oxidation mechanism of ascorbic acid.

In order to testify our reliable hypothesis, ascorbic acid was replaced with a commercially available dehydroascorbic acid in photoinduced CO₂RR to corroborate our assumption (Table 7.1, entry 3). As a result, HCOO⁻ was produced with a 74% yield, verifying the proposed assumption that dehydroascorbic acid was also competent for a sacrificial reductant. Then, we performed labeling experiments using ¹³CO₂, indicating that dehydroascorbic acid would function as a reductant to participate in photoinduced CO₂RR in 45% yield of ¹³C-formate, however, along with no labeled formate (¹²C-formate) generated in 17% yield (Table 7.1, entry 4). Additionally, formate was obtained in 30% yield even in the absence of CO₂ gas (Table 7.1, entry 5). From the above data analysis, two plausible explanations for these findings were proposed.: namely: dehydroascorbic acid directly decomposed formate and/or conversion of dehydroascorbic acid to CO₂ which was further reduced to formate under current

photocatalytic reduction of CO₂ condition. Subsequently, we continued to conduct a few control experiments from entry 6 to 8. These results fully suggested dehydroascorbic acid generated CO₂, which was further reduced to formate by the photocatalytic reaction system, rather than formate was directly generated from decomposition of dehydroascorbic acid.



Entry	Sacrificial electron donor	CO ₂	Co-catalyst	Yield/% ^a
1 ^b	H ₂ A	¹² CO ₂	BI ⁺ (I ⁻)	143
2	H ₂ A	No	BI ⁺ (I ⁻)	0
3	A	¹² CO ₂	BI ⁺ (I ⁻)	74
4	A	¹³ CO ₂	BI ⁺ (I ⁻)	H ¹³ COO ⁻ (45) H ¹² COO ⁻ (17)
5	A	No	BI ⁺ (I ⁻)	30
6	A	No	No	0
7 ^c	A	No	BI ⁺ (I ⁻)	0
8 ^d	A	No	BI ⁺ (I ⁻)	0

^a Based on the amount of H₂A or A as theoretical amount of formate product to calculate the yield and determined by ¹H NMR analysis with 1,3,5-trimethoxybenzene as internal standard; ^b K₃PO₄ (2.2 eq.) as base; ^c Without K₃PO₄; ^d Without PC 1

Table 7.1 Further demonstration two times oxidation mechanism of ascorbic acid via a few related experiments.

7.2. The Stern-Volmer experiment

Once ground state photocatalyst is irradiated by matched light, there is exceptionally active excited-state photocatalyst produced which tends to come back its ground state via dissipating energy in forms of nonradiative and/or radiative transition. However, in the presence of quencher, excited state energy in the excited state photocatalyst is transiently transferred to quencher by single electron transfer or energy transfer. As a result of interaction, Intensity of fluorescence spectra of photocatalyst is decreased. With gradually increasing amount of quencher, this trend is even more obvious. In the Stern-Volmer equation, quenching rate constant as an important parameter, the larger the value of quenching rate constant, the more effective quencher is. So, the fluorescence quenching method can further investigate reaction mechanism by Stern-Volmer experiment (Figure 7.2).²⁴

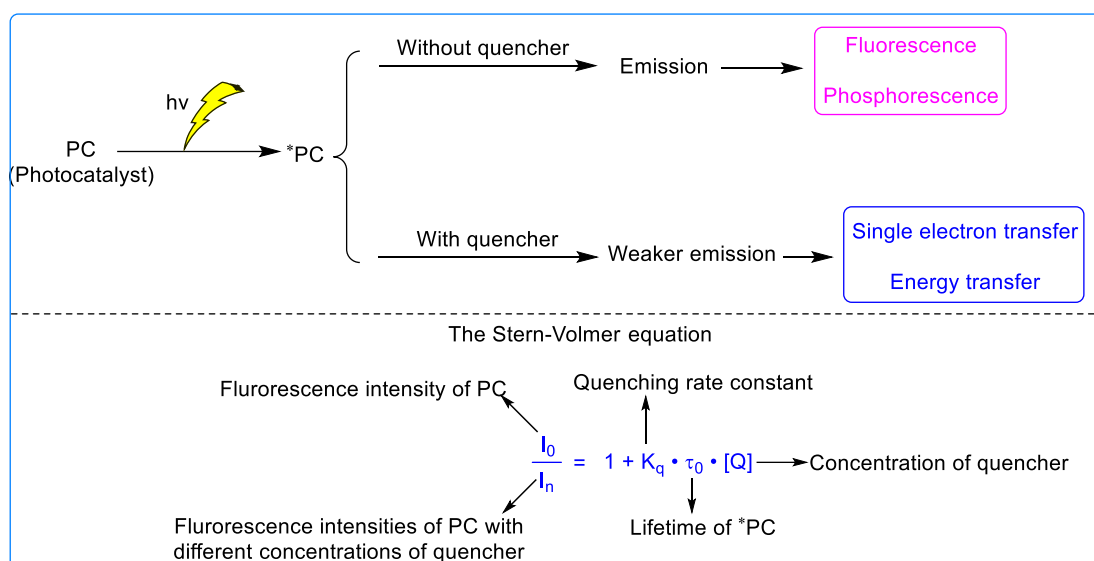


Figure 7.2. The principle of Stern-Volmer experiment and Stern-Volmer equation.

To further confirm the relationship between reaction mechanism and photocatalytic electron transfer, we investigated the quenching rate constants (k_q) based on the interactions of PC **1** as photocatalyst with various concentrations of potential quenchers (**BI⁺(I)**, **HA⁻**, **H₂A** and **BIH**) according to the Stern-Volmer equation.

General procedure of Stern-Volmer experiment using **BI⁺(I)** as a quencher: First, preparation of 10 μ M of PC **1** solution in spectrochemical DMSO in the glovebox; Next, preparation of different concentration of **BI⁺(I)**: 2 mM, 4 mM, 6 mM, 8 mM, 10 mM in spectrochemical DMSO with 10 μ M of PC **1** in the glovebox and then a small part amount of above sample solutions was introduced into 1 cm \times 1 cm quartz cuvettes, respectively. Afterwards, the fluorescence intensity of samples installed in quartz cuvette was measured using spectrofluorometer (JASCO FP-6500) with measurement parameters (measurement mode: emission; excitation wavelength: 350 nm; start wavelength: 355 nm; end wavelength: 700; band width of excitation: 10 nm; band width of emission: 5 nm; response: medium; sensitivity: low). The above procedure of experiment was performed two times under the same conditions and the averaged data was applied for the relationship of I_0/I and concentration of quencher

General procedure of Stern-Volmer experiment using **HA⁻** as a quencher: First, preparation of 10 μ M of PC **1** solution in mixture of anhydrous **CH₃CN** and distilled **H₂O** (1/1 v/v) and preparation of different concentration of **HA⁻** (washed with **DCM** and **MeOH**, respectively): 10 mM, 20 mM, 30 mM, 40mM, 50 mM along with 10 μ M of PC **1** in anhydrous **CH₃CN** and distilled **H₂O** (1/1 v/v). Next, a small part amount of above sample solutions was introduced into 1 cm \times 1 cm quartz cuvettes, respectively. and then the fluorescence intensity of samples installed in quartz cuvette was measured using spectrofluorometer (JASCO FP-6500) with measurement parameters (measurement mode: emission; excitation wavelength: 380 nm; start wavelength: 385 nm; end wavelength: 700; band width of excitation: 5 nm; band width of emission: 5 nm; response: medium; sensitivity: medium).

General procedure of Stern-Volmer experiment using **H₂A** as a quencher: First,

preparation of 10 μM of PC **1** solution in spectrochemical DMSO in the glovebox; Next, preparation of different concentration of **H₂A**: 10 mM, 20 mM, 30 mM, 40 mM, 50 mM in spectrochemical DMSO with 10 μM of PC **1** in the glovebox and then a small part amount of above sample solutions was introduced into 1 cm \times 1 cm quartz cuvettes, respectively. Afterwards, the fluorescence intensity of samples installed in quartz cuvette was measured using spectrofluorometer (JASCO FP-6500) with measurement parameters (measurement mode: emission; excitation wavelength: 395 nm; start wavelength: 400 nm; end wavelength: 700; band width of excitation: 5 nm; band width of emission: 5 nm; response: medium; sensitivity: medium).

General procedure of Stern-Volmer experiment using **BIH** as a quencher: First, preparation of 10 μM of PC **1** solution in spectrochemical DMSO in the glovebox; Next, preparation of different concentration of **BIH**: 10 mM, 20 mM, 30 mM, 40 mM, 50 mM in spectrochemical DMSO with 10 μM of PC **1** in the glovebox and then a small part amount of above sample solutions was introduced into 1 cm \times 1 cm quartz cuvettes, respectively. Afterwards, the fluorescence intensity of samples installed in quartz cuvette was measured using spectrofluorometer (JASCO FP-6500) with measurement parameters (measurement mode: emission; excitation wavelength: 395 nm; start wavelength: 400 nm; end wavelength: 700; band width of excitation: 5 nm; band width of emission: 5 nm; response: medium; sensitivity: medium).

The Stern-Volmer of PC **1** in the existence of different molarities of **BI⁺(I⁻)**, **HA⁻**, **H₂A** or **BIH** as potential quenchers resulted in corresponding quenching rate constants (k_q) are $k_q = 2.71 \times 10^9 \text{ mol}^{-1} \text{ L s}^{-1}$ for **BI⁺(I⁻)**, $k_q = -6.77 \times 10^7 \text{ mol}^{-1} \text{ L s}^{-1}$ for **HA⁻**, $2.6 \times 10^7 \text{ mol}^{-1} \text{ L s}^{-1}$ for **H₂A**, $9.90 \times 10^7 \text{ mol}^{-1} \text{ L s}^{-1}$ for **BIH** (Figure 7.3). As expected, **BI⁺(I⁻)** exhibited stronger quenching effect, whereas **HA⁻**, **H₂A** or **BIH** exhibited much weaker effects. Thus, these results were indicated that interaction of singlet excited state PC **1** with **BI⁺(I⁻)** by single electron transfer in the current reaction system was obviously confirmed.

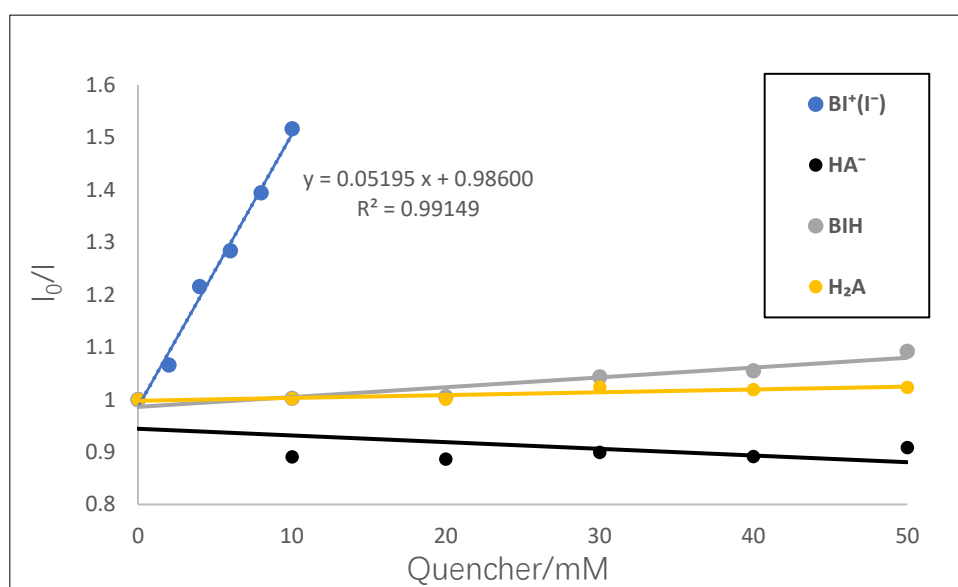


Figure 7.3. The Stern-Volmer of PC **1** in the existence of various molarities of **BI⁺(I⁻)**,

HA⁻, **H₂A** or **BIH** as potential quenchers. the ratios of fluorescence intensities (I_0/I) at 450 nm.

7.3. Exciplex between PC 1 and **BI⁺(I)**

Interaction of an excited state molecule with a ground state counterpart of a different structure forms transient the heterodimeric species, called exciplex by electron transfer each other, but occurs quickly dissociation in the ground state.¹²⁹ The formation of exciplex has frequently been used to shed light on reaction mechanisms to see if the reaction involves electron transfer. Evidence of exciplex formation is observed in the fluorescence spectrum as a broad red-shifted emission band. Accordingly, we measured fluorescence spectra of PC 1 and fluorescence spectra of mixture of PC 1 and **BI⁺(I)**. We found that two normalized spectrums were identical and suggesting that exciplex between PC 1 and **BI⁺(I)** isn't formed or captured (Figure 7.4).

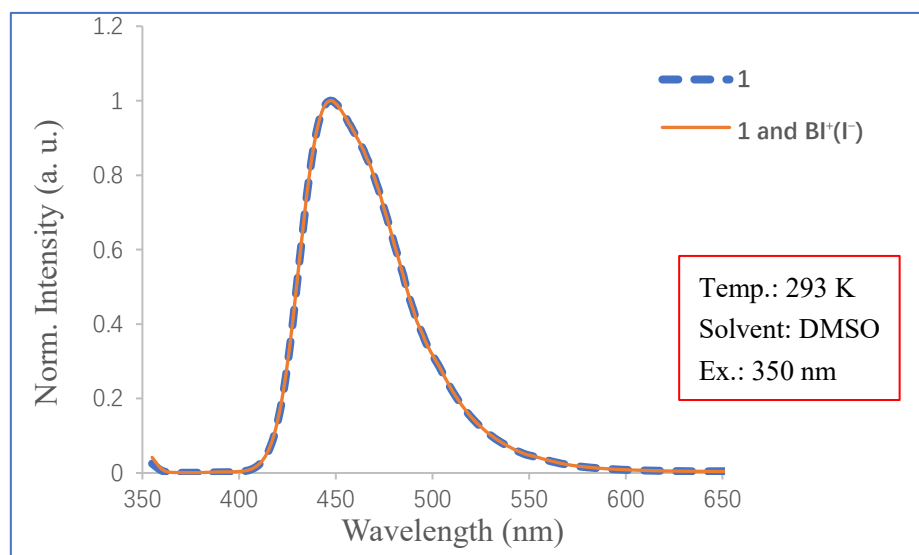


Figure 7.4. Fluorescence spectra (blue) of 10 μ M PC 1 and fluorescence spectra (orange) of 10 μ M PC 1 with 10 mM **BI⁺(I)**.

7.4. Optoelectronic data of PC 5 and **BI⁺(I)**

The electronic and optical characteristics of co-catalyst **BI⁺(I)** and PC 5 were further investigated, contributing to the analysis of the mechanistic process of photo-induced reduction of CO₂. First, the corresponding ground-state redox potentials of **BI⁺(I)** and 5 were measured by the method of cyclic voltammetry (CV), if cyclic voltammograms obtained showed reversible trends, standard redox potentials (E^0) were estimated by averaging value from the peak potentials in both directions. If CV obtained showed irreversible trends, standard redox potentials (E^0) were equal to midpoint potentials ($E_{p/2}$) which were the resulting potentials corresponding to half of the maximal current of CVs (Figure 7.5).¹³⁰ Triplet and singlet excited state energy of **BI⁺(I)** and 5 were estimated via phosphorescence and fluorescence spectra, respectively using the “10% rule”, where intensity of the emissions was equal to ten percent of the maximum level. (Figure 7.6 and Figure 7.7).¹³¹ Remarkably, the phosphorescence and

fluorescence spectra were overlapped for triplet and singlet excitation energy of $\text{BI}^+(\text{I}^-)$ in which a possible reason was because emission was only from phosphorescence spectra at room temperature ascribing to the heavy atom effect of the iodide. So, it was necessary that fluorescence spectra of $\text{BI}^+(\text{I}^-)$ was replaced with fluorescence spectra of $\text{BI}^+(\text{BF}_4^-)$ (Figure 7.6). The redox potentials of the singlet and triplet excited state compound **5** were calculated by the excitation energy and ground-state redox potential according to the Rehm-Weller equation.¹³² Optoelectronic data of $\text{BI}^+(\text{I}^-)$ and **5** were summarized in Table 7.2. Based on these data analysis, we reckoned that energy could be impossibly transferred from $^3\mathbf{5}^*$ to BI^+I^- . This attributed to a lesser excitation energy of $^3\mathbf{5}^*$ (2.64 eV) as compared to the excitation energy of $\text{BI}^+(\text{I}^-)$ (3.02 eV), additionally, as the values of $^3\mathbf{5}^*$ (-2.30 vs SCE) and $^1\mathbf{5}^*$ (-2.65 vs SCE) were much more deeply minus than the reductive potential of BI^+I^- (-1.96 vs SCE), prompting single electron transfers from $^1\mathbf{5}^*$ to BI^+I^- and/or from $^3\mathbf{5}^*$ to BI^+I^- were both possible.

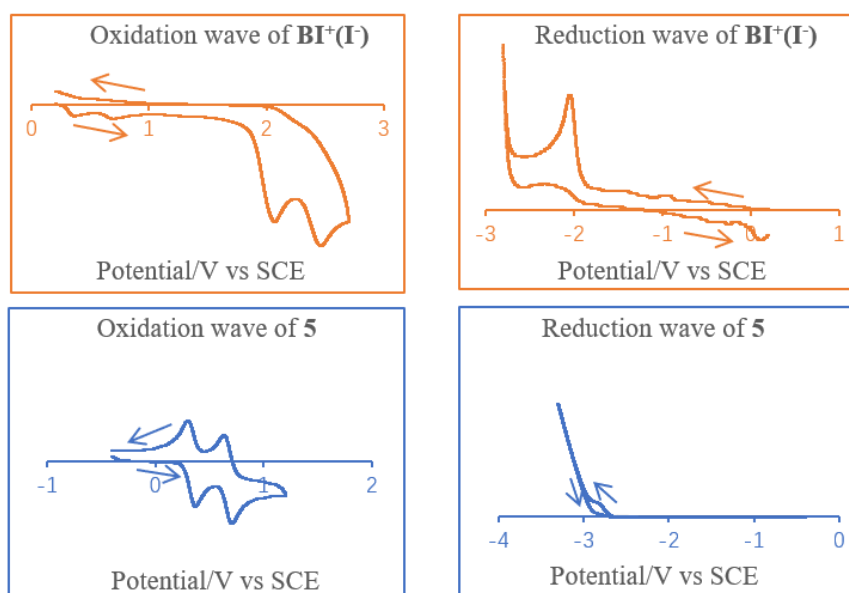


Figure 7.5. Cyclic voltammograms of 1 mM $\text{BI}^+(\text{I}^-)$ and 1 mM PC **5**. Solvent: MeCN, WE: glassy carbon, RE: Ag/Ag^+ with 0.1 M TBAP in MeCN, CE: platinum wire, electrolyte: 0.1 M TBAP, sweep rate: 100 mV/s.

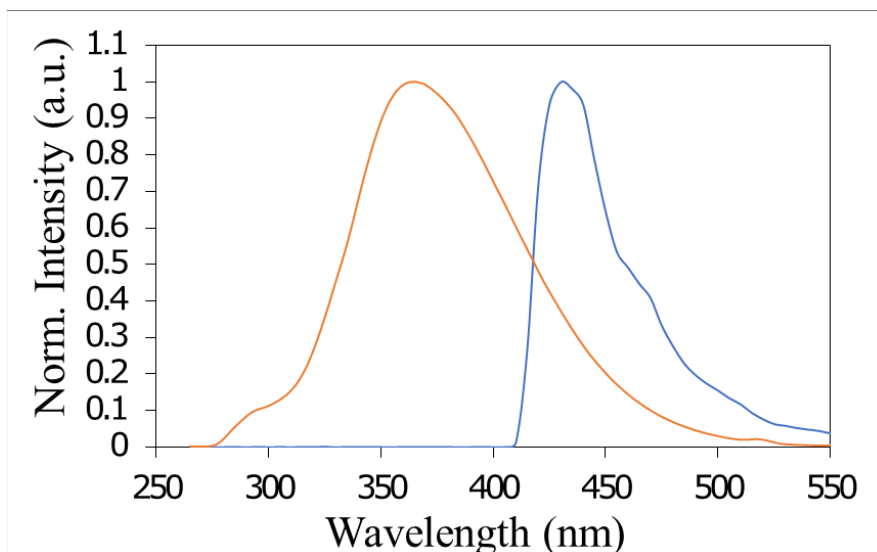


Figure 7.6. Fluorescence spectra of $\text{BI}^+(\text{BF}_4^-)$ at 293 K (orange) and phosphorescence spectrum of $\text{BI}^+(\text{I}^-)$ at 77 K (blue). Solvent: ethanol, concentration: 100 μM , excitation wavelength: 260 nm.

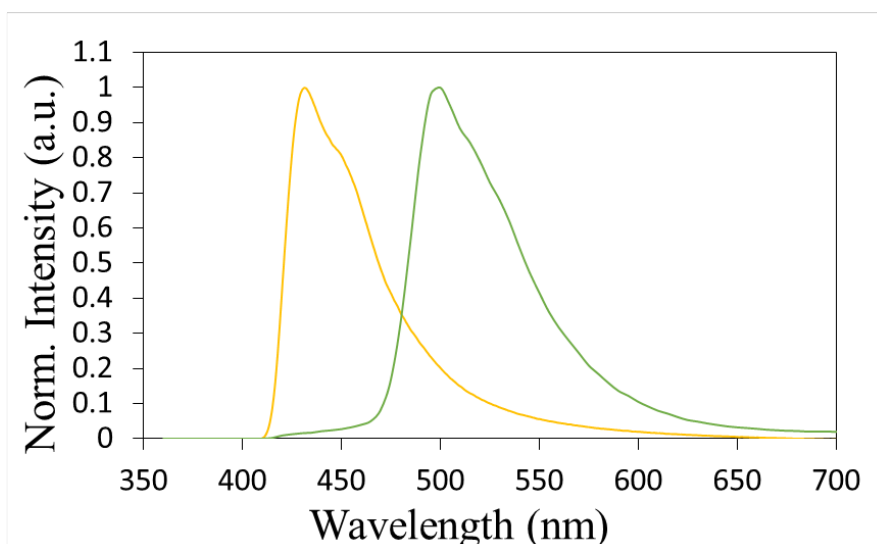


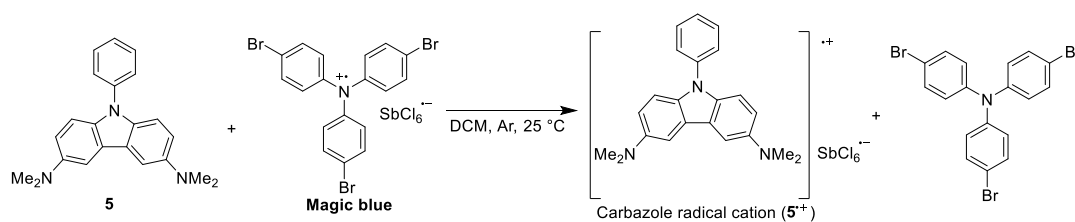
Figure 7.7. Fluorescence spectrum of PC **5** at 293 K (yellow) and phosphorescence spectrum of PC **5** at 77 K (green). Solvent: 2-Me-THF, concentration: 100 μM , excitation wavelength: 365 nm.

	E_S/eV	E_T/eV	E_{ox} (vs SCE)	E_{red} (vs SCE)	${}^1E_{\text{ox}}^*$ (vs SCE)	${}^3E_{\text{ox}}^*$ (vs SCE)
5	2.99	2.64	0.34	-2.75	-2.65	-2.30
BI^+I^-	(4.22) ^a	3.02	(0.31) ^b	-1.98	–	–

Table 7.2. Optoelectronic data of **5** and $\text{BI}^+(\text{I}^-)$ (^aThis value was calculated based on the fluorescence spectra of $\text{BI}^+(\text{BF}_4^-)$ at room temperature. ^bValue is derived from iodide oxidation.).

7.5. Generation of $5^{\bullet+}$ absorption bands based on magic blue experiment

Magic blue, as a single electron acceptor, is a powerful oxidant with the reductive potential of 0.70 V vs Fc,¹³³ which is widely applied in electron transfer chain processes as a stoichiometric and catalytic oxidant due to its good stability in air. In order to determine whether carbazole moiety generates carbazole radical cation or not in current reaction system. We employ magic blue radical cation as oxidant that reacts with carbazole moiety under argon condition and then measures UV spectra to see if there are some new peaks generated in UV spectra. First, to solutions of 100 μM PC **5** in DCM were added different equivalents of magic blue (0.1 eq., 0.4 eq., 0.7 eq. and 1.0 eq.) in glovebox, respectively and then took a part of above reaction solutions into quartz cells in order and sealed the caps (Table 7.3). Finally, take out from glovebox to quickly check UV-vis spectra as shown in Figure 7.8. We found new absorption bands (at 470, 550, 700 and more than 1100 nm) were generated in UV spectra (indicated using black arrows in Figure 7.9), At the same time, the oscillator strength of **5** radical cation ($5^{\bullet+}$) (orange bar in Figure 7.9) and **BI**⁺(**I**) (blue bar in Figure 7.9) was calculated by the time-dependent density functional theory (TD-DFT), which was roughly same with new bands generated in absorption spectra (Figure 7.9), suggesting $5^{\bullet+}$ was chemically generated in magic blue experiment and its absorption bands roughly assigned at 470, 550, 700 and more than 1000 nm.



Entry	Concentration of 5	Concentration of magic blue	Equivalent of magic blue	Solvent ^a
0 μM 5 + 10 μM magic blue	0 μM	10 μM	-	DCM
100 μM 5 + 10 μM magic blue	100 μM	10 μM	0.1	DCM
100 μM 5 + 40 μM magic blue	100 μM	40 μM	0.4	DCM
100 μM 5 + 70 μM magic blue	100 μM	70 μM	0.7	DCM
100 μM 5 + 100 μM magic blue	100 μM	100 μM	1.0	DCM

^a Removal of air by freeze-pump-thaw, three times

Table 7.3. Treatment of PC **5** with different equivalent of magic blue under argon condition.

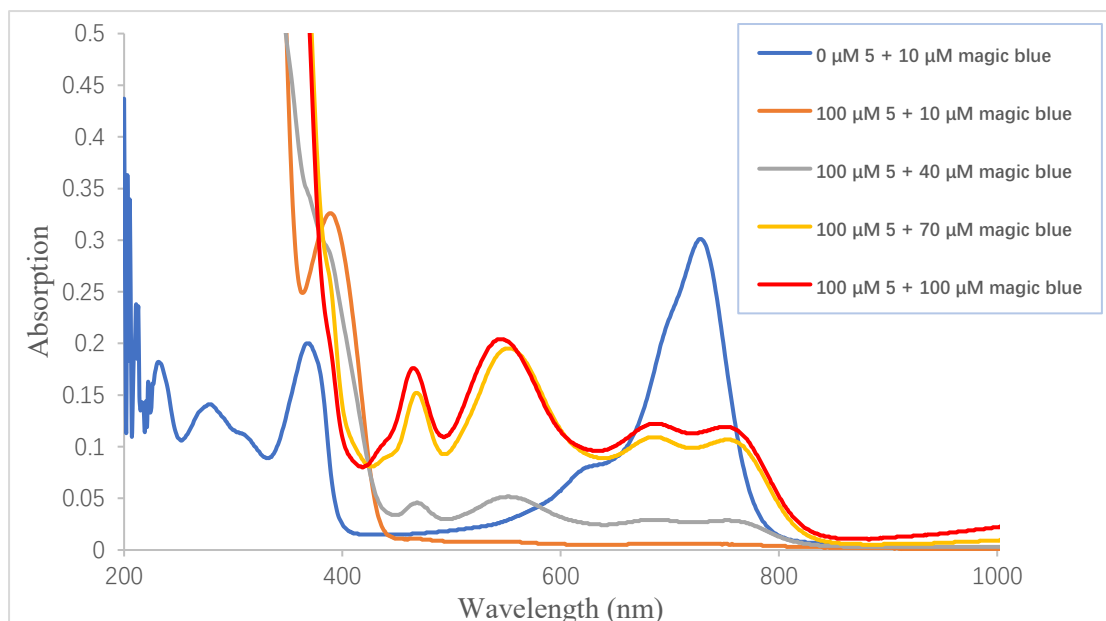


Figure 7.8. Absorption spectra of reaction solutions from treatment of 100 μM PC 5 with different concentration of magic blue (10 μM , 40 μM , 70 μM and 100 μM) in anhydrous CH_2Cl_2 under argon condition. The UV-vis spectra of 10 μM of magic blue was also plotted (blue line Figure 7.8).

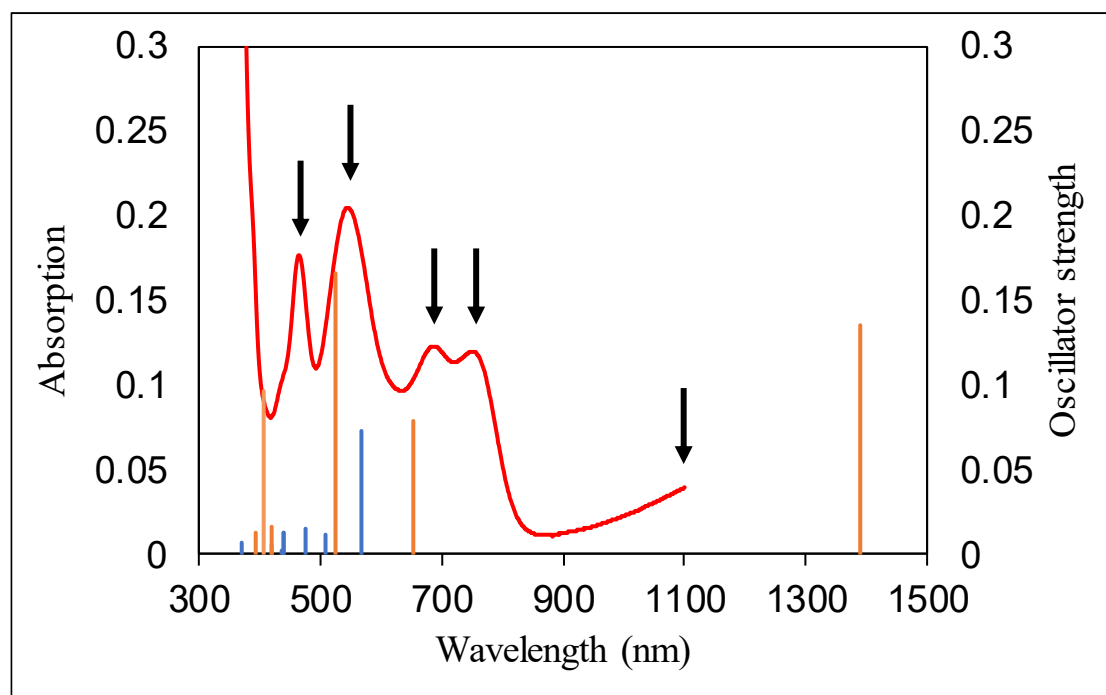


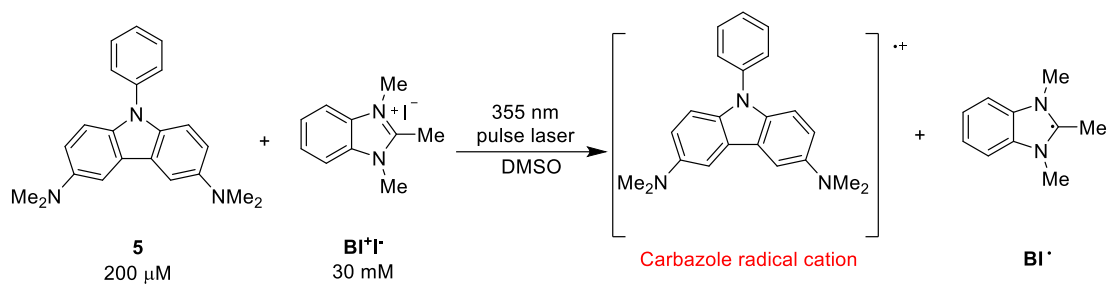
Figure 7.9. Absorption spectra of reaction solution from treatment of 100 μM PC 5 with 100 μM of magic blue, which was copied from Figure 7.8 (red line) and the calculated oscillator strength of $5^{\bullet+}$ (orange bar) and $\text{BI}^+(\text{I})$ (blue bar). The oscillator strengths were calculated by the time-dependent density functional theory (TD-DFT) method at the B3LYP/6-31++G(d,p)/CPCM (DMSO) level based on the geometries optimized by the DFT method at the ULC-BLYP/6-31++G(d)/CPCM(DMSO) level.

7.6. Certification of $5^{\bullet+}$ using transient absorption spectroscopy

Preparation the mixture solution of 200 μM PC **5** and 30 mM $\text{BI}^+(\text{I}^-)$ in spectrochemical DMSO (Scheme 7.1). The mixture solution was removed air by freeze-pump-thaw three times. Next, reaction solution was deaerated by purging the argon gas and flowed into a cuvette driven by an HPLC pump (flow rate: 2 mL/min) during the entire experiment and the cuvette was irradiated by 355 nm YAG laser (Continuum Minilite II, fwhm = 5 ns) to collect transient absorption data by time-resolved optical absorption spectrometer system (UNISOKU, TSP-1000-KK) at ambient temperature (Figure 7.10 to 7.13).

Solution of 200 μM PC **5** in spectrochemical DMSO was removed air by freeze-pump-thaw three times. Next, reaction solution was deaerated by purging the argon gas and flowed into a cuvette driven by an HPLC pump (flow rate: 2 mL/min) during the entire experiment and the cuvette was irradiated by 355 nm YAG laser (Continuum Minilite II, fwhm = 5 ns) to collect transient absorption data by time-resolved optical absorption spectrometer system (UNISOKU, TSP-1000-KK) at ambient temperature (Figure 7.14 to 7.16).

Absorption band region of $5^{\bullet+}$ was roughly assigned using magic blue experiment and the TD-DFT calculation. Next, further determination of existence of $5^{\bullet+}$ by time-resolved optical absorption spectrometer system. In Figure 7.10, there were three regions (470, 550, and 700 nm) observed from millisecond decay of long-life absorption bands, which were belonged to $5^{\bullet+}$ and BI^\bullet produced by electron transfer interaction between the excited state PC **5** and co-catalyst $\text{BI}^+(\text{I}^-)$. Additionally, absorption band of BI^\bullet was deduced to generate at 560 nm region based on calculation of TD-DFT (Figure 7.9, blue bars). Notably, these millisecond decay of long-lived absorption bands (470, 550, and 700 nm) didn't obey exponential function but total second-order kinetics, as shown in the time profiles of the absorbance changes and the inverse value of absorbance changes (Figure 7.11 to 7.12). The fact was ascribed to consumption of $5^{\bullet+}$ by the bimolecular charge-recombination interaction of $5^{\bullet+}$ with BI^\bullet . A significantly fast decay component of long-lived absorption band at 700 nm was observed in the time profiles of the absorbance changes from the region of microseconds (Figure 7.13), which was due to the T_1 - T_n absorption of **5** (Figure 7.14 to 7.16). Its decay lifetime was 1.1 μs with the existence of $\text{BI}^+(\text{I}^-)$ (Figure 7.13). Besides, the 0.89 μs of decay lifetime of $^35^*$ with the lack of $\text{BI}^+(\text{I}^-)$ was obtained (Figure 7.16). Since the lifetime of $^35^*$ didn't demonstrate noticeable change based on whether $\text{BI}^+(\text{I}^-)$ was added or not, energy transfer and/or electron transfer from $^35^*$ to $\text{BI}^+(\text{I}^-)$ pathways were not major mechanism for interaction of PC **5** with $\text{BI}^+(\text{I}^-)$. Additionally, the Stern-Volmer experiment was suggested an interaction of excited state PC with $\text{BI}^+(\text{I}^-)$ by single electron transfer in current reaction system was existed. So, $\text{BI}^+(\text{I}^-)$ was reduced to BIH , which was triggered via single electron transfer from $^15^*$ to $\text{BI}^+(\text{I}^-)$.



Scheme 7.1 Measurement of time-resolved absorption spectroscopy for the mixture solution of 200 μM PC **5** and 30 mM $\text{BI}^+(\text{I}^-)$ under argon condition.

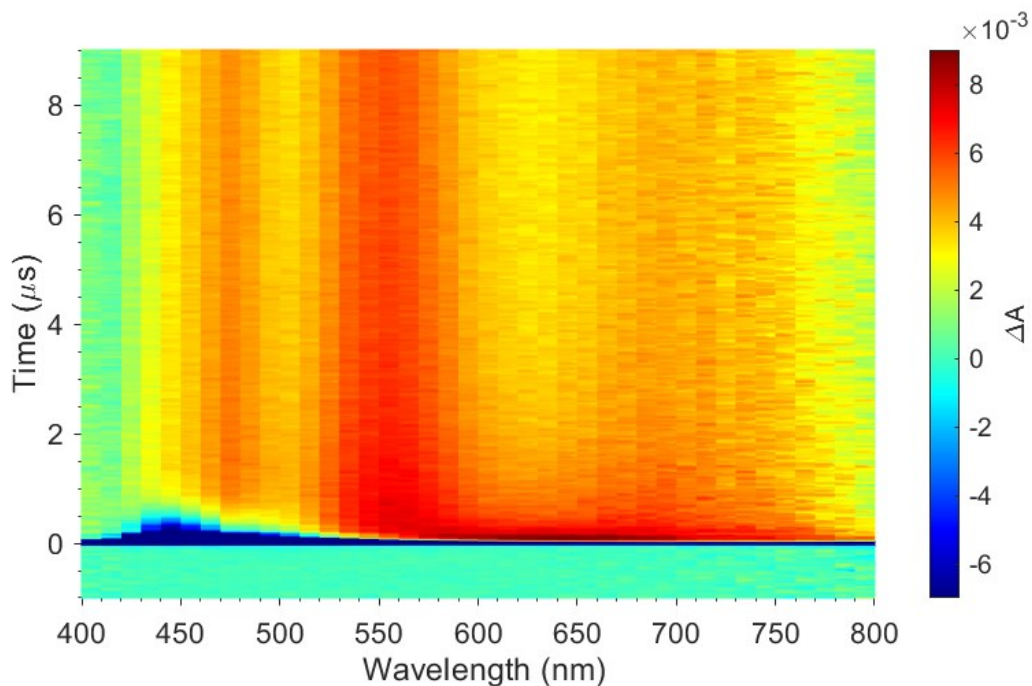


Figure 7.10. Two-dimensional transient absorption was generated by the laser irradiation of 355 nm for the mixture solution of 0.2 mM of **5** and 30 mM of $\text{BI}^+(\text{I}^-)$ in DMSO at 293 K.

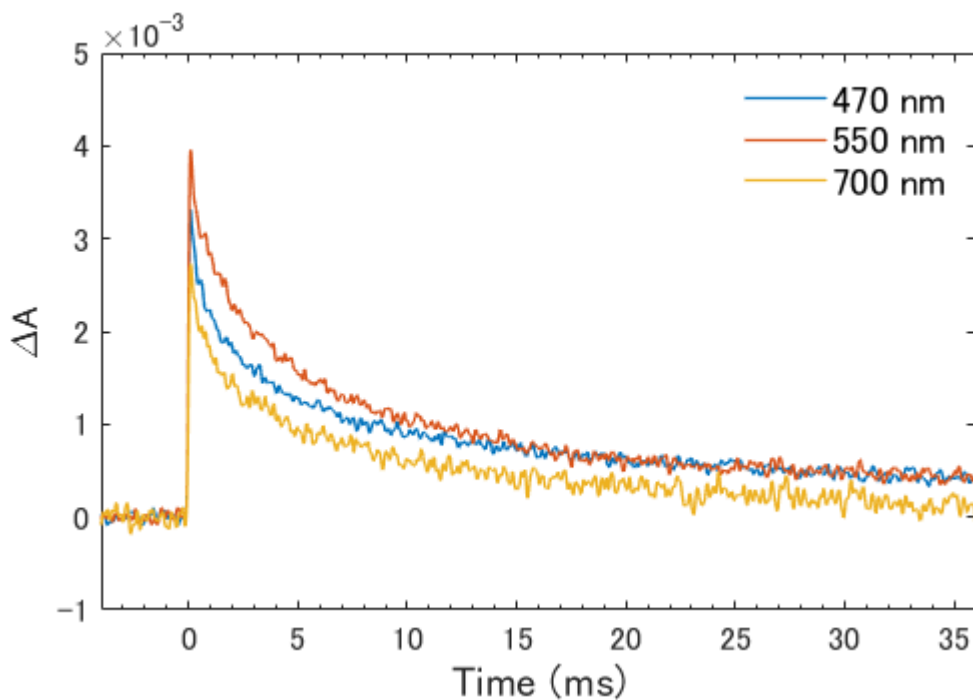


Figure 7.11. The absorbance changes (ΔA) as a function of the corresponding delay times from Figure 7.10 (Blue profile at 470 nm of wavelength, orange profile at 550 nm of wavelength and yellow profile at 700 nm of wavelength). The delay time from 0 ms to 35 ms.

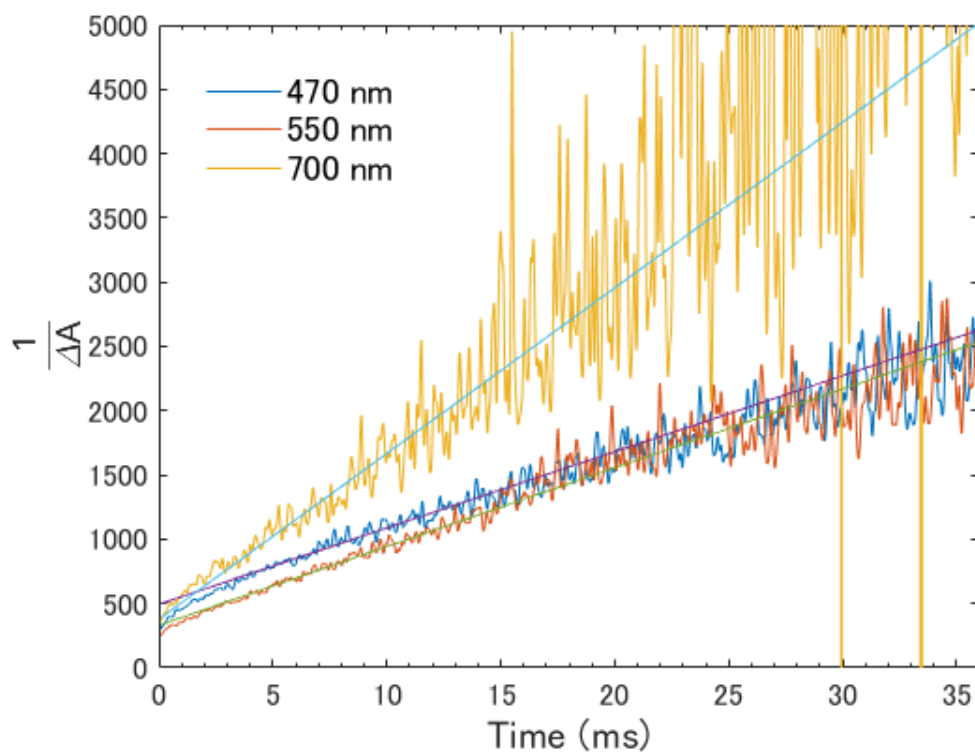


Figure 7.12. The inverse values ($1/\Delta A$) of the absorbance changes as a function of the corresponding delay times from Figure 7.11 (Blue profile at 470 nm of wavelength, orange profile at 550 nm of wavelength and yellow profile at 700 nm of wavelength). The delay time from 0 ms to 35 ms.

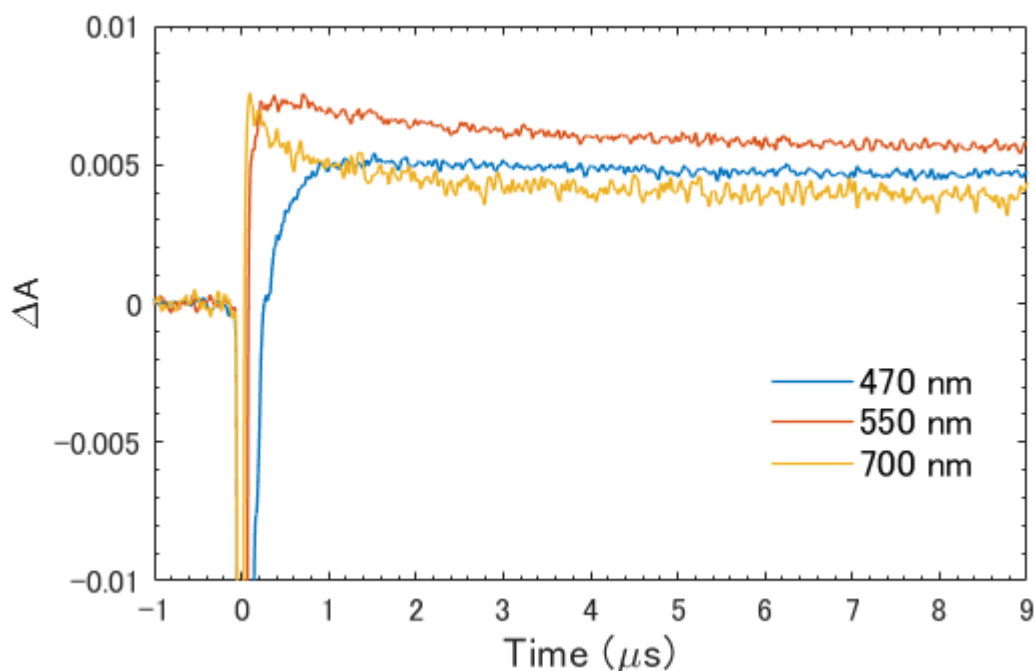


Figure 7.13. The absorbance changes (ΔA) as a function of the corresponding delay times from Figure 7.10 (Blue profile at 470 nm of wavelength, orange profile at 550 nm of wavelength and yellow profile at 700 nm of wavelength). The delay time from 0 μs to 9 μs . A significantly fast decay component of long-lived absorption band at 700 nm is observed from the region of microseconds which is due to the T_1 - T_n absorption of **5** by the triplet-triplet annihilation. Its decay lifetime is 1.1 μs in the existence of $\text{BI}^+(\text{I})$.

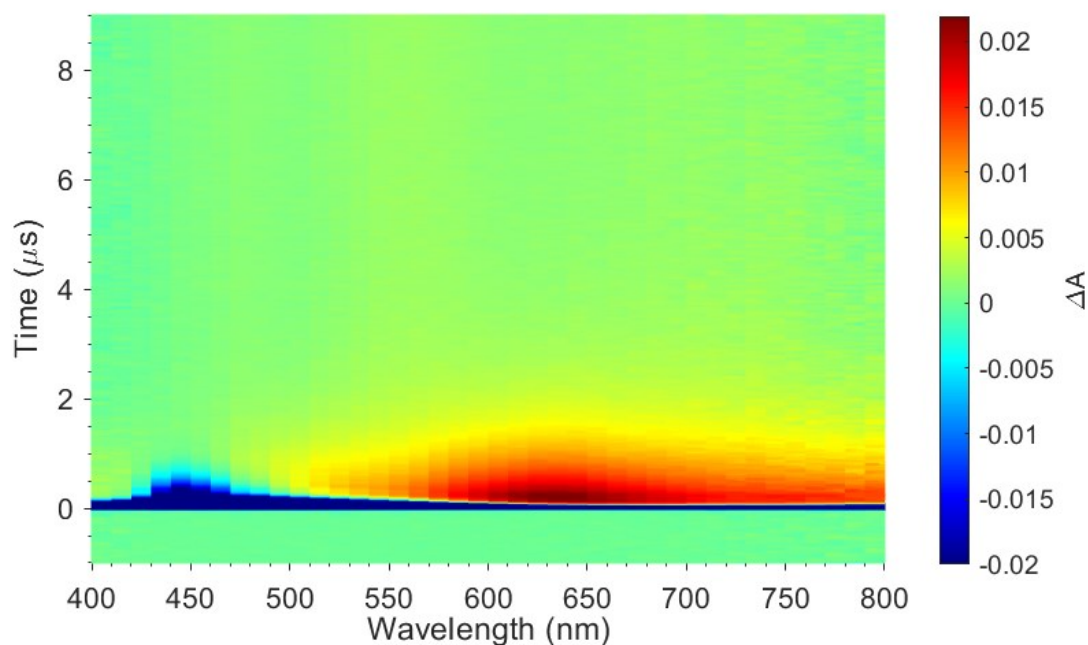


Figure 7.14. Two-dimensional transient absorption is generated by the laser irradiation of 355 nm for the solution of 0.2 mM of **5** in DMSO at 293 K. The emission signals of initial blue area around 450 nm are ascribed to the fluorescence of **5**. The resulting

absorption signals around 640 nm correspond to the T_1 - T_n absorption of **5**.

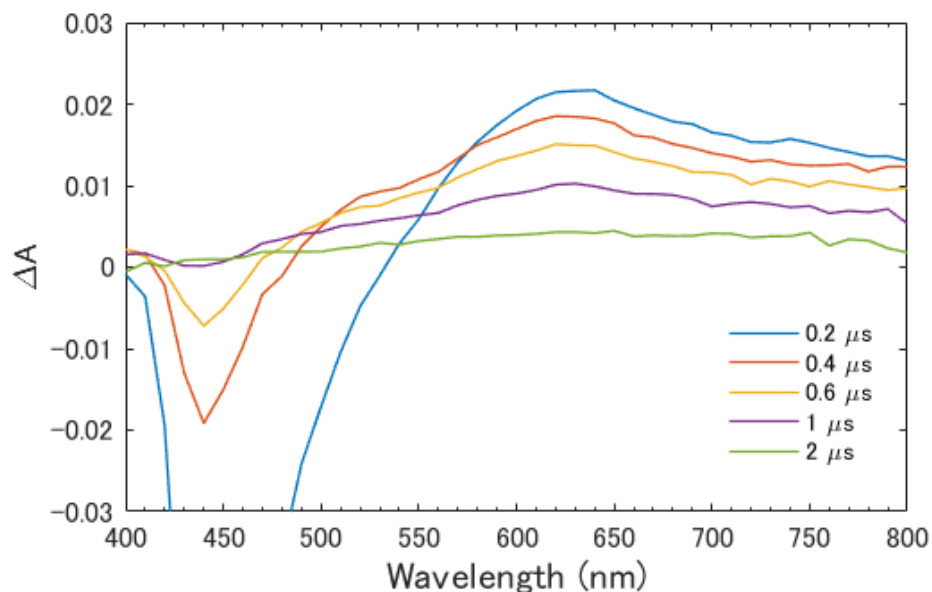


Figure 7.15. Delay time dependence of the transient absorption spectrum obtained in Figure 7.14.

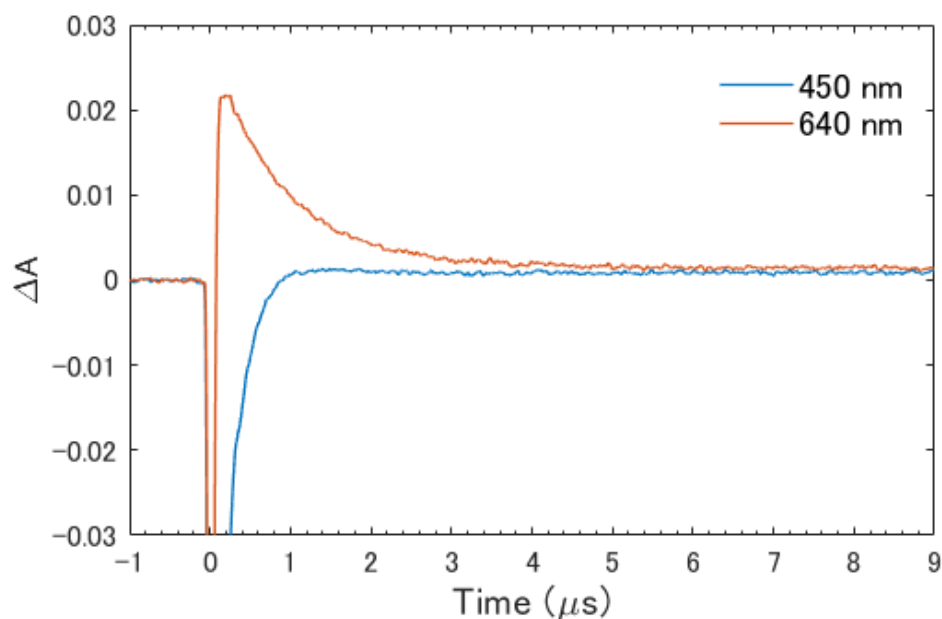
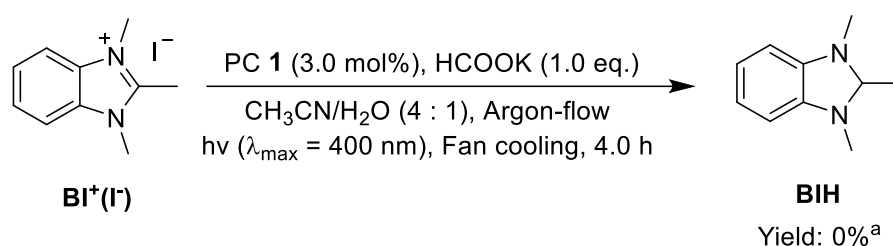


Figure 7.16. The absorbance changes (ΔA) as a function of the corresponding delay times at 450 nm (Blue profile) and 640 nm (Orange profile) obtained in Figure 6.14. The delay time from 0 μs to 9 μs . 0.89 μs of decay lifetime of ${}^3\mathbf{5}^*$ in the absence of $\mathbf{BI}^+(\mathbf{I}^-)$ is obtained at 640 nm. Since decay lifetime at 640 nm is larger than that of the emission at 450 nm by above two profiles observed, indicating emission at 450 nm is comprised of a strong prompt fluorescence and the delayed fluorescence by the triplet-triplet annihilation.

7.7. Judgment of the reversibility of photocatalytic CO₂RR

To demonstrate to see if formate functions as a reducing agent in reversible reaction of photocatalytic reduction of CO₂. So, we designed the following experiment: To a 50 mL flame-dried screw tube was placed with HCOOK (1.0 eq., 42.1 mg, 0.500 mmol), PC **1** (0.03 eq., 3.8 mg, 0.015 mmol) and **BI⁺(I⁻)** (1.0 eq., 144.1 mg, 0.500 mmol) in order and then acetonitrile (8 mL) and distilled H₂O (2 mL) were transferred to the screw tube. The reaction vessel was evacuated to remove air by freeze-pump-thaw, three times. Then argon was backfilled into the screw tube. soon afterwards, the reaction was stirred and slowly purged with argon under irradiation condition for 4 h (Scheme 7.2). Via NMR analysis, the reaction didn't proceed with a 101% of **BI⁺(I⁻)** and 99% of HCOOK remaining, suggesting that photocatalytic reduction of CO₂ was irreversible procedure in current reaction system.

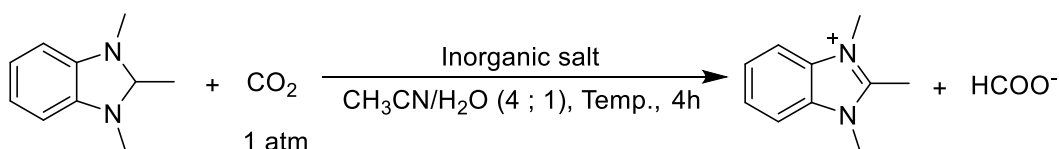


^a determined by ¹H NMR analysis with 1,3,5-trimethoxybenzene as the internal standard (added after the reaction).

Scheme 7.2. Photoinduced reduction of **BI⁺(I⁻)** to **BIH** using potassium formate as sacrificial reductant.

7.8. Investigation of benzimidazole-based hydride for CO₂ reduction to formate

Lim, C. H. and Musgrave, C. B. et al.¹²⁴ recently revealed that benzimidazole-based organohydride (**BIH**) interacted with CO₂ to yield formate using strong polar DMSO as solvent, Furthermore, an excess multi-equivalent of salt was used to provide a more polar environment, which enabled to stabilization of ionic product (HCOO⁻). To acquire a better understanding of the mechanical process of photo-induced CO₂RR, according to the report, we wanted to demonstrate whether regeneration of **BIH** from **BI⁺(I⁻)** readily captured CO₂ (1 atm CO₂) to yield HCOO⁻ in our current reaction system. First, we employed KI as inorganic salt to drive the equilibrium toward the product, as a result, there was no product obtained regardless of whether the equivalent of KI was increased or the reaction temperature was raised (Table 7.4, entries 1 to 3). And then using K₂CO₃ or KBF₄ instead of KI as inorganic salt (Table 7.4, entries 4 to 7), the reaction couldn't still proceed. Even though reaction temperature was increased to 110 °C (Table 7.4, entry 6), the product was obtained with an only trace yield, indicating that this reaction was governed by kinetics rather than thermodynamics. So, Interaction of **BIH** with CO₂ could not directly proceed in our reaction system.

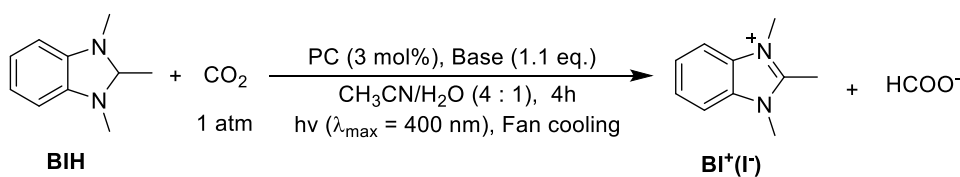


Entry	Inorganic salt	Concentration of BIH	Temp./°C	Yield of HCOO ⁻ /%
1	KI (2 eq., 0.06 M)	0.03 M	30	0
2	KI (2 eq., 0.1 M)	0.05 M	75	0
3	KI (40 eq., 1.2 M)	0.03 M	50	0
4	K ₂ CO ₃ (40 eq., 1.2 M)	0.03 M	50	0
5 ^a	K ₂ CO ₃ (2.2 eq., 0.1 M)	0.05 M	75	2
6	K ₂ CO ₃ (2 eq., 0.1 M)	0.05 M	110	9
7	KBF ₄ (20 eq., 1.0 M)	0.05 M	50	<<1

^a reaction time 8 h

Table 7.4. Treatment of **BIH** with CO₂ in the presence of inorganic salt

However, we noticed that interaction of **BIH** with CO₂ provided 15% of HCOO⁻ product in the presence of catalyst-loading based PC **1** under irradiation condition (Table 7.5, entry 1). We also further demonstrated that base was not required during the reaction (Table 7.5, entry 2). When interaction of **BIH** with CO₂ couldn't proceed under irradiation condition without PC (Table 7.5, entries 3 and 4). Based on above experimental result, we speculated on the possible mechanism: PC **1** was initiated under irradiation of 400 nm condition and produced ¹PC **1*** with an extremely minus oxidative potential ($E(\text{PC } \mathbf{1}^{\bullet+}/\text{PC } \mathbf{1}^*) = -2.75 \text{ V vs. SCE}$), which transferred one electron to CO₂ to yield resulting CO₂^{•-} ($E(\text{CO}_2/\text{CO}_2^{\bullet-}) = -2.21 \text{ V vs. SCE}$). Next, interaction of **BIH** with CO₂^{•-} produced HCOO⁻ and BI[•] product, subsequently, PC **1**^{•+} was readily captured by BI[•] to regenerate ground state PC **1**.



Entry	PC	Base	Yield of BI [•] (I ⁻)/% ^a	Yield of HCOO ⁻ /% ^a
1	PC 1	K ₂ CO ₃	41	15
2	PC 1	No	24	12
3	No	K ₂ CO ₃	8	<<1
4	No	No	6	<<1

^a determined by ¹H NMR analysis with 1,3,5-trimethoxybenzene as the internal standard (added after the reaction).

Table 7.5. Treatment of **BIH** with CO_2 provided HCOO^- product in the presence of photosensitizer

7.9. Proposed mechanism for photoinduced reduction of CO_2

The Stern-Volmer experiment was suggested an interaction of excited state PC with $\text{BI}^+(\text{I}^-)$ by single electron transfer in CO_2RR system was existed. absorption spectrum of $5^{\bullet+}$ was obtained using magic blue experiment and time-resolved optical absorption spectrometer analysis, additionally, data from time-resolved optical absorption spectrometer further indicated that energy transfer and/or electron transfer from $^35^*$ to $\text{BI}^+(\text{I}^-)$ pathways were not major mechanism for interaction of PC **5** with $\text{BI}^+(\text{I}^-)$. In addition, we also noted that photocatalytic reduced-state **BIH** reacted with CO_2 , resulting HCOO^- generated in a low yield. Based on the above experimental observations and result, photocatalytic mechanism of CO_2 reduction was proposed here (Figure 7.17). First, PC **5** was initiated under irradiation of 400 nm condition and produced $^15^*$ with an extremely minus oxidative potential ($E(5^{\bullet+}/^15^*) = -2.65$ V vs SCE), which transferred one electron to $\text{BI}^+(\text{I}^-)$ ($E_{\text{red}} = -1.96$ V vs SCE) to yield resulting $5^{\bullet+}$ and BI^\bullet . Then, active $5^{\bullet+}$ quickly accepted an electron from HA^- or **34** by form of single electron transfer to regenerate the ground-state PC **5**. As interaction of HA^- or HA^\bullet with BI^\bullet to provide **BIH** via HAT was exergonic ($\Delta H^\circ = -31.1$ or -25.4 kcal/mol in order), the process was a feasible choice. **BIH** as the source of nucleophilic hydride was not actually captured by ambient CO_2 to produce formate in a current system. However, PC **5** was re-irradiated under 400 nm condition and yielded $^1\text{PC } 5^*$ with an extremely minus redox potential ($E(\text{PC } 5^{\bullet+}/^1\text{PC } 5^*) = -2.65$ V vs. SCE), which gave one electron to CO_2 to produce resulting $\text{CO}_2^{\bullet-}$ ($E(\text{CO}_2/\text{CO}_2^{\bullet-}) = -2.21$ V vs. SCE) and then interaction of **BIH** with $\text{CO}_2^{\bullet-}$ produced HCOO^- and BI^\bullet product by hydrogen atom transfer. $\text{PC } 5^{\bullet+}$ was readily quenched by BI^\bullet , **34** or HA^- to regenerate ground state PC **5**. In addition, we have demonstrated **A** could also function as sacrificial reductant, which was further transferred to **34** and **35** with CO_2 releasing. Resulting **34** and **35** had similar role with HA^- and HA^\bullet in participating in photocatalytic CO_2RR cycle, which was consistent with over 100% yield.

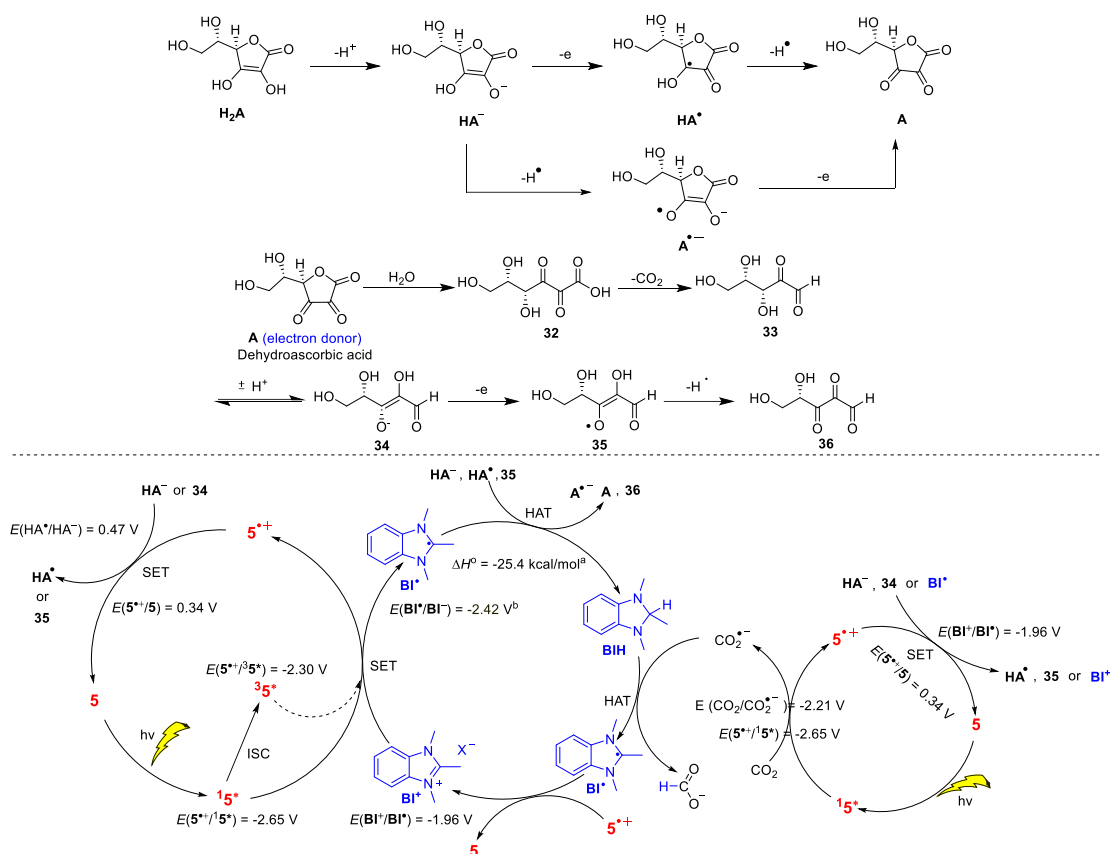


Figure 7.17. The proposed mechanism for the photoinduced reduction of CO₂. ^aStandard enthalpy change for the reaction (BI[•] + HA[•] → BIH + A) was calculated by the density functional theory (DFT) method with (U)LC-BLYP/6-31++G(d)/CPCM(DMSO) basis sets. ^bEstimated value by the DFT calculation. Standard redox potentials are referred to saturated calomel electrode (SCE). SET = single electron transfer; ISC = intersystem crossing; HAT = hydrogen atom transfer.

8. Absorption and fluorescence spectra of photocatalysts, $\text{BI}^+(\text{I}^-)$ and $\text{BI}^+(\text{BF}_4^-)$

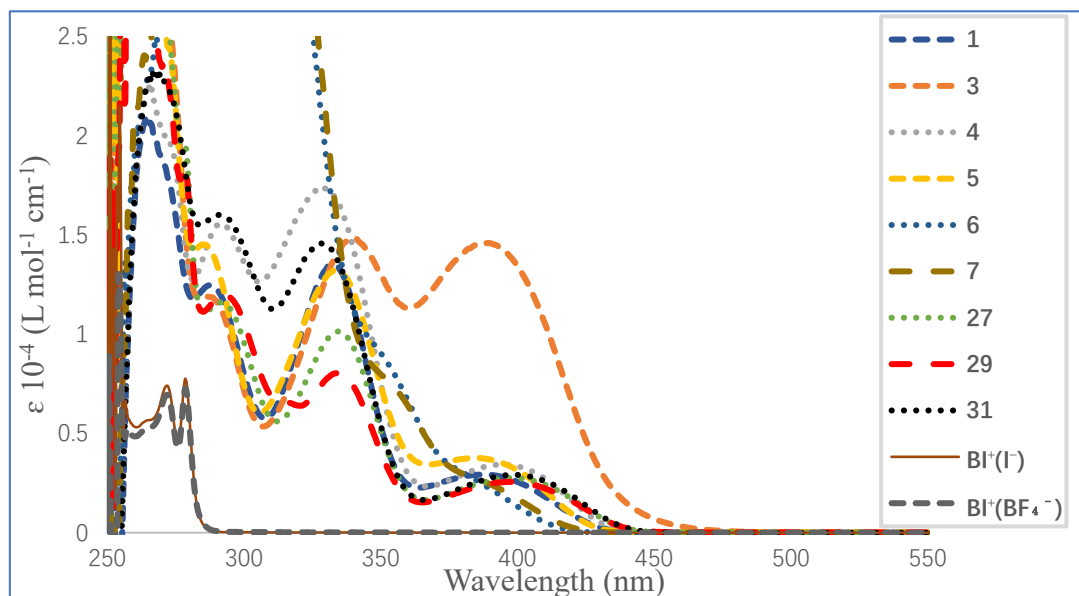


Figure 8.1. Absorption spectra of photocatalysts, $\text{BI}^+(\text{I}^-)$ and $\text{BI}^+(\text{BF}_4^-)$ at 293 K. Solvent: DMSO, concentration: 100 μM . The absorption of sample solutions was measured using UV-vis spectra (JASCO V-670) with a quartz absorption cuvette (light path: 1 cm).

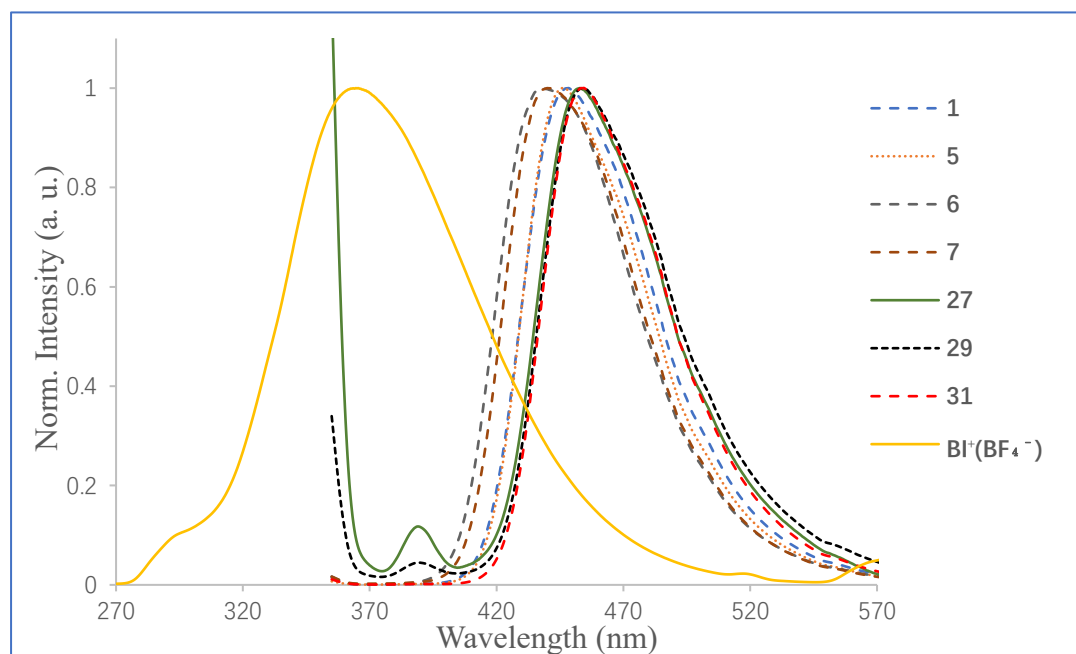


Figure 8.2. Normalized fluorescence spectra of photocatalysts and $\text{BI}^+(\text{BF}_4^-)$ at 293 K. Solvent: DMSO (ethanol for $\text{BI}^+(\text{BF}_4^-)$), concentration: 10 μM (100 μM for $\text{BI}^+(\text{BF}_4^-)$). The fluorescence intensity of sample solutions was measured using spectrofluorometer (JASCO FP-6500) with measurement parameters (measurement mode: emission; excitation wavelength: 350 nm (260 nm for $\text{BI}^+(\text{BF}_4^-)$)).

9. Photoluminescence quantum yields of photocatalysts

The fluorescence quantum yield for photocatalysts (**1**, **3**, **4**, **5**, **27**, **29** and **31**) in spectrochemical DMSO (refractive index of 1.479)¹³⁴ was measured by using fluorophore (quinine sulfate dihydrate) with a known quantum yield (0.546)¹³⁵ in 1N (0.5M) H₂SO₄ solution (refractive index of 1.346)¹³⁶ standard as the reference, The quantum yield is obtained in terms of following equation:¹³⁷

$$\Phi_f^i = \frac{F_i f_s n_i^2}{F_s f_i n_s^2} \Phi_f^s$$

(Where Φ_f^i and Φ_f^s are the quantum yield of the sample and the standard, respectively; F_i and F_s are the integrated intensities (areas) of sample and the standard, respectively; f_i and f_s the absorption factor of the sample and the standard ($f_x = 1 - 10^{-A_x}$, where A = absorbance); the refractive indices of the sample and reference solution are n_i and n_s , respectively).

Preparation of the following sample solutions: 1. Preparation of 0.5 M sulphuric acid solution (a. add slowly, with stirring, 2.8 ml of 95% sulphuric acid to about 50 ml of purified water; b. Makeup to 100 ml with purified water; c. Allow cooling ambient temperature.); 2. Preparation of 10 μ M quinine sulfate dihydrate in 0.5 M sulphuric acid solution; 3. Preparation of 10 μ M photosensitizers (**1**, **3**, **4**, **5**, **27**, **29** and **31**) in spectrochemical dimethyl sulfoxide, respectively. And next the fluorescence intensity of above solutions was measured using spectrofluorometer (JASCO FP-6500) with measurement parameters (measurement mode: emission; excitation wavelength: 350 nm; start wavelength: 355 nm; band width of excitation: 5 nm; end wavelength: 700; band width of emission: 10 nm; sensitivity: low; response: medium). The absorbance of above solutions was measured using UV-vis spectra (JASCO V-670) with a quartz absorption cuvette (light path: 1cm).

compounds	absorbance at 350 nm	F	Φ
Quinine sulfate dihydrate	0.101	169012.9943	0.546
1	0.059	73474.32538	0.468
3	0.133	625.3139953	0.002
4	0.076	221.8225947	0.001
5	0.079	98254.97331	0.478
27	0.051	602.5548054	0.004
29	0.046	2245.89041	0.018
31	0.058	68452.71853	0.443

Table 9.1. Original data of the integrated intensities and absorbances of quinine sulfate dihydrate and photocatalysts corresponding to quantum yields calculated.

10. Fluorescence lifetime

Measurements of time-resolved fluorescence were implemented using a streak scope Streak Scope C4334 with Imaging Spectrograph C5094 (Hamamatsu photonics, Ltd.). The light excitation was initiated using a ps light pulser (C10196) with 403 nm of excitation wavelength and 46 ps of the pulse length. The time profiles of the fluorescence data were fit by using single or double exponential decay functions with deconvoluting the profiles of the excitation pulses. The time profiles were averaged from 435 nm to 445 nm of the fluorescence data. All the samples were 10 μ M DMSO solution installed with a 1 cm \times 1 cm quartz cell. The samples were measured under ambient atmosphere without removal of air from the sample solutions.

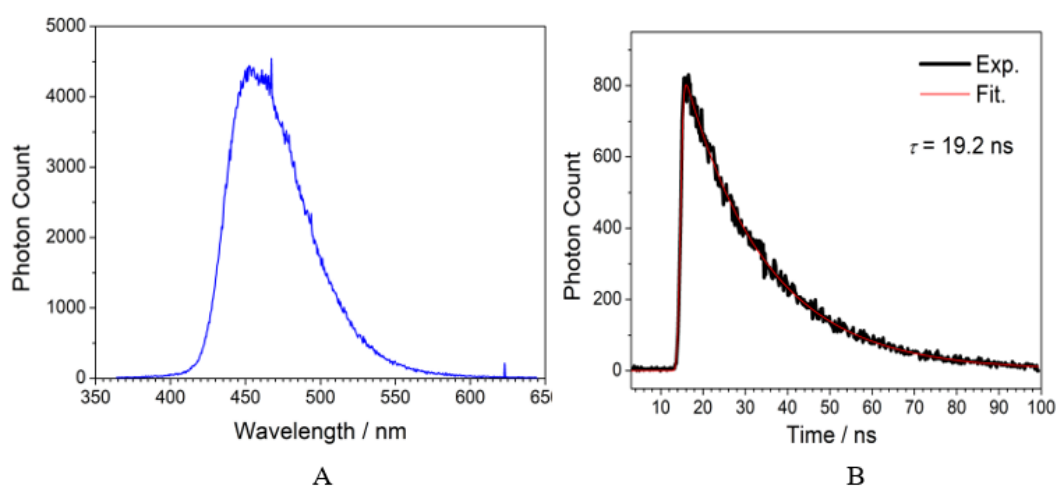


Figure 10.1. A. Fluorescence spectrum of PC 1. B. Time profile of the fluorescence overlapped with the fitting data (red line). The decay was fit using the function of $A_1 \exp(-t/\tau_1)$ with $A_1 = 874.0$ and $\tau_1 = 19.2$ ns. The fluorescence lifetime (τ) of PC 1 obtained from the fit was 19.2 ns.

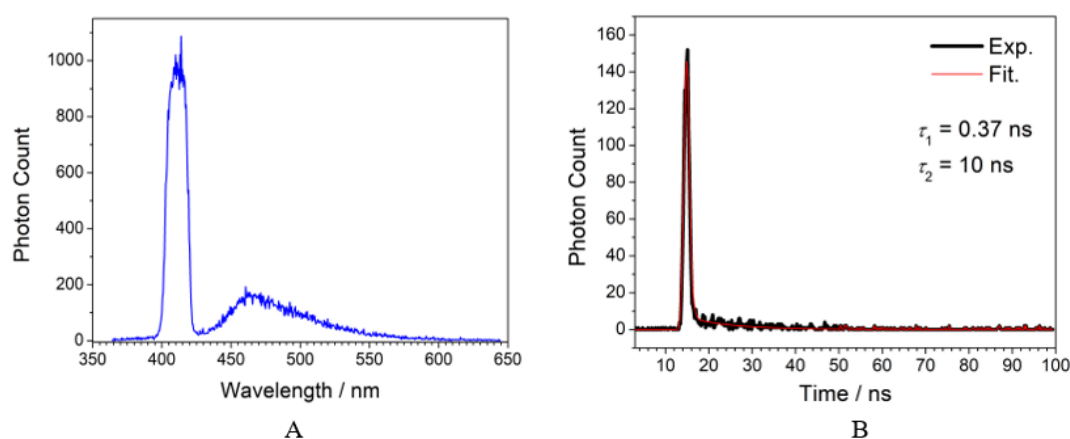


Figure 10.2 A. Fluorescence spectrum of integrated-form catalyst 27. B. Time profile of the fluorescence overlapped with the fitting data (red line). The decay was fit using the function of $A_1 \exp(-t/\tau_1) + A_2 \exp(-t/\tau_2)$ with $A_1 = 580$, $\tau_1 = 0.37$ ns, $A_2 = 7$ and $\tau_2 = 10$ ns. The data of $A_2 = 7$ and $\tau_2 = 10$ ns generated was probably because integrated-form catalyst 27 contained a tiny amount of byproduct or formed a minor D-A linked

conformer. Due to $A_1 \gg A_2$, the fluorescence lifetime (τ) of integrated-form catalyst **27** obtained from the fit was 0.37 ns.

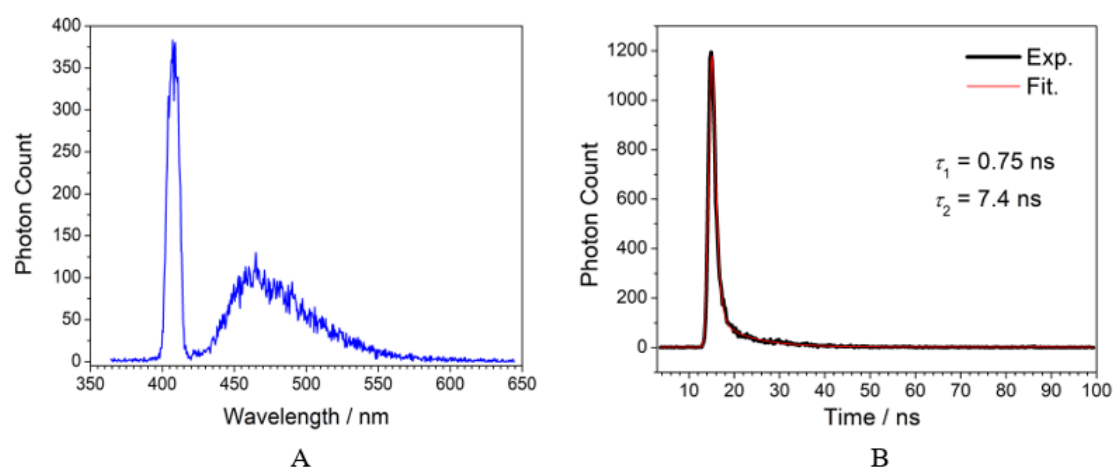


Figure 10.3 A. Fluorescence spectrum of integrated-form catalyst **29**. B. Time profile of the fluorescence overlapped with the fitting data (red line). The decay was fit using the function of $A_1 \exp(-t/\tau_1) + A_2 \exp(-t/\tau_2)$ with $A_1 = 200$, $\tau_1 = 0.75$ ns, $A_2 = 8$ and $\tau_2 = 7.4$ ns. The data of $A_2 = 8$ and $\tau_2 = 7.4$ ns generated was probably because integrated-form catalyst **29** contained a tiny amount of byproduct or formed a minor D-A linked conformer. Due to $A_1 \gg A_2$, the fluorescence lifetime (τ) of integrated-form catalyst **29** obtained from the fit was 0.75 ns.

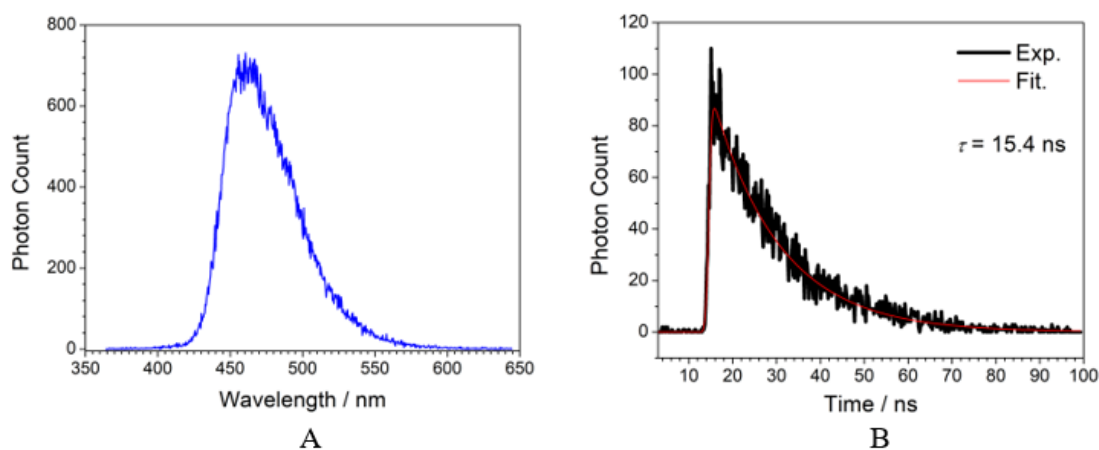


Figure 10.4. A. Fluorescence spectrum of integrated-form catalyst **31**. B. Time profile of the fluorescence overlapped with the fitting data (red line). The decay was fit using the function of $A_1 \exp(-t/\tau_1)$ with $A_1 = 96$ and $\tau_1 = 15.4$ ns. The fluorescence lifetime (τ) of integrated-form catalyst **31** obtained from the fit was 15.4 ns.

11. Determination of light intensity

It's a reliable approach that the light intensity of the LED lamp is measured by which *o*-nitrobenzaldehyde is photochemically converted into *o*-nitrosobenzoic acid since its quantum yield is high and constant at wavelength of 300-410 nm.¹³⁸ 10 mL of a solution of *o*-nitrobenzaldehyde (10 mM) in anhydrous CH₂Cl₂ and pentadecane (50 μL) was transferred to flame-dried schlenk flask (100 mL). The reaction solution was degassed by freeze-pump-thaw three times under weaker light condition. Before irradiation with a LED lamp ($\lambda = 365 \pm 20$ nm), the aliquot of the reaction mixture ($t = 0$ s) taken by glass pipette and diluted with anhydrous dichloromethane was measured using GC and calculated the integration ratio of *o*-nitrobenzaldehyde to pentadecane. Subsequently, the reaction solution was stirred under irradiation condition using a LED lamp ($\lambda = 365 \pm 20$ nm). At 30-second intervals ($t = 30$ s, 60 s, 90 s, 120 s, 150 s), the aliquots taken out of the reaction mixture by glass pipette and diluted with anhydrous CH₂Cl₂ were analyzed to obtain the concentration of *o*-nitrobenzaldehyde remaining. The above procedure of experiment was performed three times under the same conditions and the averaged data was depicted based on the relationship of concentration of *o*-nitrobenzaldehyde remaining and irradiation time (Figure 11.1).

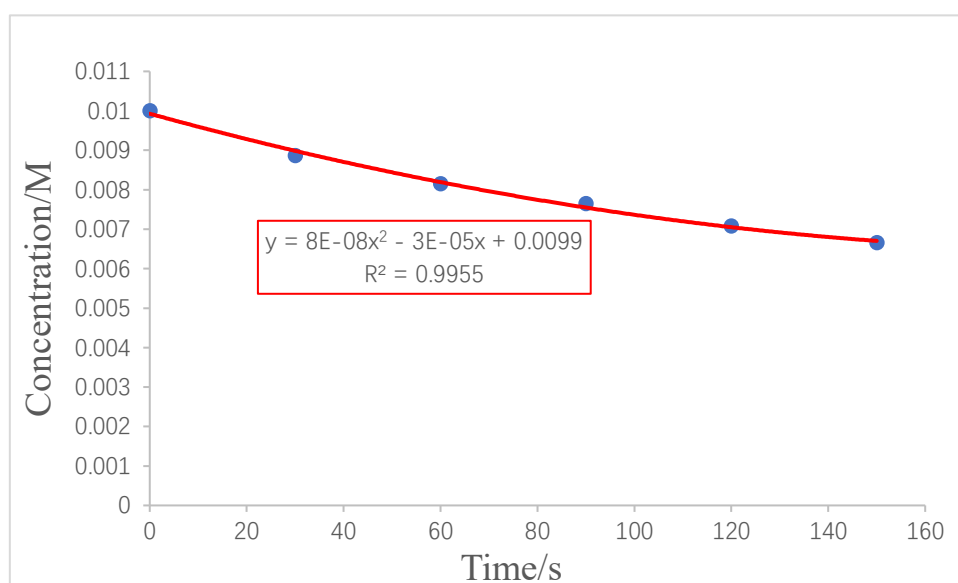


Figure 11.1 Concentration of *o*-nitrobenzaldehyde remaining in the reaction solution as a function of irradiation time. Each data point indicated as averaged value from three identical repeated experiments.

Based on a functional relationship between concentration of *o*-nitrobenzaldehyde remaining and irradiation time, given the formula: $[Act] = 8.23 \times 10^{-8} \times t^2 - 3.385 \times 10^{-5} \times t + 9.93 \times 10^{-3}$, $[Act]$ represents the concentration of *o*-nitrobenzaldehyde remaining in mol/L and t functions as the irradiation time in s. The calculation equation of light intensity from the light source is given in the following form:

$$I_0 = -\frac{Vd[Act]}{dt} \left(\frac{1}{\Phi} \right) \left(\frac{1}{1 - 10^{-\epsilon b[Act]}} \right)$$

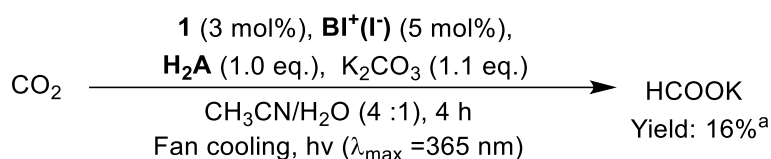
Where I_0 is the light intensity of the LED lamp in einstein s^{-1} , V refers to volume of solution in L, Φ is the quantum yield of *o*-nitrobenzaldehyde, ϵ is the molar absorption coefficient of *o*-nitrobenzaldehyde in $L\ mol^{-1}\ cm^{-1}$, and b is the minimal path length of light in cm.

In the current reaction system, the minimal path length of light (b) is 3.1 cm, the volume of reaction solution (V) is 1×10^{-2} L, the molar absorption coefficient (ϵ) of *o*-nitrobenzaldehyde (0.1 mM) in anhydrous CH_2Cl_2 at 365 nm is measured by UV-vis spectra (Shimadzu UV-1800 spectrometer with a quartz absorption cuvette, light path: 1 cm) and its ϵ is $2.3 \times 10^2\ cm^{-1}\ mol^{-1}\ L$, the initial concentration of *o*-nitrobenzaldehyde [Act] is $1.0 \times 10^{-2}\ mol\ L^{-1}$ and upon $t = 0$, $d[Act]/dt$ (the derivative of the polynomial) is -3.385×10^{-5} as well as the quantum yield of photochemical conversion of *o*-nitrobenzaldehyde into *o*-nitrosobenzoic acid is commonly received to be $\Phi = 0.5$ s. So, the light intensity of the LED lamp is calculated using above parameter values as follows:

$$I_0 = -\frac{1 \times 10^{-2} \times (-3.385 \times 10^{-5})}{0.5} \times 1 = 6.77 \times 10^{-7} (einstein/s)$$

12. Determination of the quantum yield for photocatalytic CO₂RR.

To a 100 mL flame-dried screw tube was charged with ascorbic acid (1.0 eq., 88.1 mg, 0.500 mmol), K₂CO₃ (1.1 eq., 76.0 mg, 0.550 mmol), BI⁺(I⁻) (0.05 eq., 7.2 mg, 0.025 mmol), and **1** (0.03 eq., 3.8 mg, 0.015 mmol) in order. Next, 8 mL of acetonitrile and 2 mL of distilled H₂O were transferred to the screw tube, respectively. The reaction vessel was evacuated to remove air by freeze-pump-thaw, three times. Then a backfilled-CO₂ balloon was connected to the screw tube. Finally, the reaction was stirred under irradiation condition using a LED lamp ($\lambda = 365 \pm 20$ nm) for 30 mins. After that, 1,3,5-trimethoxybenzene (40.6 mg) and 4 mL of distilled H₂O were introduced into the resultant reaction solution and then take 0.6 mL of the above solution for the ¹H NMR spectroscopic analysis using solvent suppression technique. By calculation, the amount of the product formate was determined to be 0.0795 mmol (Scheme 12.1).



^a Based on the amount of ascorbic acid as theoretical amount of formate product to calculate the yield and determined by ¹H NMR analysis with 1,3,5-trimethoxybenzene as internal standard

Scheme 12.1 Experiment of the quantum yields for photoinduced CO₂RR.

Based on the equation of the quantum yield:

$$\Phi = \frac{\text{mol}(\text{product})}{I_0 t f}, (f = 1 - 10^{-\epsilon b [\text{Act}]})$$

Where f represents the fraction of absorbed light, the minimal path length of light (b) is 3.1 cm, the concentration of photocatalyst (**1**) is 1.5×10^{-3} mol/L and the molar absorption coefficient ($\epsilon = 1.91 \times 10^3$ L mol⁻¹ cm⁻¹) of PC **1** (0.1 mM) in mixture of CH₃CN and H₂O (4/1 V/V) at 365 nm is measured by UV-vis spectra. In terms of the above data, the quantum yield (Φ) was calculated as follows:

$$\Phi = \frac{0.0795 \times 10^{-3}}{6.77 \times 10^{-7} \times 30 \times 60 \times 1} = 0.065$$

13. Conclusions

We have developed a feasible strategy that transition metal-free photocatalytic reduction of CO₂ was converted to formate using photosensitized regeneration of organohydride. In the case, ¹³C labeling experiment further confirmed the carbon source of formate derived from CO₂ through the photocatalytic reduction of CO₂.

During experiment optimization, reduced state **BIH** (without iodine sources) was employed as co-catalyst in current reaction system, revealing that iodide anion was not involved in the photocatalytic cycle. using other inorganic bases instead of potassium carbonate, prompting different forms of cations and anions of bases slightly impacted on the photoinduced reaction to some extent. In addition, other sacrificial reductants were discovered as an alternative solution to ascorbic acid. Eventually, in terms of control experiments, we noticed that photocatalyst was indispensable for photochemical reduction of CO₂ system but co-catalyst as a key component.

Initial purpose for design and synthesis of integrated-form catalysts obtained electron donor-acceptor (EDA) complex to make the reaction proceeded under red-shifted visible light irradiation condition. Even though the proposal didn't demonstrate the formation of EDA complex, photochemical reduction of CO₂ using a single molecular catalyst (incorporation of co-catalyst and photocatalyst) was conceptually viable. The formation of EDA complex from photocatalyst and co-catalyst will continue study further in the future.

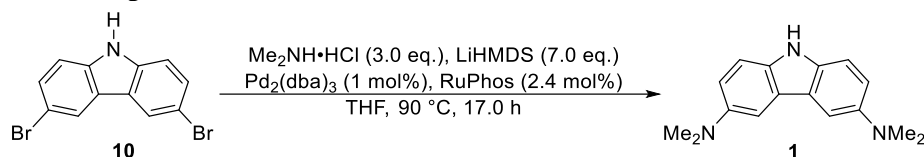
Next, potential photosensitizers were also investigated. We found that carbazole-based photocatalysts with electron-deficient substitutions were incapable of functioning as active PC to participate in reduction of CO₂. Among these organic PCs, *N*-phenyl substituted carbazole moieties behaved more strong durability in photocatalytic CO₂RR. Additionally, transition metal Ir(ppy)₃ complex as PC showed comparative activity in current reaction system. The combination of catalysts Ir(ppy)₃ complex and **BI⁺(I)** in one reaction system was a novel discovery in current study.

Besides, the durability and activity of photocatalysts and cocatalyst were further explored, implying that the catalytic amount of PC was reduced by a dramatic order of magnitude up to 0.01 mol%, As a best result, PC **7**-based photocatalytic CO₂ reduction enabled TON and TOF to meet 8820 and 2205 h⁻¹ in order. In addition, we further investigated TON and TOF which were calculated based on co-catalyst. when catalytic amount of PC **5** was set 3 mol%, the amount of co-catalyst **BI⁺(I)** was decreased up to 0.01 mol%. Its TON and TOF also exhibited dramatical increment up to 6070 and 1520/h. These dramatic values suggested that the employed photocatalysts and co-catalyst exhibited outstanding chemical activity and physical stability for photocatalytic CO₂RR. Additionally, photocatalytic reduction of CO₂ showed exclusive selectivity to yield HCOO⁻ as an only product in current reaction system, while formaldehyde, oxalate, CO, and H₂ as potential evolved products were not detected by ¹³C-labeling experiment and GC-based quantitative analysis of evolved gases experiment.

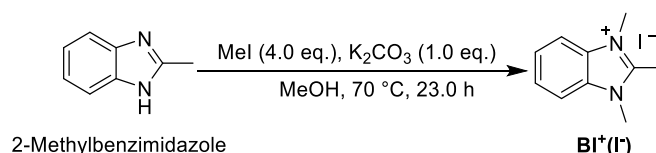
Finally, using dehydroascorbic acid instead of ascorbic acid as sacrificial reductant in the photocatalytic CO₂RR to fully corroborate that a two-time oxidation of ascorbic acid (four electrons provided per molecule) via intermediate dehydroascorbic acid was involved. Based on Stern-Volmer experiment, magic blue experiment, optoelectronic

data of PC and co-catalyst and time-resolved optical absorption spectrometer analysis, indicating that single electron transfer from $^1\mathbf{5}^*$ to $\mathbf{BI}^+(\mathbf{I}^-)$ pathway was major mechanism for interaction of PC **5** with $\mathbf{BI}^+(\mathbf{I}^-)$. Via related experiments, we further demonstrated that treatment of **BIH** with CO_2 (1 atm) could not proceed, but **BIH** reacted with CO_2 (1 atm) to provide HCOO^- product in the presence of photocatalyst under irradiation condition. It was further revealed that the possible mechanism: photocatalyst was irradiated under irradiation of 400 nm condition and produced excited state photocatalyst, which transferred one electron to CO_2 to provide resulting $\text{CO}_2^{\bullet-}$ and then interaction of **BIH** with $\text{CO}_2^{\bullet-}$ produced HCOO^- via hydrogen atom transfer.

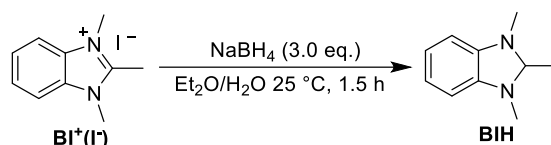
14. Synthesis experiments



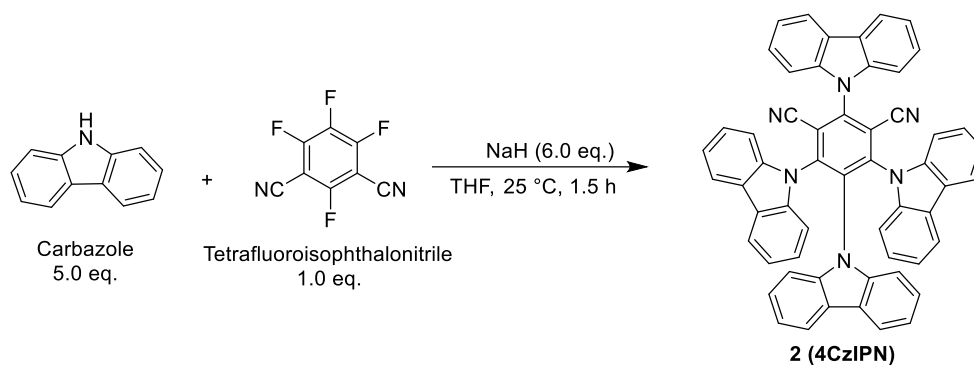
3,6-Bis(dimethylamino)-9H-carbazole (**1**): Pd₂(dba)₃ (141.9 mg, 0.155 mmol, 0.01 eq.) and Ruphos (173.6 mg, 0.372 mmol, 0.024 eq.) were charged into flame-dried screw tube in THF (15 mL) and then stirred for 5 min at room temperature under argon condition. Next, 3,6-dibromocarbazole **10** (5.0 g, 15.385 mmol, 1.00 eq.) and THF (30 mL) were added. Subsequently, LiHMDS (18.0 g, 107.572 mmol, 7.0 eq.), dimethylamine hydrochloride (3.8 g, 46.603 mmol, 3.00 eq.) and THF (30 mL) were loaded into the screw tube under argon condition, respectively. Finally, the reaction mixture was heated at 90 °C for 17 h. After the reaction, the resultant mixture was poured into water (20 mL) and stirred for 5 min and then solvent (THF) was removed from the mixture solution under reduced pressure. Thereafter, resulting suspension was extracted with ethyl acetate and water, three times and dried over anhydrous MgSO₄, and filtered. The filtrate was concentrated in vacuo. The residual solid was purified by column chromatography on silica gel (hexane : EtOAc = 1 : 1) to give yellow solid product (2.73 g, 10.776 mmol, 70% yield). ¹H NMR (400 MHz, Acetone-*d*₆) δ = 9.56 (s, 1H), 7.50 (d, *J* = 2.3 Hz, 2H), 7.30 (d, *J* = 8.8 Hz, 2H), 7.01 (dd, *J* = 8.8, 2.5 Hz, 2H), 2.94 (s, 12H) ppm. ¹³C NMR (100 MHz, Acetone-*d*₆) δ = 146.0, 135.6, 124.8, 115.9, 111.9, 105.3, 42.8 ppm. IR (neat): 3110, 3024, 2162, 1633, 1611, 1567, 1496, 1431, 1331, 1308, 1301, 1224, 1191, 1138, 1110, 1048, 960, 938, 889, 850, 805, 789, 728, 676, 645, 595 cm⁻¹. Mp 135.0-135.5 °C.



1,2,3-Trimethyl-1H-benzo[d]imidazol-3-ium iodide (**BI⁺(I⁻)**): Methyl iodide (7.3 g, 51.449 mmol, 4.00 eq.) and K₂CO₃ (1.8 g, 12.862 mmol, 1.00 eq.) were added to MeOH (26.0 mL) solution of the corresponding 2-methylbenzimidazole (1.7 g, 12.862 mmol, 1.00 eq.). The mixture was allowed to stir for 23.0 h at 70 °C, after which the mixture was concentrated and then the residue was directly purified by column chromatography on silica gel (CH₂Cl₂ : MeOH = 15 : 1) to give white solid product (2.91 g, 10.10 mmol, 78% yield). ¹H NMR (400 MHz, DMSO-*d*₆) δ = 7.99 (dd, *J* = 6.2, 3.1 Hz, 2H), 7.74–7.53 (m, 2H), 4.00 (s, 6H), 2.87 (s, 3H) ppm. ¹³C NMR (100 MHz, DMSO-*d*₆) δ = 152.3, 131.3, 125.8, 112.7, 31.7, 10.6 ppm. IR (neat): 3014, 2965, 2559, 1990, 1938, 1608, 1538, 1469, 1414, 1356, 1342, 1136, 1125, 1048, 1001, 946, 874, 788, 760, 694, 590, 575, 561 cm⁻¹. Mp 274.2-274.6 °C.

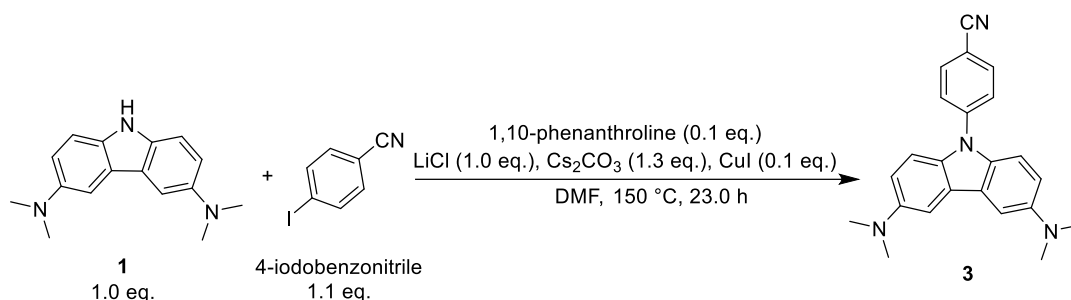


1,2,3-Trimethyl-2,3-dihydro-1*H*-benzo[*d*]imidazole (**BIH**): To a slurry of **BI⁺(I⁻)** (2.0 g, 6.941 mmol, 1.00 eq.) in Et₂O/H₂O (3/2, 14 mL) was added NaBH₄ (787.8 mg, 20.824 mmol, 3.00 eq.). After stirring at 25 °C for 1.5 h and then the resulting solution was extracted with Et₂O, three times. dried over anhydrous Na₂SO₄, and filtered. The filtrate was concentrated in vacuo at room temperature. The oil crude product was purified by flash column chromatography on silica gel (hexane : EtOAc = 5 : 1) to give colorless transparent oil product (0.93 g, 5.732 mmol, 82% yield). ¹H NMR (400 MHz, CDCl₃) δ = 6.70 (dd, *J* = 5.5, 3.2 Hz, 2H), 6.43 (dd, *J* = 5.4, 3.2 Hz, 2H), 4.11 (q, *J* = 5.3 Hz, 1H), 2.72 (s, 6H), 1.49 (d, *J* = 5.3 Hz, 3H) ppm. ¹³C NMR (100 MHz, CDCl₃) δ = 142.8, 119.3, 106.1, 86.6, 34.0, 18.6 ppm. HRMS *m/z* (ESI) calcd. for C₁₀H₁₅N₂⁺ (*M* + *H*)⁺ 163.1230, found 163.1222.

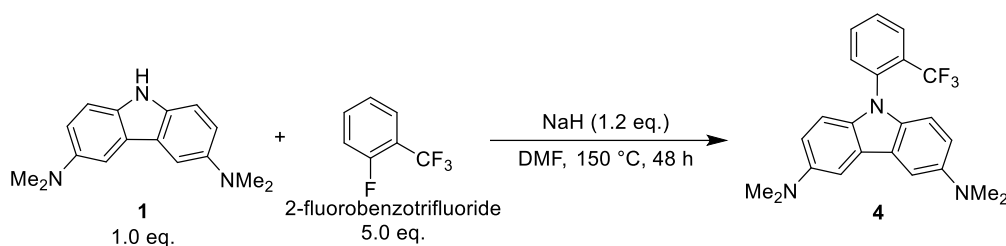


2,4,5,6-Tetra(9*H*-carbazol-9-yl)isophthalonitrile (**2**): A flame-dried screw tube was placed with carbazole (2.5 g, 14.992 mmol, 5.00 eq.) under argon condition. The reaction vessel was evacuated for 10 mins under reduced pressure and then purged with argon. Next, the screw tube was added 60% NaH (431.8 mg, 17.991 mmol, 6.00 eq.) and THF (25 mL) in order at 0 °C and then the reaction was stirred for 5 mins. Tetrafluoroisophthalonitrile (600.0 mg, 2.999 mmol, 1.00 eq.) was introduced into reaction system. After stirring for 1.5 h, the removal of solvent under reduced pressure and then the residue was soluble in dichloromethane, filtered, washed with dichloromethane, three times. The resulting filtrate was evaporated under reduced pressure and the residue was recrystallized with THF at 70 °C. Finally, recrystallized solution was placed in a -28 °C freezer for enough time and the resulting crystals was collected by filtration and washed with cooled THF. Because solvents (acetone, hexane et al.) were difficult to purge from solid, removing residual solvent at low pressure (15.0 Pa) and with heating (70 °C) using oil bath for 15.0 h to afford yellow solid product (1.4 g, 1.775 mmol, 59% yield). ¹H NMR (400 MHz, CDCl₃) δ = 8.23 (d, *J* = 7.8 Hz, 2H), 7.77–7.67 (m, 8H), 7.53–7.46 (m, 2H), 7.33 (d, *J* = 7.6 Hz, 2H), 7.23 (dd, *J* = 6.1, 2.9 Hz, 4H), 7.15–7.04 (m, 8H), 6.90–6.78 (m, 4H), 6.69–6.59 (m, 2H) ppm. ¹³C NMR (100 MHz, CDCl₃) δ = 145.4, 144.8, 140.2, 138.4, 137.1, 134.9, 127.1, 126.0, 125.1, 124.9, 124.7, 124.0, 122.6, 122.1, 121.6, 121.2, 120.6, 119.8, 116.5, 111.8, 110.1, 109.7,

109.6 ppm. IR (neat): 3048, 2234, 1599, 1540, 1489, 1480, 1443, 1332, 1309, 1294, 1220, 1150, 1118, 1028, 1005, 928, 899, 841, 767, 739, 718, 632, 616, 608, 589, 555 cm^{-1} . Mp > 290 °C.

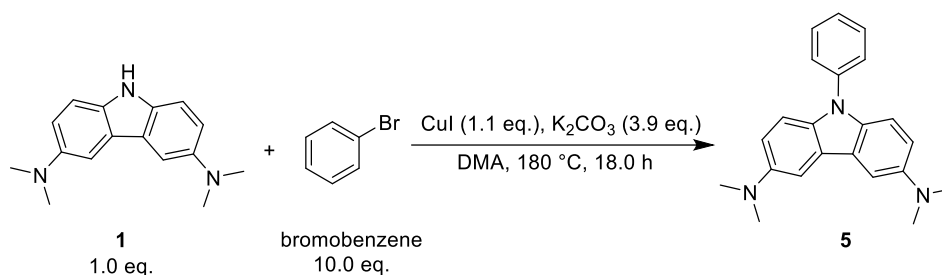


3,6-Bis(dimethylamino)-9-(4-cyanophenyl)carbazole (3): A solution of compound **1** (200.0 mg, 0.789 mmol, 1.00 eq.), 4-iodobenzonitrile (198.9 mg, 0.868 mmol, 1.10 eq.), LiCl (33.5 mg, 0.789 mmol, 1.00 eq.), CuI (15.0 mg, 0.079 mmol, 0.10 eq.), 1,10-phenanthroline monohydrate (14.2 mg, 0.079 mmol, 0.10 eq.), and Cs₂CO₃ (334.4 mg, 1.026 mmol, 1.30 eq.) in DMF (4.0 mL) was stirred for 23.0 h at 150 °C. After cooling to 25 °C, the reaction solution was quenched by adding saturated NH₄Cl solution (15 mL). Ethyl acetate (35 mL) was added, and the mixture was washed with brine six times, dried over anhydrous Na₂SO₄, filtered, and concentrated in vacuo. The residue was purified by column chromatography on silica gel (hexane : EtOAc = 2 : 1) to afford the yellow solid product (212.0 mg, 0.598 mmol, 76% yield). ¹H NMR (400 MHz, CDCl₃) δ = 7.83 (d, *J* = 8.6 Hz, 2H), 7.70 (d, *J* = 8.6 Hz, 2H), 7.40 (d, *J* = 9.0 Hz, 4H), 7.00 (d, *J* = 2.5 Hz, 2H), 3.04 (s, 12H) ppm. ¹³C NMR (100 MHz, CDCl₃) δ = 146.7, 143.3, 133.9, 133.7, 125.9, 125.3, 119.0, 114.9, 110.3, 108.7, 104.4, 42.5 ppm. IR (neat): 2839, 2791, 2216, 1603, 1578, 1512, 1498, 1471, 1436, 1372, 1329, 1216, 1171, 1106, 1061, 968, 947, 910, 826, 798, 748, 716, 661, 587, cm^{-1} . Mp 253.1-253.7 °C.

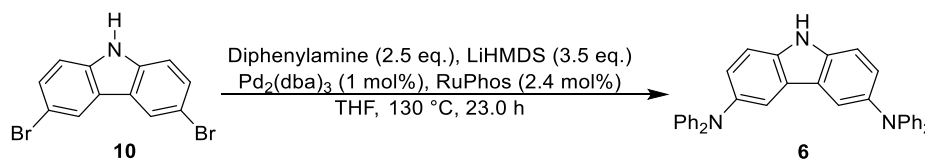


3,6-Bis(dimethylamino)-9-[2-(trifluoromethyl)phenyl]-9H-carbazole (4): 60% NaH (113.8 mg, 4.740 mmol, 1.20 eq.) was placed into flame-dried screw tube in hexane and then stirred for 30 mins under argon condition. Hexane was removed from the screw tube and then dried using vacuum line. DMF (8.0 mL) and compound **1** (1000.7 mg, 3.950 mmol, 1.00 eq.) were introduced into the screw tube and stirred for 30 mins, subsequently, 2-fluorobenzotrifluoride (3240.9 mg, 19.749 mmol, 5.00 eq.) was added. The reaction mixture was stirred at 150 °C for 48.0 h. After the reaction, the reaction solution was quenched with excess saturated NH₄Cl solution. Soon afterwards, the mixture solution was extracted with DCM, three times and washed with water, three times, dried over anhydrous MgSO₄, filtered, and concentrated under reduced pressure.

The crude product was purified by column chromatography on silica gel (benzene : EtOAc = 3 : 1) to afford the yellow solid product (681.1 mg, 1.714 mmol, 43% yield). ^1H NMR (400 MHz, CDCl_3) δ = 7.93 (dd, J = 7.8, 1.3 Hz, 1H), 7.75–7.59 (m, 2H), 7.46 (s, 2H), 7.30 (d, J = 7.7 Hz, 1H), 6.96 (dd, J = 8.9, 2.4 Hz, 2H), 6.82 (d, J = 8.8 Hz, 2H), 3.01 (s, 12H) ppm. ^{13}C NMR (100 MHz, CDCl_3) δ = 145.9, 137.8, 137.4, 132.6, 131.1 (q, $J_{\text{C-F}}$ = 30.4 Hz), 129.0, 127.6 (q, $J_{\text{C-F}}$ = 4.9 Hz), 124.4, 123.3 (q, $J_{\text{C-F}}$ = 272.1 Hz), 115.2, 110.7, 104.6, 42.9 ppm. IR (neat): 2991, 2950, 2836, 2787, 1581, 1495, 1434, 1380, 1314, 1262, 1230, 1161, 1130, 1055, 961, 943, 793, 772, 731, 679, 655, 641, 601 cm^{-1} . Mp 117.0–117.6 °C. HRMS m/z (ESI) calcd. for $\text{C}_{23}\text{H}_{23}\text{F}_3\text{N}_3^+$ ($\text{M} + \text{H}$) $^+$ 398.1839, found 398.1836.

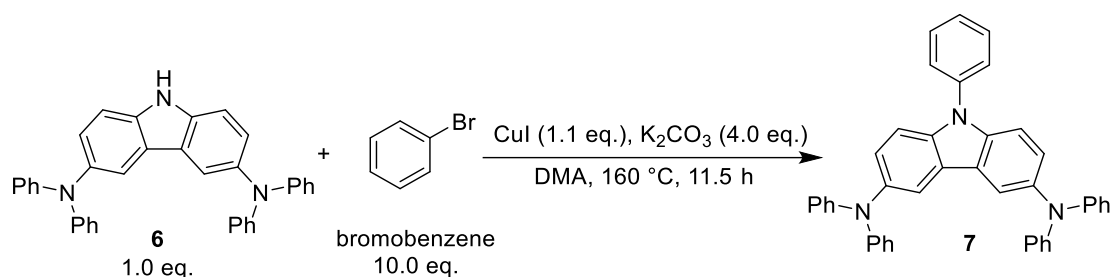


3,6-Bis(dimethylamino)-9-phenylcarbazole (5): To a flame-dried 50 mL of screw tube was charged with compound **1** (150.0 mg, 0.592 mmol, 1.00 eq.), bromobenzene (929.6 mg, 5.921 mmol, 10.00 eq.), CuI (124.0 mg, 0.651 mmol, 1.10 eq.), and K_2CO_3 (319.1 mg, 2.309 mmol, 3.90 eq.) in dimethylacetamide (3.0 mL). After stirring for 18.0 h at 180 °C. The resulting solution was quenched by adding water (50 mL). Next, excess saturated NH_3 solution was added and the mixture solution was extracted with CH_2Cl_2 , three times. The organic layer was washed with brine, five times, dried over anhydrous Na_2SO_4 , and filtered. The filtrate was concentrated in vacuo. The crude oil product was purified by column chromatography on silica gel (hexane : EtOAc = 2 : 1) to give yellow solid product (130.1 mg, 0.395 mmol, 67% yield). ^1H NMR (400 MHz, CDCl_3) δ = 7.57 (d, J = 4.5 Hz, 4H), 7.49 (d, J = 2.3 Hz, 2H), 7.43–7.33 (m, 3H), 7.03 (dd, J = 8.9, 2.5 Hz, 2H), 3.03 (s, 12H) ppm. ^{13}C NMR (100 MHz, CDCl_3) δ = 146.0, 138.9, 135.3, 129.8, 126.6, 126.5, 124.3, 115.4, 110.4, 104.8, 42.9 ppm. IR (neat): 3040, 2843, 2794, 2162, 1618, 1591, 1573, 1486, 1475, 1435, 1325, 1216, 1165, 1148, 1023, 968, 949, 836, 815, 795, 783, 761, 739, 715, 700, 659, 578 cm^{-1} . Mp 132.5–133.2 °C.

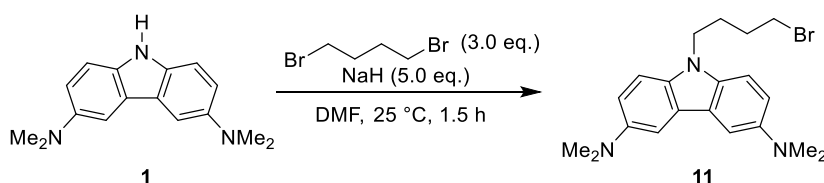


3,6-Bis(diphenylamino)-9H-carbazole (6): $\text{Pd}_2(\text{dba})_3$ (28.2 mg, 0.031 mmol, 0.01 eq.) and RuPhos (34.5 mg, 0.074 mmol, 0.024 eq.) were placed into flame-dried screw tube in THF (15.0 mL) and then stirred for 5 min. Next, 3,6-dibromocarbazole **10** (1.0 g, 3.077 mmol, 1.00 eq.), LiHMDS (1.8 g, 10.769 mmol, 3.50 eq.) and diphenylamine (1.3 g, 7.692 mmol, 2.50 eq.) were added into the screw tube, respectively under argon condition. Finally, the reaction mixture was heated at 130 °C for 23.0 h. After the

reaction, solvent was removed under reduced pressure and then was extracted with ethyl acetate, three times. Resulting organic phase was dried over anhydrous NaSO₄, and filtered. The filtrate was concentrated in vacuo. The residual solid was purified by column chromatography on silica gel (hexane : EtOAc = 15 : 1) to give white solid product (790.0 mg, 1.575 mmol, 51% yield). ¹H NMR (400 MHz, DMSO-*d*₆) δ = 11.38 (s, 1H), 7.87 (d, *J* = 1.9 Hz, 2H), 7.50 (d, *J* = 8.6 Hz, 2H), 7.26–7.14 (m, 10H), 6.99–6.85 (m, 12H) ppm. ¹³C NMR (100 MHz, DMSO-*d*₆) δ = 148.2, 138.4, 137.9, 129.2, 126.0, 123.3, 121.8, 121.3, 119.5, 112.4 ppm. IR (neat): 3404, 3034, 2162, 1703, 1583, 1484, 1463, 1453, 1309, 1270, 1228, 1176, 1144, 1076, 1027, 922, 809, 749, 694, 659, 646, 636, 598, 575 cm⁻¹. Mp 269.0-269.3 °C.

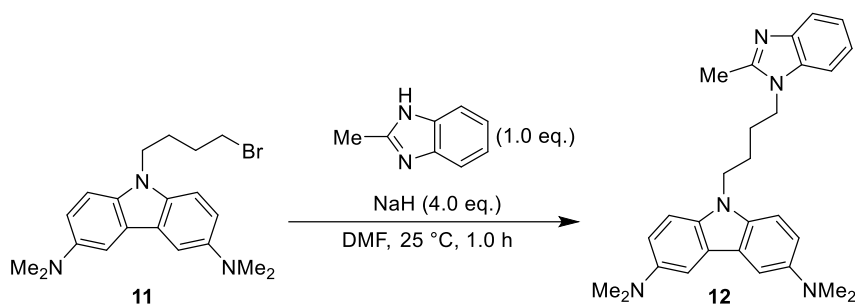


3,6-Bis(diphenylamino)-9-phenylcarbazole (**7**): To a flame-dried screw tube was charged with compound **6** (80.0 mg, 0.159 mmol, 1.0 eq.), bromobenzene (250.4 mg, 1.595 mmol, 10.00 eq.), CuI (33.4 mg, 0.175 mmol, 1.10 eq.), and K₂CO₃ (88.2 mg, 0.638 mmol, 4.00 eq.) in dimethylacetamide (1.6 mL) under argon condition and stirred for 11.5 h at 160 °C. After the reaction, the resulting solution was quenched by adding water (25.0 mL). Excess saturated NH₃ aqueous (1.0 mL) was added and the mixture solution was extracted with CH₂Cl₂, three times. The organic layer is washed with brine, five times, dried over anhydrous Na₂SO₄, and filtered. The filtrate was concentrated in vacuo. The crude product was purified by column chromatography on silica gel (hexane : EtOAc = 20 : 1) to give white solid product (76.3 mg, 0.132 mmol, 83% yield). ¹H NMR (400 MHz, DMSO-*d*₆) δ = 7.95 (s, 2H), 7.66 (dd, *J* = 14.1, 6.9 Hz, 4H), 7.53 (t, *J* = 7.2 Hz, 1H), 7.35 (d, *J* = 8.7 Hz, 2H), 7.20 (q, *J* = 6.6, 6.1 Hz, 10H), 7.00–6.83 (m, 12H) ppm. ¹³C NMR (100 MHz, DMSO-*d*₆) δ = 148.0, 139.9, 138.1, 136.7, 130.2, 129.2, 127.8, 126.8, 126.4, 123.6, 122.0, 121.6, 119.4, 111.1 ppm. IR (neat): 3065, 3036, 2162, 1953, 1584, 1480, 1452, 1309, 1268, 1225, 1176, 1153, 1027, 921, 810, 747, 712, 693, 636, 572 cm⁻¹. Mp 210.0-210.5 °C.

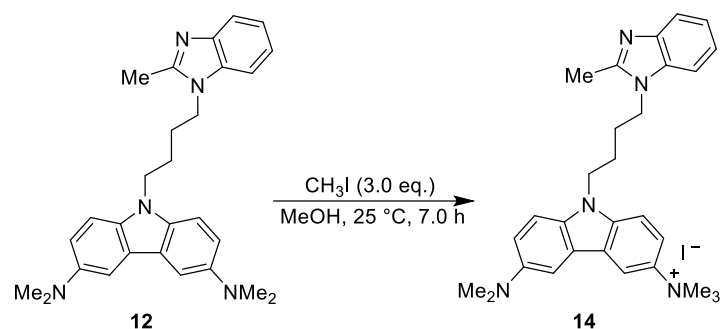


3,6-Bis(dimethylamino)-9-(4-bromobutyl)carbazole (**11**): Compound **1** (100.0 mg, 0.395 mmol, 1.00 eq.) and 60% sodium hydride (47.4 mg, 1.974 mmol, 5.00 eq.) were placed into flame-dried screw tube in DMF (2.0 mL) and then 1,4-dibromobutane (255.7 mg, 1.184 mmol, 3.00 eq.) was dropwise added into the screw tube. The reaction

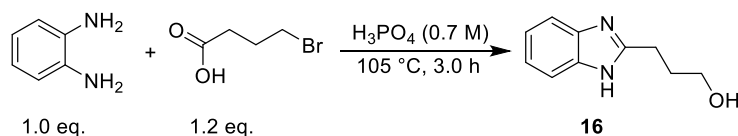
mixture was stirred for 1.5 h. After reaction, the reaction mixture was poured into 35 mL H₂O and then CH₂Cl₂ was added. The mixture was washed with brine, six times, dried over anhydrous Na₂SO₄, filtered, and concentrated under reduced pressure. The crude product was purified by column chromatography on silica gel (hexane : EtOAc = 5 : 2) to afford the green solid product (136.0 mg, 0.350 mmol, 89% yield). ¹H NMR (400 MHz, Acetone-*d*₆) δ = 7.53 (s, 2H), 7.36 (d, *J* = 8.8 Hz, 2H), 7.06 (dd, *J* = 8.9, 2.5 Hz, 2H), 4.34 (s, 2H), 3.50 (t, *J* = 6.5 Hz, 2H), 3.18–2.85 (m, 12H), 2.03–1.84 (m, 4H) ppm. ¹³C NMR (100 MHz, Acetone-*d*₆) δ = 146.0, 135.8, 124.3, 115.8, 109.9, 105.6, 42.8, 42.6, 34.4, 31.2, 28.60 ppm. IR (neat): 3382, 2944, 2787, 2162, 1633, 1607, 1573, 1484, 1440, 1317, 1215, 1134, 1055, 1024, 954, 801, 729, 608, 574 cm⁻¹. Mp 197.3–197.8 °C. HRMS *m/z* (ESI) calcd. for C₂₀H₂₇BrN₃⁺ (*M* + *H*)⁺ 388.1383, found 388.1379.



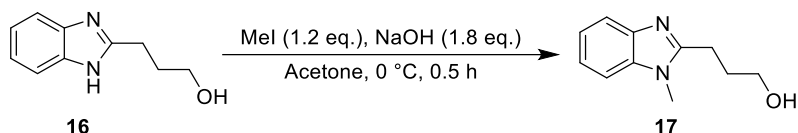
3,6-Bis(dimethylamino)-9-(4-(2-methyl-1*H*-benzo[d]imidazol-1-yl)butyl)-9*H*-carbazole (**12**): 2-methyl-1*H*-benzimidazole (34.0 mg, 0.257 mmol, 1.00 eq.) and 60% sodium hydride (24.7 mg, 1.030 mmol, 4.00 eq.) were placed into flame-dried screw tube in DMF (2.0 mL) under argon condition and then compound **11** (100.0 mg, 0.257 mmol, 1.00 eq.) was added into the screw tube. The reaction mixture was stirred for 1.0 h at 25 °C. after the reaction, the reaction mixture was poured into 35 mL H₂O and then CH₂Cl₂ (45 mL) was added, and the mixture was washed with brine, six times, dried over anhydrous Na₂SO₄, filtered, and concentrated under reduced pressure. The crude product was purified by Preparative Thin-Layer Chromatography (CH₂Cl₂ : MeOH = 20 : 1) to afford the black oil product (94.1 mg, 0.214 mmol, 83% yield). ¹H NMR (400 MHz, Acetone-*d*₆) δ = 7.67–7.39 (m, 3H), 7.37–7.20 (m, 3H), 7.14–7.07 (m, 2H), 7.02 (dd, *J* = 8.9, 2.4 Hz, 2H), 4.30 (s, 2H), 4.10 (t, *J* = 7.1 Hz, 2H), 2.94 (s, 12H), 2.44 (s, 3H), 1.93 (dt, *J* = 14.2, 6.8 Hz, 2H), 1.84 (dt, *J* = 14.7, 7.3 Hz, 2H) ppm. ¹³C NMR (100 MHz, Acetone-*d*₆) δ = 152.1, 145.9, 143.8, 136.3, 135.8, 124.2, 122.2, 121.8, 119.3, 115.7, 110.3, 110.0, 105.5, 44.0, 43.0, 42.7, 28.1, 27.2, 13.8 ppm. HRMS *m/z* (ESI) calcd. for C₂₈H₃₄N₅⁺ (*M* + *H*)⁺ 440.2809, found 440.2794.



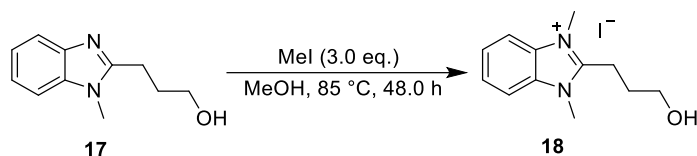
6-(dimethylamino)-*N,N,N*-trimethyl-9-(4-(2-methyl-1*H*-benzo[*d*]imidazol-1-yl)butyl)-9*H*-carbazol-3-aminium iodide (**14**): Compound **12** (50.0 mg, 0.114 mmol, 1.00 eq.) and iodomethane (48.4 mg, 0.341 mmol, 3.00 eq.) were placed in flame-dried screw tube in MeOH (1.1 mL) under argon condition and then the reaction mixture was stirred at 25 °C for 7.0 h. After the reaction, the removal of MeOH under reduced pressure. The crude product was purified by column chromatography on silica gel (CH₂Cl₂ : MeOH = 10 : 1) to afford the green solid product (35.6.0 mg, 0.061 mmol, 54% yield). ¹H NMR (400 MHz, MeOD) δ = 8.72 (d, *J* = 2.8 Hz, 1H), 7.83 (dd, *J* = 9.2, 2.8 Hz, 1H), 7.77 (s, 1H), 7.58 (d, *J* = 9.2 Hz, 1H), 7.51–7.41 (m, 2H), 7.28–7.12 (m, 4H), 4.38 (t, *J* = 6.3 Hz, 2H), 4.11 (t, *J* = 7.2 Hz, 2H), 3.77 (s, 9H), 3.00 (s, 6H), 2.43 (s, 3H), 2.02–1.87 (m, 2H), 1.79 (quint, *J* = 7.3 Hz, 2H) ppm. ¹³C NMR (100 MHz, MeOD) δ = 152.9, 147.1, 141.5, 140.8, 139.9, 137.1, 135.5, 124.2, 124.2, 124.0, 123.8, 118.4, 118.2, 117.6, 113.3, 111.4, 111.3, 111.2, 107.1, 58.5, 44.6, 43.5, 43.3, 27.9, 27.2, 13.2 ppm. IR (neat): 3362, 3011, 2923, 2504, 2161, 1715, 1609, 1574, 1485, 1462, 1403, 1317, 1230, 1128, 1059, 952, 939, 792, 744, 499, 570 cm⁻¹. Mp 199.1–199.8 °C. HRMS *m/z* (ESI) calcd. for C₂₉H₃₆N₅⁺ (*M* - I)⁺ 454.2965, found 454.2946.



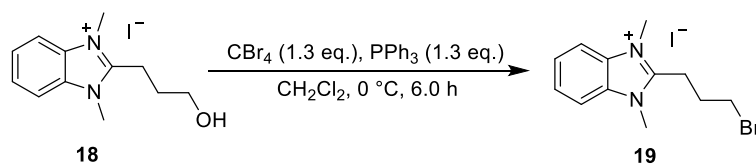
3-(1*H*-benzo[*d*]imidazol-2-yl)propan-1-ol (**16**): *o*-phenylenediamine (500.0 mg, 4.624 mmol, 1.00 eq.) and 4-bromobutyric acid (926.6 mg, 5.548 mmol, 1.20 eq.) were placed in flame-dried screw tube in H₃PO₄ (6.0 mL) under argon condition and then the reaction mixture was stirred at 105 °C for 3.0 h. After the reaction, The mixture was neutralized with excess saturated Na₂CO₃ solution and then extracted with EtOAc, three time. dried over anhydrous Na₂SO₄, filtered, and concentrated under reduced pressure. The crude solid product was washed with CH₂Cl₂, three time to afford the white solid product (576 mg, 3.269 mmol, 71% yield). ¹H NMR (400 MHz, MeOD) δ = 7.48 (dd, *J* = 6.0, 3.2 Hz, 2H), 7.18 (dd, *J* = 5.7, 3.0 Hz, 2H), 3.64 (t, *J* = 6.3 Hz, 2H), 2.97 (t, *J* = 7.6 Hz, 2H), 2.04 (quint, *J* = 6.4 Hz, 2H) ppm. ¹³C NMR (100 MHz, MeOD) δ = 156.5, 139.4, 123.2, 115.3, 62.0, 32.0, 26.3 ppm. IR (neat): 3025, 2943, 2768, 1590, 1532, 1452, 1438, 1419, 1382, 1310, 1275, 1237, 1224, 1186, 1145, 1062, 1008, 993, 842, 766, 744, 704, 625 cm⁻¹. Mp 155.0–155.8 °C. HRMS *m/z* (ESI) calcd. for C₁₀H₁₃N₂O⁺ (*M* + H)⁺ 177.1022, found 177.1023.



3-(1-methyl-1*H*-benzo[*d*]imidazol-2-yl)propan-1-ol (**17**): Compound **16** (500.0 mg, 2.837 mmol, 1.00 eq.), NaOH (200 mg, 5.000 mmol, 1.76 eq.) and iodomethane (500.0 mg, 3.523 mmol, 1.24 eq.) were placed in flame-dried screw tube in acetone (20.0 mL) under argon condition at 0 °C and then the reaction mixture was stirred at 0 °C for 0.5 h, after the reaction, the mixture was neutralized with excess saturated NaHCO₃ solution and the removal of acetone under reduced pressure, afterward, extracted with EtOAc, three time. dried over anhydrous Na₂SO₄, filtered, and concentrated under reduced pressure to afford the white solid product (502.7.0 mg, 2.642 mmol, 93% yield). ¹H NMR (400 MHz, CDCl₃) δ = 7.68 (dd, *J* = 6.0, 2.6 Hz, 1H), 7.33–7.19 (m, 3H), 3.81 (t, *J* = 5.6 Hz, 2H), 3.72 (s, 3H), 3.04 (t, *J* = 6.8 Hz, 2H), 2.15 (quint, *J* = 6.6 Hz, 2H) ppm. ¹³C NMR (100 MHz, CDCl₃) δ = 155.2, 142.0, 135.8, 122.4, 122.2, 119.1, 109.1, 62.2, 29.9, 29.6, 25.2 ppm. IR (neat): 3193, 2956, 2934, 2883, 2379, 1616, 1508, 1475, 1443, 1428, 1407, 1360, 1330, 1278, 1126, 1070, 1005, 930, 909, 891, 765, 746, 680, 567 cm⁻¹. Mp 104.2-104.6 °C. HRMS *m/z* (ESI) calcd. for C₁₁H₁₅N₂O⁺ (*M* + *H*)⁺ 191.1179, found 191.118.

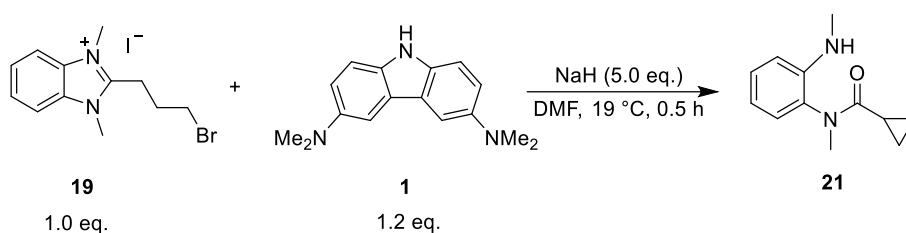


2-(3-hydroxypropyl)-1,3-dimethyl-1*H*-benzo[*d*]imidazol-3-ium iodide (**18**): Compound **17** (200.0 mg, 1.051 mmol, 1.00 eq.) and iodomethane (448.6 mg, 3.160 mmol, 3.00 eq.) were placed in flame-dried screw tube in MeOH (7.9 mL) under argon condition at 0 °C and then the reaction mixture was stirred at 85 °C for 48 h, after the reaction, the removal of MeOH under reduced pressure. The crude product was directly purified by column chromatography on silica gel (CH₂Cl₂ : MeOH = 20 : 1) to afford the brown solid product (206.0 mg, 0.620 mmol, 59% yield). ¹H NMR (400 MHz, MeOD) δ = 7.90 (dd, *J* = 6.2, 3.1 Hz, 2H), 7.67 (dd, *J* = 6.2, 3.1 Hz, 2H), 4.10 (s, 6H), 3.71 (t, *J* = 5.6 Hz, 2H), 3.44 (t, *J* = 7.5 Hz, 2H), 2.06 (quint, *J* = 6.1 Hz, 2H) ppm. ¹³C NMR (100 MHz, MeOD) δ = 155.5, 133.2, 127.6, 113.7, 61.2, 32.4, 30.1, 22.0 ppm. IR (neat): 3400, 3019, 2928, 2886, 1979, 1614, 1530, 1486, 1475, 1424, 1353, 1310, 1237, 1136, 1065, 1012, 917, 894, 802, 759, 745, 564 cm⁻¹. Mp 196.0-196.5 °C. HRMS *m/z* (ESI) calcd. for C₁₂H₁₇N₂O⁺ (*M* - *I*)⁺ 205.1335, found 205.1335.

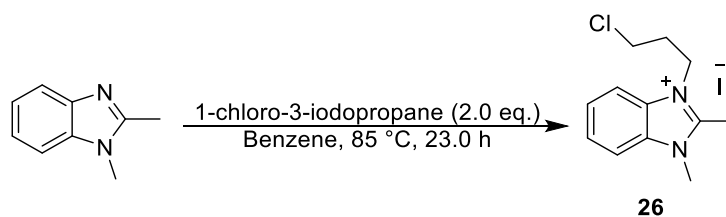


2-(3-bromopropyl)-1,3-dimethyl-1*H*-benzo[*d*]imidazol-3-ium iodide (**19**): A solution of compound **18** (100.0 mg, 0.301 mmol, 1.00 eq.), PPh₃ (102.6 mg, 0.391

mmol, 1.30 eq.) and CBr₄ (130.0 mg, 0.391 mmol, 1.30 eq.) in CH₂Cl₂ (3.0 mL) was stirred for 6.0 h at 0 °C. The crude mixture was directly purified by column chromatography on silica gel (MeOH : CH₂Cl₂ = 1 : 20 to 1 : 10) to afford the yellow solid product (85.0 mg, 0.215 mmol, 72% yield). ¹H NMR (400 MHz, MeOD) δ = 7.92 (dd, *J* = 6.2, 3.1 Hz, 2H), 7.69 (dd, *J* = 6.2, 3.2 Hz, 2H), 4.12 (s, 6H), 3.70 (t, *J* = 6.1 Hz, 2H), 3.60–3.45 (m, 2H), 2.48–2.30 (m, 2H) ppm. ¹³C NMR (100 MHz, MeOD) δ = 154.0, 133.3, 127.8, 113.8, 32.8, 32.4, 30.4, 23.6 ppm. IR (neat): 3384, 3016, 2936, 1931, 1621, 1530, 1479, 1358, 1307, 1270, 1250, 1193, 1140, 1105, 1058, 1023, 955, 899, 849, 757, 735, 555 cm⁻¹. Mp 214.0–214.5 °C. HRMS *m/z* (ESI) calcd. for C₁₂H₁₆BrN₂⁺ (*M* - I)⁺ 267.0491, found 267.0498.

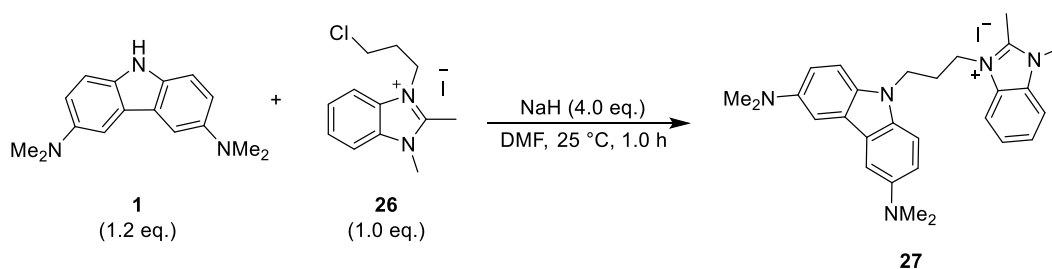


N-methyl-*N*-(2-(methylamino)phenyl)cyclopropanecarboxamide (**21**): Compound **1** (38.5 mg, 0.152 mmol, 1.20 eq.) and 60% sodium hydride (15.2 mg, 0.633 mmol, 5.00 eq.) were placed in flame-dried screw tube in DMF (1.3 mL) and then compound **19** (50.0 mg, 0.127 mmol, 1.00 eq.) was added into the screw tube. The reaction mixture was stirred at 19 °C for 0.5 h. After the reaction, CH₂Cl₂ (20.0 mL) was added and then the mixture was washed with brine, six times, dried over anhydrous Na₂SO₄, filtered, and concentrated under reduced pressure. The crude product was purified by Preparative Thin-Layer Chromatography (hexane : EtOAc = 2 : 1) to afford the yellow solid product (24.0 mg, 0.117 mmol, 93% yield). ¹H NMR (400 MHz, CDCl₃) δ = 7.25 (td, *J* = 7.8, 1.4 Hz, 1H), 7.07 (dd, *J* = 8.1, 1.5 Hz, 1H), 6.83–6.62 (m, 2H), 4.29–3.81 (m, 1H), 3.17 (s, 3H), 2.88 (d, *J* = 5.2 Hz, 3H), 1.35 (ddd, *J* = 12.6, 8.0, 4.7 Hz, 1H), 1.00 (ddt, *J* = 9.6, 4.8, 2.3 Hz, 1H), 0.94–0.85 (m, 1H), 0.59 (dq, *J* = 7.4, 2.5 Hz, 2H) ppm. ¹³C NMR (100 MHz, CDCl₃) δ = 175.1, 145.4, 129.5, 129.0, 128.5, 117.0, 110.8, 35.6, 30.4, 11.8, 8.4, 8.3 ppm. IR (neat): 3382, 3012, 2915, 2818, 2116, 1639, 1602, 1574, 1517, 1474, 1421, 1388, 1317, 1283, 1241, 1167, 1118, 1089, 1069, 1024, 932, 762, 751, 734, 585 cm⁻¹. Mp 116.3–116.9 °C. HRMS *m/z* (ESI) calcd. for C₁₂H₁₆N₂NaO⁺ (*M* + Na)⁺ 227.1155, found 227.1159.

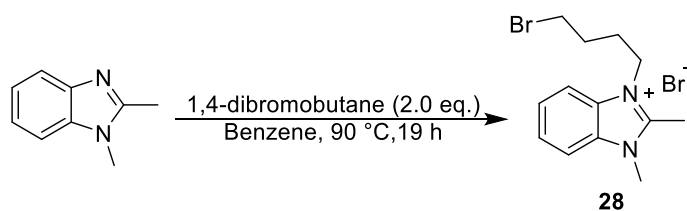


3-(3-chloropropyl)-1,2-dimethyl-1*H*-benzo[*d*]imidazol-3-ium iodide (**26**): 1,2-Dimethyl-1*H*-benzimidazole (100.0 mg, 0.684 mmol, 1.00 eq.) and 1-chloro-3-iodopropane (279.7 mg, 1.368 mmol, 2.00 eq.) were placed in flame-dried 50 mL of

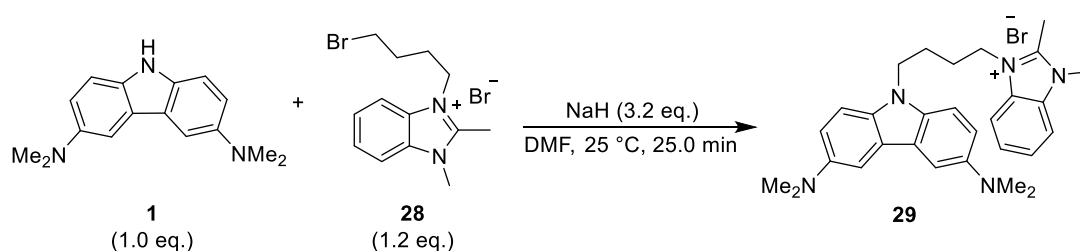
screw tube in benzene (6.8 mL) and the suspension solution was stirred at 85 °C for 23 h. After the reaction, the suspension solution was filtered by buchner funnel and washed with benzene three times to afford the white solid product (186.0 mg, 0.530 mmol, 78% yield). ¹H NMR (400 MHz, DMSO-*d*₆) δ = 8.02 (dt, *J* = 6.5, 3.7 Hz, 2H), 7.65 (dd, *J* = 6.2, 3.1 Hz, 2H), 4.61 (t, *J* = 7.0 Hz, 2H), 3.99 (s, 3H), 3.75 (t, *J* = 6.5 Hz, 2H), 2.90 (s, 3H), 2.27 (quint, *J* = 6.7 Hz, 2H) ppm. ¹³C NMR (100 MHz, DMSO-*d*₆) δ = 152.2, 131.5, 130.6, 126.0, 125.9, 112.9, 112.6, 42.5, 41.8, 31.8, 31.3, 10.7 ppm. IR (neat): 3022, 1534, 1473, 1376, 1286, 1131, 1012, 810, 761, 634, 512, 509, 505 cm⁻¹. Mp 206.5-207.8 °C. HRMS *m/z* (ESI) calcd. for C₁₂H₁₆ClN₂⁺ (*M* - I)⁺ 223.0997, found 223.0999.



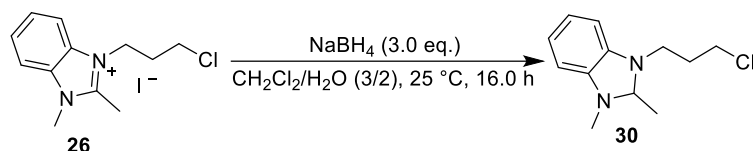
3-(3-(3,6-bis(dimethylamino)-9*H*-carbazol-9-yl)propyl)-1,2-dimethyl-1*H*-benzo[*d*]imidazol-3-ium iodide (**27**): To a flame-dried 50 mL of Schlenk tube was added 60% sodium hydride (41.1 mg, 1.712 mmol, 4.00 eq.) and compound **1** (130.0 mg, 0.513 mmol, 1.20 eq.) in DMF (1.6 mL) under argon condition. Next, the mixture solution was stirred for 5 min and then compound **26** (150.0 mg, 0.428 mmol, 1.00 eq.) was introduced to the mixture. After stirring at 25 °C for 1.0 h, silica gel was added to the crude residue and the suspension was dried under reduced pressure. The residue was directly purified by column chromatography on silica gel using dry-load sample method (hexane : EtOAc = 1 : 1 to CH₂Cl₂ : MeOH = 10 : 1) to afford the yellow solid product (146.0 mg, 0.257 mmol, 60% yield). ¹H NMR (400 MHz, Acetonitrile-*d*₃) δ = 7.68 (d, *J* = 8.3 Hz, 1H), 7.64–7.42 (m, 4H), 7.41–7.24 (m, 3H), 7.11 (d, *J* = 8.6 Hz, 2H), 4.46 (s, 2H), 4.34–4.27 (m, 2H), 3.79 (s, 3H), 2.98 (s, 12H), 2.54 (s, 3H), 2.38 (quint, *J* = 7.0 Hz, 2H) ppm. ¹³C NMR (100 MHz, Acetonitrile-*d*₃) δ = 152.0, 132.6, 131.5, 127.2, 127.1, 124.4, 116.1, 113.5, 113.3, 110.5, 100.9, 44.1, 42.9, 35.5, 32.6, 20.6, 11.2 ppm. (Comment: the number of peaks in the ¹³C NMR spectrum is less than expected from the structure due to the low solubility and the existence of the rotamers). IR (neat): 3420, 2946, 2775, 2358, 1607, 1476, 1328, 1214, 1131, 1056, 943, 799, 745, 517, 509 cm⁻¹. Mp 189.0-189.5 °C. HRMS *m/z* (ESI) calcd. for C₂₈H₃₄N₅⁺ (*M* - I)⁺ 440.2809, found 440.2806.



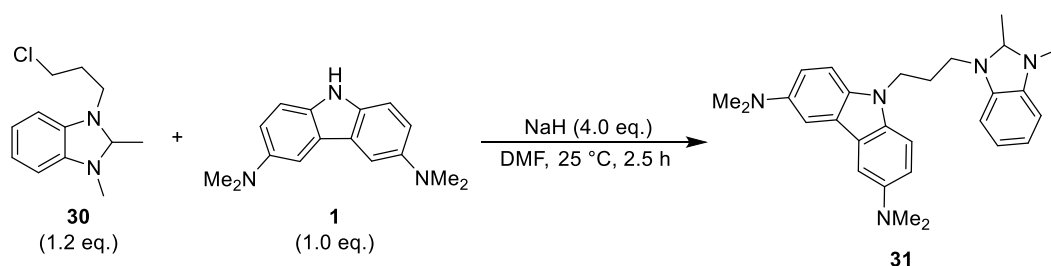
3-(4-bromobutyl)-1,2-dimethyl-1*H*-benzo[d]imidazol-3-ium bromide (**28**): To a flame-dried 50 mL of screw tube was added 1,2-dimethyl-1*H*-benzimidazole (500.0 mg, 3.420 mmol, 1.00 eq.) and dibromobutane (1.5 g, 6.840 mmol, 2.00 eq.) in benzene (13.7 mL), after stirring at 90 °C for 19 h. The suspension solution was filtered and washed with benzene three times to afford the white solid product (615.0 mg, 1.698 mmol, 50% yield). ¹H NMR (400 MHz, DMSO-*d*₆) δ = 8.05 (dd, *J* = 6.1, 3.2 Hz, 1H), 8.00 (dd, *J* = 6.2, 3.1 Hz, 1H), 7.64 (dd, *J* = 6.2, 3.1 Hz, 2H), 4.55 (t, *J* = 6.6 Hz, 2H), 3.98 (s, 3H), 3.60 (t, *J* = 6.1 Hz, 2H), 2.90 (s, 3H), 2.04–1.78 (m, 4H) ppm. ¹³C NMR (100 MHz, DMSO-*d*₆) δ = 152.0, 131.5, 130.6, 125.9, 125.8, 112.8, 112.8, 44.0, 34.4, 31.7, 28.9, 27.4, 10.6 ppm. IR (neat): 3041, 2921, 1611, 1535, 1478, 1425, 1385, 1264, 1243, 1062, 900, 797, 773, 764, 619, 556 cm⁻¹. Mp 189.0-189.5 °C. HRMS *m/z* (ESI) calcd. for C₁₃H₁₈BrN₂⁺ (M - Br)⁺ 281.0648, found 281.0652.



3-(4-(3,6-bis(dimethylamino)-9*H*-carbazol-9-yl)butyl)-1,2-dimethyl-1*H*-benzo[d]imidazol-3-ium bromide (**29**): To a flame-dried 50 mL of screw tube was added 60% sodium hydride (91.0 mg, 3.789 mmol, 3.20 eq.) and compound **1** (300.0 mg, 1.184 mmol, 1.0 eq.) in DMF (2.0 mL) under argon atmosphere and then stirred for 2 min. Next, compound **28** (514.544 mg, 1.421 mmol, 1.20 eq.) was introduced to the suspension solution. After stirring at 25 °C for 25 min. silica gel was added to the crude residue and the suspension was dried under reduced pressure. The residue was directly purified by column chromatography on silica gel using dry-load sample method (hexane : EtOAc = 1 : 2 to CH₂Cl₂ : MeOH = 10 : 1) to afford the yellow solid product which was washed with 30 mL of CH₃CN and then filtered, dried over anhydrous Na₂SO₄, filtered, and concentrated under reduced pressure to provide more pure yellow solid product (250.0 mg, 0.468 mmol, 39% yield). ¹H NMR (400 MHz, Acetone-*d*₆) δ = 7.91 (d, *J* = 8.2 Hz, 1H), 7.81 (d, *J* = 8.0 Hz, 1H), 7.68–7.52 (m, 4H), 7.38 (d, *J* = 8.9 Hz, 2H), 7.06 (d, *J* = 8.4 Hz, 2H), 4.57 (t, *J* = 7.1 Hz, 2H), 4.38 (t, *J* = 6.2 Hz, 2H), 4.09 (s, 3H), 2.96 (d, *J* = 4.2 Hz, 15H) ppm (Comment: Some of the peaks overlapped with those of acetone, which was confirmed using H–H COSY spectroscopy); ¹³C NMR (100 MHz, Acetone-*d*₆) δ = 152.7, 135.9, 132.7, 132.0, 126.9, 126.9, 124.1, 115.8, 113.5, 113.4, 110.2, 105.8, 46.3, 42.8, 32.4, 27.3, 26.7, 11.2 ppm. (Comment: the number of peaks in the ¹³C NMR spectrum is less than expected from the structure due to the low solubility and the existence of the rotamers). IR (neat): 3386, 2924, 2775, 2358, 1483, 1330, 1211, 1131, 1055, 944, 800, 745, 509, 512 cm⁻¹. Mp 164.0-164.8 °C. HRMS *m/z* (ESI) calcd. for C₂₉H₃₆N₅⁺ (M - Br)⁺ 454.2965, found 454.2962.



1-(3-chloropropyl)-2,3-dimethyl-2,3-dihydro-1*H*-benzo[*d*]imidazole (**30**): To a flame-dried 50 mL of screw tube was added compound NaBH₄ (97.1 mg, 2.567 mmol, 3.00 eq.), and **26** (300.0 mg, 0.856 mmol, 1.0 eq.) in CH₂Cl₂ (4.8 mL). After stirring at 25 °C for 10 min. Subsequently, H₂O (2.4 mL) was added to the mixture. The reaction mixture solution was stirred at 25 °C for 16 h. After the reaction, the mixture was extracted with CH₂Cl₂ three times, dried over anhydrous Na₂SO₄, filtered, and concentrated under reduced pressure. The crude product was purified by column chromatography on silica gel (hexane : EtOAc = 15 : 1) to afford the pale red oil product (145.0 mg, 0.645 mmol, 75% yield). ¹H NMR (400 MHz, Chloroform-*d*) δ = 6.72–6.58 (m, 2H), 6.48–6.30 (m, 2H), 4.37 (q, *J* = 5.3 Hz, 1H), 3.67 (ddd, *J* = 6.4, 5.3, 3.2 Hz, 2H), 3.29 (dt, *J* = 14.5, 6.3 Hz, 1H), 3.09 (dt, *J* = 14.4, 7.0 Hz, 1H), 2.70 (s, 3H), 2.17–1.97 (m, 2H), 1.47 (d, *J* = 5.3 Hz, 3H) ppm. ¹³C NMR (100 MHz, Chloroform-*d*) δ = 142.5, 142.0, 119.3, 119.0, 105.9, 105.3, 85.0, 44.9, 42.9, 33.9, 31.4, 19.6 ppm. HRMS *m/z* (ESI) calcd. for C₁₂H₁₈ClN₂⁺ (*M* + *H*)⁺ 225.1153, found 225.1154.



3,6-Bis(dimethylamino)-9-(3-(2,3-dimethyl-2,3-dihydro-1*H*-benzo[*d*]imidazol-1-yl)propyl)-9*H*-carbazole (**31**): To a flame-dried 50 mL of screw tube was added 60% sodium hydride (37.9 mg, 1.579 mmol, 4.00 eq.), and compound **1** (100.0 mg, 0.395 mmol, 1.00 eq.) in DMF (2.0 mL) under argon atmosphere. The mixture suspension was stirred for 10 min. Next, compound **30** (106.4 mg, 0.474 mmol, 1.20 eq.) was introduced to the mixture. After stirring at 25 °C for 2.5 h, CH₂Cl₂ was added and then washed with brine six times. The organic layer was dried over Na₂SO₄ and concentrated under reduced pressure. The crude residue was purified by column chromatography on silica gel (benzene: EtOAc = 10 : 1) to afford the yellow solid product (137.0 mg, 0.310 mmol, 79% yield). ¹H NMR (400 MHz, Acetone-*d*₆) δ = 7.53 (d, *J* = 2.4 Hz, 2H), 7.36 (d, *J* = 8.9 Hz, 2H), 7.05 (dd, *J* = 8.9, 2.5 Hz, 2H), 6.55–6.41 (m, 2H), 6.35–6.28 (m, 1H), 6.20–6.12 (m, 1H), 4.50–4.30 (m, 2H), 4.30 (q, *J* = 5.3 Hz, 1H), 3.25–3.15 (m, 1H), 3.11–3.02 (m, 1H), 2.94 (s, 12H), 2.63 (s, 3H), 2.08 (quint, *J* = 6.0 Hz, 2H), 1.36 (d, *J* = 5.3 Hz, 3H) ppm. ¹³C NMR (100 MHz, Acetone-*d*₆) δ = 146.0, 143.5, 142.6, 135.7, 124.3, 119.6, 119.1, 115.7, 109.9, 106.2, 105.8, 105.5, 85.2, 45.5, 42.7, 41.4, 33.9, 27.7, 19.6 ppm. IR (neat): 3052, 2950, 2859, 2785, 1601, 1493, 1380, 1327, 1204, 1129, 1058, 1018, 964, 945, 830, 792, 724, 516 cm⁻¹. Mp 48.5–49.7 °C. HRMS *m/z* (ESI) calcd. for C₂₈H₃₆N₅⁺ (*M* + *H*)⁺ 442.2965, found 442.2966.

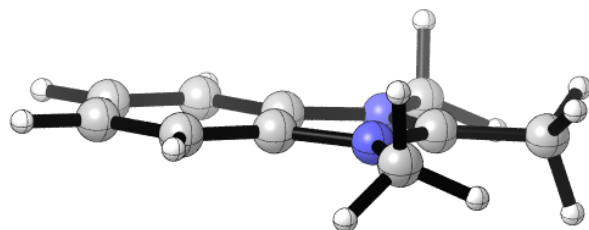
15. Computational study on carbazole radical cation and BI radical

DFT calculations All calculations were performed with the Gaussian 09 package.¹³⁹ Geometry optimization and analytical vibrational frequency analysis for the ground state were performed by the (U)LC-BLYP¹⁴⁰⁻¹⁴² DFT method with 6-31++G(d) basis set and conductor-like polarizable continuum solvation model (CPCM, DMSO or CH₃CN).¹⁴³ The excitation energies were calculated by the time-dependent (TD) DFT method using B3LYP functional with 6-31++G(d,p) basis set and conductor-like polarizable continuum solvation model (CPCM, DMSO). Frequency analyses were also carried out to identify the stationary points (no imaginary frequency was confirmed for the optimized ground state) and to estimate thermodynamic properties at 298.15 K and 1 atm and Gibbs free energies. The molecular structures were depicted by using the CYLview v1.0.561 β.¹⁴⁴

The calculated molecular structures

Cartesian coordinates of the ground state stationary points are given below:

BI⁺ (solvent = DMSO)



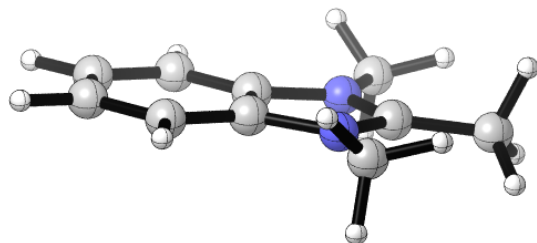
($E = -496.812248416$, $H = -496.578411$, $G = -496.628583$, NIMAG = 0, dipole moment = 5.3072 D)

CPCM(DMSO)

Center Number	Atomic Number	Atomic Type	Coordinates (Angstroms)		
			X	Y	Z
1	6	0	0.525202	-0.690776	-0.003594
2	6	0	0.525202	0.690776	-0.003594
3	6	0	1.702454	1.421857	0.002534
4	6	0	2.874646	0.700183	0.007530
5	6	0	2.874646	-0.700184	0.007530
6	6	0	1.702454	-1.421857	0.002534
7	6	0	-1.569886	0.000000	0.005989
8	1	0	1.703631	2.505805	0.007933
9	1	0	1.703631	-2.505805	0.007933
10	7	0	-0.802829	-1.086347	-0.008201
11	7	0	-0.802829	1.086347	-0.008201
12	6	0	-1.245323	-2.467397	-0.014039

13	1	0	-0.600378	-3.037463	-0.681679
14	1	0	-1.193465	-2.884384	0.992662
15	1	0	-2.264130	-2.529157	-0.388543
16	6	0	-1.245322	2.467397	-0.014038
17	1	0	-1.193455	2.884386	0.992661
18	1	0	-0.600383	3.037461	-0.681686
19	1	0	-2.264133	2.529157	-0.388534
20	1	0	3.822079	-1.228017	0.013919
21	1	0	3.822079	1.228017	0.013918
22	6	0	-3.045833	0.000000	0.029321
23	1	0	-3.421901	0.880738	0.547699
24	1	0	-3.441513	0.000005	-0.990195
25	1	0	-3.421901	-0.880742	0.547692

BI⁺ (solvent = CH₃CN)



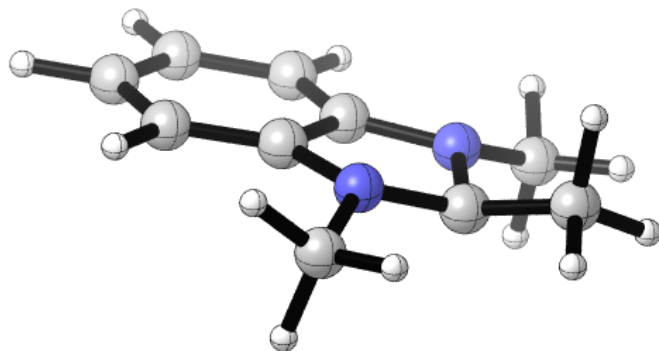
($E = -496.811756782$, $H = -496.577924$, $G = -496.628094$, NIMAG = 0, dipole moment = 5.2937 D)

CPCM(CH₃CN)

Center Number	Atomic Number	Atomic Type	Coordinates (Angstroms)		
			X	Y	Z
1	6	0	0.525206	-0.690769	-0.003543
2	6	0	0.525206	0.690769	-0.003543
3	6	0	1.702506	1.421887	0.002688
4	6	0	2.874718	0.700215	0.007781
5	6	0	2.874718	-0.700215	0.007781
6	6	0	1.702506	-1.421888	0.002688
7	6	0	-1.569977	0.000000	0.005190
8	1	0	1.703603	2.505858	0.008258
9	1	0	1.703603	-2.505858	0.008258
10	7	0	-0.802884	-1.086339	-0.008045
11	7	0	-0.802884	1.086339	-0.008045
12	6	0	-1.245270	-2.467398	-0.013416
13	1	0	-0.600413	-3.037502	-0.681122
14	1	0	-1.193117	-2.884271	0.993351

15	1	0	-2.264188	-2.529332	-0.387636
16	6	0	-1.245269	2.467399	-0.013415
17	1	0	-1.193107	2.884273	0.993349
18	1	0	-0.600418	3.037500	-0.681129
19	1	0	-2.264190	2.529332	-0.387627
20	1	0	3.822193	-1.228008	0.014349
21	1	0	3.822193	1.228008	0.014349
22	6	0	-3.045993	0.000000	0.027611
23	1	0	-3.422445	0.880733	0.545751
24	1	0	-3.440998	0.000005	-0.992193
25	1	0	-3.422446	-0.880737	0.545743

BI• (solvent = DMSO)



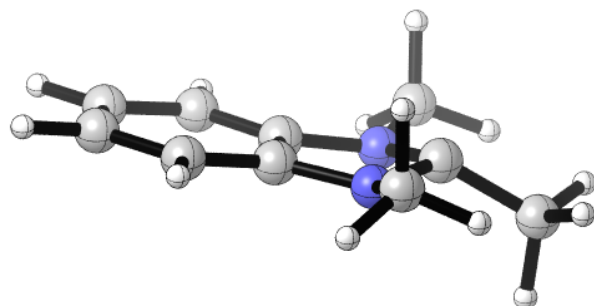
($E = -496.895549675$, $H = -496.665348$, $G = -496.715105$, NIMAG = 0, dipole moment = 1.9833 D)

CPCM(DMSO)

Center Number	Atomic Number	Atomic Type	Coordinates (Angstroms)		
			X	Y	Z
1	6	0	0.501363	0.699793	0.066495
2	6	0	0.501340	-0.699801	0.066361
3	6	0	1.679290	-1.411209	0.047762
4	6	0	2.875936	-0.690873	0.050264
5	6	0	2.875958	0.690793	0.050384
6	6	0	1.679335	1.411167	0.048022
7	6	0	-1.641811	0.000018	-0.162701
8	1	0	1.684060	-2.495850	0.029015
9	1	0	1.684137	2.495810	0.029370
10	7	0	-0.813576	1.116167	0.067349
11	7	0	-0.813608	-1.116135	0.067408
12	6	0	-1.188851	2.456619	-0.291693

13	1	0	-0.602618	3.171658	0.287789
14	1	0	-1.027833	2.649994	-1.360268
15	1	0	-2.240173	2.622624	-0.059675
16	6	0	-1.188971	-2.456588	-0.291530
17	1	0	-1.028002	-2.650029	-1.360099
18	1	0	-0.602764	-3.171633	0.287972
19	1	0	-2.240298	-2.622508	-0.059464
20	6	0	-3.034972	0.000033	0.363587
21	1	0	-3.052085	0.000201	1.464749
22	1	0	-3.586077	0.876116	0.017537
23	1	0	-3.586002	-0.876208	0.017809
24	1	0	3.818146	1.229496	0.040219
25	1	0	3.818107	-1.229604	0.040035

BI• (solvent = CH₃CN)



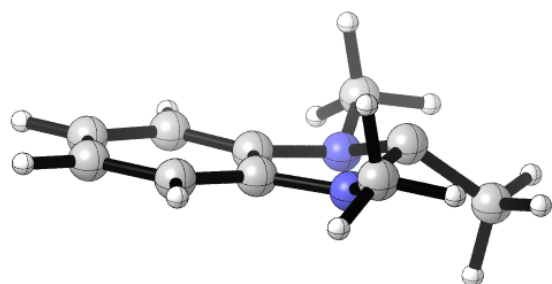
($E = -496.895500319$, $H = -496.665297$, $G = -496.715055$, NIMAG = 0, dipole moment = 1.9793 D)

CPCM(CH₃CN)

Center Number	Atomic Number	Atomic Type	Coordinates (Angstroms)		
			X	Y	Z
1	6	0	-0.501363	0.699793	-0.066495
2	6	0	-0.501340	-0.699801	-0.066361
3	6	0	-1.679290	-1.411209	-0.047762
4	6	0	-2.875936	-0.690873	-0.050264
5	6	0	-2.875958	0.690793	-0.050384
6	6	0	-1.679335	1.411167	-0.048022
7	6	0	1.641811	0.000018	0.162701
8	1	0	-1.684060	-2.495850	-0.029015
9	1	0	-1.684137	2.495810	-0.029370
10	7	0	0.813576	1.116167	-0.067349
11	7	0	0.813608	-1.116135	-0.067408

12	6	0	1.188851	2.456619	0.291693
13	1	0	0.602618	3.171658	-0.287789
14	1	0	1.027833	2.649994	1.360268
15	1	0	2.240173	2.622624	0.059675
16	6	0	1.188971	-2.456588	0.291530
17	1	0	1.028002	-2.650029	1.360099
18	1	0	0.602764	-3.171633	-0.287972
19	1	0	2.240298	-2.622508	0.059464
20	6	0	3.034972	0.000033	-0.363587
21	1	0	3.052085	0.000201	-1.464749
22	1	0	3.586077	0.876116	-0.017537
23	1	0	3.586002	-0.876208	-0.017809
24	1	0	-3.818146	1.229496	-0.040219
25	1	0	-3.818107	-1.229604	-0.040035

BI-



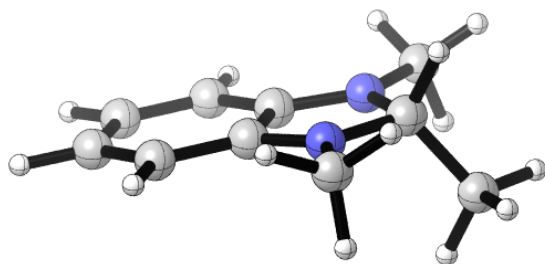
($E = -496.965225920$, $H = -496.737395$, $G = -496.785036$, NIMAG = 0, dipole moment = 4.5651 D)

CPCM(CH₃CN)

Center Number	Atomic Number	Atomic Type	Coordinates (Angstroms)		
			X	Y	Z
1	6	0	-0.466284	0.704178	-0.116064
2	6	0	-0.466284	-0.704177	-0.116065
3	6	0	-1.647844	-1.405326	-0.063295
4	6	0	-2.856466	-0.687320	-0.053100
5	6	0	-2.856466	0.687321	-0.053099
6	6	0	-1.647844	1.405327	-0.063294
7	6	0	1.688565	0.000000	0.320019
8	1	0	-1.654937	-2.490422	-0.037761
9	1	0	-1.654937	2.490422	-0.037759
10	7	0	0.841332	1.132414	-0.142596
11	7	0	0.841331	-1.132414	-0.142597
12	6	0	1.129397	2.431642	0.390469

13	1	0	0.576341	3.203142	-0.151671
14	1	0	0.872088	2.497769	1.461689
15	1	0	2.193362	2.647612	0.283217
16	6	0	1.129396	-2.431642	0.390470
17	1	0	0.872079	-2.497770	1.461688
18	1	0	0.576345	-3.203143	-0.151674
19	1	0	2.193362	-2.647609	0.283225
20	6	0	2.973724	0.000000	-0.473817
21	1	0	2.790316	-0.000001	-1.566128
22	1	0	3.585238	0.876409	-0.235366
23	1	0	3.585238	-0.876409	-0.235365
24	1	0	-3.796248	1.231055	-0.025545
25	1	0	-3.796249	-1.231054	-0.025546

BIH^{•+}



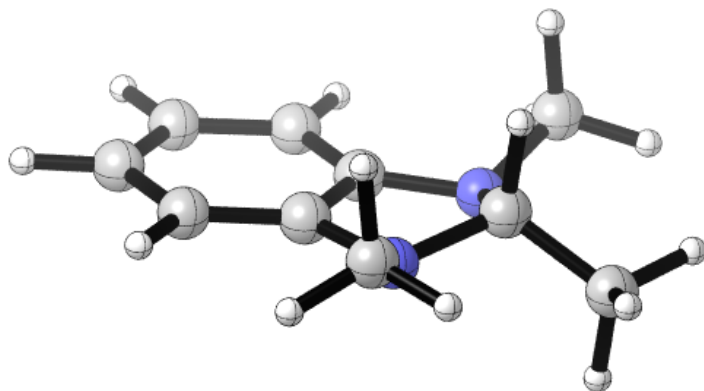
($E = -497.362359055$, $H = -497.117826$, $G = -497.167442$, NIMAG = 0, dipole moment = 2.8620 D)

CPCM(DMSO)

Center Number	Atomic Number	Atomic Type	Coordinates (Angstroms)		
			X	Y	Z
1	6	0	-0.488505	0.711100	0.080863
2	6	0	-0.488504	-0.711101	0.080863
3	6	0	-1.682552	-1.430075	-0.050128
4	6	0	-2.835696	-0.708481	-0.172678
5	6	0	-2.835697	0.708479	-0.172678
6	6	0	-1.682553	1.430074	-0.050127
7	6	0	1.680912	0.000001	0.285336
8	1	0	-1.687813	-2.513330	-0.058869
9	1	0	-1.687815	2.513328	-0.058868
10	7	0	0.770961	1.126100	0.223633
11	7	0	0.770962	-1.126100	0.223633
12	6	0	1.234746	2.491074	0.253773
13	1	0	0.464958	3.128607	0.687270

14	1	0	2.126078	2.553993	0.878447
15	1	0	1.472985	2.846024	-0.752250
16	6	0	1.234750	-2.491072	0.253774
17	1	0	2.126069	-2.553994	0.878466
18	1	0	0.464955	-3.128610	0.687251
19	1	0	1.473011	-2.846016	-0.752247
20	6	0	2.692296	0.000001	-0.841465
21	1	0	2.185020	0.000000	-1.808547
22	1	0	3.331604	0.881737	-0.769920
23	1	0	3.331606	-0.881733	-0.769919
24	1	0	-3.781245	1.229097	-0.277002
25	1	0	-3.781244	-1.229100	-0.277002
26	1	0	2.193187	0.000001	1.257139

BIH



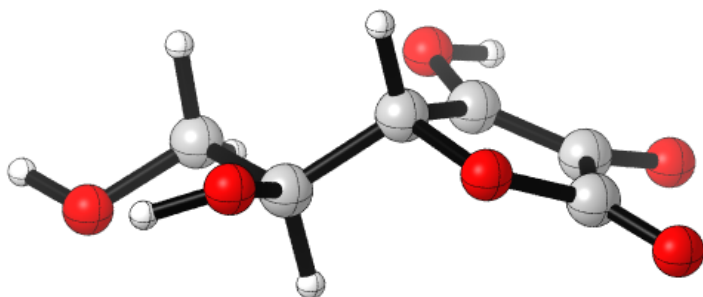
($E = -497.534366894$, $H = -497.291258$, $G = -497.339136$, NIMAG = 0, dipole moment = 3.0771 D)

CPCM(DMSO)

Center Number	Atomic Number	Atomic Type	Coordinates (Angstroms)		
			X	Y	Z
1	6	0	-0.511550	0.698855	-0.122662
2	6	0	-0.511550	-0.698855	-0.122662
3	6	0	-1.686902	-1.405758	-0.069499
4	6	0	-2.887877	-0.689134	-0.029892
5	6	0	-2.887877	0.689133	-0.029892
6	6	0	-1.686903	1.405757	-0.069499
7	6	0	1.635899	0.000000	0.189531
8	1	0	-1.692371	-2.490607	-0.054819
9	1	0	-1.692372	2.490606	-0.054820
10	7	0	0.809389	1.137847	-0.196800

11	7	0	0.809389	-1.137846	-0.196800
12	6	0	1.147257	2.412036	0.383916
13	1	0	0.537055	3.197899	-0.063336
14	1	0	0.990993	2.422085	1.473370
15	1	0	2.191336	2.650777	0.178106
16	6	0	1.147257	-2.412035	0.383915
17	1	0	0.990993	-2.422086	1.473369
18	1	0	0.537057	-3.197899	-0.063337
19	1	0	2.191337	-2.650776	0.178106
20	6	0	2.991514	0.000000	-0.468961
21	1	0	2.877736	0.000000	-1.555331
22	1	0	3.567011	0.879371	-0.171260
23	1	0	3.567011	-0.879371	-0.171261
24	1	0	-3.827462	1.230889	0.012677
25	1	0	-3.827462	-1.230890	0.012677
26	1	0	1.762074	0.000000	1.295273

HA⁻ (solvent = DMSO)



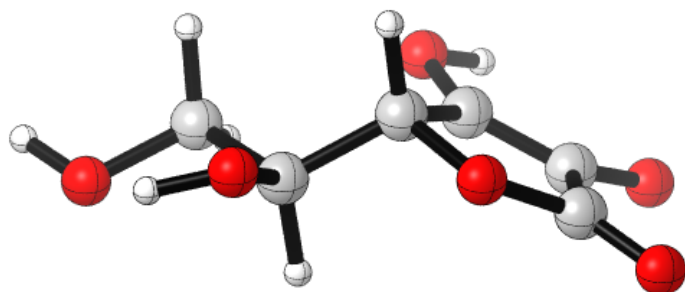
($E = -682.823596534$, $H = -682.670457$, $G = -682.720429$, NIMAG = 0, dipole moment = 15.9818 D)

CPCM(DMSO)

Center Number	Atomic Number	Atomic Type	Coordinates (Angstroms)		
			X	Y	Z
1	6	0	0.687682	0.914282	0.296483
2	6	0	1.911895	0.572429	-0.139053
3	6	0	1.920542	-0.906619	-0.087656
4	6	0	-0.145538	-0.263785	0.639815
5	1	0	-0.404996	-0.306870	1.703773
6	8	0	2.805343	-1.682184	-0.377069
7	8	0	0.732976	-1.361133	0.370476
8	8	0	2.901969	1.314478	-0.501680

9	8	0	0.229214	2.180186	0.475984
10	1	0	0.956332	2.780700	0.232376
11	6	0	-1.404446	-0.457750	-0.173867
12	1	0	-1.118321	-0.584540	-1.226691
13	6	0	-2.359974	0.708016	-0.056051
14	1	0	-1.944506	1.598340	-0.532408
15	1	0	-2.557959	0.925159	0.999952
16	8	0	-3.549381	0.286996	-0.702487
17	1	0	-4.275598	0.892316	-0.497224
18	8	0	-2.039895	-1.627301	0.293421
19	1	0	-2.957729	-1.592875	-0.026966

HA⁻ (solvent = CH₃CN)



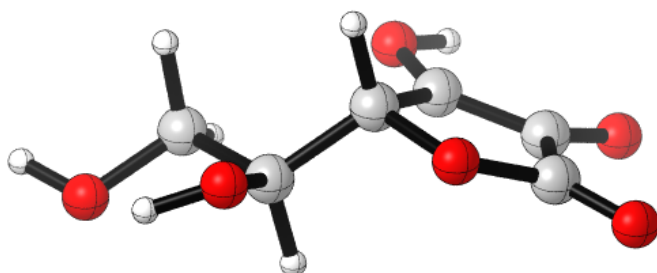
($E = -682.822829841$, $H = -682.669687$, $G = -682.719664$, NIMAG = 0, dipole moment = 15.9306 D)

CPCM(CH₃CN)

Center Number	Atomic Number	Atomic Type	Coordinates (Angstroms)		
			X	Y	Z
1	6	0	0.687404	0.913703	0.296572
2	6	0	1.911765	0.572659	-0.139316
3	6	0	1.920934	-0.906661	-0.088417
4	6	0	-0.145316	-0.264715	0.639754
5	1	0	-0.404227	-0.308232	1.703888
6	8	0	2.805461	-1.681946	-0.378841
7	8	0	0.733270	-1.361695	0.369513
8	8	0	2.901087	1.315483	-0.501422
9	8	0	0.229181	2.179737	0.477780
10	1	0	0.956948	2.779723	0.234772
11	6	0	-1.404676	-0.458832	-0.173160
12	1	0	-1.118802	-0.587587	-1.225815
13	6	0	-2.358721	0.708304	-0.057429
14	1	0	-1.941935	1.597268	-0.535188

15	1	0	-2.556558	0.927450	0.998194
16	8	0	-3.548862	0.288110	-0.703292
17	1	0	-4.274531	0.893745	-0.497296
18	8	0	-2.041459	-1.626741	0.296172
19	1	0	-2.958674	-1.592693	-0.025862

HA• (solvent = DMSO)

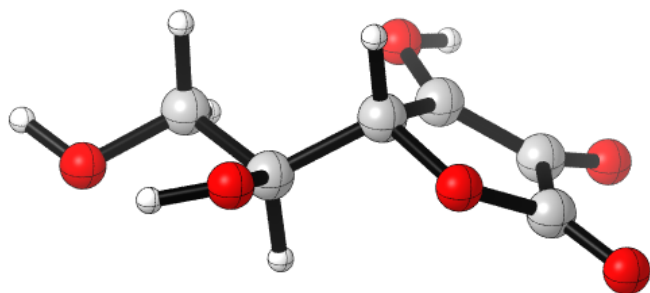


($E = -682.657384744$, $H = -682.503545$, $G = -682.554186$, NIMAG = 0, dipole moment = 11.1883 D)

CPCM(DMSO)

Center Number	Atomic Number	Atomic Type	Coordinates (Angstroms)		
			X	Y	Z
1	6	0	0.664901	0.957579	0.286749
2	6	0	1.942245	0.580334	-0.140207
3	6	0	1.947565	-0.923043	-0.073793
4	6	0	-0.148757	-0.239314	0.622794
5	1	0	-0.397219	-0.263644	1.688564
6	8	0	2.839125	-1.674583	-0.345386
7	8	0	0.748291	-1.329507	0.362958
8	8	0	2.876738	1.307337	-0.484785
9	8	0	0.217071	2.172439	0.423289
10	1	0	0.903789	2.825675	0.176158
11	6	0	-1.409920	-0.440900	-0.191115
12	1	0	-1.136408	-0.531925	-1.250475
13	6	0	-2.402128	0.691973	-0.027534
14	1	0	-2.034058	1.607660	-0.496385
15	1	0	-2.587670	0.879425	1.036021
16	8	0	-3.579651	0.234440	-0.662560
17	1	0	-4.332579	0.792296	-0.420808
18	8	0	-1.985159	-1.639224	0.262196
19	1	0	-2.910617	-1.636481	-0.040143

HA• (solvent = CH₃CN)

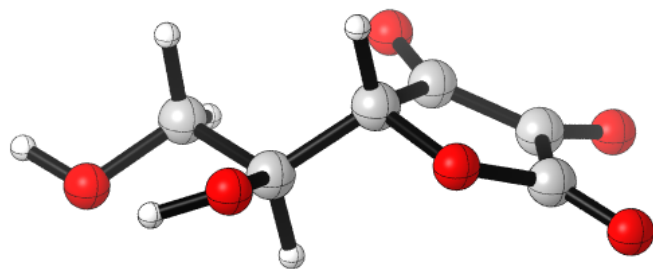


($E = -682.657151823$, $H = -682.503309$, $G = -682.553942$, NIMAG = 0, dipole moment = 11.1670 D)

CPCM(CH₃CN)

Center Number	Atomic Number	Atomic Type	Coordinates (Angstroms)		
			X	Y	Z
1	6	0	0.664901	0.957579	0.286749
2	6	0	1.942245	0.580334	-0.140207
3	6	0	1.947565	-0.923043	-0.073793
4	6	0	-0.148757	-0.239314	0.622794
5	1	0	-0.397219	-0.263644	1.688564
6	8	0	2.839125	-1.674583	-0.345386
7	8	0	0.748291	-1.329507	0.362958
8	8	0	2.876738	1.307337	-0.484785
9	8	0	0.217071	2.172439	0.423289
10	1	0	0.903789	2.825675	0.176158
11	6	0	-1.409920	-0.440900	-0.191115
12	1	0	-1.136408	-0.531925	-1.250475
13	6	0	-2.402128	0.691973	-0.027534
14	1	0	-2.034058	1.607660	-0.496385
15	1	0	-2.587670	0.879425	1.036021
16	8	0	-3.579651	0.234440	-0.662560
17	1	0	-4.332579	0.792296	-0.420808
18	8	0	-1.985159	-1.639224	0.262196
19	1	0	-2.910617	-1.636481	-0.040143

A• (solvent = DMSO)

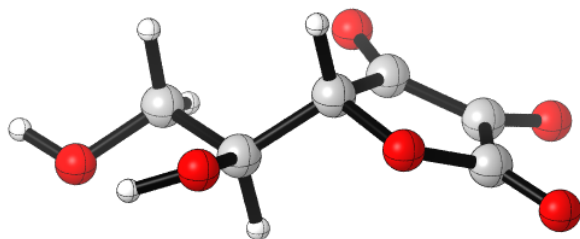


($E = -682.235035359$, $H = -682.094173$, $G = -682.144165$, NIMAG = 0, dipole moment = 13.8511 D)

CPCM(DMSO)

Center Number	Atomic Number	Atomic Type	Coordinates (Angstroms)		
			X	Y	Z
1	6	0	0.649249	1.041391	0.304603
2	6	0	1.941352	0.626299	-0.136111
3	6	0	1.955273	-0.845592	-0.067324
4	6	0	-0.136186	-0.210607	0.633056
5	1	0	-0.388774	-0.239406	1.697226
6	8	0	2.849469	-1.615132	-0.338534
7	8	0	0.763399	-1.294257	0.374118
8	8	0	2.914970	1.331045	-0.503488
9	8	0	0.203491	2.186333	0.433860
10	6	0	-1.388716	-0.416249	-0.184680
11	1	0	-1.111316	-0.479614	-1.245907
12	6	0	-2.399163	0.694659	-0.003846
13	1	0	-2.030942	1.628701	-0.431244
14	1	0	-2.604027	0.844237	1.062153
15	8	0	-3.566795	0.245886	-0.671730
16	1	0	-4.322888	0.800798	-0.434399
17	8	0	-1.963311	-1.636811	0.226965
18	1	0	-2.882692	-1.630628	-0.091543

A⁺ (solvent = CH₃CN)

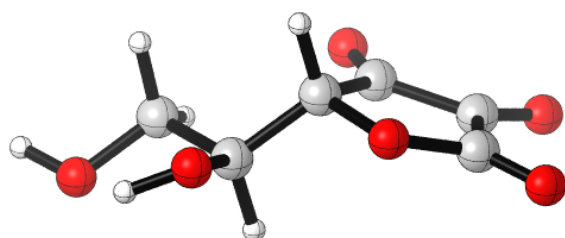


($E = -682.234321411$, $H = -682.093458$, $G = -682.143441$, NIMAG = 0, dipole moment = 13.8102 D)

CPCM(CH₃CN)

Center Number	Atomic Number	Atomic Type	Coordinates (Angstroms)		
			X	Y	Z
1	6	0	0.649047	1.041140	0.305067
2	6	0	1.941131	0.626674	-0.136140
3	6	0	1.955467	-0.845405	-0.067780
4	6	0	-0.135966	-0.211229	0.633197
5	1	0	-0.388611	-0.240335	1.697352
6	8	0	2.849638	-1.614685	-0.339458
7	8	0	0.763675	-1.294570	0.373928
8	8	0	2.914487	1.331645	-0.503569
9	8	0	0.202660	2.185860	0.435303
10	6	0	-1.388638	-0.416862	-0.184395
11	1	0	-1.111244	-0.481489	-1.245536
12	6	0	-2.398416	0.694763	-0.004783
13	1	0	-2.029736	1.628061	-0.433357
14	1	0	-2.603040	0.845792	1.061085
15	8	0	-3.566477	0.245663	-0.671825
16	1	0	-4.320235	0.806919	-0.442166
17	8	0	-1.963980	-1.636696	0.228468
18	1	0	-2.882916	-1.631152	-0.091149

A (solvent = DMSO)



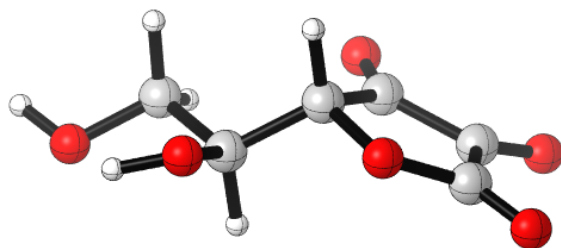
($E = -682.060306102$, $H = -681.918073$, $G = -681.968133$, NIMAG = 0, dipole moment = 7.5774 D)

CPCM(DMSO)

Center Number	Atomic Number	Atomic Type	Coordinates (Angstroms)		
			X	Y	Z

1	6	0	0.609361	1.076020	0.282279
2	6	0	2.003267	0.635004	-0.133084
3	6	0	1.981406	-0.883432	-0.054040
4	6	0	-0.152920	-0.184278	0.605372
5	1	0	-0.384417	-0.216805	1.674011
6	8	0	2.877903	-1.632867	-0.299152
7	8	0	0.768538	-1.261811	0.337492
8	8	0	2.923228	1.321187	-0.451563
9	8	0	0.226533	2.206996	0.343771
10	6	0	-1.414498	-0.402670	-0.200156
11	1	0	-1.162729	-0.430844	-1.268470
12	6	0	-2.447162	0.679706	0.037665
13	1	0	-2.116367	1.637663	-0.370084
14	1	0	-2.634394	0.789928	1.111520
15	8	0	-3.607762	0.216015	-0.623066
16	1	0	-4.380095	0.731620	-0.350494
17	8	0	-1.931164	-1.644745	0.201762
18	1	0	-2.856926	-1.671862	-0.098651

A (solvent = CH₃CN)



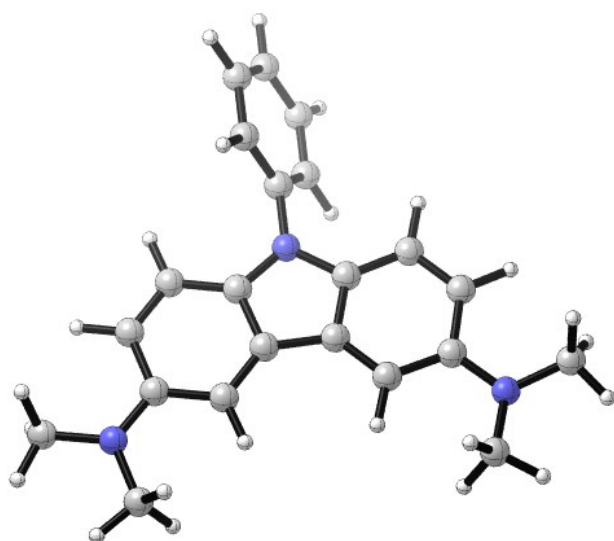
($E = -682.060115853$, $H = -681.917887$, $G = -681.967967$, NIMAG = 0, dipole moment = 7.5670 D)

CPCM(CH₃CN)

Center Number	Atomic Number	Atomic Type	Coordinates (Angstroms)		
			X	Y	Z
1	6	0	0.609027	1.075761	0.282338
2	6	0	2.003242	0.635205	-0.132553
3	6	0	1.981565	-0.883332	-0.054761
4	6	0	-0.152855	-0.184952	0.605356
5	1	0	-0.384216	-0.217756	1.674011
6	8	0	2.878133	-1.632299	-0.300630
7	8	0	0.768848	-1.262187	0.337148
8	8	0	2.923161	1.321745	-0.450355

9	8	0	0.225628	2.206590	0.344234
10	6	0	-1.414522	-0.403501	-0.199841
11	1	0	-1.162587	-0.433295	-1.268096
12	6	0	-2.446378	0.680076	0.036349
13	1	0	-2.114921	1.637100	-0.373069
14	1	0	-2.633318	0.792255	1.110076
15	8	0	-3.607416	0.216264	-0.623496
16	1	0	-4.379086	0.733959	-0.353110
17	8	0	-1.931960	-1.644586	0.203852
18	1	0	-2.857492	-1.672016	-0.097160

5^{•+}



($E = -1013.26714965$, $H = -1012.827998$, $G = -1012.903539$, NIMAG = 0, dipole moment = 10.3949 D)

CPCM(DMSO)

Center Number	Atomic Number	Atomic Type	Coordinates (Angstroms)		
			X	Y	Z
1	6	0	-2.883305	-1.749540	-0.044370
2	6	0	-1.476350	-1.963847	-0.042953
3	6	0	-0.640010	-0.892224	-0.034609
4	6	0	-1.158730	0.429296	-0.024770
5	6	0	-2.545718	0.663073	-0.039709
6	6	0	-3.380081	-0.404965	-0.047796
7	1	0	-1.071887	-2.967371	-0.050636
8	1	0	-2.940500	1.672433	-0.047488
9	1	0	-4.446845	-0.230519	-0.060979

10	6	0	0.806405	-0.760736	-0.040850
11	6	0	1.071324	0.603403	-0.034334
12	6	0	1.831516	-1.686449	-0.036323
13	6	0	2.368287	1.073251	-0.007934
14	6	0	3.157047	-1.240037	-0.034414
15	1	0	1.598303	-2.743158	-0.031676
16	6	0	3.392592	0.150817	-0.005841
17	1	0	2.589696	2.134796	0.015775
18	1	0	4.408008	0.522566	0.018181
19	7	0	-0.143434	1.311063	-0.023817
20	7	0	-3.728177	-2.783295	-0.046585
21	7	0	4.206767	-2.129270	-0.061437
22	6	0	-5.167429	-2.574112	-0.045721
23	1	0	-5.665303	-3.539528	-0.034582
24	1	0	-5.475350	-2.015998	0.840701
25	1	0	-5.479348	-2.033867	-0.942020
26	6	0	-3.231534	-4.149959	-0.050238
27	1	0	-4.075492	-4.833642	-0.055727
28	1	0	-2.627828	-4.338424	-0.940363
29	1	0	-2.633297	-4.345016	0.842244
30	6	0	3.934644	-3.532054	0.134817
31	1	0	4.868337	-4.088974	0.072007
32	1	0	3.475252	-3.738119	1.111798
33	1	0	3.270909	-3.918258	-0.643527
34	6	0	5.541466	-1.653287	0.212962
35	1	0	5.626300	-1.191990	1.206462
36	1	0	6.233671	-2.492590	0.166964
37	1	0	5.865222	-0.922938	-0.533311
38	6	0	-0.263043	2.726727	-0.001183
39	6	0	0.235883	3.468008	-1.058078
40	6	0	-0.870215	3.344813	1.077572
41	6	0	0.123874	4.846019	-1.031577
42	1	0	0.702624	2.964011	-1.898290
43	6	0	-0.988628	4.723104	1.090957
44	1	0	-1.240735	2.747636	1.904718
45	6	0	-0.490377	5.473704	0.039665
46	1	0	0.513138	5.432100	-1.857507
47	1	0	-1.466507	5.212344	1.933237
48	1	0	-0.580171	6.554980	0.055240

Table 15.1 Calculation of the excitation energies by the TD-DFT method (B3LYP/6-31G++G(d,p)/CPCM (dms0))

BI*	5**
-----	-----

wavelength /nm	oscillator strength	wavelength /nm	oscillator strength
568	0.0734	1390	0.1349
508	0.0124	653	0.0784
477	0.0147	524	0.166
440	0.0133	436	0.0016
439	0.0130	420	0.0056
406	0.0957	418	0.0163
370	0.0071	394	0.0132

Calculation of the enthalpy difference for HAT process

(1)



$$\begin{aligned} & H(\text{BIH}) + H(\text{A}^{\bullet-}) - H(\text{BI}^\bullet) - H(\text{HA}^-) \\ &= (-497.291258) + (-682.094173) - (-496.665348) - (-682.670457) \\ &= -0.049626 \text{ (hartree)} \\ &= -31.1 \text{ kcal mol}^{-1} \end{aligned}$$

(2)



$$\begin{aligned} & H(\text{BIH}) + H(\text{A}) - H(\text{BI}^\bullet) - H(\text{HA}^\bullet) \\ &= (-497.291258) + (-681.918073) - (-496.665348) - (-682.503545) \\ &= -0.040438 \text{ (hartree)} \\ &= -25.4 \text{ kcal mol}^{-1} \end{aligned}$$

(3)



$$\begin{aligned} & H(\text{BIH}^{\bullet+}) + H(\text{A}^{\bullet-}) - H(\text{BI}^{++}) - H(\text{HA}^-) \\ &= (-497.117826) + (-682.094173) - (-496.578411) - (-682.670457) \\ &= 0.036869 \text{ (hartree)} \\ &= 23.1 \text{ kcal mol}^{-1} \end{aligned}$$

Estimation of the redox potential of the BI[•]/BI⁻ couple

The redox potential can be estimated from the calculated free energies with the combination of the known redox potential obtained experimentally, as follows.^{18,19}

$$\begin{aligned} & E^\circ(\text{ox1/red1}) - E^\circ(\text{ox2/red2}) \\ &= \{[\Delta G(\text{ox1}) - \Delta G(\text{red1})] - [\Delta G(\text{ox2}) - \Delta G(\text{red2})]\} / n_e F \end{aligned}$$

where E° = standard redox potential relative to the SCE, ΔG = Gibbs free energy

difference in kcal mol⁻¹ calculated using the (U)LC-BLYP DFT method with 6-31++G(d) basis set and conductor-like polarizable continuum solvation model (CPCM, CH₃CN), $n_e = 1$, and $F = 23.061$ kcal mol⁻¹ V⁻¹.

$E^\circ(\mathbf{BI}^+/\mathbf{BI}^\bullet) = -1.96$ V vs SCE (experimentally obtained from the CV)

$$\begin{aligned} E^\circ(\mathbf{BI}^+/\mathbf{BI}^\bullet) - E^\circ(\mathbf{BI}^\bullet/\mathbf{BI}^-) &= \{[\Delta G(\mathbf{BI}^+) - \Delta G(\mathbf{BI}^\bullet)] - [\Delta G(\mathbf{BI}^\bullet) - \Delta G(\mathbf{BI}^-)]\} / n_e F \\ &= \{[(-311639.1) - (-311693.7)] - [(-311693.7) - (-311737.6)]\} / n_e F \\ &= 10.7 / n_e F \\ &= 0.464 \text{ V} \end{aligned}$$

$$E^\circ(\mathbf{BI}^\bullet/\mathbf{BI}^-) = -1.96 - 0.464 = -2.42 \text{ V vs SCE}$$

16. Reference

1. Ritchie, H.; Roser, M.; Rosado, P. "Energy". *Our world in data*. **2020**.
2. Armaroli, N.; Balzani, V. *Angew. Chem. Int. Ed.* **2007**, *46*, 52-66.
3. Pan, H.; Heagy, M. D. *Nanomaterials*, **2020**, *10*, 2422-2445.
4. Li, X.; Yu, J.; Jaroniec, M.; Chen, X. *Chem. Rev.* **2019**, *119*, 3962-4179.
5. Dogutan, D. K.; Nocera, D. G. *Acc. Chem. Res.* **2019**, *52*, 3143-3148.
6. Farquhar, G. D.; Von Caemmerer, S.; Berry, J. A. *Plant Physiol.* **2001**, *125*, 42-45.
7. Berardi, S.; Drouet, S.; Francàs, L.; Gimbert-Suriñach, C.; Guttentag, M.; Richmond, C.; Stoll, T.; Llobet, A. *Chem. Soc. Rev.*, **2014**, *43*, 7501-7519.
8. Ye, S.; Ding, C.; Liu, M.; Wang, A.; Huang, Q.; Li, C. *Adv. Mater.* **2019**, *31*, 1902069.
9. Habisreutinger, S. N.; Schmidt-Mende, L.; Stolarczyk, J. K. *Angew. Chem. Int. Ed.* **2013**, *52*, 7372-7408.
10. Friedlingstein, P.; O'Sullivan, M.; Jones, M. W. et al. *Earth Syst. Sci. Data*, **2020**, *12*, 3269-3340.
11. Lin, J.; Tian, W.; Zhang, H.; Duan, X.; Sun, H.; Wang, S. *Energy Fuels*, **2021**, *35*, 7-24.
12. Hietala, J.; Vuori, A.; Johnsson, P.; Pollari, I.; Reutemann, W.; Kieczka, K. *Ullmann's encycl. ind. chem.* **2016**, *1*, 1-22.
13. Lee, S. E.; Nasirian, A.; Kim, Y. E.; Fard, P. T.; Kim, Y.; Jeong, B.; Kim, S. J.; Baeg, J. O.; Kim, J. *J. Am. Chem. Soc.* **2020**, *142*, 19142-19149.
14. Sato, S.; Morikawa, T.; Saeki, S.; Kajino, T.; Motohiro, T. *Angew. Chem. Int. Ed.* **2010**, *49*, 5101-5105.
15. Cauwenbergh, R.; Das, S. *Green Chem.* **2021**, *23*, 2553-2574.
16. Tamaki, Y.; Koike, K.; Ishitani, O. *Chem. Sci.* **2015**, *6*, 7213-7221.
17. Bahuguna, A.; Sasson, Y. *ChemSusChem.* **2021**, *14*, 1258-1283.
18. Klán, P.; Wirz, J. *Photochemistry of Organic Compounds: From Concepts to Practice*, **2009**. <https://doi.org/10.1002/9781444300017>.
19. Gilbert, J. C.; Martin, S. F. *Experimental organic chemistry: a miniscale & microscale approach*. Cengage Learning, **2015**.
20. Bach, R. D.; Schlegel, H. B. *J. Phys. Chem. A.* **2020**, *124*, 4742-4751.
21. Cano-Yelo, H.; Deronzier, A. *J. Photochem.* **1987**, *37*, 315-321.
22. Prier, C. K.; Rankic, D. A.; MacMillan, D. W. *Chem. Rev.* **2013**, *113*, 5322-5363.
23. Stephenson, C. R.; Yoon, T. P.; MacMillan, D. W. *Visible light photocatalysis in organic chemistry*, **2018**.
24. Cauwenbergh, R.; Das, S. *Synlett*, **2022**, *33*, 129-149.
25. Shaw, M. H.; Twilton, J.; MacMillan, D. W. *J. Org. Chem.* **2016**, *81*, 6898-6926.
26. Tucker, J. W.; Stephenson, C. R. *J. Org. Chem.* **2012**, *77*, 1617-1622.
27. Szczepaniak, G.; Urbaniak, K.; Wierzbička, C. et al. *ChemSusChem.* **2015**, *8*, 4139-4148.
28. French, J. M.; Caras, C. A.; Diver, S. T. *Org. Lett.* **2013**, *15*, 5416-5419.
29. Ding, M.; Jiang, X.; Zhang, L.; Cheng, Z.; Zhu, X. *Macromol. Rapid Commun.* **2015**, *36*, 1702-1721.
30. Nicewicz, D. A.; Nguyen, T. M. *ACS Catal.* **2014**, *4*, 355-360.
31. Ravelli, D.; Fagnoni, M.; Albini, A. *Chem. Soc. Rev.* **2013**, *42*, 97-113.

32. Marin, M. L.; Santos-Juanes, L.; Arques, A.; Amat, A. M.; Miranda, M. A. *Chem. Rev.*, **2012**, *112*, 1710-1750.
33. Skubi, K. L.; Blum, T. R.; Yoon, T. P. *Chem. Rev.* **2016**, *116*, 10035-10074.
34. Fagnoni, M.; Dondi, D.; Ravelli, D.; Albini, A. *Chem. Rev.* **2007**, *107*, 2725-2756
35. Forster, T. *Discuss. Faraday Soc.* **1959**, *27*, 7-17.
36. Sahoo, H. J. *Photochem. Photobiol. C Photochem. Rev.* **2011**, *12*, 20-30.
37. Dexter, D. L. *J. Chem. Phys.* **1953**, *21*, 836-850.
38. Scandola, F.; Indelli, M. T.; Chiorboli, C.; Bignozzi, C. A. *Top. Curr. Chem.* **1990**, *158*, 73-149.
39. Brunschwig, B.; Sutin, N. *J. Am. Chem. Soc.* **1978**, *100*, 7568-7577.
40. Demas, J. N.; Harris, E. W.; McBride, R. P. *J. Am. Chem. Soc.* **1977**, *99*, 3547-3551.
41. Ra, E. C.; Kim, K. Y.; Kim, E. H.; Lee, H.; An, K.; Lee, J. S. *ACS Catal.* **2020**, *10*, 11318-11345.
42. MacDowell, N.; Florin, N.; Buchard, A.; Hallett, J.; Galindo, A.; Jackson, G.; Adjiman, C. S.; Williams, C. K.; Shah, N.; Fennell, P. *Energy Environ. Sci.* **2010**, *3*, 1645-1669.
43. Boot-Handford, M. E.; Abanades, J. C.; Anthony, E. J. et al. *Energy Environ. Sci.* **2014**, *7*, 130-189.
44. Haszeldine, R. S. *Science*, **2009**, *325*, 1647-1652.
45. Xiaoding, X.; Moulijn, J. A. *Energy Fuels*, **1996**, *10*, 305-325.
46. Tamura, M.; Honda, M.; Nakagawa, Y.; Tomishige, K. *J. Chem. Technol. Biotechnol.* **2014**, *89*, 19-33.
47. Ganesh, I. *Mater. Sci. Forum*, **2013**, *764*, 1-82.
48. Yuan, G.; Qi, C.; Wu, W.; Jiang, H. *Curr. Opin. Green Sustain. Chem.* **2017**, *3*, 22-27.
49. Ochedi, F. O.; Liu, D.; Yu, J.; Hussain, A.; Liu, Y. *Environ. Chem. Lett.* **2021**, *19*, 941-967.
50. Birdja, Y. Y.; Pérez-Gallent, E.; Figueiredo, M. C.; Göttle, A. J.; Calle-Vallejo, F.; Koper, M. T. *Nat. Energy*, **2019**, *4*, 732-745.
51. Shen, J.; Kortlever, R.; Kas, R. et al. *Nat. Commun.* **2015**, *6*, 1-8.
52. Shen, J.; Kolb, M. J.; Göttle, A. J.; Koper, M. T. M. *J. Phys. Chem. C.* **2016**, *120*, 15714-15721.
53. Rosen, B. A.; Hod, I. *Adv. Mater.* **2018**, *30*, 1706238.
54. Francke, R.; Schille, B.; Roemelt, M. *Chem. Rev.* **2018**, *118*, 4631-4701.
55. Feng, D. M.; Zhu, Y. P.; Chen, P.; Ma, T. Y. *Catalysts*, **2017**, *7*, 373-390.
56. Elgrishi, N.; Chambers, M. B.; Wang, X.; Fontecave, M. *Chem. Soc. Rev.* **2017**, *46*, 761-796.
57. Zhang, F.; Zhang, H.; Liu, Z. *Curr. Opin. Green Sustain. Chem.* **2019**, *16*, 77-84.
58. Wang, M.; Chen, L.; Lau, T. C.; Robert, M. *Angew. Chem. Int.* **2018**, *57*, 7769-7773.
59. Jones, J. P.; Prakash, G. S.; Olah, G. A. *Isr. J. Chem.* **2014**, *54*, 1451-1466.
60. Zhang, L.; Zhao, Z. J.; Gong, J. *Angew. Chem. Int. Ed.* **2017**, *56*, 11326-11353.
61. Duan, X.; Xu, J.; Wei, Z.; Ma, J.; Guo, S.; Wang, S.; Liu, H.; Dou, S. *Adv. Mater.* **2017**, *29*, 1701784.

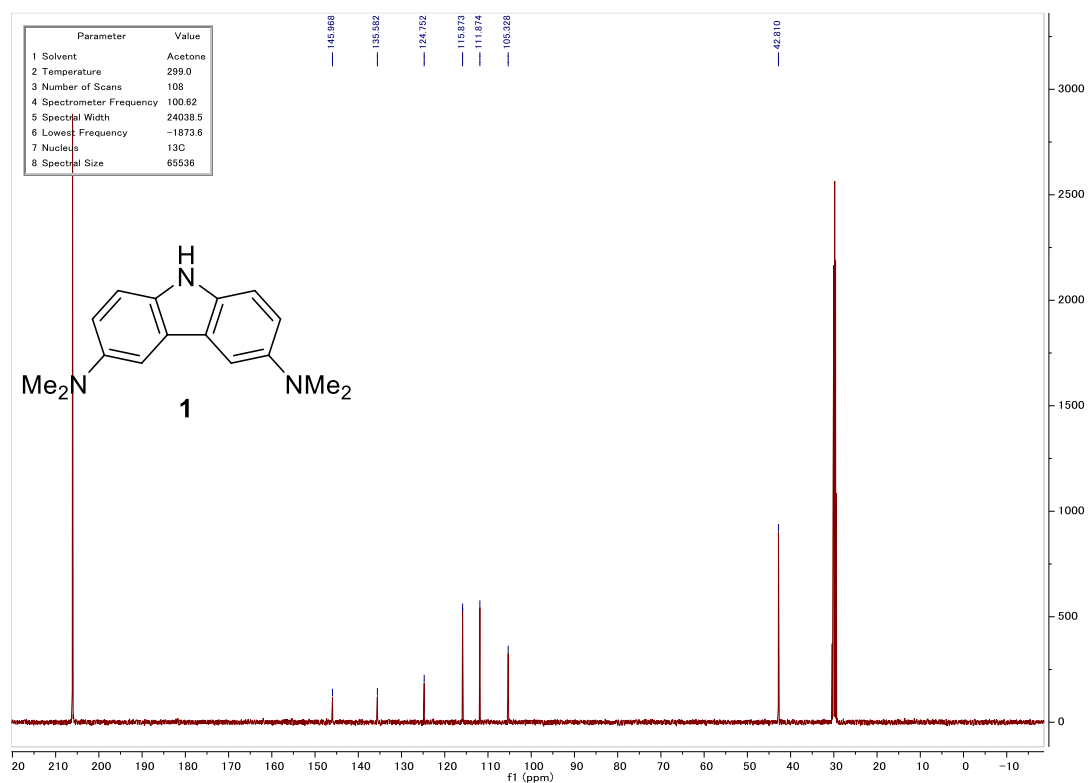
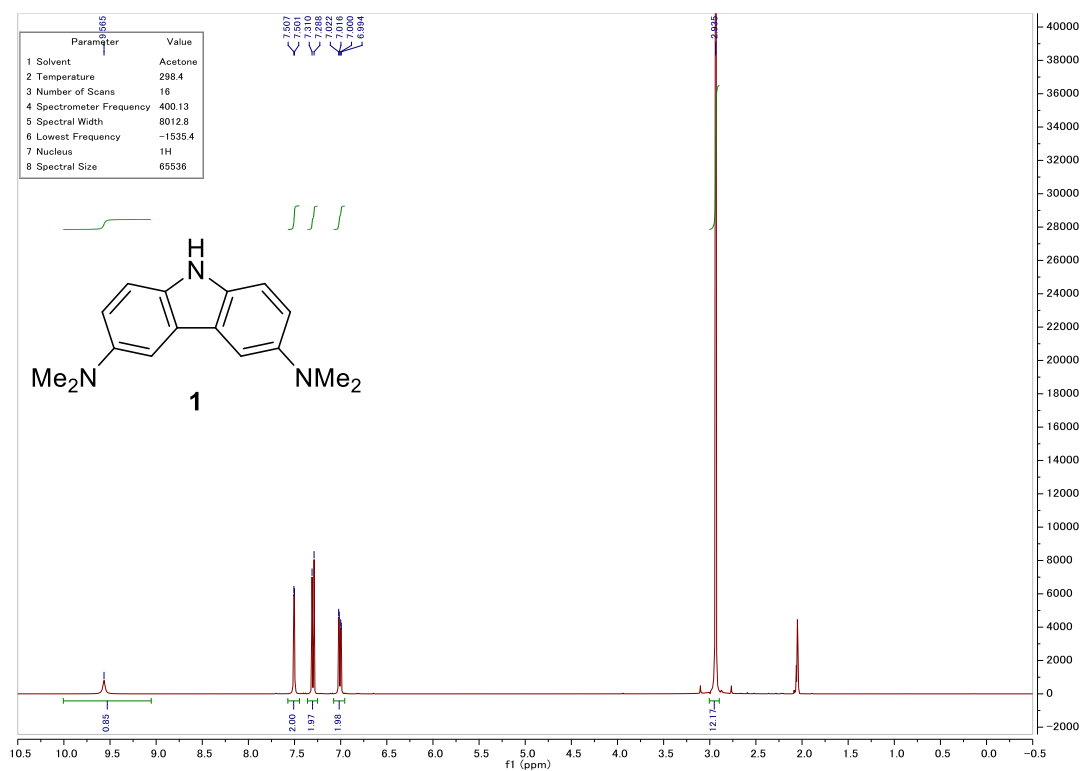
62. Li, Q.; Zhu, W.; Fu, J.; Zhang, H.; Wu, G.; Sun, S. *Nano Energy*, **2016**, *24*, 1-9.
63. Hu, X. M.; Hval, H. H.; Bjerglund, E. T. et al. *ACS Catal.* **2018**, *8*, 6255-6264.
64. Sun, X.; Lu, L.; Zhu, Q.; Wu, C.; Yang, D.; Chen, C.; Han, B. *Angew. Chem. Int. Ed.* **2018**, *57*, 2427-2431.
65. Jiao, Y.; Zheng, Y.; Chen, P.; Jaroniec, M.; Qiao, S. Z. *J. Am. Chem. Soc.* **2017**, *139*, 18093-18100.
66. Ju, W.; Bagger, A.; Hao, G. P.; Varela, A. S.; Sinev, I.; Bon, V.; Cuenya, B. R.; Kaskel, S.; Rossmeisl, J.; Strasser, P. *Nat. Commun.* **2017**, *8*, 1-9.
67. Ding, C.; Feng, C.; Mei, Y.; Liu, F.; Wang, H.; Dupuis, M.; Li, C. *Appl. Catal. B.* **2020**, *268*, 118391.
68. Maina, J. W.; Pozo-Gonzalo, C.; Kong, L.; Schütz, J.; Hill, M.; Dumée, L. F. *Mater. Horiz.* **2017**, *4*, 345-361.
69. Gong, Y. N.; Jiao, L.; Qian, Y.; Pan, C. Y. et al. *Angew. Chem. Int. Ed.* **2020**, *59*, 2705-2709.
70. Shao, P.; Yi, L.; Chen, S.; Zhou, T.; Zhang, J. *J. Energy Chem.* **2020**, *40*, 156-170.
71. Liu, J.; Wöll, C. *Chem. Soc. Rev.* **2017**, *46*, 5730-5770.
72. Kumar, R. S.; Kumar, S. S.; Kulandainathan, M. A. *Electrochem. commun.* **2012**, *25*, 70-73.
73. Schneider, J.; Jia, H.; Muckerman, J. T.; Fujita, E. *Chem. Soc. Rev.* **2012**, *41*, 2036-2051.
74. Shen, H.; Peppel, T.; Strunk, J.; Sun, Z. *Sol. RRL.* **2020**, *4*, 1900546.
75. Li, K.; Peng, B.; Peng, T. *ACS Catal.* **2016**, *6*, 7485-7527.
76. Hawecker, J.; Lehn, J. M.; Ziessel, R. *J. Chem. Soc. Chem. Commun.* **1983**, *9*, 536-538.
77. Liao, W. M.; Zhang, J. H.; Hou, Y. J.; Wang, H. P.; Pan, M. *Inorg. Chem. Commun.* **2016**, *73*, 80-89.
78. Kamada, K.; Jung, J.; Wakabayashi, T.; Sekizawa, K.; Sato, S.; Morikawa, T.; Fukumi, S.; Saito, S. *J. Am. Chem. Soc.* **2020**, *142*, 10261-10266.
79. Arikawa, Y.; Tabata, I.; Miura, Y.; Tajiri, H.; Seto, Y.; Horiuchi, S.; Umakoshi, K. *Chem. Eur. J.* **2020**, *26*, 5603-5606.
80. Vu, N. N.; Kaliaguine, S.; Do, T. O. *Adv. Funct. Mater.* **2019**, *29*, 1901825.
81. Wang, K.; Fu, J.; Zheng, Y.; *Appl. Catal. B: Environ.* **2019**, *254*, 270-282.
82. Xiong, Z.; Wang, H.; Xu, N.; Li, H.; Fang, B.; Zhao, Y.; Zhang, j.; Zheng, C. *Int. J. Hydrog. Energy*, **2015**, *40*, 10049-10062.
83. Kamat, P. V. Kamat, *J. Phys. Chem. Lett.* **2012**, *3*, 663.
84. Eng, H. W.; Barnes, P. W.; Auer, B. M.; Woodward, P. M. *J. Solid State Chem.* **2003**, *175*, 94-109.
85. Kudo, A.; Kato, H.; Nakagawa, S. *J. Phys. Chem. B.* **2000**, *104*, 571-575.
86. Park, H. A.; Choi, J. H.; Choi, K. M.; Lee, D. K.; Kang, J. K. *J. Mater. Chem.*, **2012**, *22*, 5304-5307.
87. Liu, L.; Fan, W.; Zhao, X.; Sun, H.; Li, P.; Sun, L. *Langmuir*, **2012**, *28*, 10415-10424.
88. Handoko, A. D.; Tang, J. *Int. J. Hydrog. Energy*, **2013**, *38*, 13017-13022.
89. Wang, J.; Lin, S.; Tian, N.; Ma, T.; Zhang, Y.; Huang, H. *Adv. Funct. Mater.* **2021**,

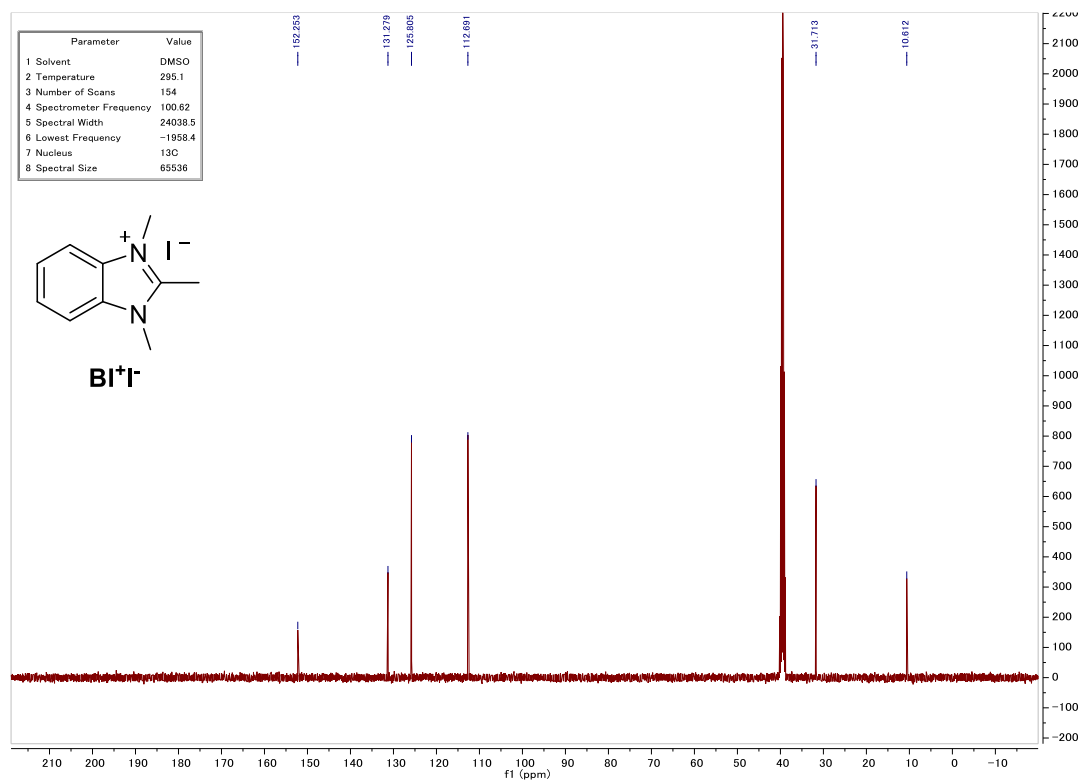
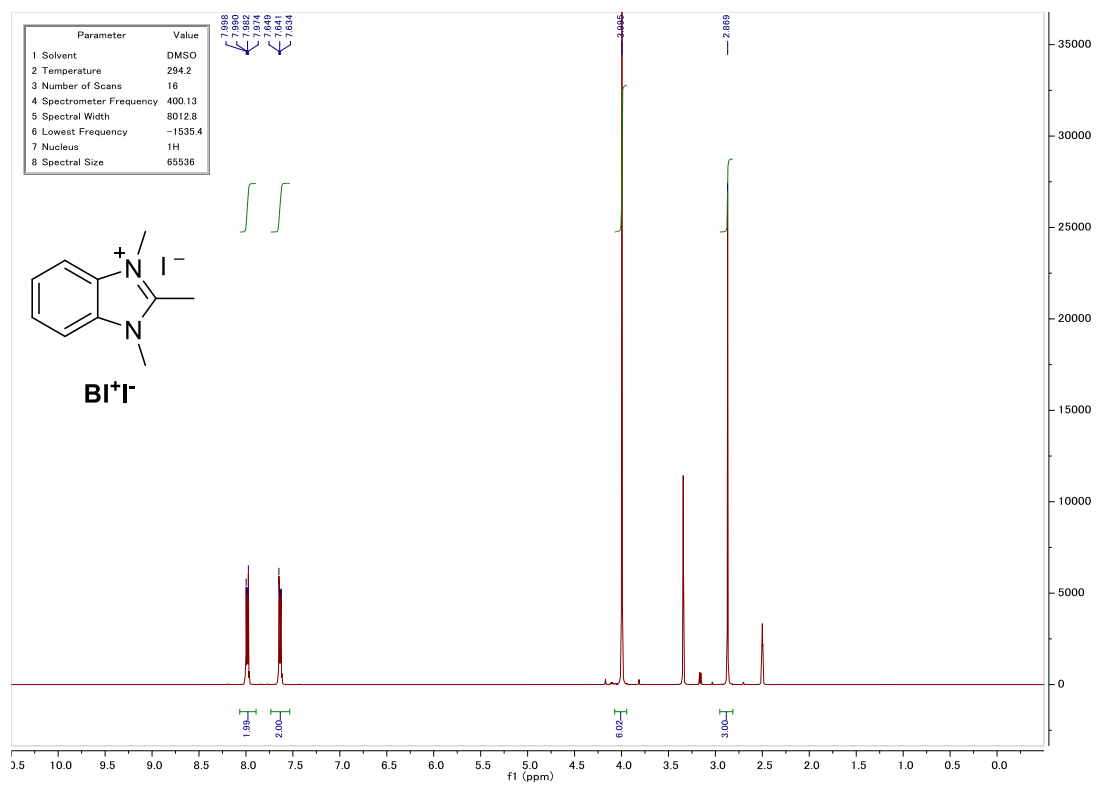
- 31, 2008008.
90. Liu, B. J.; Torimoto, T.; Yoneyama, H. *J. Photochem. Photobiol. A*, **1998**, *113*, 93-97.
91. Fan, F. R.; Leempoel, P.; Bard, A. J. *J. Electrochem. Soc.* **1983**, *130*, 1866.
92. Inoue, H.; Moriwaki, H.; Maeda, K.; Yoneyama, H. *J. Photochem. Photobiol. A*, **1995**, *86*, 191-196.
93. Meng, X.; Yu, Q.; Liu, G.; Shi, L.; Zhao, G.; Liu, H.; Li, P.; Chang, k.; Kako, T.; Ye, J. *Nano Energy*, **2017**, *34*, 524-532.
94. Jiao, X.; Chen, Z.; Li, X.; Sun, Y.; Gao, S.; Yan, W.; Wang, C. M.; Zhang, Q.; Lin, Y.; Luo, Y.; Xie, Y. *J. Am. Chem. Soc.* **2017**, *139*, 7586-7594.
95. Kuriki, R.; Sekizawa, K.; Ishitani, O.; Maeda, K. *Angew. Chem., Int. Ed.* **2015**, *54*, 2406-2409.
96. Xiang, Q.; Yu, J.; Jaroniec, M. *Chem. Soc. Rev.* **2012**, *41*, 782-796.
97. Yang, M. Q.; Xu, Y. *Nanoscale Horiz.* **2016**, *1*, 185-200.
98. Liu, B.; Ye, L.; Wang, R.; Yang, J.; Zhang, Y.; Guan, R.; Tian, L.; Chen, X. *ACS Appl. Mater. Interfaces*, **2018**, *10*, 4001-4009.
99. Low, J.; Cheng, B.; Yu, J.; Jaroniec, M. *Energy Storage Mater.* **2016**, *3*, 24-35.
100. Velasco-Soto, M. A.; Pérez-García, S. A.; Alvarez-Quintana, J.; Cao, Y.; Nyborg, L.; Licea-Jiménez, L. *Carbon*, **2015**, *93*, 967-973.
101. Gupta, V.; Sharma, N.; Singh, U.; Arif, M.; Singh, A. *Optik*, **2017**, *143*, 115-124.
102. Wang, S.; Yao, W.; Lin, J.; Ding, Z.; Wang, X. *Angew. Chem., Int. Ed.* **2014**, *126*, 1052-1056.
103. Fu, Y.; Sun, D.; Chen, Y.; Huang, R.; Ding, Z.; Fu, X.; Li, Z. *Angew. Chem., Int. Ed.* **2012**, *51*, 3364-3367.
104. Wang, X.; Wisser, F.; Canivet, J.; Fontecave, M.; Mellot-Draznieks, C. *ChemSusChem*, **2018**, *11*, 3315-3322.
105. Sadeghi, N.; Sharifnia, S.; Do, T. O. *J. Mater. Chem. A*, **2018**, *6*, 18031-18035.
106. Wang, Y.; Huang, N. Y.; Shen, J. Q.; Liao, P. Q.; Chen, X. M.; Zhang, J. P. *J. Am. Chem. Soc.* **2018**, *140*, 38-41.
107. Sun, D.; Fu, Y.; Liu, W.; Ye, L.; Wang, D.; Yang, L.; Fu, X. Z.; Li, Z. *Eur. J. Chem.* **2013**, *19*, 14279-14285.
108. Zhou, A.; Dou, Y.; Zhao, C.; Zhou, J.; Wu, X. Q.; Li, J. R. *Appl. Catal. B.* **2020**, *264*, 118519.
109. Scott, D. J.; Fuchter, M. J.; Ashley, A. E. *Chem. Soc. Rev.* **2017**, *46*, 5689-5700.
110. Mömmling, C. M.; Otten, E.; Kehr, G.; Fröhlich, R.; Grimme, S.; Stephan, D. W.; Erker, G. *Angew. Chem. Int. Ed.* **2009**, *48*, 6643-6646.
111. Berkefeld, A.; Piers, W. E.; Parvez, M. *J. Am. Chem. Soc.* **2010**, *132*, 10660-10661.
112. Courtemanche, M. A.; Légaré, M. A.; Maron, L.; Fontaine, F. G. *J. Am. Chem. Soc.* **2013**, *135*, 9326-9329.
113. Enders, D.; Niemeier, O.; Henseler, A. *Chem. Rev.* **2007**, *107*, 5606-5655.
114. Bobbink, F. D.; Das, S.; Dyson, P. J. *Nat. Protoc.* **2017**, *12*, 417-428.
115. Riduan, S. N.; Zhang, Y.; Ying, J. Y. *Angew. Chem. Int. Ed.* **2009**, *48*, 3322-3325.
116. Zhu, X.; Tian, C.; Veith, G. M.; Abney, C. W.; Dehaut, J.; Dai, S. *J. Am. Chem. Soc.* **2016**, *138*, 11497-11500.

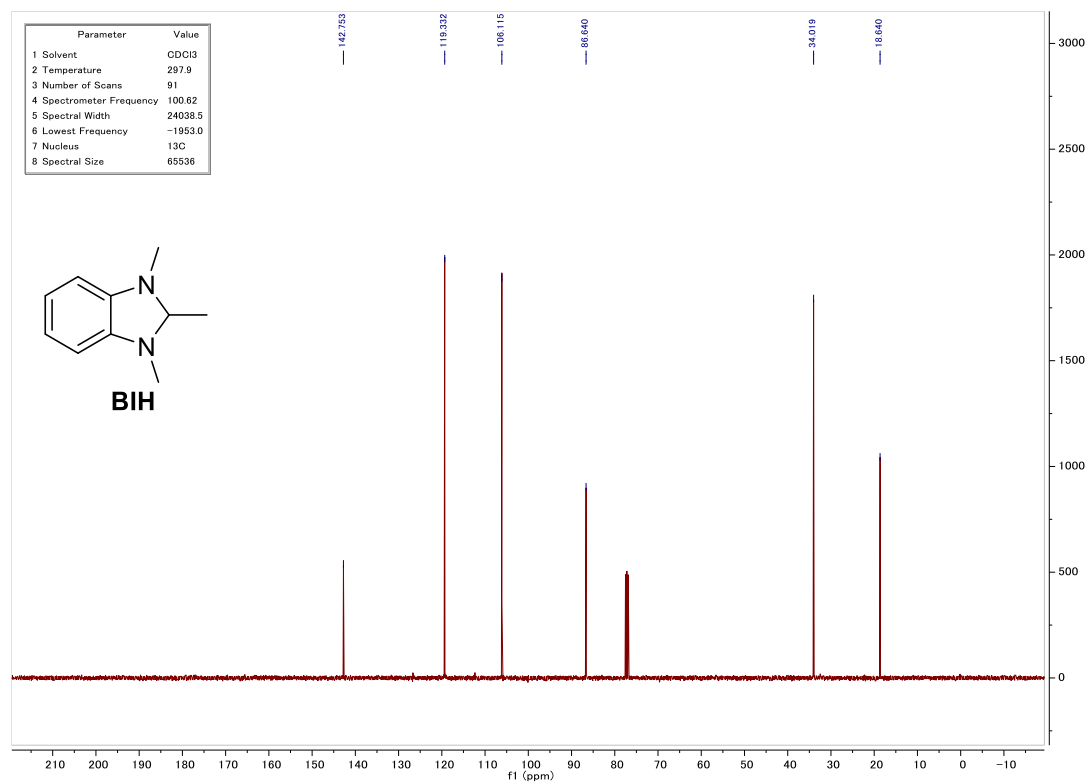
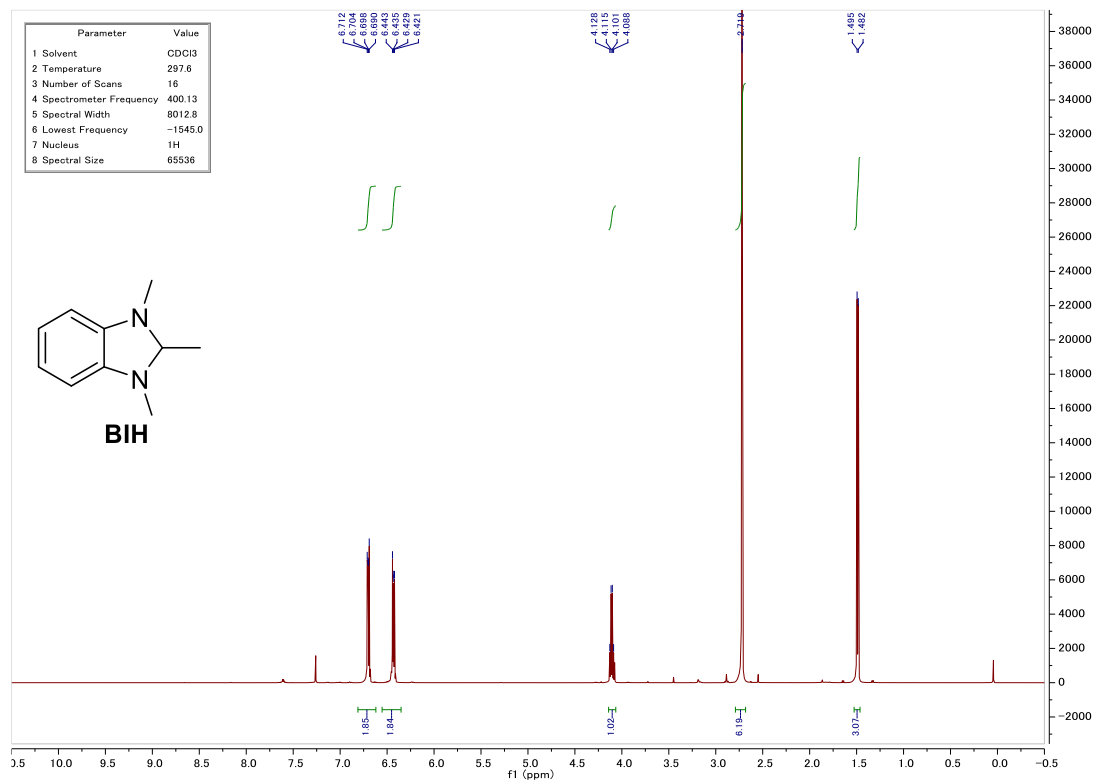
117. To, J. W.; He, J.; Mei, J.; Haghpanah, R.; Chen, Z.; Kurosawa, T.; Chen, S.; Bae, W. G.; Pan, L.; Tok, J. B. H.; Wilcox, J.; Bao, Z. *J. Am. Chem. Soc.* **2016**, *138*, 1001-1009.
118. Zeng, Y.; Zou, R.; Zhao, Y. *Adv. Mater.* **2016**, *28*, 2855-2873.
119. Wen, F.; Zhang, F.; Wang, Z.; Yu, X.; Ji, G.; Li, D.; Tong, S.; Wang, Y.; Han, B.; Liu, Z. *Chem. Sci.* **2021**, *12*, 11548-11553.
120. Guo, S.; Zhang, H.; Chen, Y.; Liu, Z.; Yu, B.; Zhao, Y.; Yang Z.; Han, B.; Liu, Z. *ACS Catal.* **2018**, *8*, 4576-4581.
121. Rehm, D.; Weller, A. *Isr. J. Chem.* **1970**, *8*, 259-271.
122. Matsubara, R.; Yabuta, T.; Md Idros, U.; Hayashi, M.; Ema, F.; Kobori, Y.; Sakata, K. *J. Org. Chem.* **2018**, *83*, 9381-9390.
123. Yabuta, T.; Hayashi, M.; Matsubara, R. *J. Org. Chem.* **2021**, *86*, 2545-2555.
124. Lim, C. H.; Ilic, S.; Alherz, A.; Worrell, B. T.; Bacon, S. S.; Hynes, J. T.; Glusac, K. D.; Musgrave, C. B. *J. Am. Chem., Soc.* **2019**, *141*, 272-280.
125. Crisenza, G. E.; Mazzarella, D.; Melchiorre, P. *J. Am. Chem. Soc.* **2020**, *142*, 5461-5476.
126. Woźniak, Ł.; Murphy, J. J.; Melchiorre, P. *J. Am. Chem. Soc.* **2015**, *137*, 5678-5681.
127. Arceo, E.; Jurberg, I. D.; Alvarez-Fernández, A.; Melchiorre, P. *Nat. Chem.* **2013**, *5*, 750-756.
128. Kimoto, E.; Tanaka, H.; Ohmoto, T.; Choami, M. *Anal. Biochem.* **1993**, *214*, 38-44.
129. Tablet, C.; Ionescu, S. *Rev. Roum. Chim.* **2021**, *66*, 59-63.
130. Roth, H. G.; Romero, N. A.; Nicewicz, D. A. *Synlett*, **2016**, *27*, 714-723.
131. Ota, E.; Wang, H.; Frye, N. L.; Knowles, R. R. *J. Am. Chem. Soc.* **2019**, *141*, 1457-1462.
132. Romero, N. A.; Nicewicz, D. A. *Chem. Rev.* **2016**, *116*, 10075-10166.
133. Connelly, N. G.; Geiger, W. E. *Chem. Rev.* **1996**, *96*, 877-910.
134. Angulo, G.; Brucka, M.; Gerecke, M.; Grampp, G.; Jeannerat, D.; Milkiewicz, J.; Mitrev, Y.; Radzewicz, C.; Rosspeintner, A.; Vauthey, E.; Wnuk, P. *Phys. Chem. Chem. Phys.* **2016**, *18*, 18460-18469.
135. Melhuish, W. H. *J. Phys. Chem.* **1961**, *65*, 229-235.
136. Zheng, Y.; Duan, Y.; Ji, K.; Wang, R. L.; Wang, B. *RSC Adv.*, **2016**, *6*, 25242-25245.
137. Brouwer, A. M. *Pure Appl. Chem.* **2011**, *83*, 2213-2228.
138. Willett, K. L.; Hites, R. A. *J. Chem. Educ.* **2000**, *77*, 900-902.
139. Frisch, M. J.; Trucks, G. W.; Schlegel, H. B.; Scuseria, G. E.; Robb, M. A.; Cheeseman, J. R.; Scalmani, G.; Barone, V.; Petersson, G. A.; Nakatsuji, H.; Caricato, M.; Li, X.; Hratchian, H. P.; Izmaylov, A. F.; Bloino, J.; Zheng, G.; Sonnenberg, J. L.; Hada, M.; Ehara, M.; Toyota, K.; Fukuda, R.; Hasegawa, J.; Ishida, M.; Nakajima, T.; Honda, Y.; Kitao, O.; Nakai, H.; Vreven, T.; Throssell, K.; Montgomery Jr. J. A.; Peralta, J. E.; Ogliaro, F.; Bearpark, M. J.; Heyd, J. J.; Brothers, E. N.; Kudin, K. N.; Staroverov, V. N.; Kobayashi, R.; Normand, J.; Raghavachari, K.; Rendell, A. P.; Burant, J. C.; Iyengar, S. S.; Tomasi, J.; Cossi, M.; Rega, N.; Millam, J. M.; Klene, M.; Knox, J. E.; Cross, J. B.; Bakken, V.; Adamo, C.; Jaramillo, J.; Gomperts, R.; Startmann, R. E.;

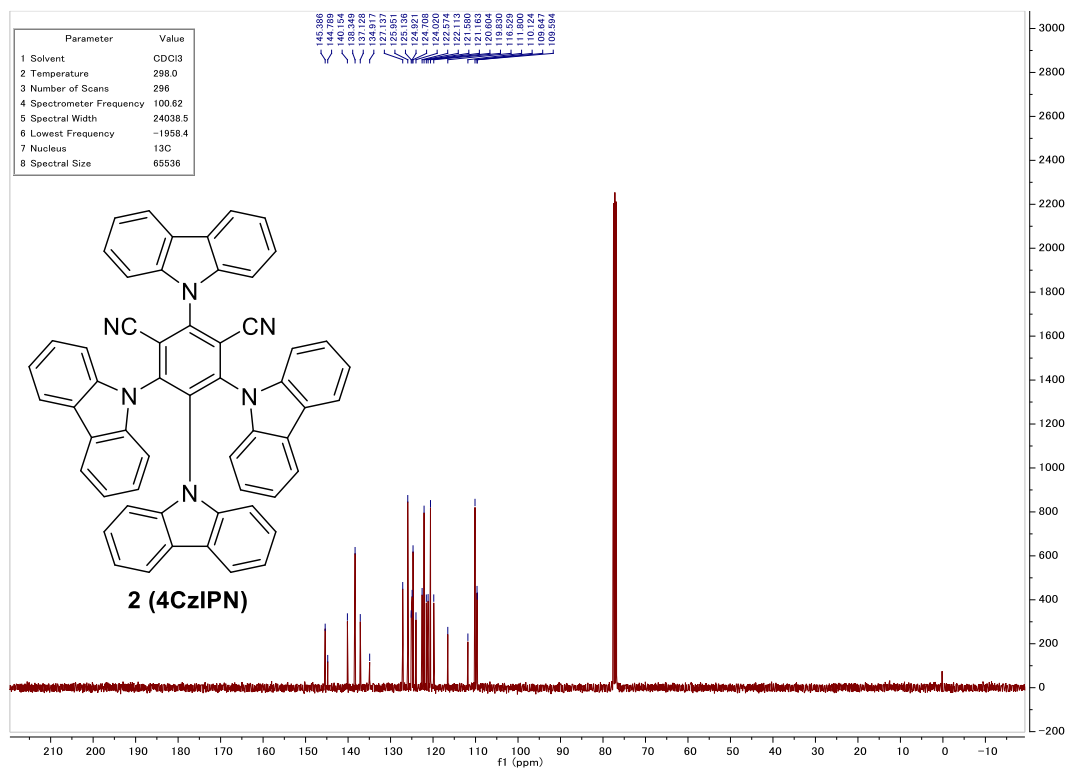
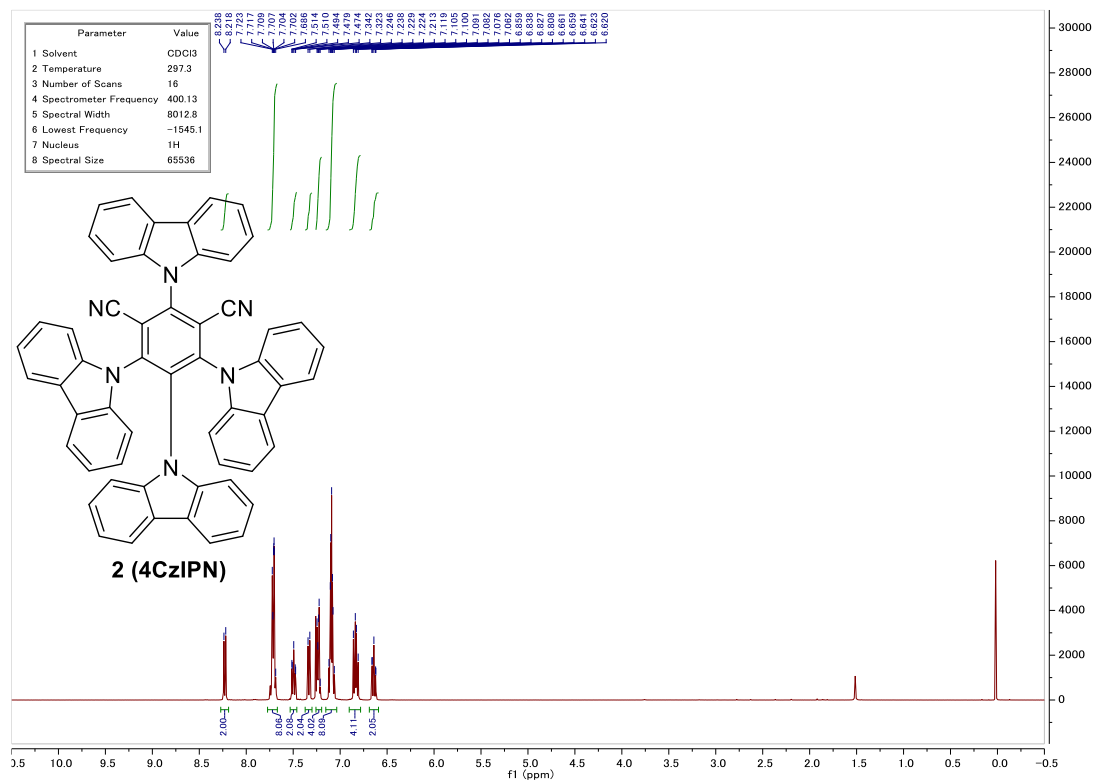
- Yazyev, O.; Austin, A. J.; Cammi, R.; Pomelli, C.; Ochterski, J. W.; Martin, R. L.; Morokuma, K.; Zakrzewski, V. G.; Voth, G. A.; Salvador, P.; Dannenberg, J. J.; Dapprich, S.; Daniels, A. D.; Farkas, O.; Foresman, J. B.; Ortiz, J. V.; Cioslowski, J.; Fox, D. J. Gaussian 09, Gaussian, Inc., Wallingford, CT. **2009**.
140. Tsuneda, T.; Song, J.-W.; Suzuki, S.; Hirao, K. *J. Chem. Phys.* **2020**, *133*, 174101.
141. Tsuneda, T.; Hirao, K. *Wiley Interdiscip. Rev.: Comput. Mol. Sci.* **2014**, *4*, 375-390.
142. Tsuneda, T.; Singh, R. K. *J. Comput. Chem.* **2014**, *35*, 1093-1100.
143. Tomasi, J.; Mennucci, B.; Cammi, R. *Chem. Rev.* **2005**, *105*, 2999-3094.
144. CYLview, 1.0b; Legault, C. Y. Université de Sherbrooke. **2009**.

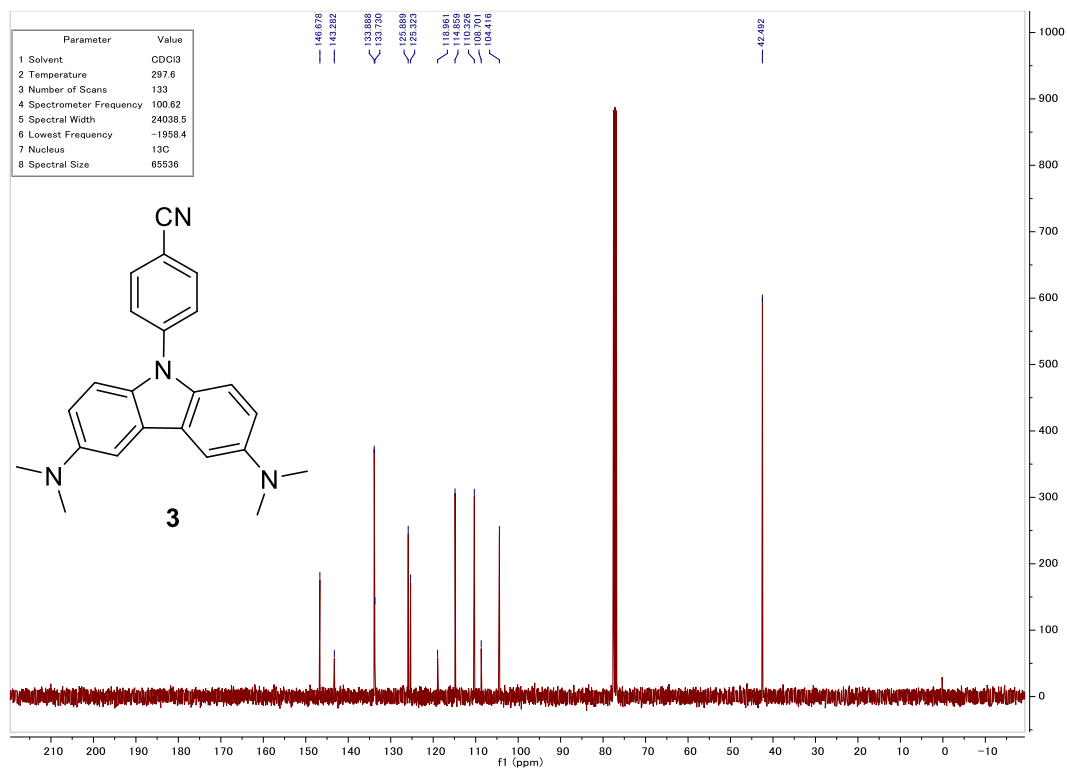
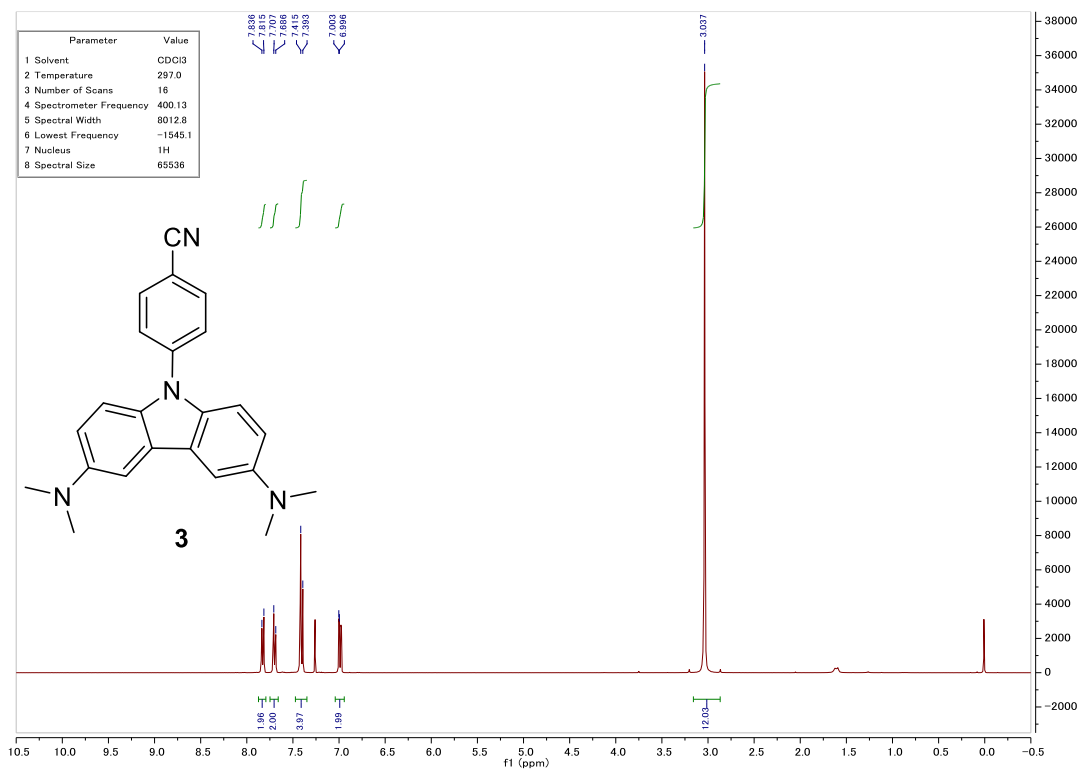
17. NMR spectra

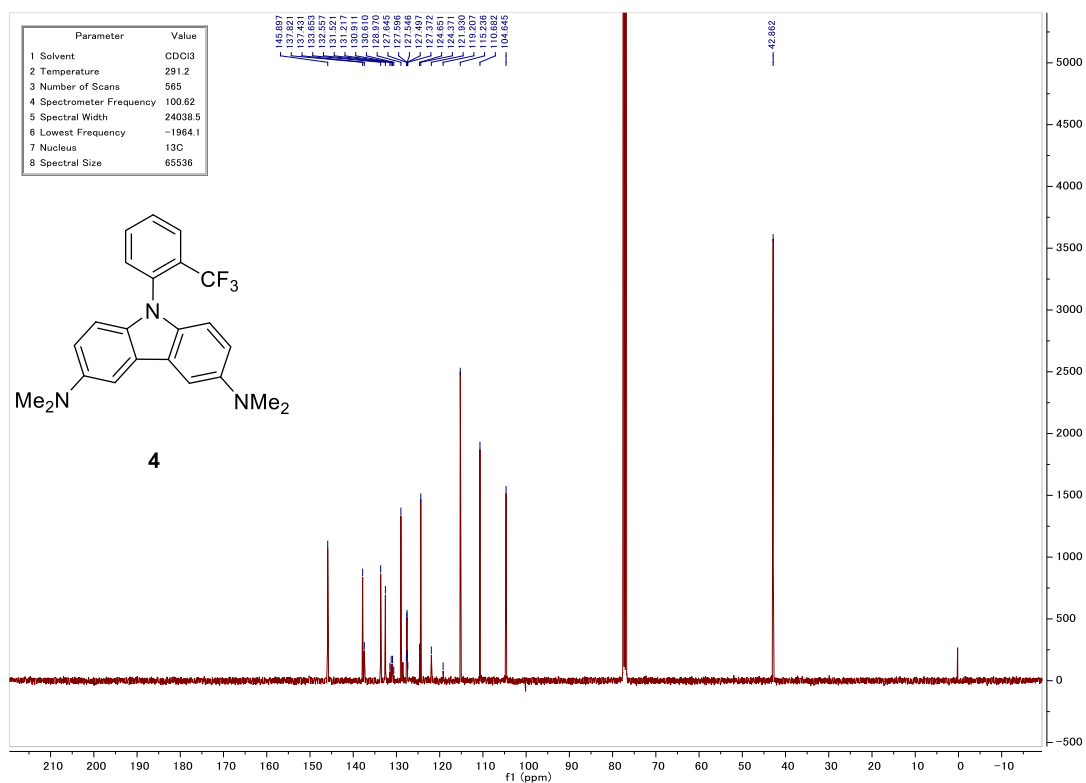
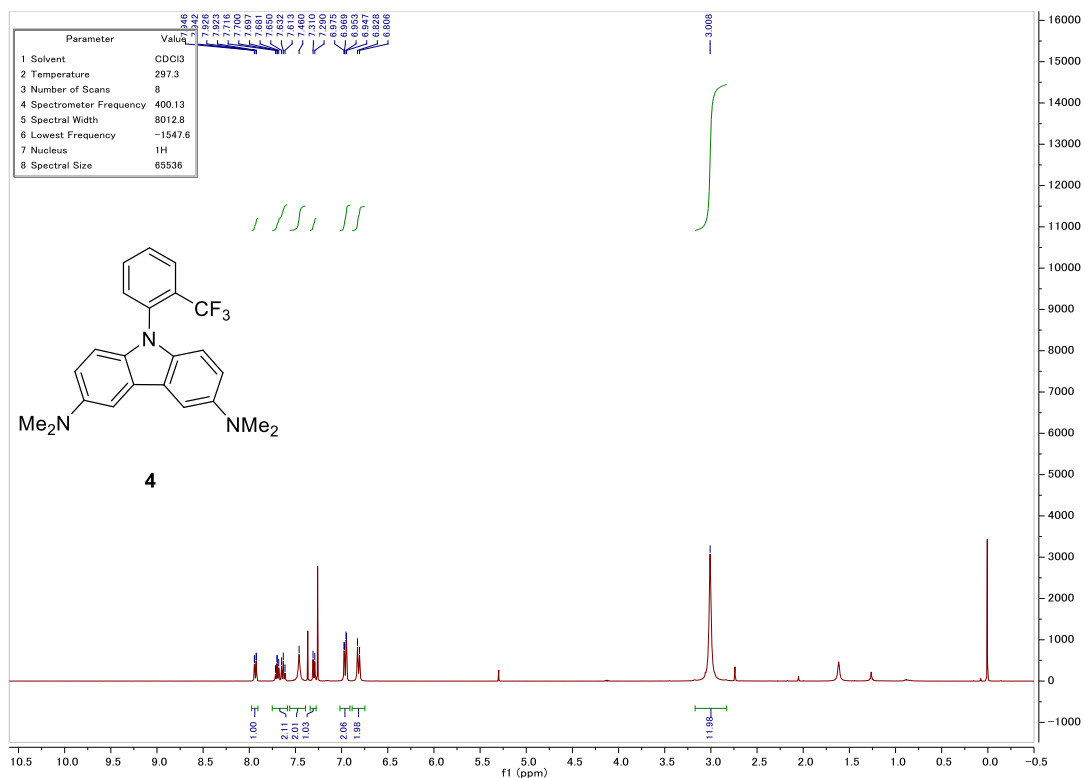


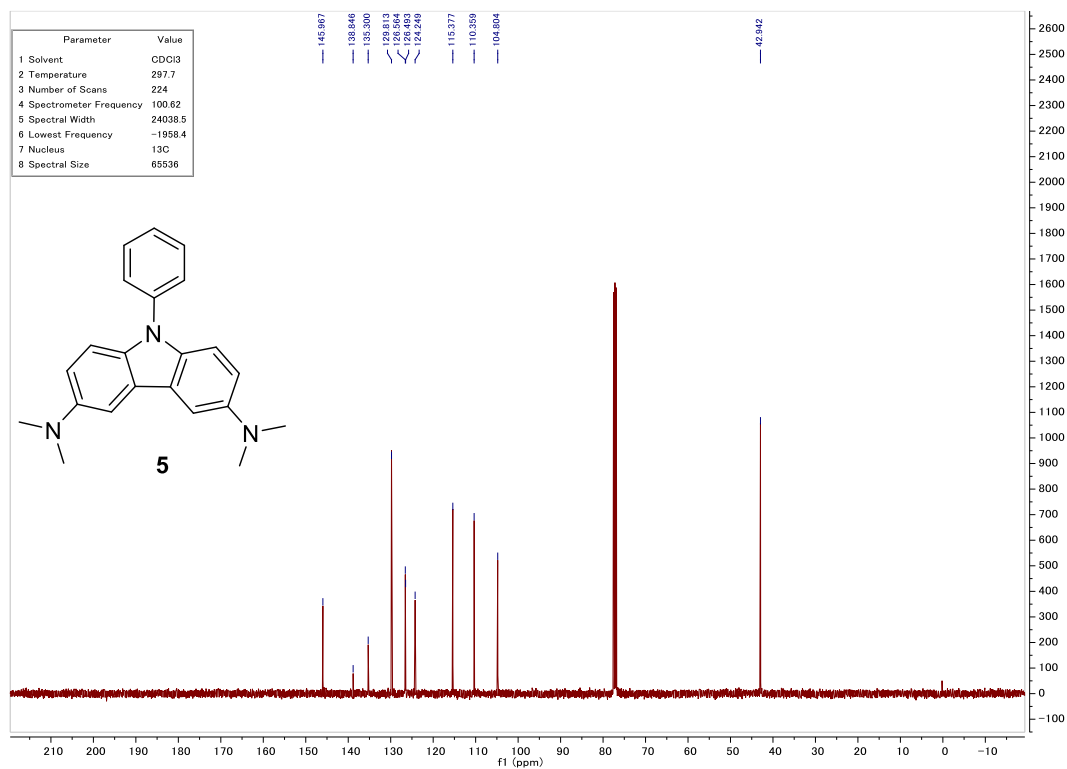
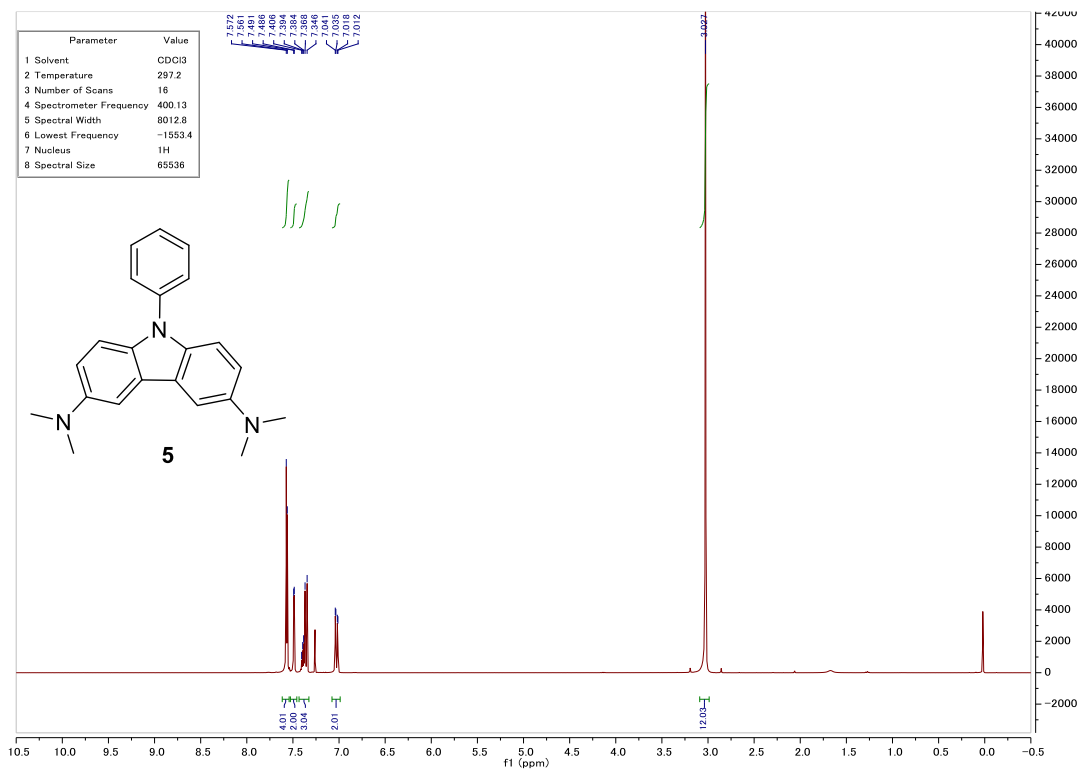


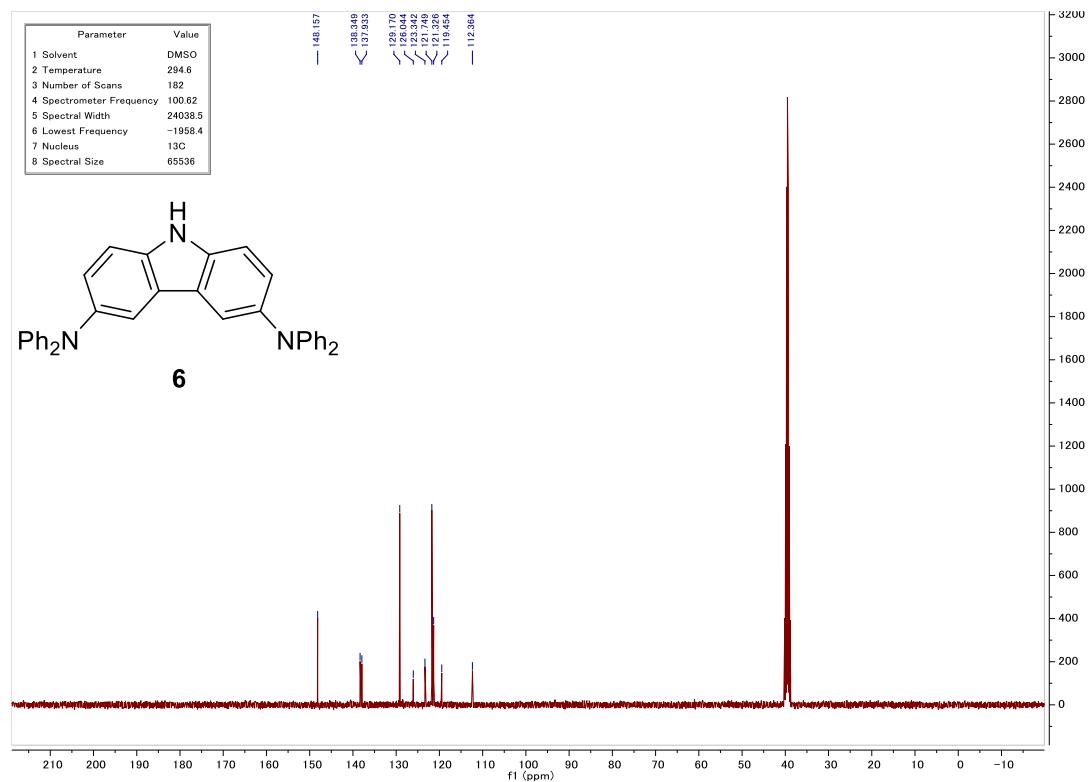
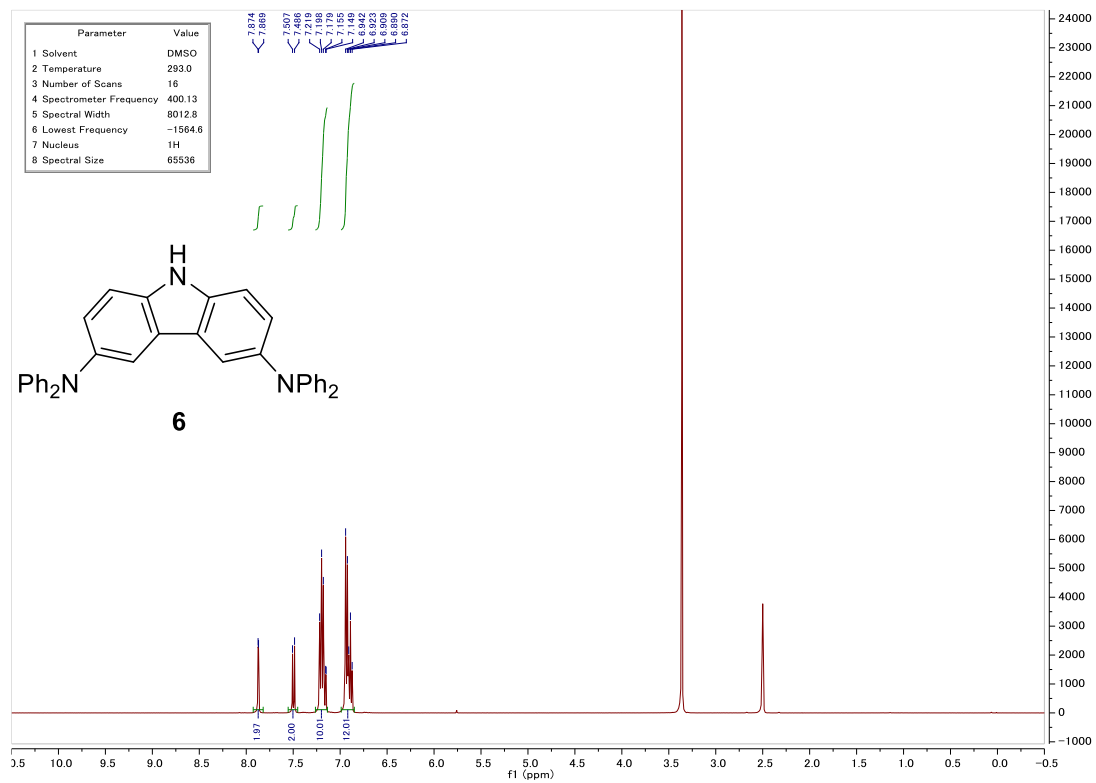


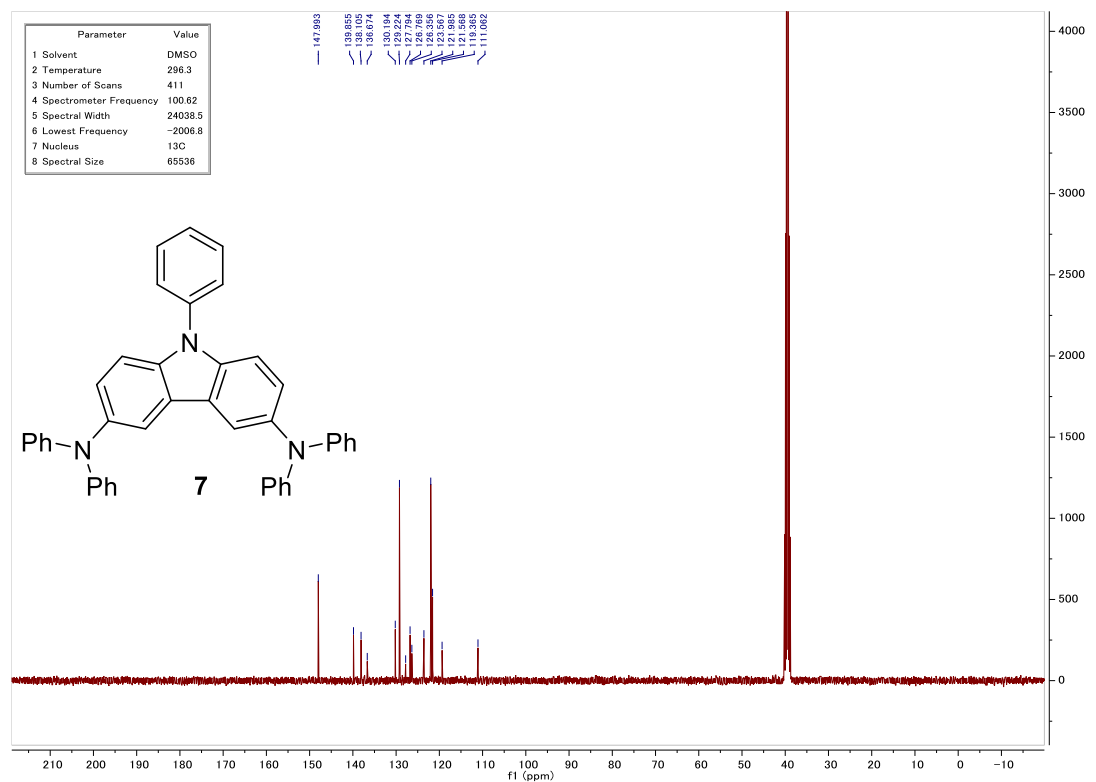
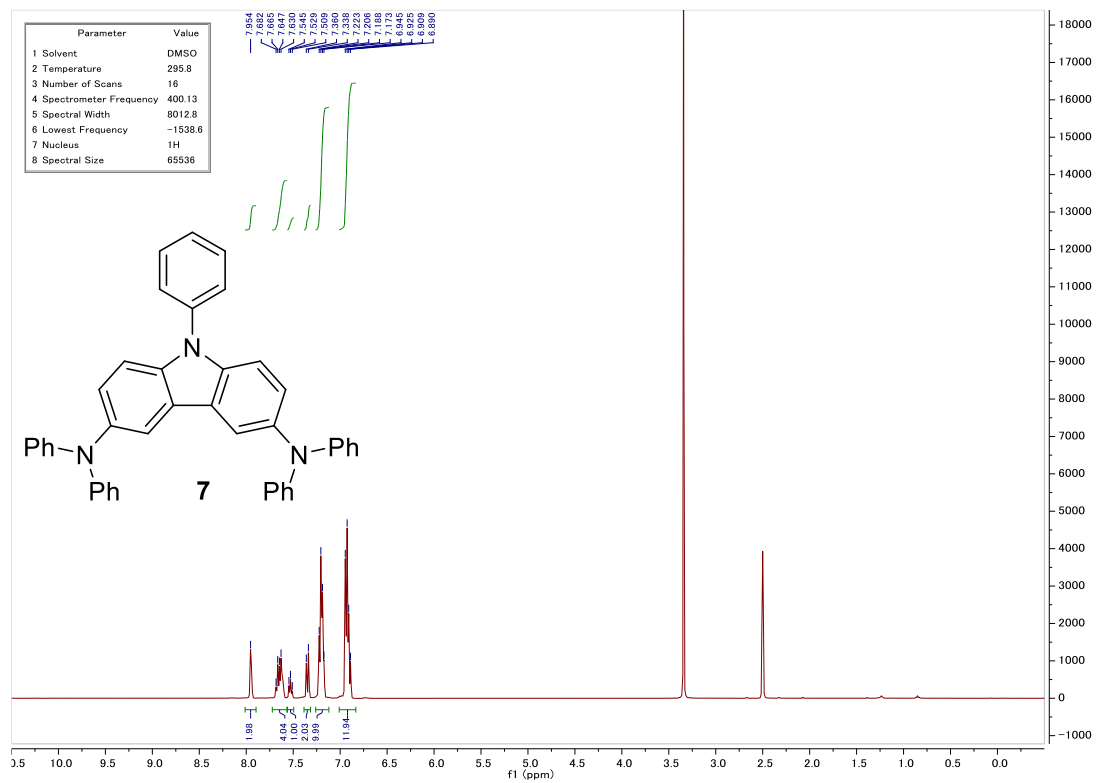


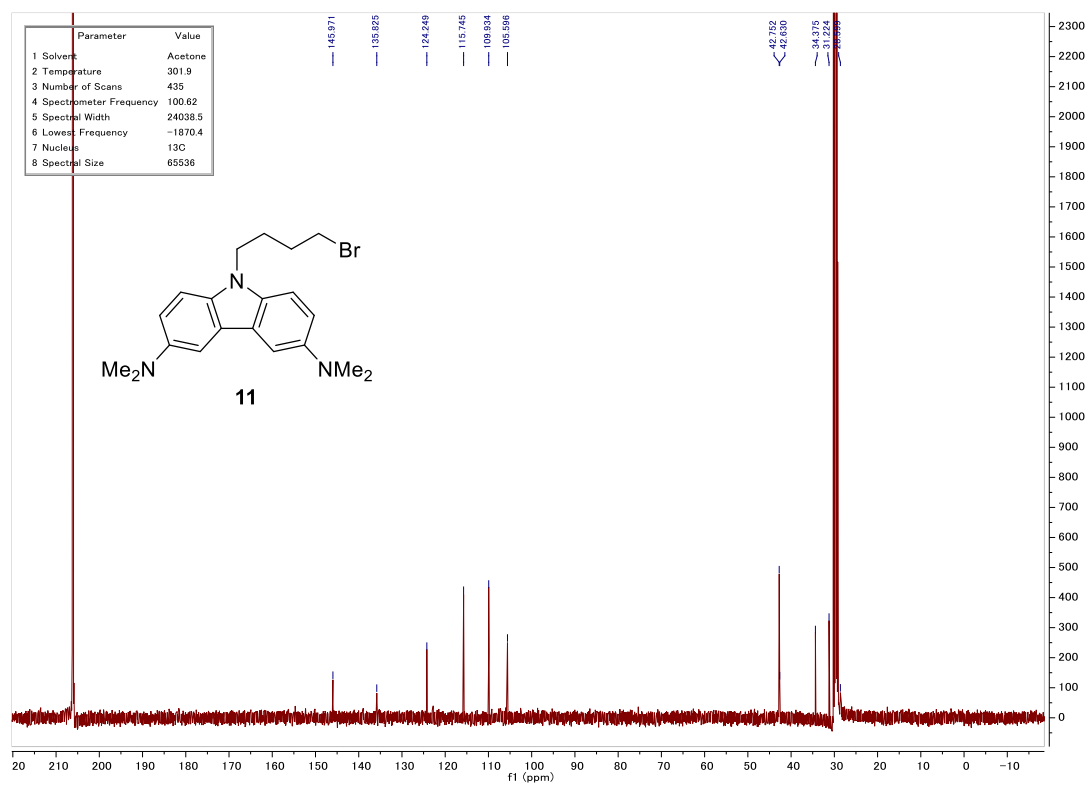
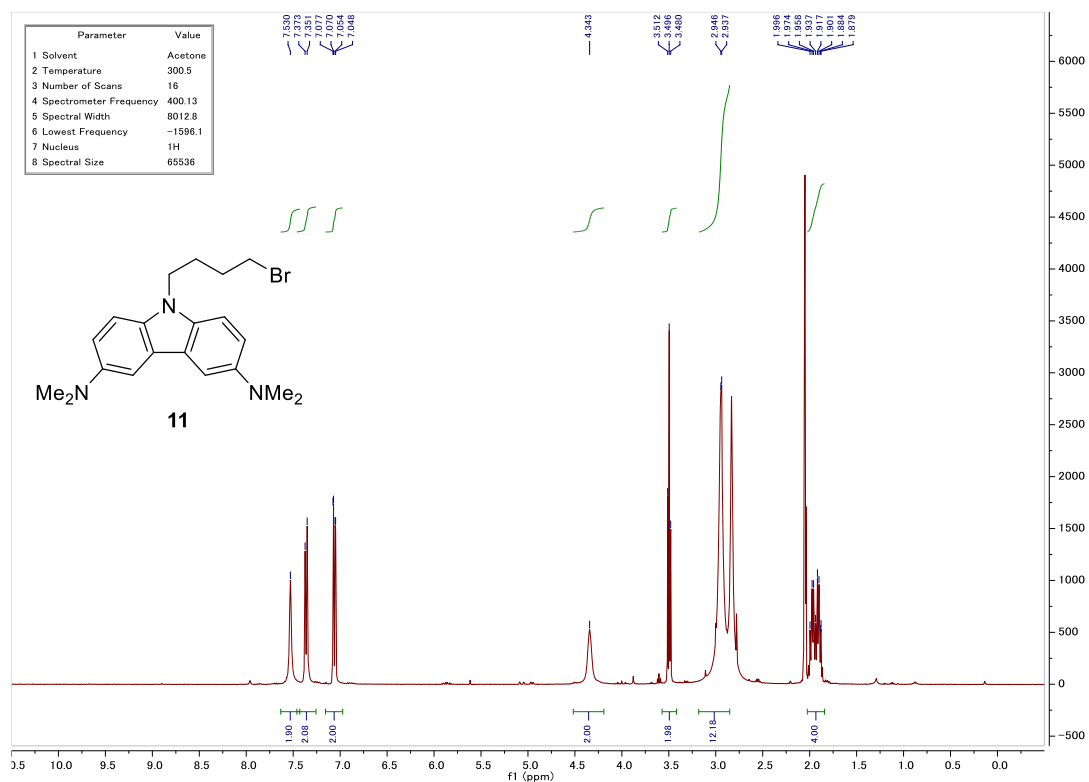


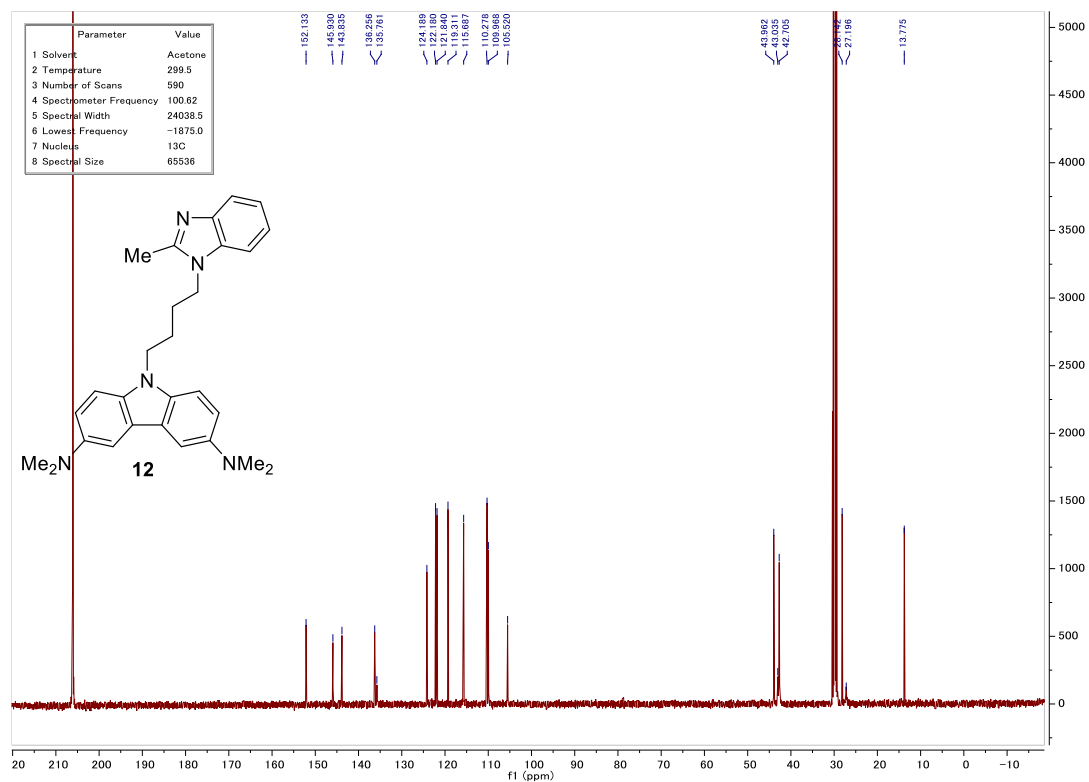
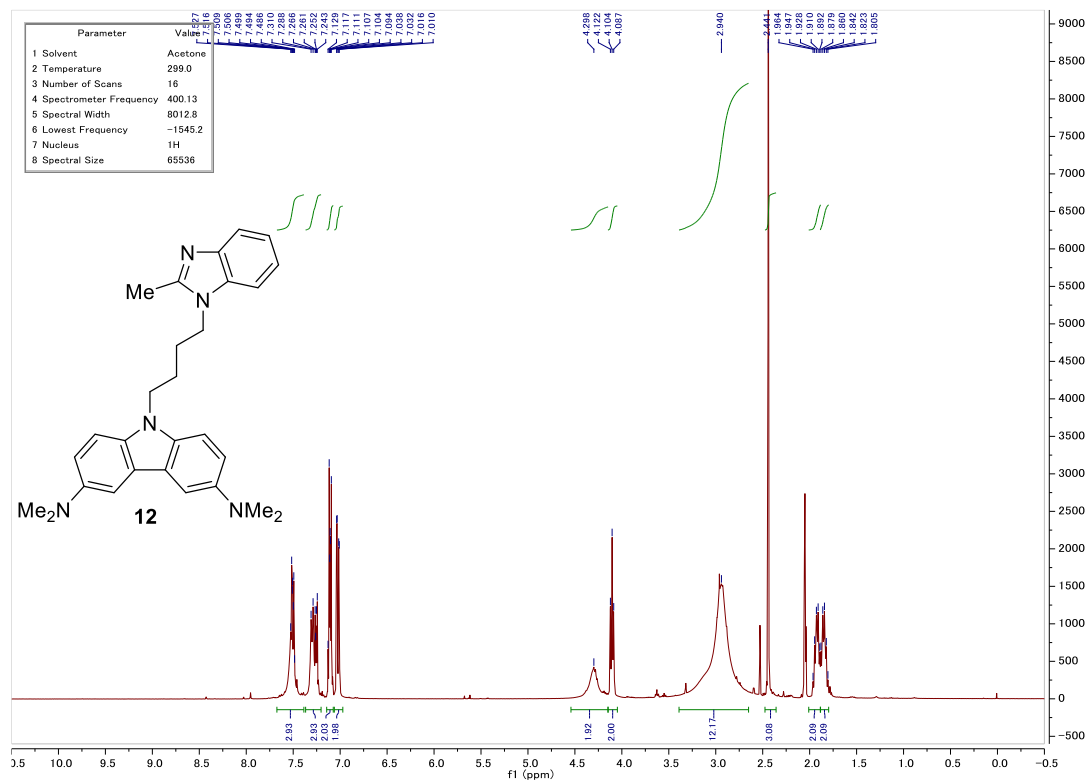


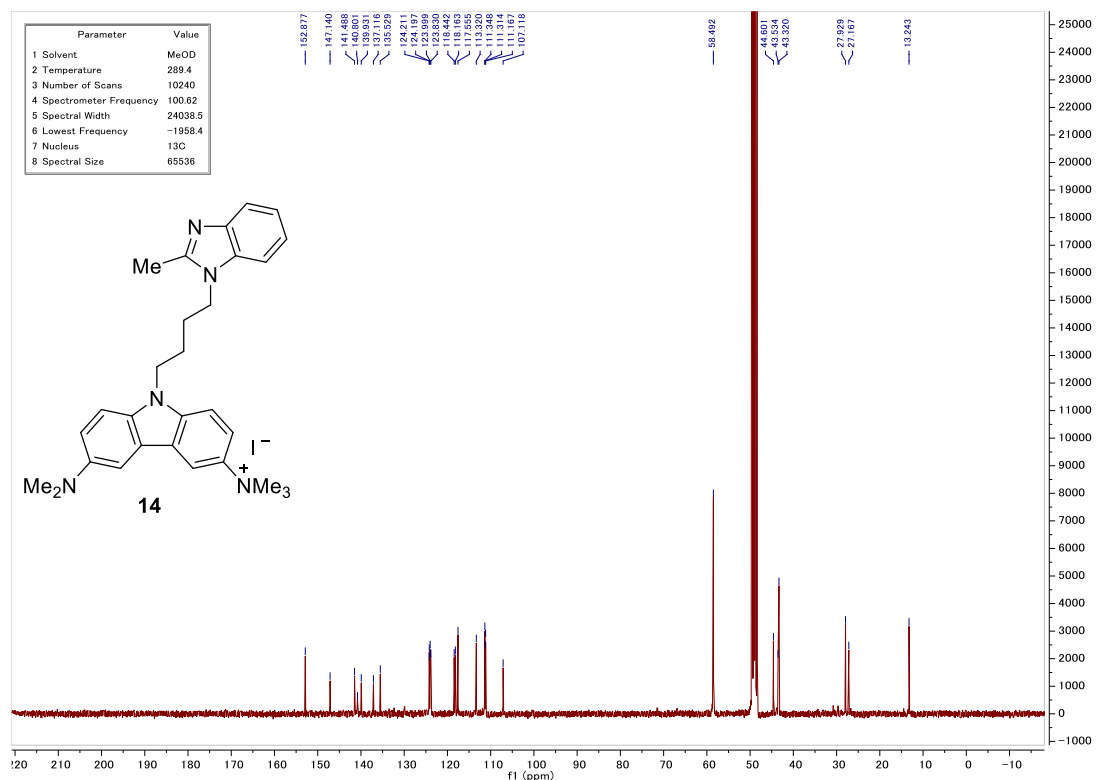
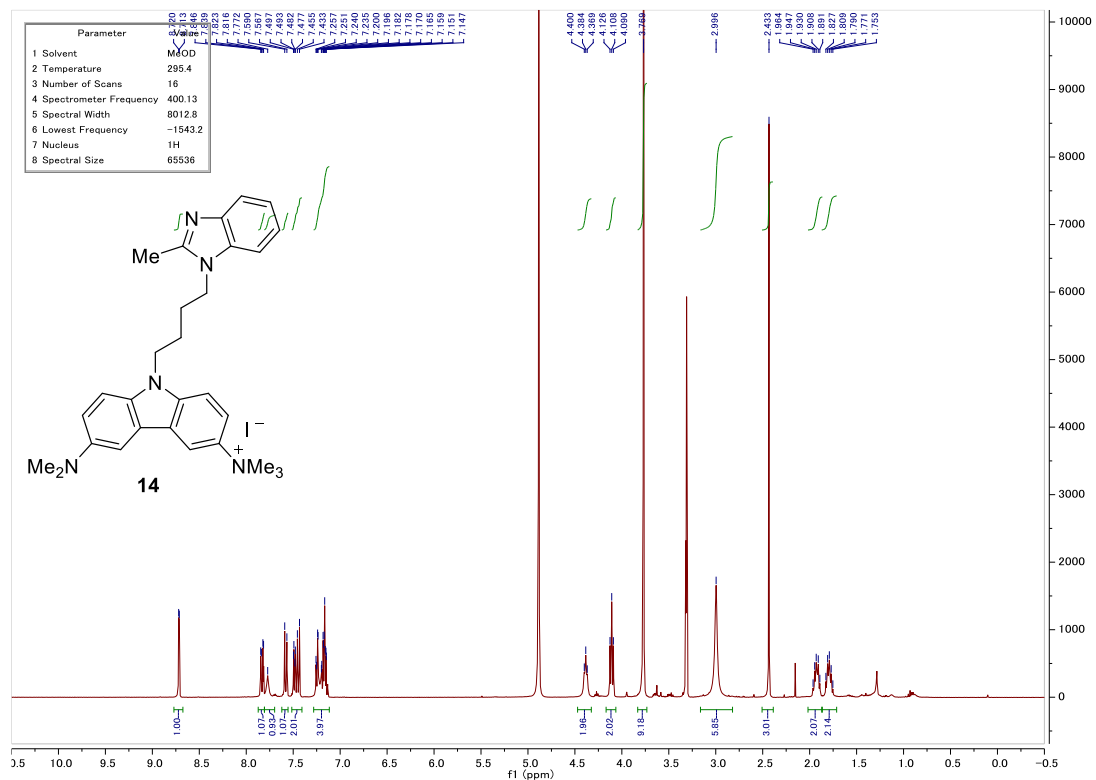


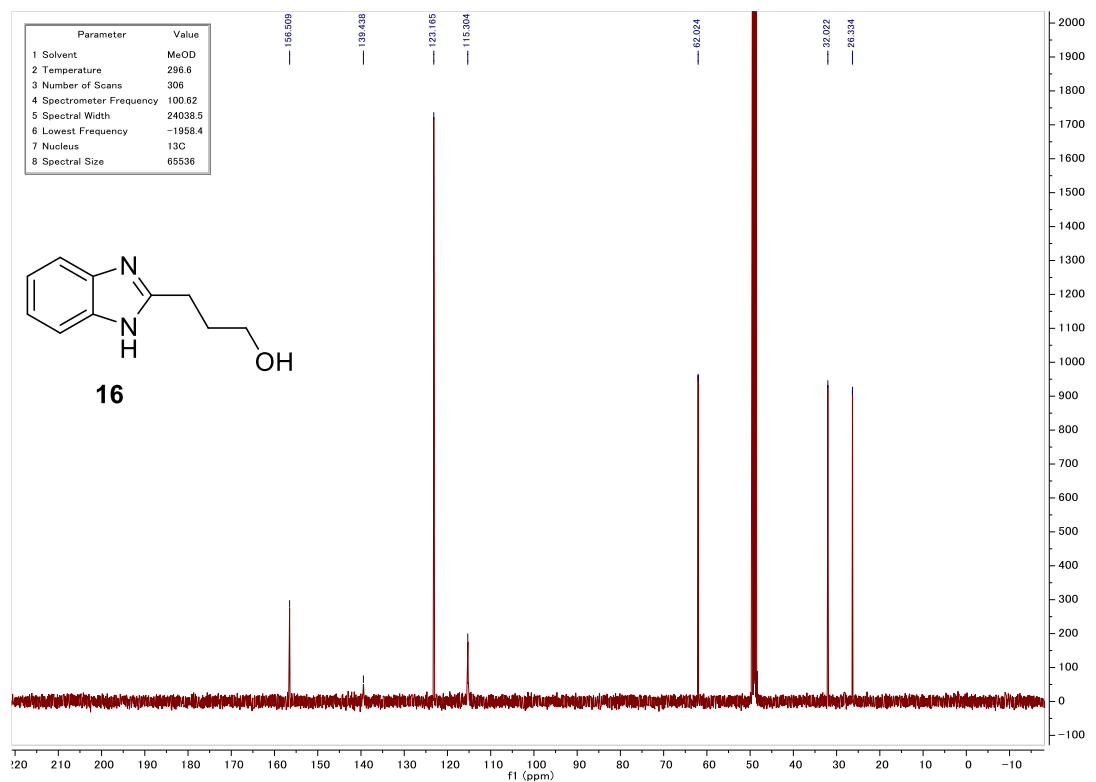
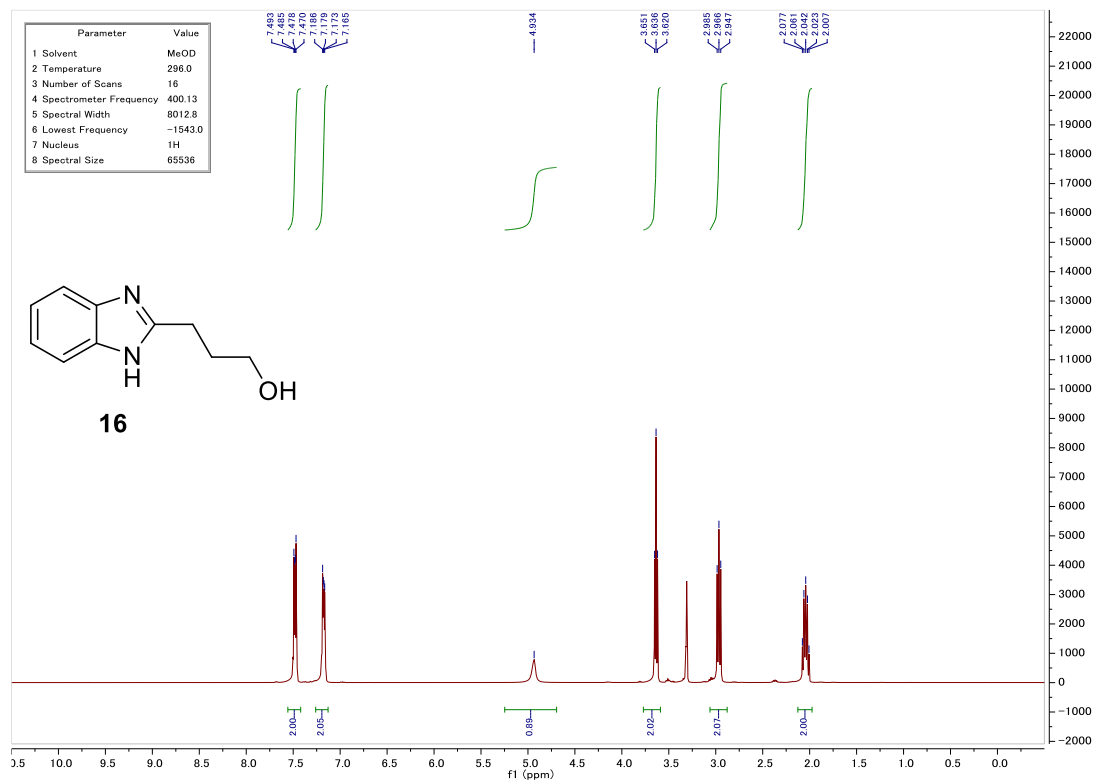


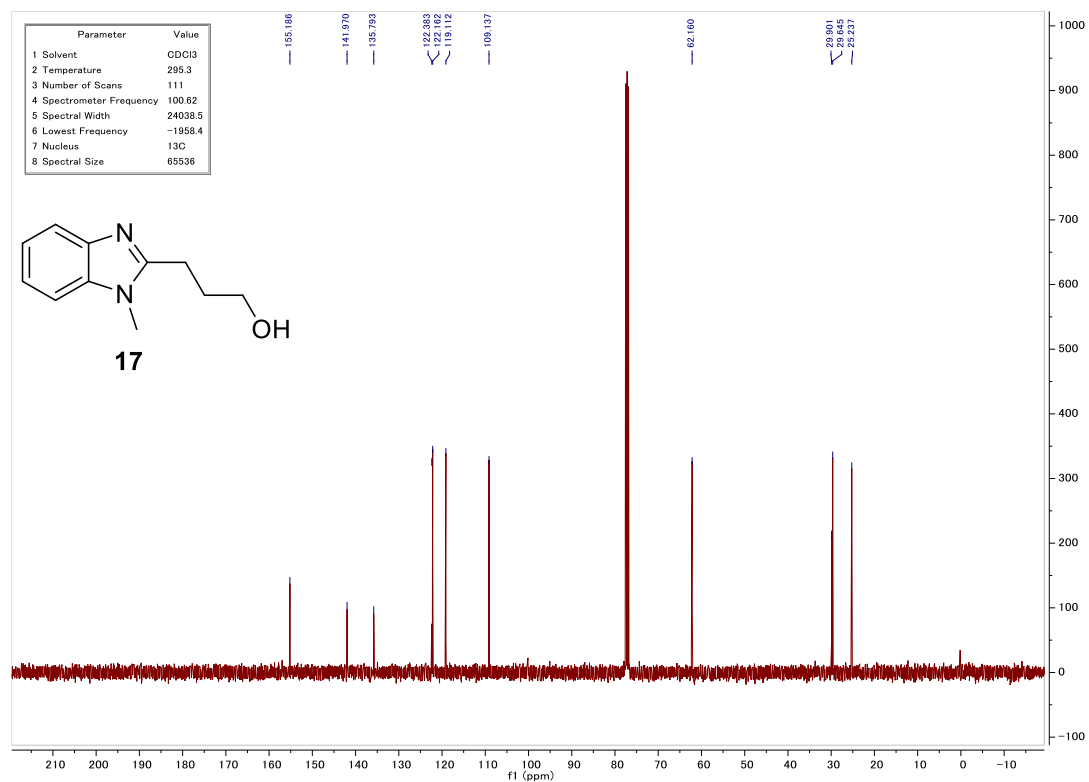
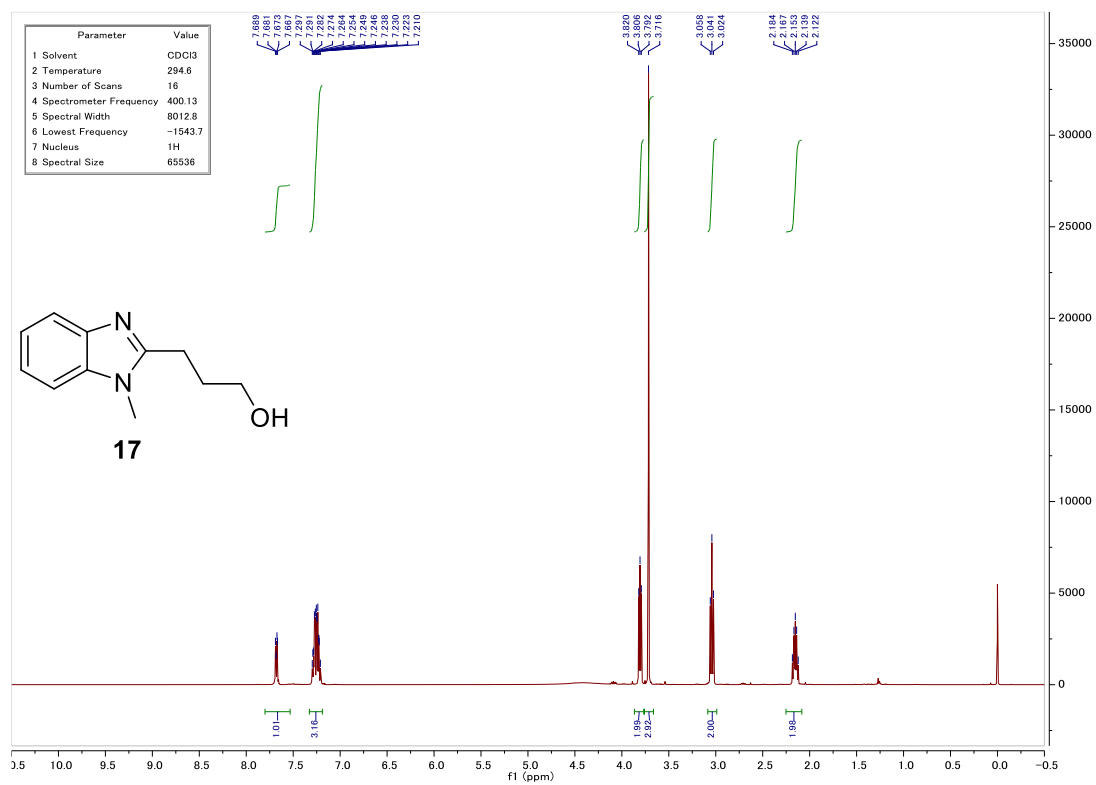


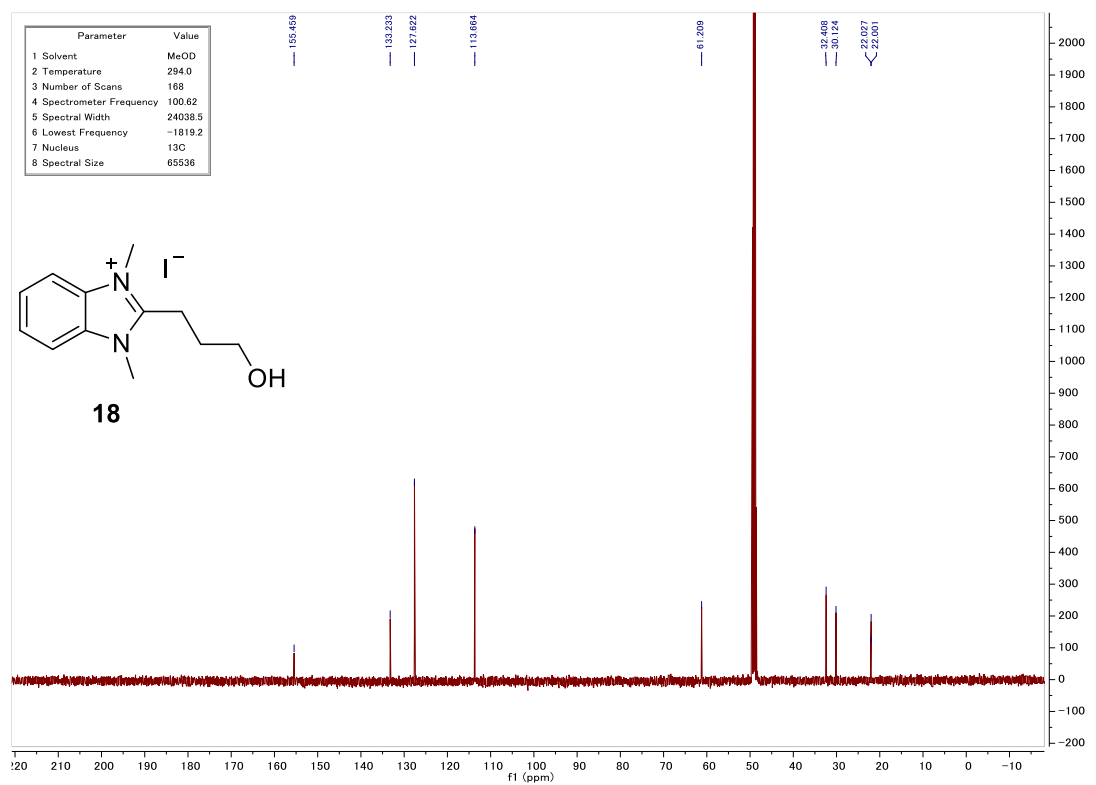
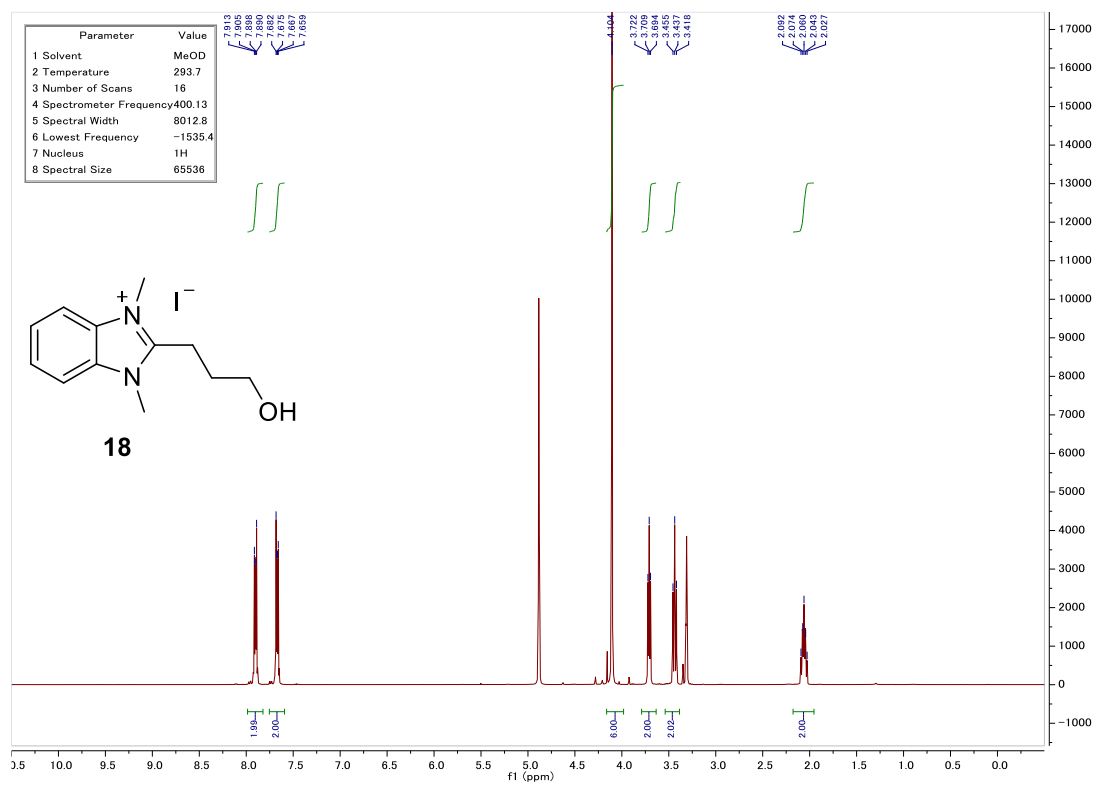


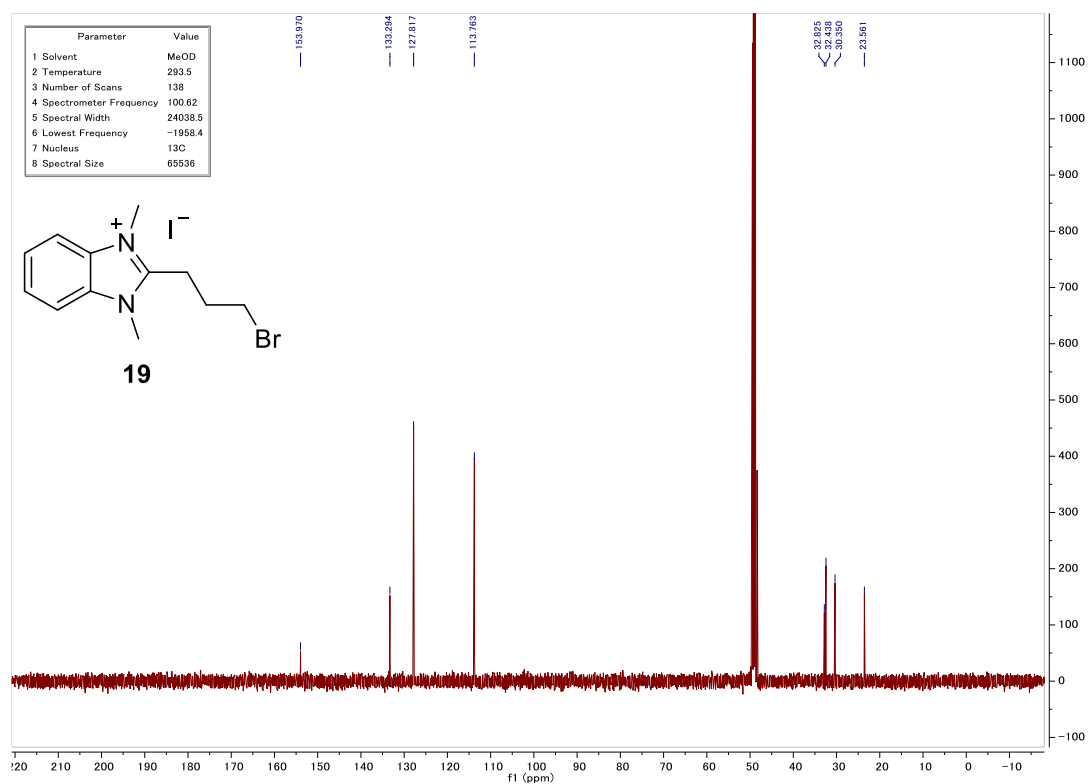
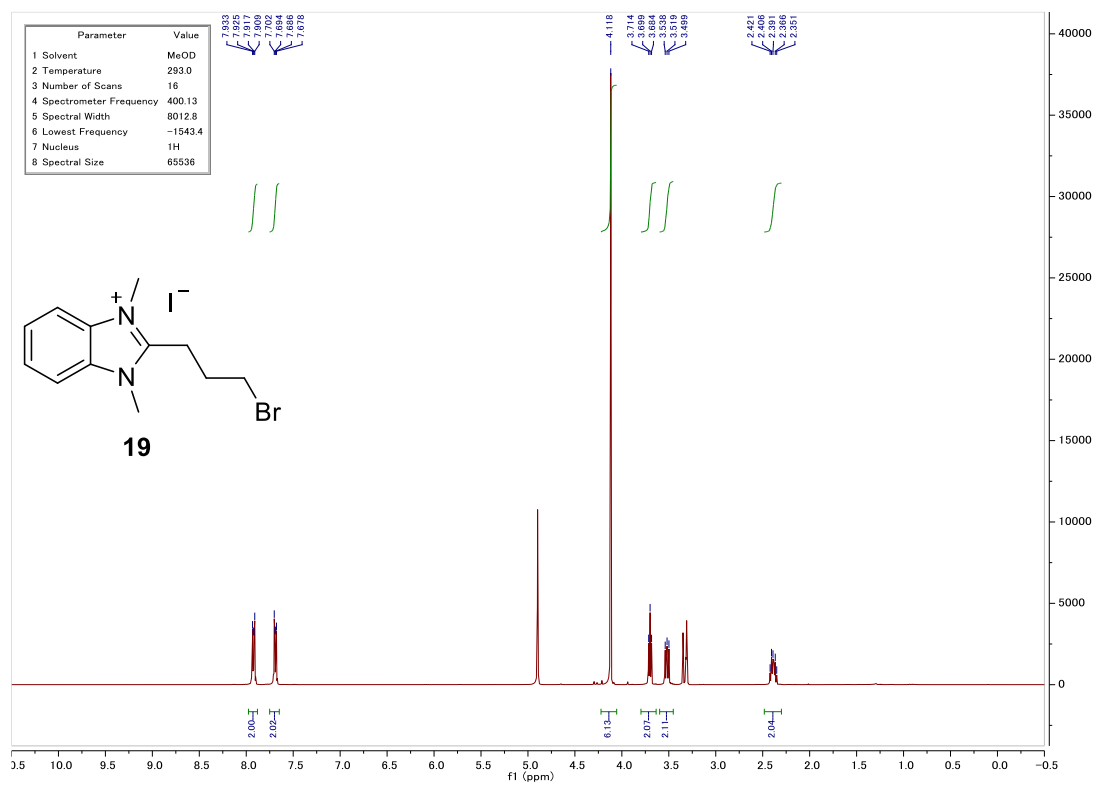


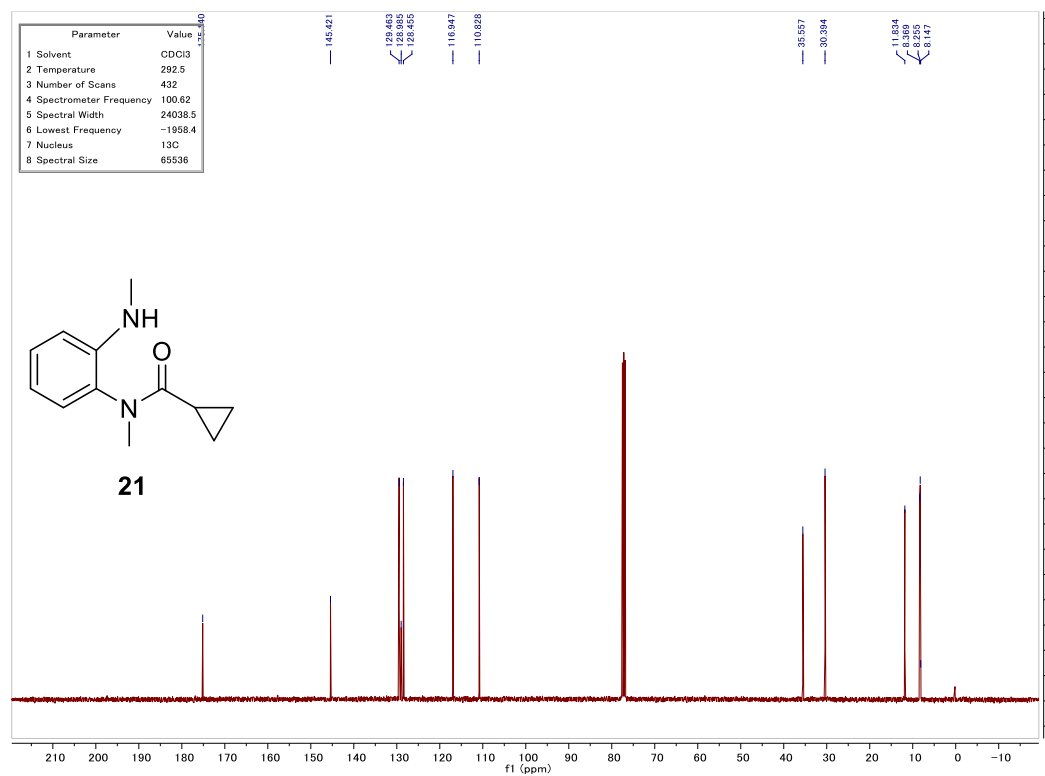
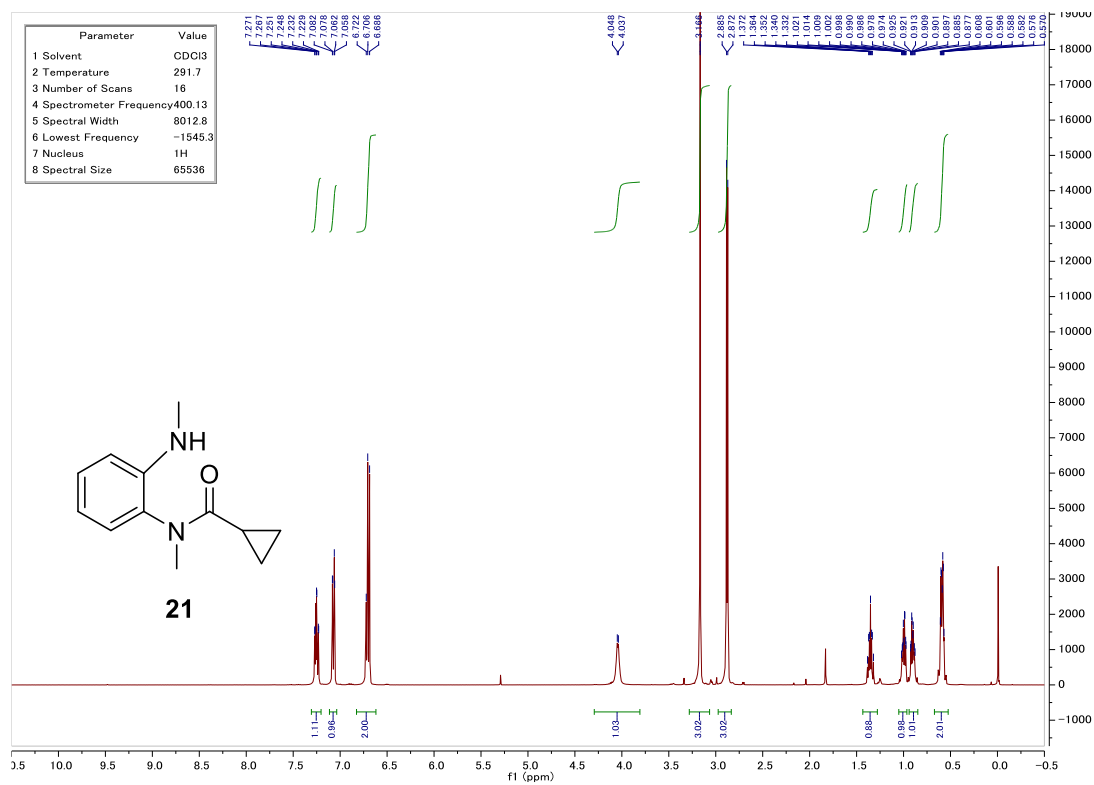


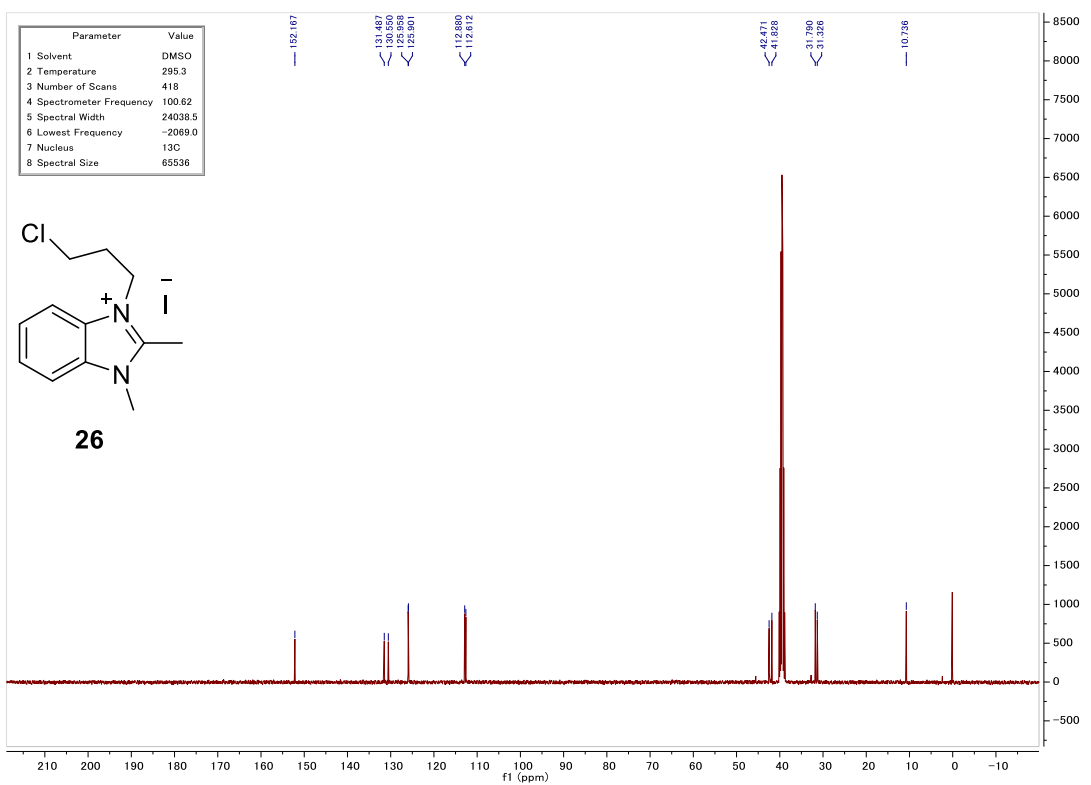
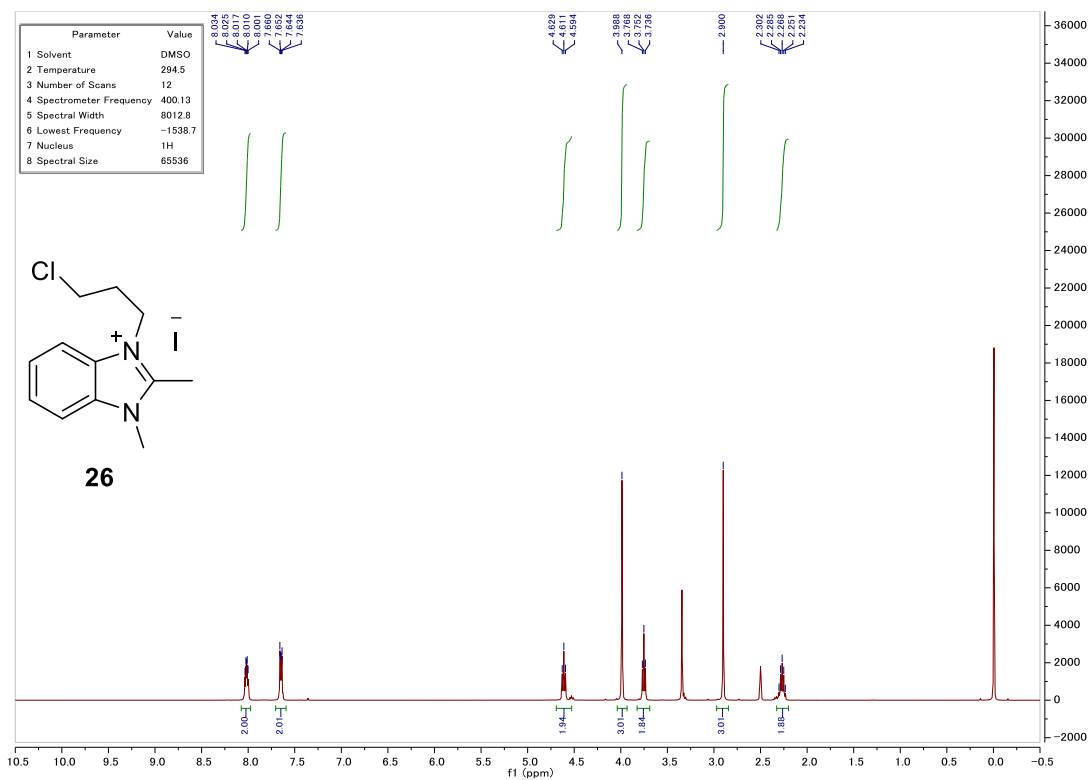


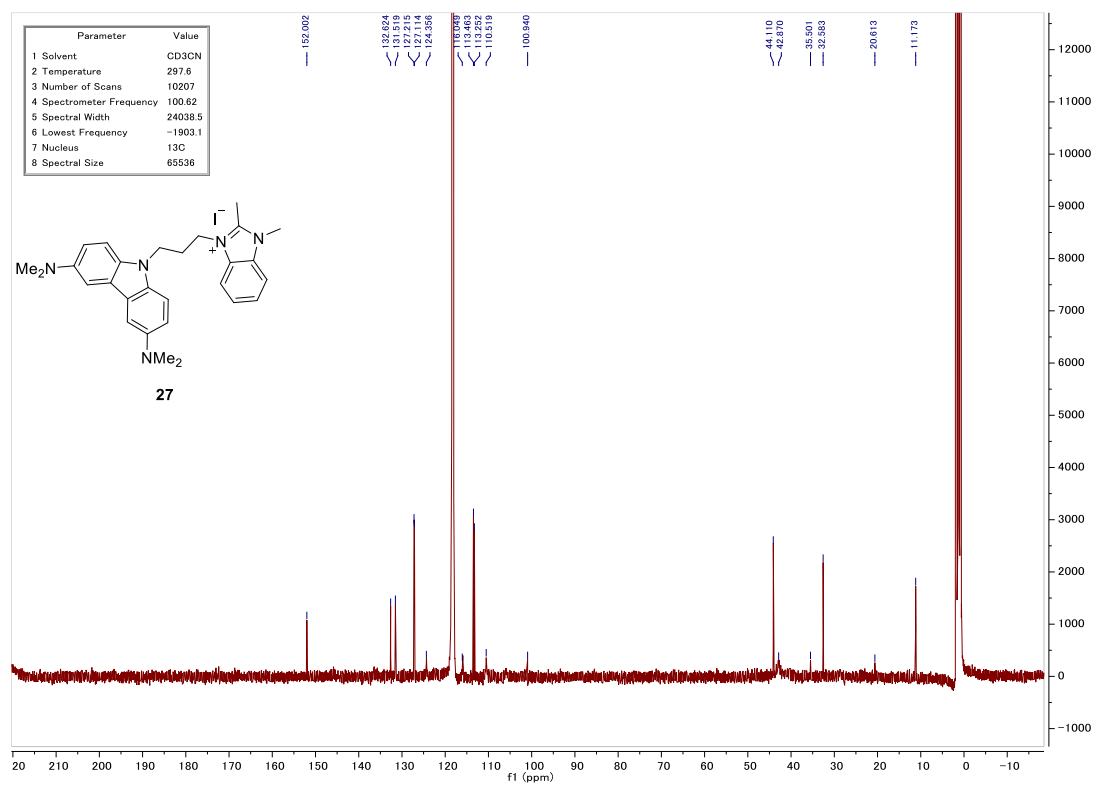
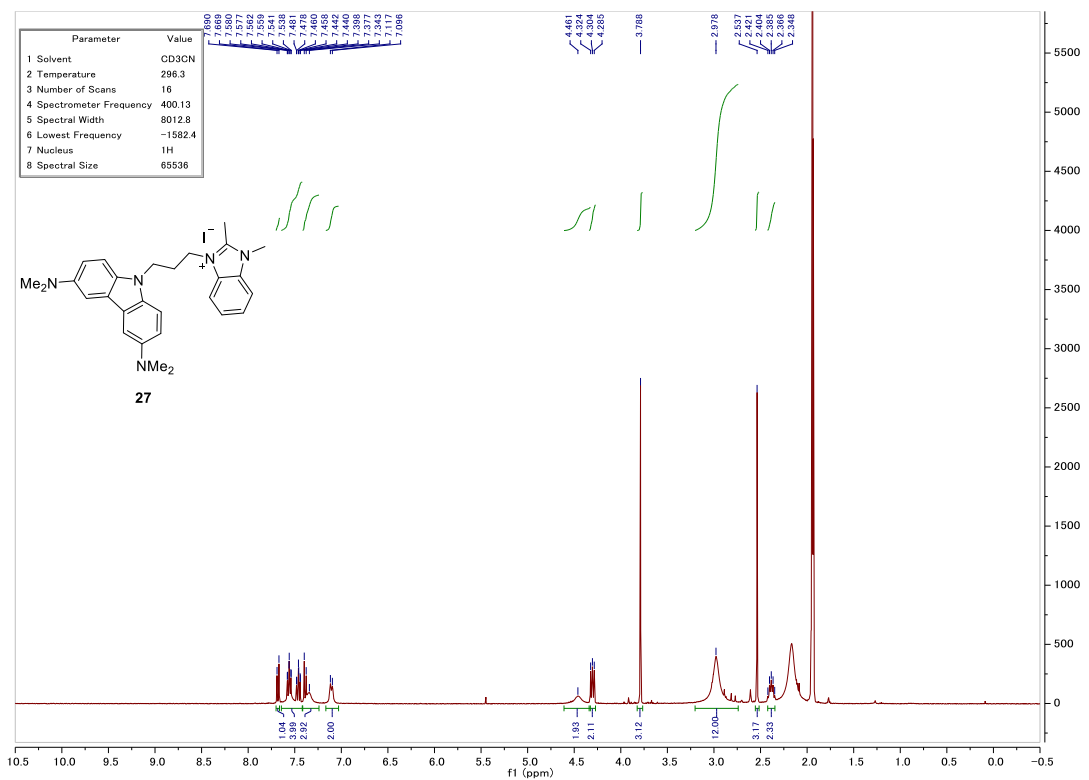


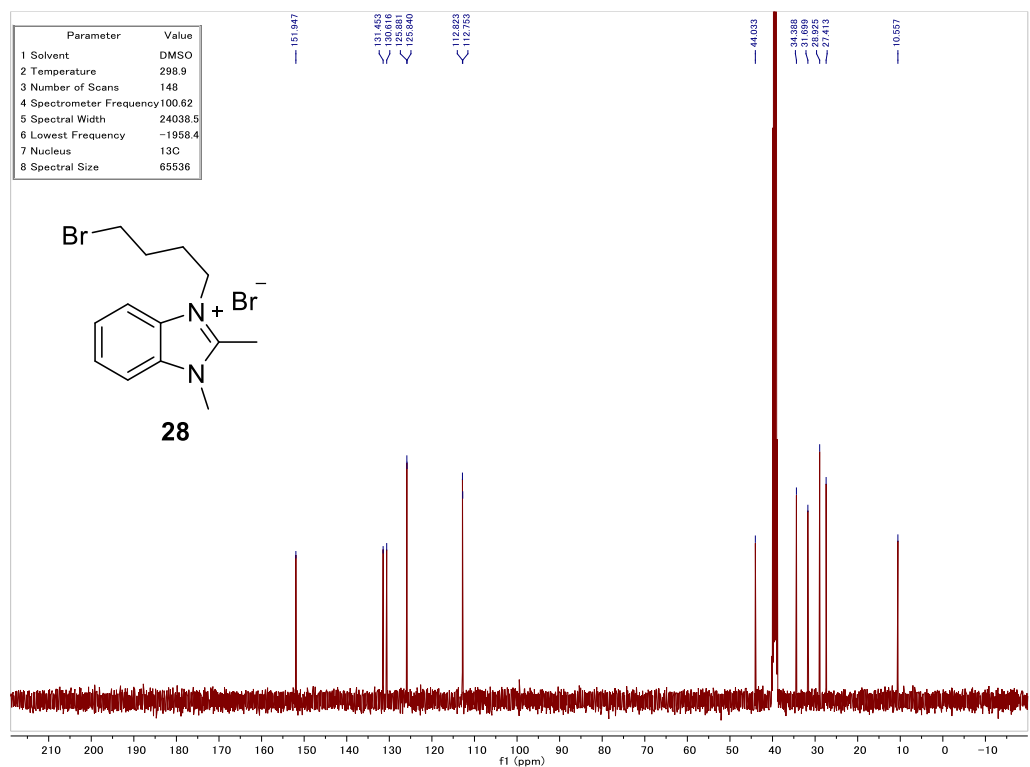
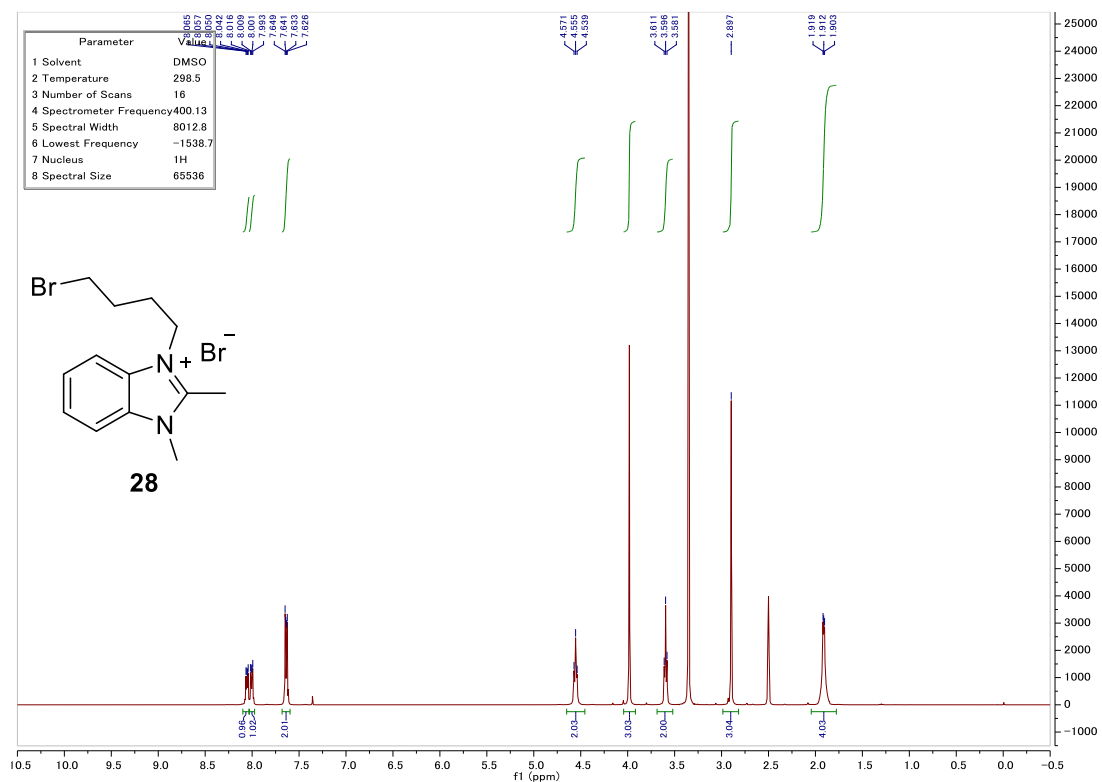


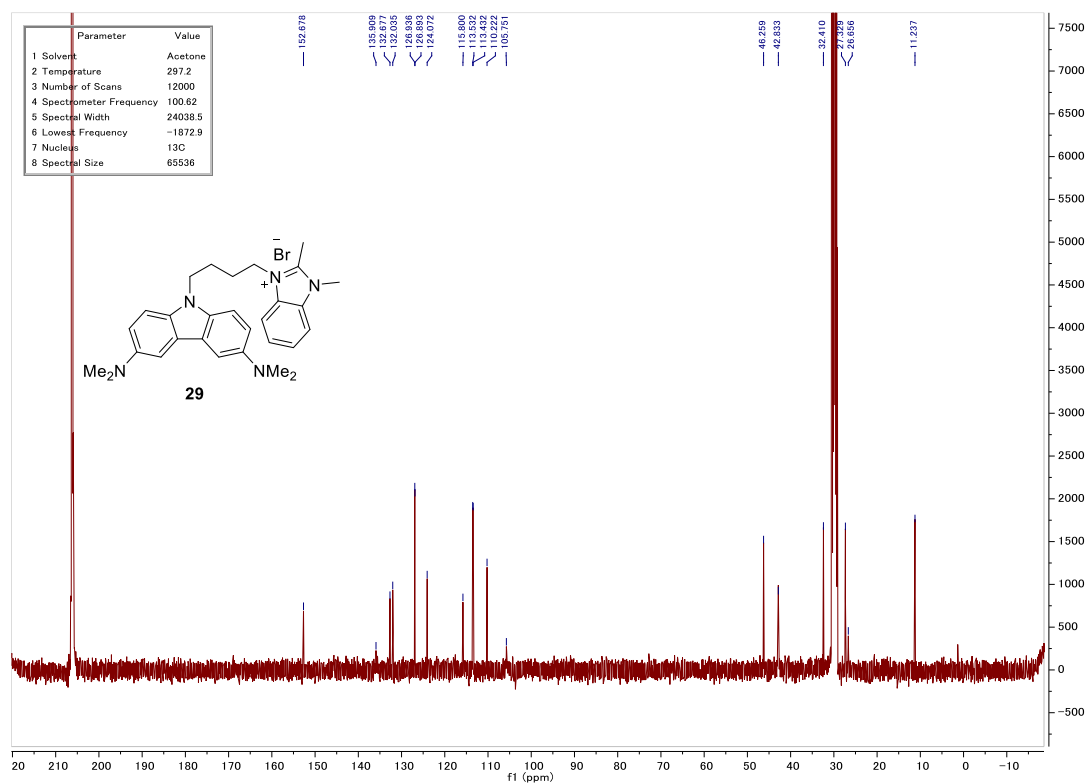
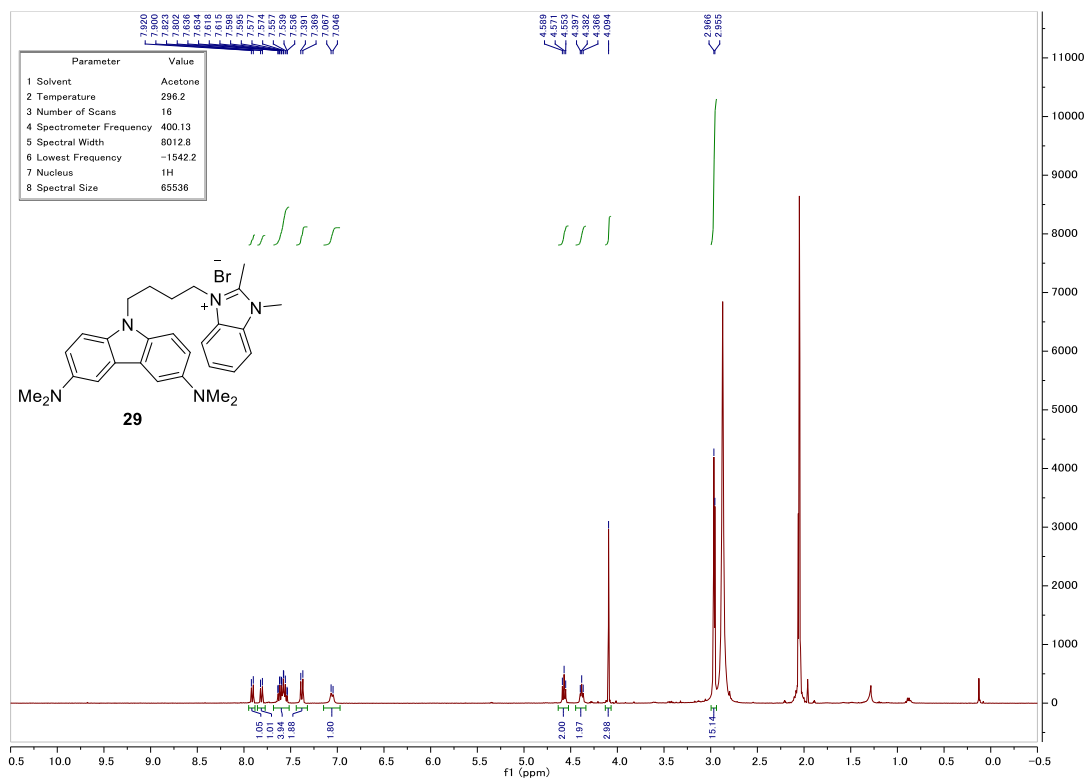


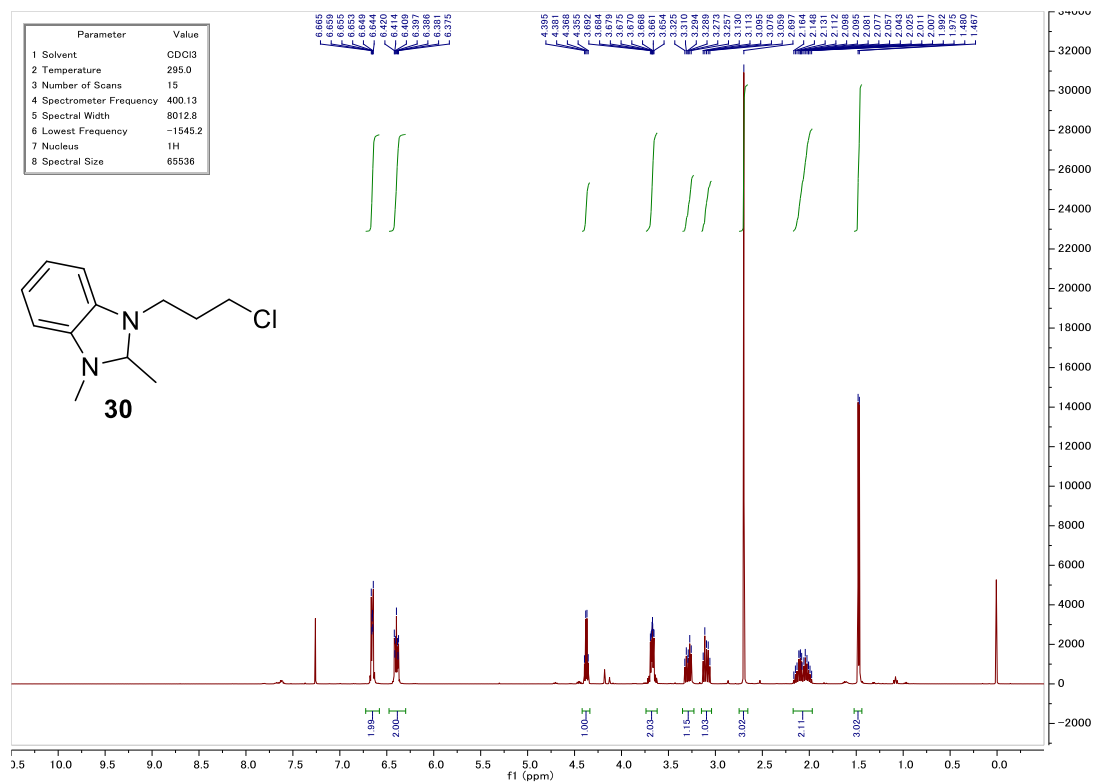
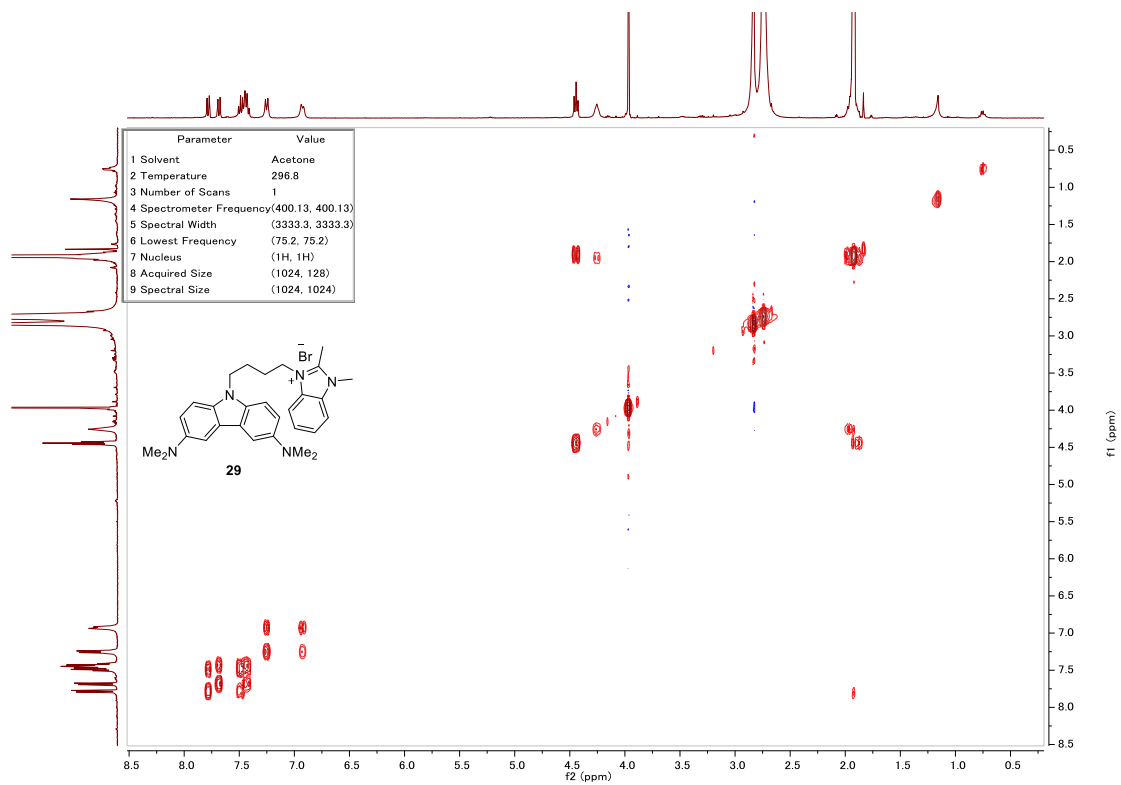


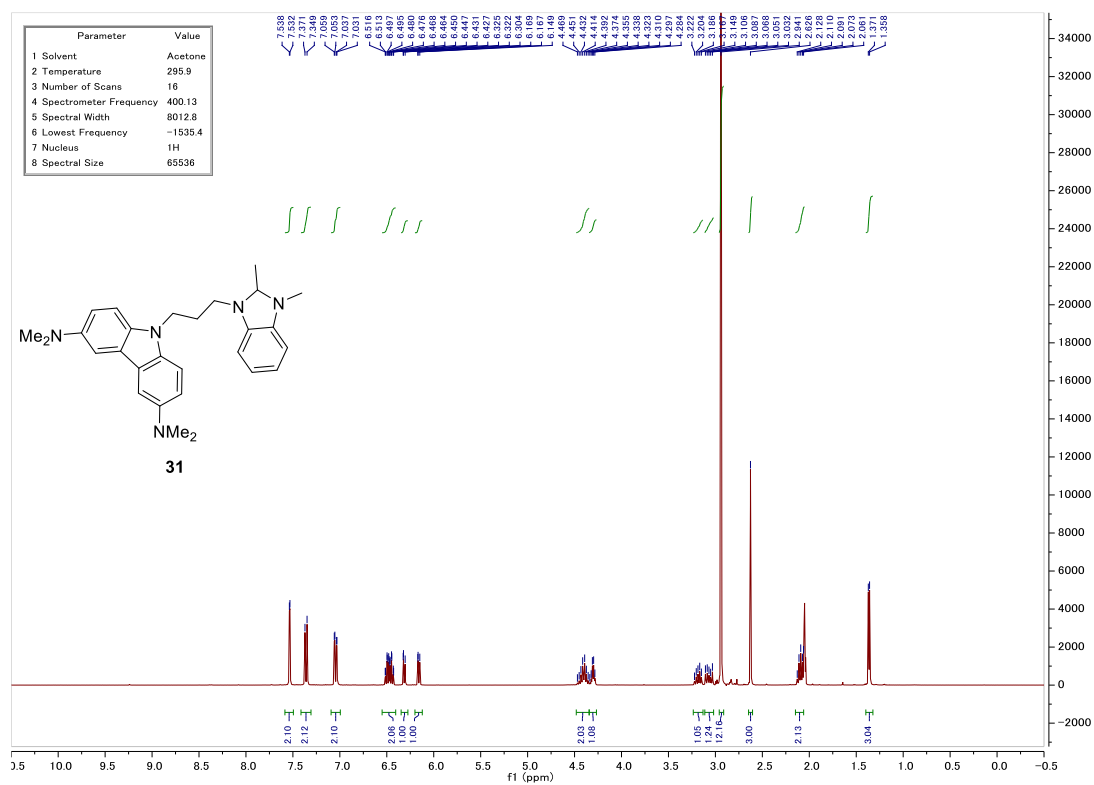
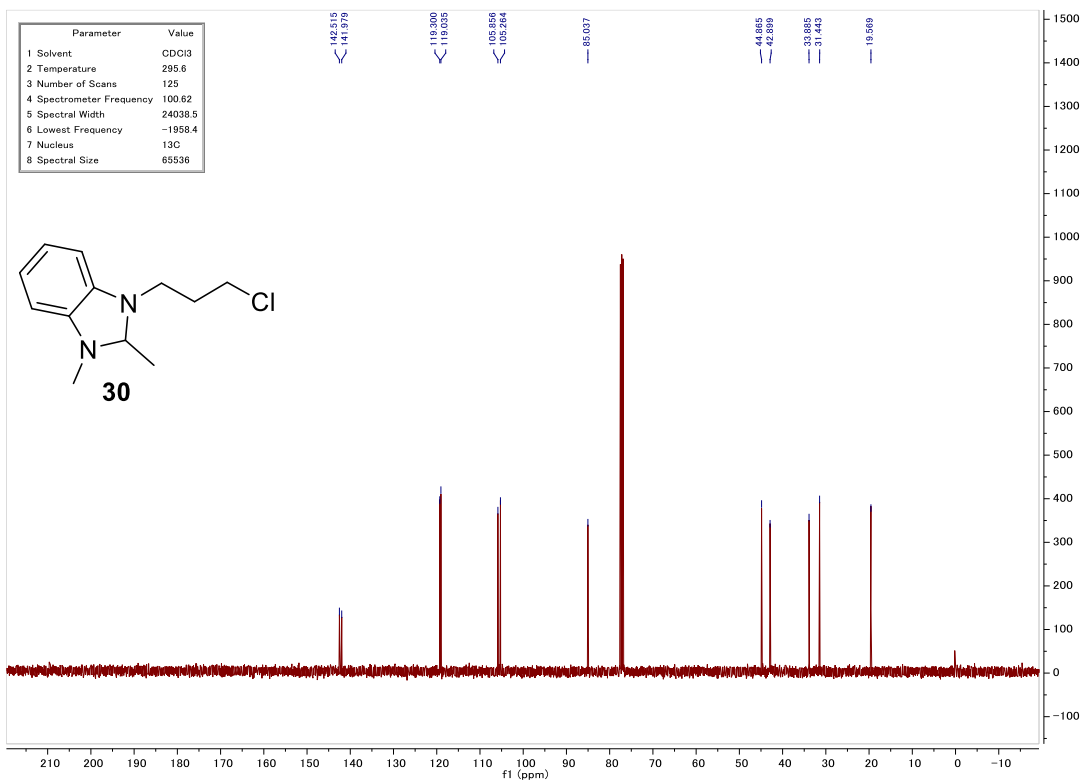


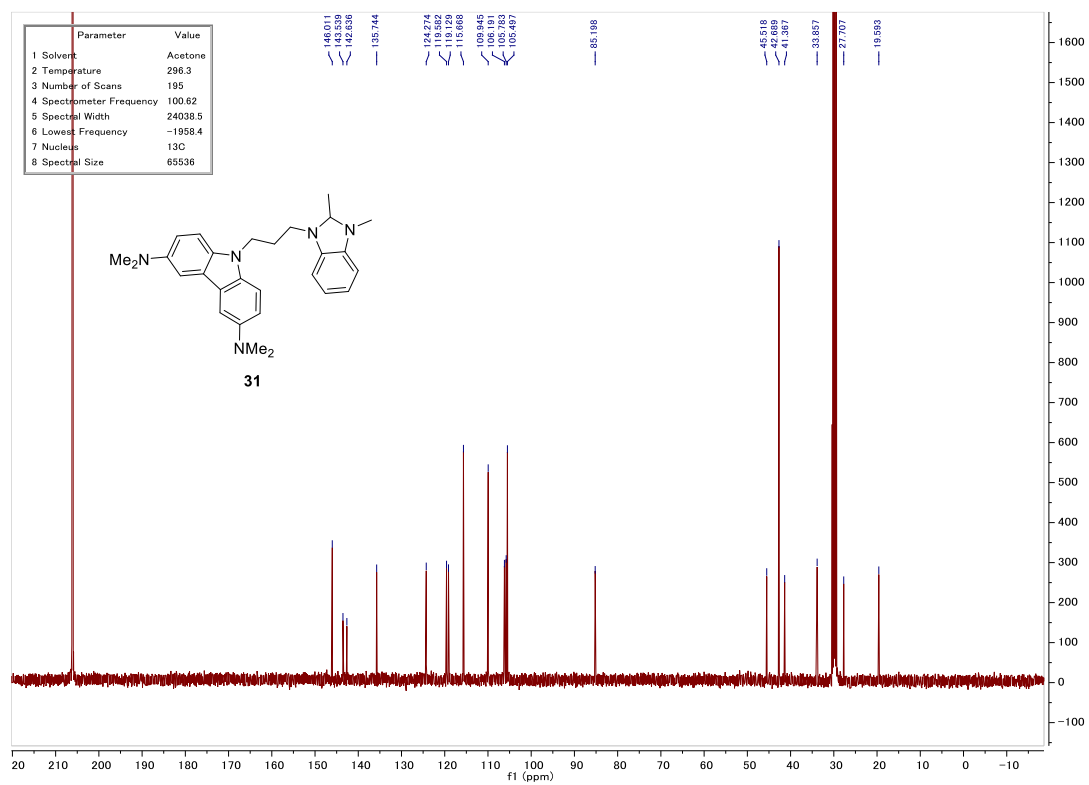












18. List of publications

1. Matsubara, R.; Kim, H.; Sakaguchi, T.; Xie, W.; Zhao, X.; Nagoshi, Y.; Wang, C.; Tateiwa, M.; Ando, A.; Hayashi, M.; Yamanaka, M.; Tsuneda, T. Modular Synthesis of Carbon-Substituted Furoxans via Radical Addition Pathway. Useful Tool for Transformation of Aliphatic Carboxylic Acids Based on "Build-and-Scrap" Strategy. *Org. Lett.* **2020**, *22*, 1182-1187.
2. Xie, W.; Hayashi, M.; Matsubara, R. Borylfuroxans: Synthesis and Applications. *Org. Lett.* **2021**, *23*, 4317-4321.
3. Xie, W.; Xu, J.; Idros, U. M.; Katsuhira, J.; Fuki, M.; Hayashi, M.; Kobori, Y.; Matsubara, R. Non-metal photochemical reduction of CO₂ to formate with organohydride-recycle strategy. (Submitted to Nature Chemistry in December 2021, doi number of pre-print: 10.26434/chemrxiv-2021-ch3ts).